Application of Boron Nitride Nanotube Interlayers for Thermal Management of 2D and 3D Printed Flexible Electronics

By Kaitlin Wagner

A THESIS

SUBMITTED TO THE UNIVERSITY OF OTTAWA

IN PARTIAL FULFILLMENT OF THE REQUIREMENTS FOR THE

DOCTOR OF PHILOSOPHY DEGREE IN CHEMICAL ENGINEERING

DEPARTMENT OF CHEMICAL AND BIOLOGICAL ENGINEERING

FACULTY OF ENGINEERING

UNIVERSITY OF OTTAWA

Abstract

The development of flexible printed electronics, which are compatible with low-cost fabrication techniques, lightweight and can be fabricated over large areas, enables the integration of devices into existing architectures with diverse form factors that rigid silicon-based electronics cannot accomplish. However, flexible substrates derived from thermoplastics are typically temperature sensitive and are susceptible to degradation when exposed to elevated temperatures during device fabrication and the application of high voltages during operation. To address these deficiencies, highly efficient thermal management techniques and materials that can be integrated directly into flexible electronic devices without compromising their electrical properties and performance are required.

My thesis presents the development and application of thin films fabricated from boron nitride nanotubes (BNNT) as an interlayer for thermal management in printed electronic structures. I first report the efficacy of the ultra-thin BNNT interlayers to reduce heat damage caused to the substrate during intense pulsed light sintering of molecular ink traces, successfully demonstrating the fabrication of highly conductive and morphologically uniform traces. I then translate this concept towards utilizing the thermally conductive properties of the BNNT interlayer to improve heating uniformity in screen-printed flexible transparent heaters at high generated temperatures without significantly affecting trace morphology. Next, I substitute the traditional chlorinated solvent base of the BNNT dispersion for ethanol, resulting in no adverse effects to the electrical, mechanical or thermal properties of the transparent heater architecture and enabling opportunities to utilize chemically sensitive device materials. Finally, I demonstrate that the BNNT interlayer successfully dissipates mechanical and thermal stress imparted on 2D printed traces that were transformed into 3D features using thermoforming techniques. Overall, my thesis demonstrates a significant contribution to knowledge towards the development of printed electronics on temperature sensitive plastic substrates.

Résumé

Le développement des appareils électroniques imprimées qui sont compatibles avec des procédés de fabrication simple et peu coûteux, ainsi que légère, souple, pliable et peuvent être fabriquées sur de grandes surfaces, permet l'intégration des appareils dans les architectures diverses qui ne sont pas accessibles aux électroniques rigides qui sont fabriqués avec le silicium. Cependant, les substrats flexibles dérivés de thermoplastiques sont généralement sensibles à la température et se dégradent lorsqu'ils sont exposés à des températures élevées pendant les processus de fabrication et avec l'appui des hautes tensions pendant le fonctionnement. Pour faire face à ces problèmes, des techniques de gestion thermique efficaces et des matériaux qui peuvent être intégrés directement dans les architectures et dispositifs électroniques flexibles sans compromettre leurs performances électroniques sont nécessaires.

Ma thèse représente le développement et l'application des couches minces fabriquées avec des nanotubes de nitrure de bore (BNNT, *Boron Nitride Nanotubes*) en tant que couche intermédiaire pour la gestion et pour l'atténuation de chaleur dans les dispositifs électroniques imprimées. J'ai d'abord rapporté l'efficacité de la couche intermédiaire ultra-mince de BNNT pour diminuer les dommages causés par la chaleur au substrat pendant le frittage par lumière pulsée des traces d'encre moléculaire imprimées et démontre la fabrication des traces hautement conductrices et morphologiquement uniformes. J'ai utilisé ensuite les propriétés thermoconductrices de la couche intermédiaire de BNNT pour améliorer l'uniformité du chauffage dans les appareils de chauffage transparents flexibles tout en maintenant l'intégrité du dispositif à des températures élevées. Ensuite, j'ai remplacé les solvants chlorés traditionnel pour la dispersion des BNNT par l'éthanol, ce qui n'a eu aucun effet sur les performances électriques, mécaniques ou thermiques des appareils de chauffage transparente et a ouvert la voie à l'utilisation de matériaux sensibles aux produits chimiques. Enfin, je montre que la couche intermédiaire de BNNT dissipe les contraintes mécaniques et thermiques sur des traces imprimées en 2D qui ont été transformées en caractéristiques 3D à l'aide de techniques de thermoformage. Dans l'ensemble, ma thèse apportent une contribution significative à la connaissance du développement de l'électronique imprimée sur des substrats plastiques sensibles.

Acknowledgements

I would first like to thank my supervisors, Dr. Benoît Lessard and Dr. Chantal Paquet, who were both integral in the development and guidance of the work presented in this thesis. You have both given me sincere mentorship throughout my graduate studies, and I will be forever grateful for the welcoming opportunity to conduct my work at the National Research Council facilities. I would also like to thank those who I worked closely with at the National Research Council for their knowledge and expertise, as well as their continuous support during my years in their laboratories. Finally, I want to express gratitude towards both past and present members of the Lessard Research Group, who's many facets of research kept me curious and consistently reminded of how vast and impactful the world of scientific research can be.

A special thanks to my parents Glenn and Johanna, and my Tante who unconditionally listened, supported, and loved me regardless of whether science was or wasn't working. To my sister Elise, there is no one else I would want to share an office with during a global pandemic, and I thank you for being an important source of inspiration for me during this time. To my Uncle Roy, although I never had the pleasure of meeting you, I am honored to have completed graduate school in the same department you received your Master's degree. I hypothesize that it runs in the family.

I want to thank several individuals who helped me traverse graduate school and made the experience as joyful as possible. To Ben, Chris, Curtis, Halynne, Rose, and Tousi, your friendship throughout this process was integral to my success. Without you, how would I have learned that polymers are in fact not small molecules or successfully determined that "these are metals". For those far away from me – Nirvana, Sam, and Whitney – thank you for keeping me close to your hearts these past six years.

Finally, thank you to my thesis committee, Dr. Tricia Carmichael, Dr. Pierre Berini, Dr. Adya Karthikeyan, and Dr. Samuel Huberman, for your time and consideration in reading and assessing the work that summarizes my doctoral thesis.

List of Peer-Reviewed Journal Article Contributions

Publications as Lead Author

Statement of contributions are found at the beginning of each chapter.

1. **Wagner, K.**; Kell, A. J.; Liu, X.; Gaburici, L.; Manion, J.; Paquet, C.; Lessard, B.H. Improving printed and thermoformed conductors on polycarbonate with a BNNT thin film interlayer for next-generation in-mold electronics. *Advanced Electronic Materials*, **2025**, Submitted Manuscript.

2. Kell, A. J.*; **Wagner, K.***; Liu, X.*; Lessard, B. H.; Paquet, C. Advanced Applications of Metal–Organic Decomposition Inks in Printed Electronics. *ACS Appl. Electron. Mater.* **2024**, *6* (1), 1–23. *(*equal contribution*)

3. **Wagner, K.**; Zou, S.; Martinez-Rubi, Y.; Kell, A. J.; Paquet, C.; Lessard, B. H. Towards Sustainable Transparent Flexible Heaters: Integration of a BNNT Interlayer Using Green Solvent Substitution. *Flex. Print. Electron.* **2023**, *8* (2), 025005.

4. **Wagner, K.**; Kell, A. J.; Martinez-Rubi, Y.; Paquet, C.; Lessard, B. H. Engineering Silver Microgrids with a Boron Nitride Nanotube Interlayer for Highly Conductive and Flexible Transparent Heaters. *Adv Materials Technologies* **2022**, 2200037.

5. **Wagner, K.**; Paquet, C.; Martinez-Rubi, Y.; Genest, M.; Guan, J.; Sampson, K. L.; Kim, K. S.; Kell, A. J.; Malenfant, P. R. L.; Lessard, B. H. Boron Nitride Nanotube Coatings for Thermal Management of Printed Silver Inks on Temperature Sensitive Substrates. *Adv. Electron. Mater.* **2021**, *7* (5), 2001035.

Publications as Co-Author

The full abstract and statement of contributions are found in Chapter 7.

1. Tousignant, M. N.; Tischler, V.; **Wagner, K.**; Lin, Z. S.; Brusso, J.; Izquierdo, R.; Lessard, B. H. Aerosol Jet Printed Temperature Sensors Using an Environmentally Friendly Bilayer Dielectric. *Flex. Print. Electron.* **2024**, *9* (1), 015012.

Table of Contents

List of Figures

List of Tables

Nomenclature

AFM: atomic force microscopy

Ag: silver

AgND: silver neodecanoate

BN: boron nitride

BNNT: boron nitride nanotubes

C: carbon

CCC: current carrying capacity

CNT: carbon nanotubes

Cu: copper

EDS: energy dispersive x-ray spectroscopy

EtOH: ethanol

FPM: feet per minute

I: current

IPL: intense pulsed light

IR: infrared

ITO: indium tin oxide

J: joule

K: thermal conductivity

L: nominal length

MINK: molecular ink

MW: molecular weight

NIR: near infrared

NP: nanoparticle

NW: nanowire

P: generated Joule power

rra-P3HT: regiorandom poly(3-hexylthiophene)

PET: polyethylene terephthalate

PLA: polylactic acid

PVB: poly(vinyl) butyral

Q: solution flowrate

R: electrical resistance

R_a: average roughness

R_q: root-mean-square roughness

R_s: sheet resistance

R_t: peak to valley height roughness

R2R: roll-to-roll

RMS: root mean square

SEM: scanning electron microscopy

S%: solid content

%T: optical transmittance

T: temperature

t: time

T_g: glass transition temperature

T_m: melting temperature

T_{rt}: room temperature

τ: exponential time constant

t_z: thickness

TCE: transparent conductive electrode

UV: ultra-violet

UV-Vis: UV-visible spectroscopy

V: applied voltage

λ: wavelength

w: nominal width

W: coating width

Ω: ohm

Chapter 1: Thesis Introduction

A portion of this chapter was published in the journal "ACS Applied Electronic Materials": Kell, A. J.; Wagner, K.; Liu, X.; Lessard, B. H.; Paquet, C. Advanced Applications of Metal–Organic Decomposition Inks in Printed Electronics. ACS Appl. Electron. Mater. 2024, 6 (1), 1–23.

1.1. Printed electronics

Electronic devices and their components have been incorporated into the lives of over half the world's population to some degree. The continuous improvement of active electronics in the world has fueled significant research and development efforts towards achieving the fastest and most inexpensive fabrication routes possible. Printed electronics offer several key advantages over conventional electronics, achieving cost-effective, large-scale manufacturing using additive techniques while simultaneously reducing material waste and production expenses. Their flexibility allows for the development of lightweight, bendable, and even stretchable devices, making them ideal for wearable technology, biomedical sensors, and flexible displays. Additionally, printed electronics can be fabricated on diverse substrates, including plastics and textiles, expanding their applications beyond rigid circuit boards.

Printing technologies enable solution-based deposition and processing at low temperatures, which is ideal for high throughout fabrication, and are considered inexpensive fabrication techniques in comparison to energy-intensive processes such as physical vapour deposition and focused ion beam processing.[1–4] Technologies such as screen printing,[5,6] ink-jet printing,[7–9] and gravure printing,[10,11] have all been demonstrated to successfully fabricate various layers in printed electronic device architectures, ranging from basic components such as passive electrodes to fully functioning devices such as solar cells, thin film transistors, and organic light emitting diodes.[12–16] The ability to integrate them into roll-to-roll manufacturing processes enhances scalability, making them a promising technology for next-generation electronic devices.

Printing techniques to fabricate devices brings about opportunities to combine printable materials and substrates in new ways with easily customizable electronic designs, however they also introduce complications, where the whole material package (solvent, inks) must share similar compatibilities (temperature, chemical, environmental stability). Metal printed conductors are among the most common and basic components of electronic and electrochemical applications and

their processing is critical to the resulting device performance. Changes such as the substrate chemistry, the ink formulation, and processing conditions all influence the final device performance and therefore it is necessary to optimize the print for the respective application.

1.2. Printed transparent electrodes

The goal of any conductive electrode is to achieve continuous steady-state operation upon application of an electrical field. The greater the amount of current travelling through the electrode upon applied voltage results in a higher power output for a device and ultimately the better the devices' performance and efficiency. **Figure 1.1** illustrates an example of a silver grid transparent and flexible conductive electrode designed and fabricated by Yang and co-workers.[17] Depending on the application, such as smart windows, touch screens or light emitting diodes, it is important that the electrodes are also transparent, and these are referred to as transparent conductive electrodes (TCEs). Printed TCEs can be applied to plastic substrates while remaining visually transparent, yet electrically conductive, leading to their integration into applications that require a light weight, flexible and transparent properties.[18] It is crucial to simultaneously optimize the conductivity and the transparency, developing a structure property and process relationships between electrical performance and optical transparency of the TCE, since typically as the transparency is increased, the conductivity is reduced. However, choice in materials, manufacturing process and environment will all greatly influence the conductive properties of flexible electrodes and therefore need to be carefully designed. In an attempt to maximize performance metrics, current printed electronic components and devices are being pushed to their energy and power density limits, leading to high heat accumulation in the printed components.[19] Furthermore, in order to incorporate rapid processing techniques for increased production, photonic sintering techniques like intense pulsed light and laser sintering have been employed due to their extremely short processing timeframes.[7,20–22] Such heat accumulation during both fabrication and operation, combined with the desire to miniaturize device architectures for easier integration into existing architecture necessitates a highly versatile thermal management tool.

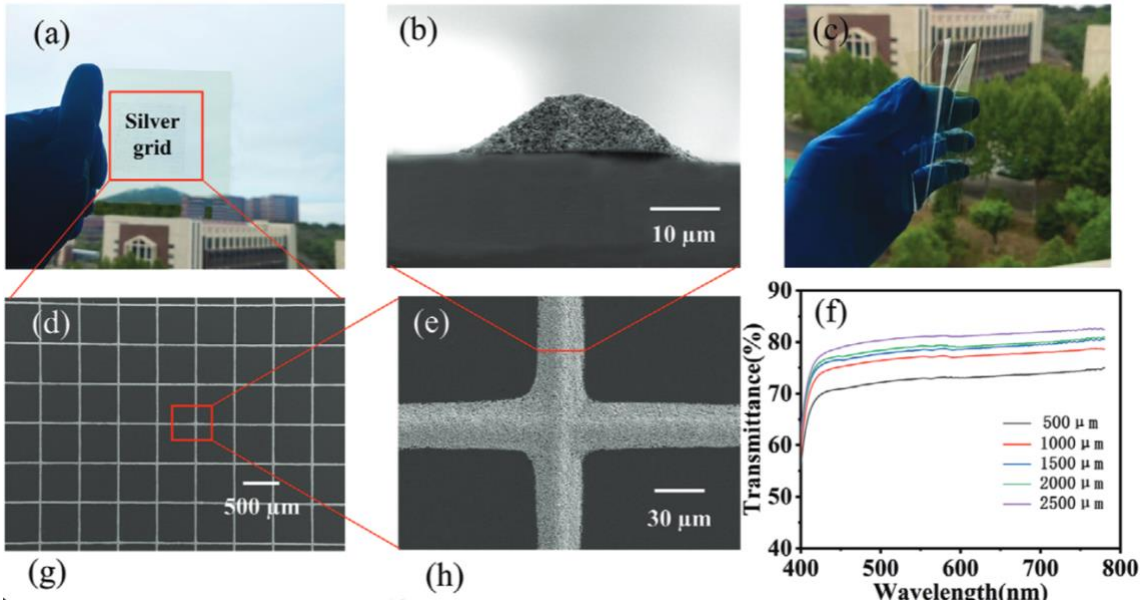

Figure 1.1. a) Macroscopic image of the fabricated harsh-environment flexible transparent electrodes (HFTE), b) SEM image of the cross-section of the silver wire in (e), c) macroscopic image of the fabricated HFTE under bending, d) SEM image of the silver mesh in (a), e) SEM image of the intersection points of the pattern in (d), and (f) representing the optical transmittance of the HTFE with the substrate present. (Reproduced from ref 17, Copyright Wiley 2022)

1.2.1 Transparent heaters based on printed electronics

Electrodes have been demonstrated in a variety of applications in electronic devices such as solar cells and thin film transistors, however they can inherently operate as a heating element without the assistance of other organic or inorganic layers. The performance of an electrode as a printed heater hinges on both the electrical and thermal conductivity of the conductor and substrate respectively, while the electrode's design plays a large role in determining temperature uniformity and how efficiently the heat spreads throughout the electrode structure.

Printed heaters have one primary function, to uniformly release heat, and have been demonstrated across a wide variety of applications. Utilizing TCEs as a heater allows for easy placement into existing architecture, as the device structures are lightweight and transparent. Similar to traditional heating elements, printed heaters are extremely useful in sub-zero climates that experience heavy build-up of snow and ice over the winter months. Objects such as stop lights, vehicle head lights and windshields can be shrouded by ice or snow during inclement weather, and

in these situations a transparent heater can release heat across the plastic encasing of the bulb or a glass frame above freezing temperatures without significantly reducing the amount of light traveling past the heater or reducing visibility while driving. Lee *et al.* demonstrated a AgNW heater with a graphene oxide and silane over-coating protective layer as a replacement for traditional heating wires in rear automobile windows. The heater displayed a high optical transmittance of 91%, and upon applied voltage demonstrated an increase in surface temperature from -15 ˚C to up to 30 ˚C within 5 minutes.[23] A study completed by Park *et al*. developed an embedded AgNP large-area patterned metal mesh, demonstrating heating rates of 1.9, 3.4 and 4.5 ˚C s^{-1} upon applied voltages of 8, 15, and 21 V respectively. The mechanical robustness was demonstrated by little change in resistance after a 10,000 bending cycle testing, and a consistent uniform temperature distribution highlighted applications intended for defrosting and de-icing in electric vehicles that require low power operation.[24] This type of application can also expand to instances where fog buildup can cloud windows on buildings or vehicles. Cheong *et al*. demonstrated the use of a large area (5.2 x 3.1 cm) ZTO/Ag/ZTO transparent heater on glass for defogging humid air, achieving a steady-state temperature increase from 29.3 ˚C to 44.2 ˚C in as little as 50 s and successfully removing all water droplets hindering the chamber's visibility.[25]

Printed heaters have also recently become integrated into a variety of biomedical applications due to their design versatility and compatibility with flexible substrates. One primary function of printed heaters is their usefulness as thermotherapy pads.[26–30] Printed heaters can be placed onto the surface of the skin to apply heat to areas of the body within a 40-50 ˚C temperature range to facilitate pain relief, inflammation prevention, and to improve blood circulation. Another biomedical application explored for printed heaters is thermal-activated drug delivery.[31,32] The transparency of flexible printed heaters is a key feature of this technology, as it provides medical professionals with the ability to visually monitor the release of the drug into the skin. One limitation of this application is that it requires near full biocompatibility across each device layer so as to not introduce any toxic or dangerous materials into the body, which can ultimately limit the type of substrate and printed heater material used. Lastly, flexible heaters in biomedical applications have extended to thermal sterilization for harmful bacteria such as E. coli, S. pneumoniae, and S. faecalis, amongst other bacterial strains.[33] A flexible wireless mesh heater was developed by Chen *et al*. to sterilize E. coli for lab-on-a-chip devices.[34] The heater achieved uniform heat distribution at 55 ˚C which was demonstrated to be sufficient enough to halt growth

and eradicate an E. coli colony placed within the heater area. Additionally, Kim *et al*. designed a Cu-plated polyacrylonitrile microfiber layer for added thermal sterilization in reusable face masks.[35] The heating microfiber layer achieved a maximum operational temperature of 152 ˚C and antibacterial performance was enhanced when heat was generated, observed by a reduction in E. coli density. Further applications into sterilization of bacteria strains can be advantageous in eradicating and reducing infection rates of potentially harmful diseases either in wearable applications or to incorporate printed heaters into surfaces commonly shared by the general public such as on public transportation for rapid sterilization.

1.2.2 Material choice

The material used to fabricate the TCE has the greatest impact on its baseline conductivity, and so minimizing the resistance of the printed material is crucial. Various printable materials have been developed for electrode fabrication, primarily categorized into conductive oxides, polymers, carbon-based materials, nanocomposites, and metals.[36] Indium tin oxide (ITO) in particular is a well-established metal oxide that has been favoured as a TCE material due to its wide band gap, high conductivity and notable optical transparency.[37] Despite these favourable properties, the feasibility of ITO films for continued mass production has come into question due to high-cost deposition techniques, poor mechanical durability, and finite indium resources.[38,39] In response, researchers have become interested in studying and expanding upon other materials that are more compatible with printed electronics techniques, with a summary of material electro-optical properties in comparison to ITO shown in **Figure 1.2**.

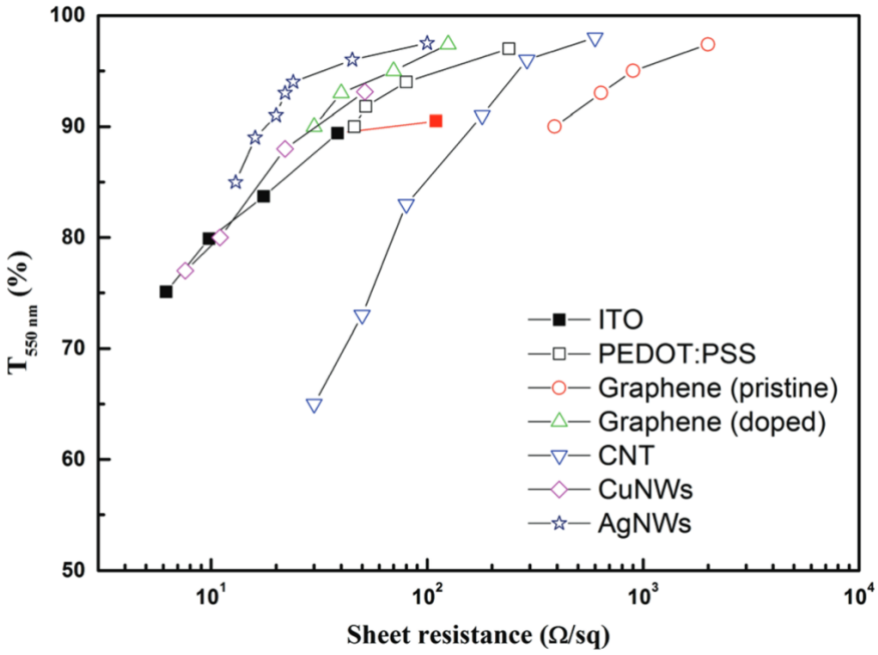

Figure 1.2. Sheet resistance versus light transmittance (@ 550 nm) for several typical transparent electrode materials (Reproduced from ref 40, Copyright The Royal Society of Chemistry 2020)

Advancements in printing technologies and printable ink formulations have created new avenues for fabricating metal electrodes more rapidly and at lower processing energy requirements. Metal electrodes are typically derived from gold (Au), copper (Cu), or silver (Ag), and can be paired with various polymers and carbon-based materials to create highly conductive composite materials. Gold electrodes have demonstrated high conductive performance and little to no oxidation in ambient atmosphere; however, their extremely high cost and brittleness prevents them from being integrated into large scale fabrication processes and flexible applications.[41,42] Copper electrodes are inexpensive and can be processed at very low energy and temperature requirements, and as such there has been significant research in developing Cu ink formulations, ranging across Cu nanowires (NW),[43–45] Cu nanoparticle (NP) inks,[22,46,47] and Cu growth crystals[25] to name a few. However, their inherent oxidation to the surrounding environments both limits their application over time or requires a degree of encapsulation that may not be compatible with flexible device architectures. Similar to Cu ink, Ag inks have been developed in a multitude of formulations, including but not limited to AgNW inks,[48] AgNP inks,[49,50] Ag flake-based inks,[51] and Ag molecular inks (MINKs).[52,53] Silver ink formulations boast high conductivity similar to that of gold electrodes at a fraction of the cost and have demonstrated high compatibility with

flexible substrates.[54] Similar to Cu inks, Ag inks have relatively low processing temperature requirements (100 - 200˚C) that achieve uniform features, however their resistance to oxidation is significantly higher than Cu, making Ag inks the optimal trade-off of cost and performance for high throughput electrode fabrication. Ag MINKs are particularly advantageous for printed electronics in comparison to the Ag flake-based and AgNP inks, as they exhibit high conductive performance, high current carrying capacity, and low surface roughness upon printing.[52]

MINKs differ from particle-based inks by having only molecular components, affording them unique properties in comparison to the nanoparticle and flake inks typically used in printed electronics. For instance, due to their molecular nature, MINKs do not suffer from the same challenges as particle-based inks, as they can easily flow through narrow restrictions including fine screen meshes (screen printing) and nozzles (inkjet, aerosol jet, and direct-write/extrusion printing), enabling high-resolution printing. MINKs are most commonly silver and copper carboxylates that, once heated or treated with light, will self-reduce into their metal states. The ligands and ink components become volatile during the sintering step, leaving behind a conductive metal trace with low or no residue. Ligands coordinated to the metal center influence the chemical and physical properties of the precursor compounds, such as the solubility of the metal precursor in the carrier (i.e., solvent) and the decomposition mechanism and temperature, as well as the stability of the nucleating and growing nanoparticles that make up the metal films once fully formed. Formulation with compatible components, such as carriers, binders, and rheology modifiers, affords the ink with desirable printing qualities. The ink formulation can also be tuned to ensure that the ink decomposes into a metal with optimal morphology leading to good electrical and mechanical properties. Therefore, Ag MINK formulations have been selected for this thesis because they hold significant potential in fabricating high performance, low-cost electrodes.

1.2.3 Processing techniques

Printed MINKs must be sintered to reduce the metal salt precursor into a metal and remove the organic components remaining in the traces of the ink to produce a conductive trace. Once gone, the metal precursor coalesces to form a continuous metal film within the deposited area of the ink, rendering the feature conductive and ultimately operational. A variety of factors can dictate the type of processing technique employed, such as the conversion time and energy requirements

of the ink, the heat sensitivity of the substrate, as well as the cost and compatibility of the technology for the target industry.

Thermal sintering is one of the commonly used techniques to process MINK traces, as it can be easily tailored to reach any reasonable temperature required to remove the unwanted organic matter from printed ink and unveil the desired metal feature.[55] This technique is well known to make morphologically uniform features with reliable repeatability for large-area printed features. However, since the decomposition temperature of the ink dictates the overall temperature within the oven chamber, the resulting heat accumulation and off-gassing from reaction byproducts limits the type of substrate that can withstand the conversion process. As such, other techniques have been developed to provide more control over the sintering location and temperature.

Photonic sintering uses wavelengths of light ranging between ultraviolet (UV) and infrared (IR) to sinter MINKs. An important benefit of photonic sintering is that it enables the use of low-cost and temperature sensitive substrates (e.g. polyethylene terephthalate) with MINKs that would otherwise require temperature-tolerant, expensive substrates (e.g., polyimide). During photonic sintering, the ink layer absorbs light, which is converted to heat and used to sinter the MINK layer. **Figure 1.3** highlights how differently the MINK material reduces when exposed to thermal and photonic sintering, exposing how the dense or porous nature of the traces can affect morphology. In photonic sintering, the heat generated remains localized within the volume of the ink and thus minimizes damage to the substrate. Photonic sintering can include intense pulsed light (IPL), UV, NIR or laser sintering.[56]

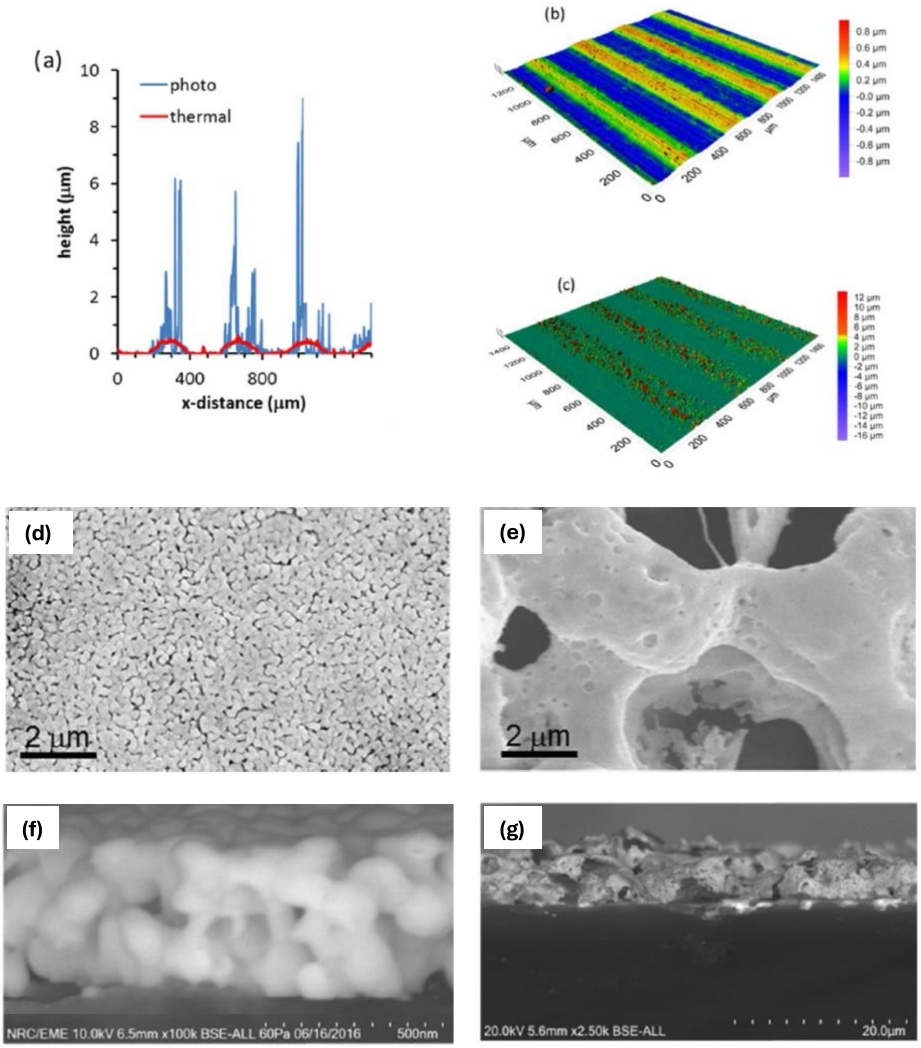

Figure 1.3. Cross-sectional analysis of screen-printed lines (a), where the thermally sintered lines are relatively smooth (red line) in comparison to the photonically sintered traces (blue line). Representative surface profile images of screen-printed ~200 µm wide traces after thermal (b, top right) and photonic sintering (c, bottom right). SEM images of screen-printed traces that have been thermally (d) and photonically (e) sintered.as well as a cross-sectional SEM image of the traces processed via thermal (f) and photonic sintering (g). (Reproduced from ref 52, Copyright American Chemical Society 2017)

Intense pulsed light (IPL) sintering uses micro- to milli-second pulses of high-intensity broad-band light to reduce metal precursors in MINKs into NPs.[57] The NPs subsequently absorb light, leading to further heat generation. The localized temperatures reached during IPL sintering

not only facilitate the coalescence of metal NPs to produce metallic films but also allow ink components to become volatile, forming residue-free metal films. Provided the correct combination of MINK and substrate are selected, the rapid and localized heating in the ink layer ensures that the surrounding substrate will not reach thermal equilibrium with the ink and therefore avoids thermal damage. As a result, substrates, that would normally be incompatible with a MINK due to its high decomposition temperature, can be used with IPL sintering. Although IPL sintering is an efficient method to process MINK, the morphology of the metal films tends to have less dense, less uniform, rough, and porous microstructures because of the metal precursor rapidly decomposing and the reaction byproducts quickly evaporating. **Figure 1.4** highlights how the morphology of the given metal feature can change at varying IPL sintering energies. Given that the main component of the MINK is the carrier and carboxylate anions, high energy and/or longer sintering time may be required to remove all the volatiles, causing damage to the substrate and suboptimal electrical performance of the metal film. Thus, tuning the IPL process parameters has been the focus of much research. Kalashnyk *et al.* used IPL sintering to convert inkjet-printed metal-organic decomposition inks that were based on copper formate and 2-amino-2-methyl-1-propanol to produce conductive copper features on PET under ambient conditions, suggesting that the electrical performance of sintered traces largely depends on the IPL power density used.[58] Song *et al.* reported IPL sintering of a Cu metal-organic decomposition ink made with copper nitrate hydrate in butoxyethanol with ethyl cellulose, producing resistivities of 5 μΩ cm at an IPL energy density of 8.5 J/cm^2. Lower energy densities (5.5 J/cm^2) increased the resistivity of the Cu film to ~1000 μΩ cm due to insufficient energy to fully reduce the copper precursor, whereas increasing the IPL energy to 9.5 J/cm^2 results in damage to the PET substrate and increased the resistivity of the copper film.[59]

In similar fashion to IPL sintering, MINKs can be exposed to UV light to produce conductive traces. The light intensity used in UV sintering is much lower than IPL sintering, however the decomposition mechanism is analogous, where the metal precursor is photo-reduced by UV light to create metal NPs that subsequently absorb light more effectively and further decompose the remaining metal precursor through an exothermic process localized within the deposited ink. Ranges of UV light, such as UVV (395 – 455 nm), UVA (320 – 395 nm), UVB (280 – 320 nm), and UVC (200 – 280 nm), can be used to push the same photoreduction process as IPL sintering, however in most cases, UV exposure alone is insufficient to convert MOD inks

to conductive traces. The only successful example of UV-sintered MINK printed traces was reported by Liu *et al*.[60] A silver oxalate/amino alcohol-based MINK was screen printed into 8 cm long traces with line widths of ~424, 530, and 628 μm on PET and exposed to UV irradiation for 4.5 min to form traces with resistivity values of on average of 12 μΩ cm. The UV dose used, 60.5 J/cm^2, enabled the conversion of the MINK metallic silver without damaging the underlying PET substrate. Experiments illustrated that the traces reached temperatures higher than those of the surrounding substrates, revealing that heat was generated through the UV-induced exothermic decomposition of the MINK as well as by the subsequent absorption of UV light by the as-produced Ag NPs' plasmon bands. For instance, a 2 cm printed circle on PET reached 150 °C while the areas with no ink reached 120 °C.

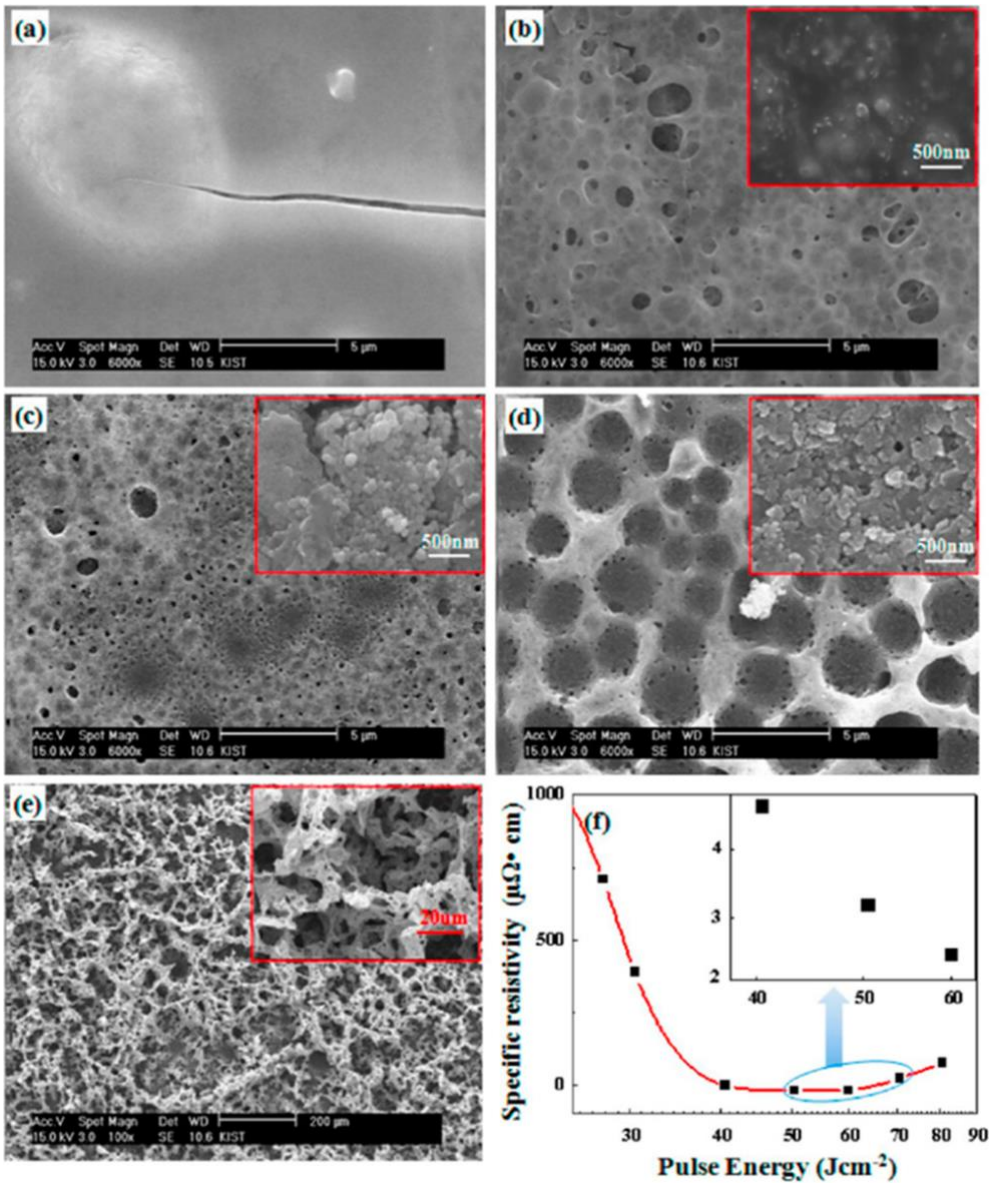

Figure 1.4. Microstructure and electric resistivity after the IPL treatment of the fabricated pattern with the Cu ion ink: (a) 16.5 J/ cm^2; (b) 30.5 J/cm^2; (c) 40.6 J/cm^2; (d) 50.5 J/cm^2; (e) 70.5 J/cm^2. (f) Electric resistivity as a function of IPL energy (Inset: high-magnification image; pattern thickness 4 ± 0.4 μm) (Reproduced from ref 59, Copyright American Chemical Society, 2013)

As detailed in these processing techniques, heat accumulation in the trace is a consequence of the photoreduction process. Interactions between the heated trace and the underlying thermoplastic substrate needs to be inspected to ensure that internal temperature does not significantly exceed the glass transition temperature of the substrate, as this could lead to deformation and more severely, melting of the substrate.

1.3. Performance Metrics

1.3.1 Electrical characterization (Resistance, Resistivity, CCC)

An electrode is a fundamental and simple component in a multitude of electronic devices, and so it is key that electrical performance is maximized while still considering manufacturing features such as efficiency, cost, and production time. For printed TCEs, resistance is typically analyzed in terms of sheet resistance R_s, where current is thought of as travelling through a thin film analogous to a two-dimensional system and therefore travelling exclusively parallel across the electrode.[61] The sheet resistance of a uniform geometry in two dimensions can be calculated as follows:

$$R = \frac{\rho}{t_z}\frac{L}{W} = R_s\frac{L}{W} \ [\Omega] \qquad [1.1]$$

where ρ is the resistivity, t_z is the thickness, L is the length, W is the width, and R_s is the sheet resistance. Another common electrical performance metric for printed electronic features is the current carrying capacity (CCC), which measures the amount of current a conducting material can withstand until it is no longer conductive.[62] For printed TCEs, reaching the CCC is typically caused by heat accumulation in the trace upon applied voltage, which leads to the underlying plastic substrate warping or melting and ultimately delaminating or deforming and breaking the TCE. Factors such as the ink material, substrate material, trace area, and processing conditions that affect the morphology of the conductive trace can all influence the electrical conductivity and response to elevated temperatures.

1.3.2 Thermal characterization

TCEs operate as a printed heater through resistive heating, or the Joule heating effect, which occurs when current is applied across a conductive material, resulting in the conductor experiencing stress due to the material's internal electrical resistance.[62] The current stress originates from interactions between the body of the conductor and with the charge carriers, where particle collisions between kinetically charged particles and atomic ions within conductor scatter randomly, converting energy from the electric field into thermal energy. As such, the conductor begins to exhibit a temperature increase until steady state is achieved, and the resulting power emitted defined as:

$$P = \ I^2R \ [W] \qquad [1.2]$$

where P is the generated Joule power, I is the current travelling through the resistor, R is the resistance of the conductor, and t is the operating time.[18,26,62] In addition to the conduction described above, heat will also flow through convection with the surrounding air and environment, as well as through radiation emitted from the now-hot surface of the conductor.[18] Joule heating is occurs when the outputted power is higher than that of the input voltage, and the larger this difference the more efficiently electrical energy is being converted into Joule heating.[63] **Figure 1.5** demonstrates an example of how temperature can increase as a result of Joule heating in a copper mesh electrode designed by Jang and coworkers, both at a constant applied voltage and a cyclic on/off voltage testing. As a result, the material choice and processing conditions holds great importance when designing printed electronics to ensure a low internal resistance and high measured conductivity.

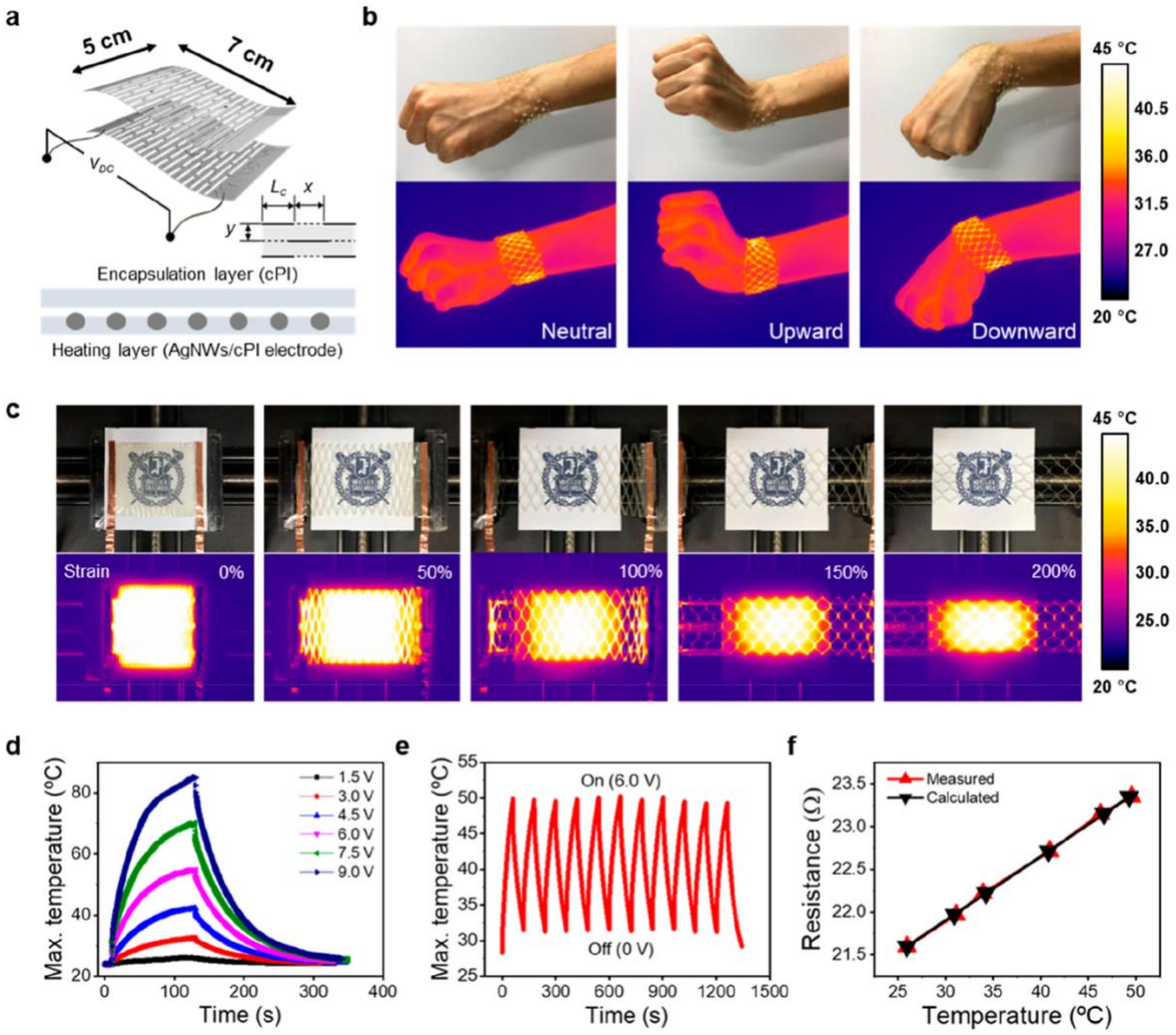

Figure 1.5. A) Transparent kirigami heater and its electrothermal performance. (a) Schematic illustration of uniaxial transparent kirigami heater (cutting dimensions: Lc = 15 mm, x = 1.7 mm, and y = 1.7 mm). (b) Wearable transparent kirigami heater that operates on the wrist at input voltage of 4.5 V and performs under dynamic movements (upward and downward). (c) Electrothermal and mechanical stability test verified by stretching under strain elongations of 0%, 50%, 100%, 150% and 200%. (d) Maximum temperature at increasing input voltages from 1.5 to 9.0 V. (e) Cyclic operation temperature at 6 V. (f) Resistance versus temperature of calculated and measured graph of transparent kirigami heater. (Reproduced from ref 28, Copyright American Chemical Society, 2017)

In certain instances, where uneven morphology of a printed trace can affect the metal-to-metal contact and lead to a localized increase in the internal resistance, a feature known as a hot spot can occur. In a hot spot, when a high operation voltage is applied, the small area of high resistance causes excessive heat generation, leading to failure in the trace within the localized area. Therefore, infrared (IR) thermal imaging is typically employed as a qualitative characterization technique to visualize heat distribution upon applied voltage. When the voltage is increased and to determine electrical characteristics such as the CCC, thermal imaging is key in determining whether there is a definitive failure point present in the trace that can be addressed through material or processing optimizations. Furthermore, thermal characterization through thermal imaging can provide insight for other operational conditions, such as in transparent heaters where heat uniformity is a key performance factor.

1.3.3 Mechanical Characterization

Substrates utilized in printed electronics are flexible in nature and therefore are subjected to a certain amount of bending during the fabrication process, especially in processes such as gravure and roll-to-roll printing. As a result, adhesion of the printed material to the substrate is imperative for producing functional printed electronics components. The adhesion of the metal grid TCE to the substrate will also be dependent on the choice of plastic substrate itself, as differing surface energies between substrate materials can affect the wettability and spreading of the ink and subsequently the contact area at the substrate-ink interface. Additionally, the design of the grid electrode and the internal angle of the chosen geometry can also influence how the ink is deposited onto the substrate. Various methods for improving adhesion to the substrate during the fabrication process have been attempted, such as adding polymer binders to the ink formulations, or using certain ultra-violet (UV) sintering techniques that assist in improving adhesion to the substrate.[52,64]

Once device fabrication is complete, there are several mechanical tests to determine an electrode's adherence to the substrate, including but not limited to torsion/twisting testing, bending tests, and tape adhesion testing.[65,66] During each test, the TCE is monitored for any apparent cracking of the material or delamination and flaking of the electrode from the substrate in order to determine how mechanical changes affect the overall resistance or conductance, as significant mechanical damage can render the electrode non-conductive. These types of characterization will be critical when designing and selecting our printed electrodes.

1.4. Transitioning 2D to 3D Printed Electronics

An emerging area of interest in printed electronics is the development of structural electronics that makes use of conductive features in or on 3D objects. The conductive 3D features can be directly printed on conformal surfaces, or generated from 2D prints, and shaped into a 3D object through forming or directly printing into 3D conductive shapes. In-mold electronics (IME) makes use of the ability to thermoform and stretch/elongate 2D printed electronics to create functional 3D objects. This technology provides design freedom to manufacturers, enabling them to add more function and aesthetic appeal to everyday objects such as appliances and electronics. In addition, IME provides value for automotive and aerospace manufacturers, where it can enable the development of lightweight products that can be assembled with less wiring and mechanical switches. The challenge in IME lies in the thermoforming step that transforms 2D substrates into a 3D part or object. During thermoforming, the substrate and the functional traces deposited on it must withstand significant localized elongations as it transitions from a 2D to a 3D geometry, as shown in **Figure 1.6**.[67] These areas of elongation can cause deformations to the printed traces as it stretches to accommodate for the volume change, leading to higher electrical resistance at the harsh elongation points.

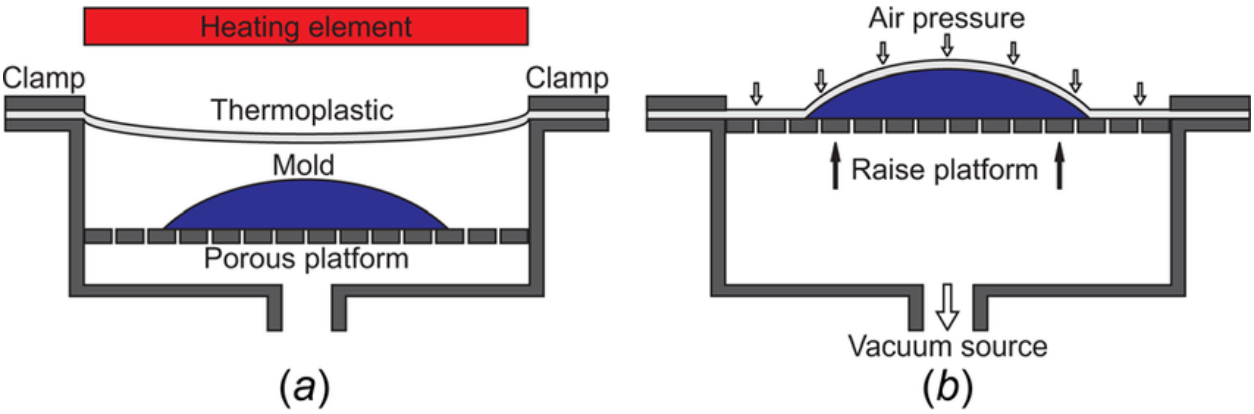

Figure 1.6. Schematic of the thermoforming process. (a) Heating of a thermoplastic sheet softens it above a positive mold. (b) Pressure difference from a vacuum source forms the softened thermoplastic onto a positive mold into the desired shape. (Reproduced from ref 67, Copyright ASME, 2015)

While silver flake inks containing elastomeric additives that impart stretchability to the traces are a common material in IME applications, MINKs are also well suited to these types of

applications because their electrical and mechanical properties can be optimized through a variety of different sintering processes such as heat, light, plasma, and even chemical methods. Liu and coworkers demonstrated that silver oxalate-based MINKs can be treated with broad-band UV light to create a "skin" of silver nanoparticles at the trace−air interface.[60] The skin is shown to slow the evaporation of solvent and amine additives and ensures that the partially sintered traces maintain fluidity throughout the thermoforming process to allow the transition from 2D to 3D. This process, unique to MINKs, is powerful because it produces conductive 3D traces that can be elongated up to 50%, more than those of commercially available inks designed for IME applications, without cracking or breaking. In addition, the electrical properties of the traces produced from the MINKs are superior to those of commercial flake inks because they can accommodate the elongation required during the transition from 2D to 3D architectures without the addition of nonconductive elastomeric components.

1.5. Thermal Management in Printed Electronics

1.5.1 Thermal Degradation of Thermoplastic Substrates

The use of flexible substrates is one of the key benefits of utilizing printing technologies to fabricate electronics, facilitating the production of lightweight and bendable electronic structures for integration into existing architectures. A variety of flexible substrates have been demonstrated to be compatible with screen printing and roll-to-roll processing including but not limited to plastic substrates, paper products, and composite materials.[28,68,69] Plastic substrates are the most widely used flexible substrate in printed electronics, however their usefulness is highly dependent on the glass transition temperature (T_g) and melting temperature (T_m) of the substrate. The T_g is reached when the rigid state of the amorphous regions of the plastic becomes rubbery.[68] When considering commercially available plastic substrates, there is a trade-off between temperature resistivity and cost; high-temperature substrates like polyimide (T_g = 300 °C) that can withstand high processing temperatures are typically high in cost, and low-temperature substrates like polycarbonate (T_g = 147 °C) are inexpensive but cannot withstand exposure to elevated temperatures necessary for device fabrication. **Table 1.1** contains further details about measured T_g and T_m of popular recyclable and biodegradable plastic substrates in printed electronics.

Table 1.1. Thermal Properties of Commercial Polymers. (Reproduced from ref 68, Copyright Elsevier 2018)

Type of polymers	Glass transition temperature [˚C]	Melting temperature [˚C]
Polycaprolactone	- 60	64
Polycarbonate	147	288 - 316
Polyethylene naphtholate	120	270
Polyethylene terephthalate	70 - 80	255
Polyether sulphone	230	500
Polyimide	300	375 - 401
Polylactic acid	50 - 80	150 - 180

The temperature restrictions due to a plastic substrate's T_g and T_m ultimately dictates both the maximum allowable processing temperature and operating temperature. From a fabrication standpoint, a simple solution appears to be to reduce the temperature of the thermal sintering or annealing of the printed feature so as not to reach the T_g of the substrate, however metallic ink formulations typically have high thermal requirements to decompose the organic components in the ink formulation and to properly adhere the ink to the substrate. Additionally, reducing the processing temperature and increasing the thermal exposure time only escalates the overall processing time, energy, and cost, ultimately reaching a time frame that is no longer feasible with the characteristic rapid processing of printed electronics. From an operational standpoint, certain TCE applications such as printed heaters necessitate high power input for optimal performance, which in turn can cause heat accumulation in the electronic component equal to or greater than the T_g of the substrate, even exceeding the substrate's T_m. This heat accumulation can lead to deformation and warpage of the substrate at the substrate-feature interface, resulting in adverse changes to the mechanical stability and conductive performance of the printed component over time.[22,52] This level of thermal degradation can reduce the operational life span of a device. In response, incorporating a simultaneously electrically insulating and thermally conductive film

between the substrate and the TCE, like that shown in **Figure 1.7**, may assist in improving thermal diffusion across the electrode structure and effectively shield both the electrode and substrate from warping over time.

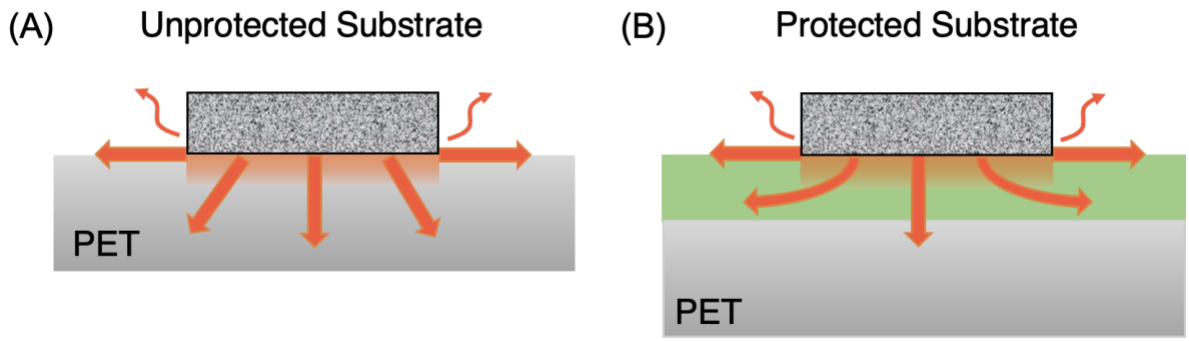

Figure 1.7. Schematic of how heat generated in a silver MINK trace dissipates A) directly into the underlying substrate when left unprotected and B) when a protective interlayer is placed at the substrate-trace interface

1.5.2 Thermal Management Materials

There have been several different methods to incorporate thermal management materials into electronic device architectures. Filler-matrix structures are widely used due to their electrically insulating properties however they tend to exhibit low thermal conductivity.[70] Utilizing fillers such as gallium nitride, silicon, and copper have improved the thermal conductivity of the matrices, but the allowable filling content to maintain the structural integrity of the polymer limits the maximum measured thermal conductivity.[70] Similar to filler-matrix structures, composites of phase change materials such as paraffin, eicosanoids, and stearic acid fitted with additives to improve thermal conductivity have been demonstrated in a thermal management capacity, however they are limited by the latent heat of the phase change material and if reached can lead to failure of the composite.[19] Although matrices as described above can achieve high thermal conductivity and provide a clear demonstration of thermal management of electronics, they are not necessarily feasible for printed electronics applications. Such matrices are typically opaque in nature, and as such can no longer be considered for TCE based applications, such as in clear packaging, wearable electronics, or biomedical applications. Therefore, it is necessary to utilize a stable free-standing material that exhibits high thermal conductivity while retaining electrically insulating and optical properties.

Furthermore, the chosen material must not only be mechanically compatible with the characteristic flexible and transparent substrates used in printed electronics, but additionally inert with the surrounding environment and any subsequent layers deposited over top of the material. One potential material that has recently garnered interest and significant research is the use of boron nitride and its derivatives in thermal management applications.

1.6. Boron Nitride Nanomaterials

Boron nitride (BN) is composed of inorganic boron and nitrogen atoms alternating in equal parts to create a monoatomic planar sheet.[71] BN is well known to share structural similarities to carbon-based graphene, with both sheets displaying interlinked hexagonal structures at the atomic level. There are different derivatives of BN such as boron nitride nanosheets and boron nitride nanotubes (BNNTs) that have been demonstrated in thermal management applications.[72–75] The intrinsic properties of BNNTs, including but not limited to their thermal stability, resistance to oxidation, and chemical inertness has made them a promising application in sensor and emitter applications on top of thermal management.[76]

BNNTs and carbon nanotubes (CNTs) are simply their respective atomic sheets rolled into tubular forms through a variety of physical and chemical synthesis methods.[77] High-purity CNTs are characteristically a black powder, whereas high-purity BNNTs have no strong absorption in the visible range. While they have structural similarities, their intrinsic properties differ greatly. BNNTs are inherently electrically insulating and exhibit high chemical and thermal stability. They also achieve high thermal conductivity and mechanical properties that rival the performance of CNTs.[78,79] There are three primary nano-structural models that can be fashioned from wrapping BN sheets into nanotubes: arm-chair, zig-zag, and helical. Each of the three structural models are achieved by varying at which (*n, m*) indices the wrapping begins, as demonstrated in **Figure 1.8A**,[80] and the nanotube's outer diameter typically ranges between 10 – 90 nm, shown in **Figure 1.8B**.[81] In addition to the individual tube structural conformities, the subsequent placement of tubes to create a BNNT film is dictated by preferential stacking orders.[77] Also known as tube alignment, the inherent layering of BNNTs can influence the final properties of the BNNT film structure. BNNTs may also be tuned to stack in different arrays relative to the substrate that they are placed on.[82] Tubes can be aligned to stand perpendicular or parallel to the substrate surface, ultimately affecting thermal conductance and stability.

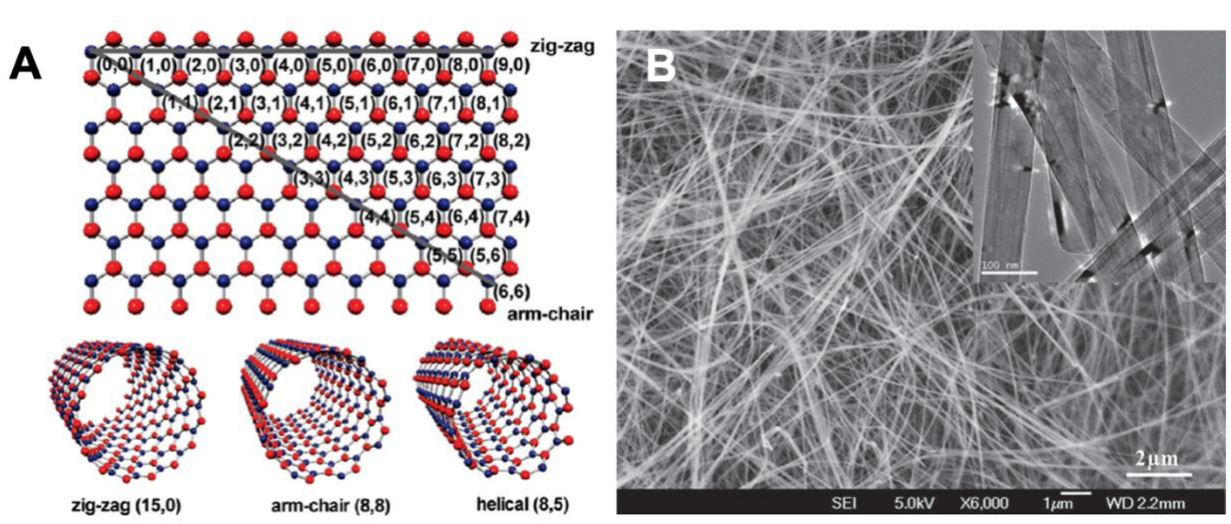

Figure 1.8. A) Monoatomic planar BN sheet demonstrating possible wrapping fashions of each available (n, m) indices b) SEM image of BNNT with TEM image of the BNNTs inset (Reproduced from ref 80, Copyright American Chemical Society 2010, and ref 81, Copyright Wiley 2013)

1.6.1 BNNT Thermal Conductivity and Stability

Many different BNNT properties have been investigated to maximize integration into electronic devices and interfaces. For applications in electronics thermal management, thermal stability and thermal conductivity are of primary interest.[71] Density functional theory calculations confirm BNNTs are able to achieve a relatively high thermal conductivity (k) value for an electrically insulating material, ranging between 100-300 W/mK.[83] It has also been theoretically proven to reach as high as 350 W/mK, matching that of pure CNT films.[84] It was also determined theoretically that length and diameter of the nanotube directly influences the thermal conductivity, such that as they both increase, the thermal conductivity proportionally increases.[85–87] Furthermore, in-plane (*002*) thermal conductivity, which dictates current that travels across the x and y planes, tends to exhibit significantly improved charge travel than out-of-plane thermal conductivity in the z direction.[72,74,88] This is due to the structural alignment of the final film, as the atoms exposed in the outer layer can better transfer charge across tubes in the parallel direction. In addition to this phenomena, inherent isotropic disorder of the charge interactions across the in-plane direction can also positively affect the k value.[89]

The thermal stability of BNNTs is a key advantage when considering BNNTs as a thermal insulating layer, and they exhibit a very high resistance to oxidation. Golberg *et al.* demonstrated that pure CNTs show oxidation damage at 500 ˚C, whereas BNNTs can remain thermally stable up to 900 ˚C.[78] This stability factor has been strongly linked to tube structure perfection, indicating that any defects ultimately lower these thermal stability capabilities.[79] Zhang *et al.* theoretically determined that while freestanding BNNTs wrapped below the (*3,0*) indices are not stable at room temperature, any BNNT larger than (*3,0*) were stable up to 1873 ˚C.[90] As the BNNT diameter increases, any deviation from the chirality of the tube structure has a negligible effect on thermal stability and is therefore inherently stable.

1.6.2 Functionalization of BNNTs

BNNT materials are typically synthesized as a bulk dry material, and when nanotubes are directly added to a solution, the material tends to aggregate in bundles or ropes due to the inherent hydrophobicity of the sidewalls and their intrinsic strong van der Waal forces, severely limiting solvent compatibility.[91] To address this, the BNNT material can be functionalized to improve tube-tube interactions, typically through covalent or non-covalent functionalization, defect radiation, or in-filling of the nanotubes.[92] Non-covalent functionalization in particular has been demonstrated as a favourable technique due to the simplicity of π-π interactions, inducing a wrapping structure visualized in **Figure 9** that doesn't require defect sites to attach polymers like covalent functionalization. A variety of polymers have been explored to non-covalently functionalize BNNTs, such poly[m-phenylenevinylene-co-(2, 5-dioctoxy-pphenylenevinylene)], poly(2,7-carbazole), and poly(3-hexyl-thiophene), that allows for a uniform and stable dispersion in organic solvents.[93–95] Further research focuses on expanding the available solvent base to include more sustainable options such as alcohols or water. However, it is important to tailor the solvent to a compatible polymer, and to acknowledge potential changes in thermal and optical properties of the BNNT dispersion, depending on the weight percentage of polymer necessary to maintain a stable dispersion.

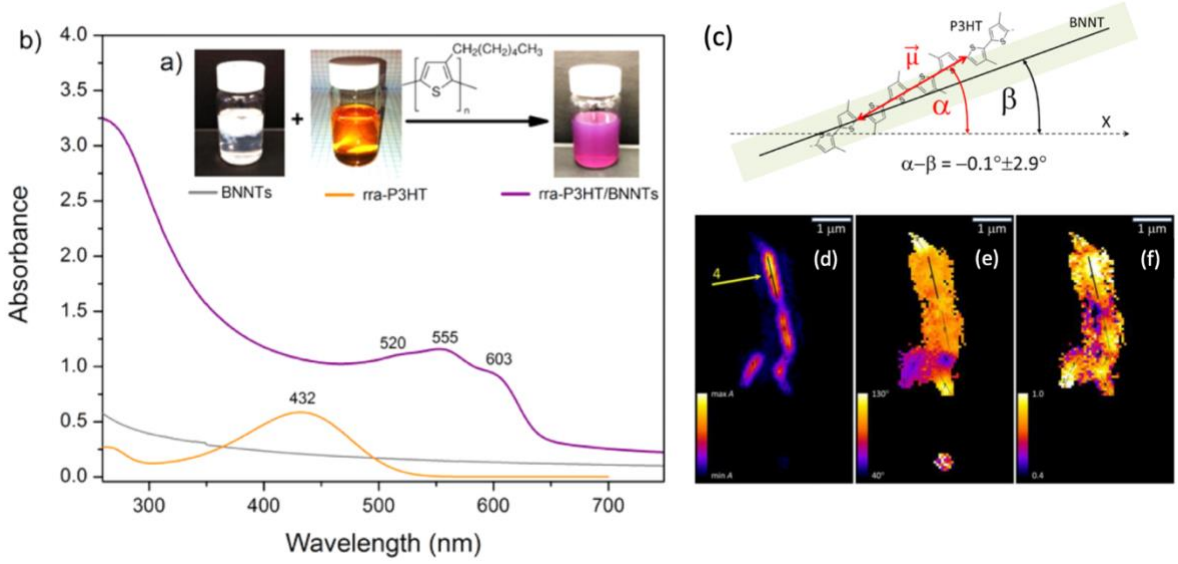

Figure 9. (a) Photos and (b) absorption spectra of BNNT (0.2 mg/ mL), rra-P3HT solution, and rra-P3HT/BNNT suspensions in $CHCl_3$ (rra-P3HT to BNNT weight ratio = 0.08). (c) Schematic diagram of a P3HT fragment bound to a BNNT (α and β are the orientation angles of the excitation dipole moment ($\vec{\mu}$) and the BNNT axis, respectively). Parameter mapping images corresponding to the fluorescence images of rra-P3HT/BNNT. (d-f) Fluorescence intensity amplitude (A), excitation dipole moment angle (α), and modulation (M) obtained from pixel-by-pixel fits to eq 1. BNNT orientation is indicated by the numbered line segments, with an arrow indicating fragment #4. (Reproduced from ref 96, Copyright American Chemical Society 2015)

1.6.3 BNNTs in Thermal Management

BNNTs have been employed in thermal management primarily through maximizing their thermal stability and thermal conductivity so that the tube network can withstand a larger applied current and better dissipate heat as temperatures rise. BNNTs in thermal management applications can appear either as a filler in a polymer matrix or as a free-standing thin film. As a filler, BNNT networks act to improve the thermal conductivity of a polymer film, and have been successfully demonstrated with a variety of polymers, including but not limited to BNNT:poly(sterene), BNNT:poly(methyl methacrylate), and BNNT:poly (vinyl butyral).[73] The maximum achievable thermal conductivity is ultimately limited by high interfacial thermal resistance between the BNNTs and the adjacent polymer surface. Various techniques have been introduced to reduce the internal resistance of the composite material, including introducing other fillers such as cellulosic

derivatives,[73,97] and metal nanoparticles, or covalently and non-covalently functionalizing the surface of the BN prior to integration into the polymer structure.[98,99] It is possible that these techniques could be incorporated into free-standing BNNT films in order to improve the thermal conductivity without sacrificing optical transparency. Exploring and optimizing a free-standing film for printed TCEs can provide a level of thermal management for the fine line features without compromising the integrity or require additions to the ink formulation or the substrate. There are no significant scale-up efforts to incorporate BNNTs as a heat management tool in printed electronics, and as such developing and exploring its' capabilities can provide groundwork in improving TCE and device operability across multiple different applications and industries.

1.7. Scope of Interest

This thesis examines the use of a nano-thin interlayer of BNNTs as a heat mitigation solution during the fabrication and operation of flexible printed 2D and 3D printed microelectrodes derived from MINK formulations. The BNNTs' intrinsic thermally conductive yet electrically insulating properties are employed to maximize conductive performance of the printed electronic structures, with additional thermal and mechanical characterization explored to maintain device integrity through all layers.

Chapter 2 explores the first-time use of the BNNTs as a thermal management tool in high-energy intensive processing of micron-thin printed electronics structures. Increasing BNNT surface concentration is related to the resulting energy output from the sintering process to minimize sheet resistance of screen-printed linear traces at different trace widths. Profilometric and SEM & EDS characterization analysed the change in trace morphology upon inclusion of the BNNTs at different surface concentrations to visualize the improvement in substrate uniformity because of the heat dissipative properties of the BNNTs preventing heat damage. Applied voltage testing provides insight into how morphological differences can affect both electrical performance and heat distribution in the trace, while temperature decay calculations were used to better characterize the speed of heat dissipation upon inclusion of the BNNTs.

Chapter 3 expands upon the effects of applied voltage on the traces similarly presented in **Chapter 2** through an operational standpoint, translating the BNNTs' thermal dissipative properties for improved transparent heater performance. Microgrid electrodes were meticulously designed with relationships explored between geometric design and processing conditions to

maximize both transparency and conductive performance. Rigorous flexibility testing and characterization were completed on the microgrids to analyze the influence of BNNTs on reducing mechanical stress imparted on the grids during deformation. The microgrid heaters with and without the BNNT interlayer were subjected to applied voltage testing and IR thermal imaging, while varying the BNNT layer thickness was investigated to achieve improvements on heat distribution to maximize thermal performance. Additional profilometric and SEM characterization further analyzed the change in trace morphology due to latent heat generated in the traces dissipating into the substrate during operation.

Chapter 4 returns to the BNNT dispersion itself, with special interest on replacing the previously used chlorinated solvent base and its corresponding functional dispersive polymer with a chemically diverse alternative. This work reports on the first-time use of poly(vinyl butyral) polymer and ethanol solvent as a dispersive medium for the nano-thin BNNT interlayer in printed electronics. Processing conditions were altered to optimize the change in vapour properties of the new solvent system, leading to UV-Vis, SEM, AFM, and contact angle measurements to provide an in-depth analysis on the change in BNNT film quality between the two systems. Taking the champion microgrid transparent heater design from **Chapter 3**, similar mechanical and thermal characterizations were conducted on grids to confirm no adverse effects to the heater performance when substituting the chlorinated-dispersed BNNT explored in **Chapter 2** for the green-solvent dispersed BNNT interlayer studied in this chapter.

Chapter 5 investigated the usefulness of the BNNT interlayer to reduce thermal stress on traces that were transformed from 2D to 3D through the process of thermoforming. Extensive electrical characterization was completed on varying trace geometries, observing an improvement in trace conductivity at the harsh elongation point of the trace with the BNNTs present, and a relationship developed between the thinning of the substrate and its influence on trace conductivity. Thermal characterization and imagery provided insight into the change in current carrying capacity for traces printed with and without the BNNT interlayer, as well as the intensity of hot spot formation at the highest points of elongation. Qualitative SEM and microscope imaging showed how the BNNTs integrate themselves into the trace upon stretching of the ink alongside the substrate during the thermoforming process.

Finally, **Chapter 6** presents overall conclusions for each of the chapters presented in this thesis, as well as future recommendations and potential research directions for further use of BNNTs in – exploring the use of other temperature-sensitive materials in printed electronics, as well as BNNTs' radiation shielding properties for emerging 2D and 3D aerospace applications.

1.8 References

(1) Hu, J.; Holt, K. B.; Foord, J. S. Focused Ion Beam Fabrication of Boron-Doped Diamond Ultramicroelectrodes. *Anal. Chem.* **2009**, *81* (14), 5663–5670. https://doi.org/10.1021/ac9003908.

(2) Sun, J.; Luo, X.; Chang, W.; Ritchie, J. M.; Chien, J.; Lee, A. Fabrication of Periodic Nanostructures by Single-Point Diamond Turning with Focused Ion Beam Built Tool Tips. *J. Micromechanics Microengineering* **2012**, *22* (11), 115014. https://doi.org/10.1088/0960-1317/22/11/115014.

(3) Lang, F.; Gluba, M. A.; Albrecht, S.; Rappich, J.; Korte, L.; Rech, B.; Nickel, N. H. Perovskite Solar Cells with Large-Area CVD-Graphene for Tandem Solar Cells. *J. Phys. Chem. Lett.* **2015**, *6* (14), 2745–2750. https://doi.org/10.1021/acs.jpclett.5b01177.

(4) Jung, C.; Kim, S. M.; Moon, H.; Han, G.; Kwon, J.; Hong, Y. K.; Omkaram, I.; Yoon, Y.; Kim, S.; Park, J. Highly Crystalline CVD-Grown Multilayer MoSe2 Thin Film Transistor for Fast Photodetector. *Sci. Rep.* **2015**, *5* (1), 15313. https://doi.org/10.1038/srep15313.

(5) Winther-Jensen, B.; Krebs, F. C. High-Conductivity Large-Area Semi-Transparent Electrodes for Polymer Photovoltaics by Silk Screen Printing and Vapour-Phase Deposition. *Sol. Energy Mater. Sol. Cells* **2006**, *90* (2), 123–132. https://doi.org/10.1016/j.solmat.2005.02.004.

(6) He, X.; Shen, G.; Xu, R.; Yang, W.; Zhang, C.; Liu, Z.; Chen, B.; Liu, J.; Song, M. Hexagonal and Square Patterned Silver Nanowires/PEDOT:PSS Composite Grids by Screen Printing for Uniformly Transparent Heaters. *Polymers* **2019**, *11* (3), 468. https://doi.org/10.3390/polym11030468.

(7) Norita, S.; Kumaki, D.; Kobayashi, Y.; Sato, T.; Fukuda, K.; Tokito, S. Inkjet-Printed Copper Electrodes Using Photonic Sintering and Their Application to Organic Thin-Film Transistors. *Org. Electron.* **2015**, *25*, 131–134. https://doi.org/10.1016/j.orgel.2015.06.026.

(8) Galagan, Y.; Coenen, E. W. C.; Sabik, S.; Gorter, H. H.; Barink, M.; Veenstra, S. C.; Kroon, J. M.; Andriessen, R.; Blom, P. W. M. Evaluation of Ink-Jet Printed Current Collecting Grids and Busbars for ITO-Free Organic Solar Cells. *Sol. Energy Mater. Sol. Cells* **2012**, *104*, 32–38. https://doi.org/10.1016/j.solmat.2012.04.039.

(9) Homenick, C. M.; James, R.; Lopinski, G. P.; Dunford, J.; Sun, J.; Park, H.; Jung, Y.; Cho, G.; Malenfant, P. R. L. Fully Printed and Encapsulated SWCNT-Based Thin Film Transistors via a Combination of R2R Gravure and Inkjet Printing. *ACS Appl. Mater. Interfaces* **2016**, *8* (41), 27900–27910. https://doi.org/10.1021/acsami.6b06838.

(10) Secor, E. B.; Lim, S.; Zhang, H.; Frisbie, C. D.; Francis, L. F.; Hersam, M. C. Gravure Printing of Graphene for Large-Area Flexible Electronics. *Adv. Mater.* **2014**, *26* (26), 4533–4538. https://doi.org/10.1002/adma.201401052.

(11) Grau, G.; Cen, J.; Kang, H.; Kitsomboonloha, R.; Scheideler, W. J.; Subramanian, V. Gravure-Printed Electronics: Recent Progress in Tooling Development, Understanding of

Printing Physics, and Realization of Printed Devices. *Flex. Print. Electron.* **2016**, *1* (2), 023002. https://doi.org/10.1088/2058-8585/1/2/023002.
(12) Li, D.; Han, T.; Ruan, H. Solution-Assembled Ordered Grids Constructed with Silver Nanowires as Transparent Conductive Electrodes. *ACS Omega* **2018**, *3* (7), 7191–7195. https://doi.org/10.1021/acsomega.8b01320.
(13) Gupta, R.; Walia, S.; Hösel, M.; Jensen, J.; Angmo, D.; Krebs, F. C.; Kulkarni, G. U. Solution Processed Large Area Fabrication of Ag Patterns as Electrodes for Flexible Heaters, Electrochromics and Organic Solar Cells. *J. Mater. Chem. A* **2014**, *2* (28), 10930. https://doi.org/10.1039/c4ta00301b.
(14) Krebs, F. C. All Solution Roll-to-Roll Processed Polymer Solar Cells Free from Indium-Tin-Oxide and Vacuum Coating Steps. *Org. Electron.* **2009**, *10* (5), 761–768. https://doi.org/10.1016/j.orgel.2009.03.009.
(15) Chen, R.; Lan, L. Solution-Processed Metal-Oxide Thin-Film Transistors: A Review of Recent Developments. *Nanotechnology* **2019**, *30* (31), 312001. https://doi.org/10.1088/1361-6528/ab1860.
(16) Wang, S.; Zhang, H.; Zhang, B.; Xie, Z.; Wong, W.-Y. Towards High-Power-Efficiency Solution-Processed OLEDs: Material and Device Perspectives. *Mater. Sci. Eng. R Rep.* **2020**, *140*, 100547. https://doi.org/10.1016/j.mser.2020.100547.
(17) Yang, J.; Zi, D.; Zhu, X.; Li, H.; Li, Z.; Sun, L.; Zhang, G.; Wang, F.; Peng, Z.; Lan, H. Printed Flexible Transparent Electrodes for Harsh Environments. *Adv. Mater. Technol.* **2022**, *7* (5), 2101087. https://doi.org/10.1002/admt.202101087.
(18) Papanastasiou, D. T.; Schultheiss, A.; Muñoz-Rojas, D.; Celle, C.; Carella, A.; Simonato, J.; Bellet, D. Transparent Heaters: A Review. *Adv. Funct. Mater.* **2020**, *30* (21), 1910225. https://doi.org/10.1002/adfm.201910225.
(19) Ling, Z.; Zhang, Z.; Shi, G.; Fang, X.; Wang, L.; Gao, X.; Fang, Y.; Xu, T.; Wang, S.; Liu, X. Review on Thermal Management Systems Using Phase Change Materials for Electronic Components, Li-Ion Batteries and Photovoltaic Modules. *Renew. Sustain. Energy Rev.* **2014**, *31*, 427–438. https://doi.org/10.1016/j.rser.2013.12.017.
(20) Polino, G.; Shanmugam, S.; Bex, G. J. P.; Abbel, R.; Brunetti, F.; Di Carlo, A.; Andriessen, R.; Galagan, Y. Photonic Flash Sintering of Ink-Jet-Printed Back Electrodes for Organic Photovoltaic Applications. *ACS Appl. Mater. Interfaces* **2016**, *8* (3), 2325–2335. https://doi.org/10.1021/acsami.5b11394.
(21) Galagan, Y.; Coenen, E. W. C.; Abbel, R.; van Lammeren, T. J.; Sabik, S.; Barink, M.; Meinders, E. R.; Andriessen, R.; Blom, P. W. M. Photonic Sintering of Inkjet Printed Current Collecting Grids for Organic Solar Cell Applications. *Org. Electron.* **2013**, *14* (1), 38–46. https://doi.org/10.1016/j.orgel.2012.10.012.
(22) Niittynen, J.; Sowade, E.; Kang, H.; Baumann, R. R.; Mäntysalo, M. Comparison of Laser and Intense Pulsed Light Sintering (IPL) for Inkjet-Printed Copper Nanoparticle Layers. *Sci. Rep.* **2015**, *5* (1), 8832. https://doi.org/10.1038/srep08832.
(23) Lee, S. M.; Lee, J. H.; Bak, S.; Lee, K.; Li, Y.; Lee, H. Hybrid Windshield-Glass Heater for Commercial Vehicles Fabricated via Enhanced Electrostatic Interactions among a Substrate, Silver Nanowires, and an over-Coating Layer. *Nano Res.* **2015**, *8* (6), 1882–1892. https://doi.org/10.1007/s12274-014-0696-4.
(24) Park, J.-H.; Seok, H.-J.; Kamaraj, E.; Park, S.; Kim, H.-K. Highly Transparent and Flexible Ag Nanowire-Embedded Silk Fibroin Electrodes for Biocompatible Flexible and

Transparent Heater. *RSC Adv.* **2020**, *10* (53), 31856–31862. https://doi.org/10.1039/D0RA05990K.

(25) Cheong, W.; Kim, Y.; Lee, J.; Hong, C.; Choi, H.; Kwak, Y.; Kim, Y. J.; Kim, Y. S. High-Performance Transparent Electrodes for Automobile Windshield Heaters Prepared by Combining Metal Grids and Oxide/Metal/Oxide Transparent Electrodes. *Adv. Mater. Technol.* **2019**, *4* (4), 1800550. https://doi.org/10.1002/admt.201800550.

(26) Lan, W.; Chen, Y.; Yang, Z.; Han, W.; Zhou, J.; Zhang, Y.; Wang, J.; Tang, G.; Wei, Y.; Dou, W.; Su, Q.; Xie, E. Ultraflexible Transparent Film Heater Made of Ag Nanowire/PVA Composite for Rapid-Response Thermotherapy Pads. *ACS Appl. Mater. Interfaces* **2017**, *9* (7), 6644–6651. https://doi.org/10.1021/acsami.6b16853.

(27) Choi, S.; Park, J.; Hyun, W.; Kim, J.; Kim, J.; Lee, Y. B.; Song, C.; Hwang, H. J.; Kim, J. H.; Hyeon, T.; Kim, D.-H. Stretchable Heater Using Ligand-Exchanged Silver Nanowire Nanocomposite for Wearable Articular Thermotherapy. *ACS Nano* **2015**, *9* (6), 6626–6633. https://doi.org/10.1021/acsnano.5b02790.

(28) Jang, N.-S.; Kim, K.-H.; Ha, S.-H.; Jung, S.-H.; Lee, H. M.; Kim, J.-M. Simple Approach to High-Performance Stretchable Heaters Based on Kirigami Patterning of Conductive Paper for Wearable Thermotherapy Applications. *ACS Appl. Mater. Interfaces* **2017**, *9* (23), 19612–19621. https://doi.org/10.1021/acsami.7b03474.

(29) Kang, T.; Kim, S. H.; Kim, M.; Cho, E.; Lee, S. Highly Flexible, Hydrophobic, and Large Area Plasma-polymer-fluorocarbon/Cu/SiN $_x$ Transparent Thin Film Heater and Thermotherapy Pad Application. *Plasma Process. Polym.* **2020**, *17* (4), 1900188. https://doi.org/10.1002/ppap.201900188.

(30) Sharma, V.; Koivikko, A.; Yiannacou, K.; Lahtonen, K.; Sariola, V. Flexible Biodegradable Transparent Heaters Based on Fractal-like Leaf Skeletons. *Npj Flex. Electron.* **2020**, *4* (1), 27. https://doi.org/10.1038/s41528-020-00091-8.

(31) Evanghelidis, A.; Beregoi, M.; Diculescu, V. C.; Galatanu, A.; Ganea, P.; Enculescu, I. Flexible Delivery Patch Systems Based on Thermoresponsive Hydrogels and Submicronic Fiber Heaters. *Sci. Rep.* **2018**, *8* (1), 17555. https://doi.org/10.1038/s41598-018-35914-2.

(32) Bagherifard, S.; Tamayol, A.; Mostafalu, P.; Akbari, M.; Comotto, M.; Annabi, N.; Ghaderi, M.; Sonkusale, S.; Dokmeci, M. R.; Khademhosseini, A. Dermal Patch with Integrated Flexible Heater for on Demand Drug Delivery. *Adv. Healthc. Mater.* **2016**, *5* (1), 175–184. https://doi.org/10.1002/adhm.201500357.

(33) Xu, X.; Liu, X.; Tan, L.; Cui, Z.; Yang, X.; Zhu, S.; Li, Z.; Yuan, X.; Zheng, Y.; Yeung, K. W. K.; Chu, P. K.; Wu, S. Controlled-Temperature Photothermal and Oxidative Bacteria Killing and Acceleration of Wound Healing by Polydopamine-Assisted Au-Hydroxyapatite Nanorods. *Acta Biomater.* **2018**, *77*, 352–364. https://doi.org/10.1016/j.actbio.2018.07.030.

(34) Xing Chen; Lele Song; Assadsangabi, B.; Jie Fang; Mohamed Ali, M. S.; Takahata, K. Wirelessly Addressable Heater Array for Centrifugal Microfluidics and Escherichia Coli Sterilization. In *2013 35th Annual International Conference of the IEEE Engineering in Medicine and Biology Society (EMBC)*; IEEE: Osaka, 2013; pp 5505–5508. https://doi.org/10.1109/EMBC.2013.6610796.

(35) Kim, Y.-I.; Kim, M.-W.; An, S.; Yarin, A. L.; Yoon, S. S. Reusable Filters Augmented with Heating Microfibers for Antibacterial and Antiviral Sterilization. *ACS Appl. Mater. Interfaces* **2021**, *13* (1), 857–867. https://doi.org/10.1021/acsami.0c16471.

(36) Hecht, D. S.; Hu, L.; Irvin, G. Emerging Transparent Electrodes Based on Thin Films of Carbon Nanotubes, Graphene, and Metallic Nanostructures. *Adv. Mater.* **2011**, *23* (13), 1482–1513. https://doi.org/10.1002/adma.201003188.
(37) Hong, S.; Yeo, J.; Kim, G.; Kim, D.; Lee, H.; Kwon, J.; Lee, H.; Lee, P.; Ko, S. H. Nonvacuum, Maskless Fabrication of a Flexible Metal Grid Transparent Conductor by Low-Temperature Selective Laser Sintering of Nanoparticle Ink. *ACS Nano* **2013**, *7* (6), 5024–5031. https://doi.org/10.1021/nn400432z.
(38) Galagan, Y.; J.M. Rubingh, J.-E.; Andriessen, R.; Fan, C.-C.; W.M. Blom, P.; C. Veenstra, S.; M. Kroon, J. ITO-Free Flexible Organic Solar Cells with Printed Current Collecting Grids. *Sol. Energy Mater. Sol. Cells* **2011**, *95* (5), 1339–1343. https://doi.org/10.1016/j.solmat.2010.08.011.
(39) Zou, J.; Yip, H.-L.; Hau, S. K.; Jen, A. K.-Y. Metal Grid/Conducting Polymer Hybrid Transparent Electrode for Inverted Polymer Solar Cells. *Appl. Phys. Lett.* **2010**, *96* (20), 203301. https://doi.org/10.1063/1.3394679.
(40) Li, W.; Zhang, H.; Shi, S.; Xu, J.; Qin, X.; He, Q.; Yang, K.; Dai, W.; Liu, G.; Zhou, Q.; Yu, H.; Silva, S. R. P.; Fahlman, M. Recent Progress in Silver Nanowire Networks for Flexible Organic Electronics. *J. Mater. Chem. C* **2020**, *8* (14), 4636–4674. https://doi.org/10.1039/C9TC06865A.
(41) Liana, D. D.; Raguse, B.; Wieczorek, L.; Baxter, G. R.; Chuah, K.; Gooding, J. J.; Chow, E. Sintered Gold Nanoparticles as an Electrode Material for Paper-Based Electrochemical Sensors. *RSC Adv.* **2013**, *3* (23), 8683. https://doi.org/10.1039/c3ra00102d.
(42) Zhao, Y.; Wang, B.; Tan, J.; Yin, H.; Huang, R.; Zhu, J.; Lin, S.; Zhou, Y.; Jelinek, D.; Sun, Z.; Youssef, K.; Voisin, L.; Horrillo, A.; Zhang, K.; Wu, B. M.; Coller, H. A.; Lu, D. C.; Pei, Q.; Emaminejad, S. Soft Strain-Insensitive Bioelectronics Featuring Brittle Materials. *Science* **2022**, *378* (6625), 1222–1227. https://doi.org/10.1126/science.abn5142.
(43) Li, X.; Wang, Y.; Yin, C.; Yin, Z. Copper Nanowires in Recent Electronic Applications: Progress and Perspectives. *J. Mater. Chem. C* **2020**, *8* (3), 849–872. https://doi.org/10.1039/C9TC04744A.
(44) Huang, W.; Li, J.; Zhao, S.; Han, F.; Zhang, G.; Sun, R.; Wong, C.-P. Highly Electrically Conductive and Stretchable Copper Nanowires-Based Composite for Flexible and Printable Electronics. *Compos. Sci. Technol.* **2017**, *146*, 169–176. https://doi.org/10.1016/j.compscitech.2017.04.030.
(45) Li, Z.; Khuje, S.; Chivate, A.; Huang, Y.; Hu, Y.; An, L.; Shao, Z.; Wang, J.; Chang, S.; Ren, S. Printable Copper Sensor Electronics for High Temperature. *ACS Appl. Electron. Mater.* **2020**, *2* (7), 1867–1873. https://doi.org/10.1021/acsaelm.0c00358.
(46) Wu, W.; Liu, L.; Dai, Z.; Liu, J.; Yang, S.; Zhou, L.; Xiao, X.; Jiang, C.; Roy, V. A. L. Low-Cost, Disposable, Flexible and Highly Reproducible Screen Printed SERS Substrates for the Detection of Various Chemicals. *Sci. Rep.* **2015**, *5* (1), 10208. https://doi.org/10.1038/srep10208.
(47) Tam, S. K.; Ng, K. M. High-Concentration Copper Nanoparticles Synthesis Process for Screen-Printing Conductive Paste on Flexible Substrate. *J. Nanoparticle Res.* **2015**, *17* (12), 466. https://doi.org/10.1007/s11051-015-3277-x.
(48) Liang, J.; Tong, K.; Pei, Q. A Water-Based Silver-Nanowire Screen-Print Ink for the Fabrication of Stretchable Conductors and Wearable Thin-Film Transistors. *Adv. Mater.* **2016**, *28* (28), 5986–5996. https://doi.org/10.1002/adma.201600772.

(49) Fernandes, I. J.; Aroche, A. F.; Schuck, A.; Lamberty, P.; Peter, C., R.; Hasenkamp, W.; Rocha, T. L. A. C. Silver Nanoparticle Conductive Inks: Synthesis, Characterization, and Fabrication of Inkjet-Printed Flexible Electrodes. *Nature* **2020**, *10* (8878), 11.
(50) Shen, W.; Zhang, X.; Huang, Q.; Xu, Q.; Song, W. Preparation of Solid Silver Nanoparticles for Inkjet Printed FLexible Electronics with High Conductivity. **2014**, 7.
(51) Cronin, H. M.; Stoeva, Z.; Brown, M.; Shkunov, M.; Silva, S. R. P. Photonic Curing of Low-Cost Aqueous Silver Flake Inks for Printed Conductors with Increased Yield. *ACS Appl. Mater. Interfaces* **2018**, *10* (25), 21398–21410. https://doi.org/10.1021/acsami.8b04157.
(52) Kell, A. J.; Paquet, C.; Mozenson, O.; Djavani-Tabrizi, I.; Deore, B.; Liu, X.; Lopinski, G. P.; James, R.; Hettak, K.; Shaker, J.; Momciu, A.; Ferrigno, J.; Ferrand, O.; Hu, J. X.; Lafrenière, S.; Malenfant, P. R. L. Versatile Molecular Silver Ink Platform for Printed Flexible Electronics. *ACS Appl. Mater. Interfaces* **2017**, *9* (20), 17226–17237. https://doi.org/10.1021/acsami.7b02573.
(53) Choi, Y.; Seong, K.; Piao, Y. Metal−Organic Decomposition Ink for Printed Electronics. *Adv. Mater. Interfaces* **2019**, *6* (20), 1901002. https://doi.org/10.1002/admi.201901002.
(54) Bardeen, J. Electrical Conductivity of Metals. *J. Appl. Phys.* **1940**, *11*, 25.
(55) Roshanghias, A.; Krivec, M.; Baumgart, M. Sintering Strategies for Inkjet Printed Metallic Traces in 3D Printed Electronics. *Flex. Print. Electron.* **2017**, *2* (4), 045002. https://doi.org/10.1088/2058-8585/aa8ed8.
(56) Neermann, S.; Steindl, M.; Franke, J.; Mayer, E.; Schmidt, M. Qualification of NIR, UV and Laser Irradiation as Alternative Photonic Sintering Methods for Printed Electronics. In *2020 Pan Pacific Microelectronics Symposium (Pan Pacific)*; IEEE: HI, USA, 2020; pp 1–8. https://doi.org/10.23919/PanPacific48324.2020.9059353.
(57) Jang, Y.-R.; Joo, S.-J.; Chu, J.-H.; Uhm, H.-J.; Park, J.-W.; Ryu, C.-H.; Yu, M.-H.; Kim, H.-S. A Review on Intense Pulsed Light Sintering Technologies for Conductive Electrodes in Printed Electronics. *Int. J. Precis. Eng. Manuf.-Green Technol.* **2021**, *8* (1), 327–363. https://doi.org/10.1007/s40684-020-00193-8.
(58) Kalashnyk, N.; Rousseau, D.; Noel, S.; Chretien, P.; Brezard-Oudot, A.; Leblanc, Th.; Houze, F.; Hauquier, F.; Derycke, V.; Berthelot, T. Printed Copper Connections on Flexible Substrates. In *2019 IEEE Holm Conference on Electrical Contacts*; IEEE: Milwaukee, WI, USA, 2019; pp 350–358. https://doi.org/10.1109/HOLM.2019.8923847.
(59) Song, S. M.; Cho, S. M. Copper Ion Inks Capable of Screen Printing and Intense Pulsed-Light Sintering on PET Substrates. *ACS Appl. Electron. Mater.* **2022**, *4* (4), 1882–1890. https://doi.org/10.1021/acsaelm.2c00098.
(60) Liu, X.; Li, D.; Fukutani, H.; Trudeau, P.; Khoun, L.; Mozenson, O.; Sampson, K. L.; Gallerneault, M.; Paquet, C.; Lacelle, T.; Deore, B.; Ferrand, O.; Ferrigno, J.; Malenfant, P. R. L.; Kell, A. J. UV-Sinterable Silver Oxalate-Based Molecular Inks and Their Application for In-Mold Electronics. *Adv. Electron. Mater.* **2021**, *7* (9), 2100194. https://doi.org/10.1002/aelm.202100194.
(61) Koishiyev, G. T.; Sites, J. R. Impact of Sheet Resistance on 2-D Modeling of Thin-Film Solar Cells. *Sol. Energy Mater. Sol. Cells* **2009**, *93* (3), 350–354. https://doi.org/10.1016/j.solmat.2008.11.015.
(62) Alhendi, M.; Sivasubramony, R. S.; Weerawarne, D. L.; Iannotti, J.; Borgesen, P.; Poliks, M. D. Assessing Current-Carrying Capacity of Aerosol Jet Printed Conductors. *Adv. Eng. Mater.* **2020**, *22* (11), 2000520. https://doi.org/10.1002/adem.202000520.

(63) Kim, H.-J.; Kim, Y.; Jeong, J.-H.; Choi, J.-H.; Lee, J.; Choi, D.-G. A Cupronickel-Based Micromesh Film for Use as a High-Performance and Low-Voltage Transparent Heater. *J. Mater. Chem. A* **2015**, *3* (32), 16621–16626. https://doi.org/10.1039/C5TA03348A.
(64) Lin, F.; Yin, D.; Li, T.; Lai, L.; Xia, M. Research on the Calibration of Ultraviolet Energy Meters; Han, S., Tan, J., Eds.; Beijing, China, 2016; p 101550P. https://doi.org/10.1117/12.2244603.
(65) Klein, S. A.; Aleksov, A.; Subramanian, V.; Malatkar, P.; Mahajan, R. Mechanical Testing for Stretchable Electronics. *J. Electron. Packag.* **2017**, *139* (2), 020905. https://doi.org/10.1115/1.4036389.
(66) Rezaee, M.; Tsai, L.-C.; Haider, M. I.; Yazdi, A.; Sanatizadeh, E.; Salowitz, N. P. Quantitative Peel Test for Thin Films/Layers Based on a Coupled Parametric and Statistical Study. *Sci. Rep.* **2019**, *9* (1), 19805. https://doi.org/10.1038/s41598-019-55355-9.
(67) Haldane, D. W.; Casarez, C. S.; Karras, J. T.; Lee, J.; Li, C.; Pullin, A. O.; Schaler, E. W.; Yun, D.; Ota, H.; Javey, A.; Fearing, R. S. Integrated Manufacture of Exoskeletons and Sensing Structures for Folded Millirobots. *J. Mech. Robot.* **2015**, *7* (2), 021011. https://doi.org/10.1115/1.4029495.
(68) Shrivastava, A. Introduction to Plastics Engineering. In *Introduction to Plastics Engineering*; Elsevier, 2018; pp 1–16. https://doi.org/10.1016/B978-0-323-39500-7.00001-0.
(69) Lee, T.-W.; Lee, S.-E.; Jeong, Y. G. Carbon Nanotube/Cellulose Papers with High Performance in Electric Heating and Electromagnetic Interference Shielding. *Compos. Sci. Technol.* **2016**, *131*, 77–87. https://doi.org/10.1016/j.compscitech.2016.06.003.
(70) Cui, Y.; Li, M.; Hu, Y. Emerging Interface Materials for Electronics Thermal Management: Experiments, Modeling, and New Opportunities. *J. Mater. Chem. C* **2020**, 10.1039.C9TC05415D. https://doi.org/10.1039/C9TC05415D.
(71) Zhi, C.; Bando, Y.; Tang, C.; Golberg, D. Boron Nitride Nanotubes. *Mater. Sci. Eng. R Rep.* **2010**, *70* (3–6), 92–111. https://doi.org/10.1016/j.mser.2010.06.004.
(72) Chen, J.; Huang, X.; Sun, B.; Jiang, P. Highly Thermally Conductive Yet Electrically Insulating Polymer/Boron Nitride Nanosheets Nanocomposite Films for Improved Thermal Management Capability. *ACS Nano* **2019**, *13* (1), 337–345. https://doi.org/10.1021/acsnano.8b06290.
(73) Fu, C.; Li, Q.; Lu, J.; Mateti, S.; Cai, Q.; Zeng, X.; Du, G.; Sun, R.; Chen, Y.; Xu, J.; Wong, C.-P. Improving Thermal Conductivity of Polymer Composites by Reducing Interfacial Thermal Resistance between Boron Nitride Nanotubes. *Compos. Sci. Technol.* **2018**, *165*, 322–330. https://doi.org/10.1016/j.compscitech.2018.07.010.
(74) Hu, Z.; Wang, S.; Liu, Y.; Qu, Z.; Tan, Z.; Wu, K.; Shi, J.; Liang, L.; Lu, M. Constructing a Layer-by-Layer Architecture to Prepare a Transparent, Strong, and Thermally Conductive Boron Nitride Nanosheet/Cellulose Nanofiber Multilayer Film. *Ind. Eng. Chem. Res.* **2020**, *59* (10), 4437–4446. https://doi.org/10.1021/acs.iecr.9b05602.
(75) Jakubinek, M. B.; Niven, J. F.; Johnson, M. B.; Ashrafi, B.; Kim, K. S.; Simard, B.; White, M. A. Thermal Conductivity of Bulk Boron Nitride Nanotube Sheets and Their Epoxy-Impregnated Composites: Thermal Conductivity of Bulk Boron Nitride Nanotube Sheets. *Phys. Status Solidi A* **2016**, *213* (8), 2237–2242. https://doi.org/10.1002/pssa.201533010.
(76) Ding, H.; Guan, J.; Lu, P.; Mihailov, S. J.; Kingston, C. T.; Simard, B. Boron Nitride Nanotubes for Optical Fiber Chemical Sensing Applications. *IEEE Sens. Lett.* **2020**, *4* (10), 1–4. https://doi.org/10.1109/LSENS.2020.3023702.

(77) Golberg, D.; Bando, Y.; Tang, C. C.; Zhi, C. Y. Boron Nitride Nanotubes. *Adv. Mater.* **2007**, *19* (18), 2413–2432. https://doi.org/10.1002/adma.200700179.
(78) Golberg, D.; Bando, Y.; Kurashima, K.; Sato, T. Synthesis and Characterization of Ropes Made of BN Multiwalled Nanotubes. *Scr. Mater.* **2001**, *44* (8–9), 1561–1565. https://doi.org/10.1016/S1359-6462(01)00724-2.
(79) Chen, Y.; Zou, J.; Campbell, S. J.; Le Caer, G. Boron Nitride Nanotubes: Pronounced Resistance to Oxidation. *Appl. Phys. Lett.* **2004**, *84* (13), 2430–2432. https://doi.org/10.1063/1.1667278.
(80) Golberg, D.; Bando, Y.; Huang, Y.; Terao, T.; Mitome, M.; Tang, C.; Zhi, C. Boron Nitride Nanotubes and Nanosheets. *ACS Nano* **2010**, *4* (6), 2979–2993. https://doi.org/10.1021/nn1006495.
(81) Huang, X.; Zhi, C.; Jiang, P.; Golberg, D.; Bando, Y.; Tanaka, T. Polyhedral Oligosilsesquioxane-Modified Boron Nitride Nanotube Based Epoxy Nanocomposites: An Ideal Dielectric Material with High Thermal Conductivity. *Adv. Funct. Mater.* **2013**, *23* (14), 1824–1831. https://doi.org/10.1002/adfm.201201824.
(82) Terao, T.; Zhi, C.; Bando, Y.; Mitome, M.; Tang, C.; Golberg, D. Alignment of Boron Nitride Nanotubes in Polymeric Composite Films for Thermal Conductivity Improvement. *J. Phys. Chem. C* **2010**, *114* (10), 4340–4344. https://doi.org/10.1021/jp911431f.
(83) Stewart, D. A.; Savić, I.; Mingo, N. First-Principles Calculation of the Isotope Effect on Boron Nitride Nanotube Thermal Conductivity. *Nano Lett.* **2009**, *9* (1), 81–84. https://doi.org/10.1021/nl802503q.
(84) Chang, C. W.; Fennimore, A. M.; Afanasiev, A.; Okawa, D.; Ikuno, T.; Garcia, H.; Li, D.; Majumdar, A.; Zettl, A. Isotope Effect on the Thermal Conductivity of Boron Nitride Nanotubes. *Phys. Rev. Lett.* **2006**, *97* (8), 085901. https://doi.org/10.1103/PhysRevLett.97.085901.
(85) Jiang, J.-W.; Wang, J.-S. Theoretical Study of Thermal Conductivity in Single-Walled Boron Nitride Nanotubes. *Phys. Rev. B* **2011**, *84* (8), 085439. https://doi.org/10.1103/PhysRevB.84.085439.
(86) Li, T. A Comparison between the Mechanical and Thermal Properties of Single-Walled Carbon Nanotubes and Boron Nitride Nanotubes. *Phys. E* **2017**, 6.
(87) Xiao, Y.; Yan, X. H.; Cao, J. X.; Ding, J. W.; Mao, Y. L.; Xiang, J. Specific Heat and Quantized Thermal Conductance of Single-Walled Boron Nitride Nanotubes. *Phys. Rev. B* **2004**, *69*, 205415–205420.
(88) Zhi, C.; Bando, Y.; Terao, T.; Tang, C.; Kuwahara, H.; Golberg, D. Towards Thermoconductive, Electrically Insulating Polymeric Composites with Boron Nitride Nanotubes as Fillers. *Adv. Funct. Mater.* **2009**, *19* (12), 1857–1862. https://doi.org/10.1002/adfm.200801435.
(89) Xiao, M.; Du, B. X. Review of High Thermal Conductivity Polymer Dielectrics for Electrical Insulation. *High Volt.* **2016**, *1* (1), 34–42. https://doi.org/10.1049/hve.2016.0008.
(90) Zhang, Z.; Guo, W.; Dai, Y. Freestanding (3,0) Boron Nitride Nanotube: Expected to Be Stable Well over Room Temperature. *Appl. Phys. Lett.* **2008**, *93* (22), 223108. https://doi.org/10.1063/1.3040007.
(91) Gao, Z.; Fujioka, K.; Sawada, T.; Zhi, C.; Bando, Y.; Golberg, D.; Aizawa, M.; Serizawa, T. Noncovalent Functionalization of Boron Nitride Nanotubes Using Water-Soluble Synthetic Polymers and the Subsequent Preparation of Superhydrophobic Surfaces. *Polym. J.* **2013**, *45* (5), 567–570. https://doi.org/10.1038/pj.2012.170.

(92) Gao, Z.; Zhi, C.; Bando, Y.; Golberg, D.; Serizawa, T. Noncovalent Functionalization of Boron Nitride Nanotubes in Aqueous Media Opens Application Roads in Nanobiomedicine. *Nanobiomedicine* **2014**, *1*, 7. https://doi.org/10.5772/60000.
(93) McWilliams, A. D. S.; Martínez-Jiménez, C.; Shumard, K. R.; Pasquali, M.; Martí, A. A. Dispersion and Individualization of Boron Nitride Nanotubes. *J. Mater. Res.* **2022**, *37* (24), 4459–4482. https://doi.org/10.1557/s43578-022-00696-x.
(94) Rice, N. A.; Bodnaryk, W. J.; Tamblyn, I.; Jakubek, Z. J.; Lefebvre, J.; Lopinski, G.; Adronov, A.; Homenick, C. M. Noncovalent Functionalization of Boron Nitride Nanotubes Using Poly(2,7-carbazole)s. *J. Polym. Sci.* **2020**, *58* (13), 1889–1902. https://doi.org/10.1002/pol.20200164.
(95) Martinez-Rubi, Y.; Jakubek, Z. J.; Jakubinek, M. B.; Kim, K. S.; Cheng, F.; Couillard, M.; Kingston, C.; Simard, B. Self-Assembly and Visualization of Poly(3-Hexyl-Thiophene) Chain Alignment along Boron Nitride Nanotubes. *J. Phys. Chem. C* **2015**, *119* (47), 26605–26610. https://doi.org/10.1021/acs.jpcc.5b09049.
(96) Martinez-Rubi, Y.; Jakubek, Z. J.; Jakubinek, M. B.; Kim, K. S.; Cheng, F.; Couillard, M.; Kingston, C.; Simard, B. Self-Assembly and Visualization of Poly(3-Hexyl-Thiophene) Chain Alignment along Boron Nitride Nanotubes. *J. Phys. Chem. C* **2015**, *119* (47), 26605–26610. https://doi.org/10.1021/acs.jpcc.5b09049.
(97) Zeng, X.; Sun, J.; Yao, Y.; Sun, R.; Xu, J.-B.; Wong, C.-P. A Combination of Boron Nitride Nanotubes and Cellulose Nanofibers for the Preparation of a Nanocomposite with High Thermal Conductivity. *ACS Nano* **2017**, *11* (5), 5167–5178. https://doi.org/10.1021/acsnano.7b02359.
(98) Yang, N.; Zeng, X.; Lu, J.; Sun, R.; Wong, C.-P. Effect of Chemical Functionalization on the Thermal Conductivity of 2D Hexagonal Boron Nitride. *Appl. Phys. Lett.* **2018**, *113* (17), 171904. https://doi.org/10.1063/1.5050293.
(99) Quiles-Díaz, S.; Martínez-Rubí, Y.; Guan, J.; Kim, K. S.; Couillard, M.; Salavagione, H. J.; Gómez-Fatou, M. A.; Simard, B. Enhanced Thermal Conductivity in Polymer Nanocomposites via Covalent Functionalization of Boron Nitride Nanotubes with Short Polyethylene Chains for Heat-Transfer Applications. *ACS Appl. Nano Mater.* **2019**, *2* (1), 440–451. https://doi.org/10.1021/acsanm.8b01992.

Chapter 2. Boron nitride nanotube coatings for thermal management of printed silver inks on temperature sensitive substrates

This chapter is adapted from work published in "Advanced Electronic Materials": Wagner, K.; Paquet, C.; Martinez-Rubi, Y.; Genest, M.; Guan, J.; Sampson, K. L.; Kim, K. S.; Kell, A. J.; Malenfant, P. R. L.; Lessard, B. H. Boron Nitride Nanotube Coatings for Thermal Management of Printed Silver Inks on Temperature Sensitive Substrates. Adv. Electron. Mater. ***2021****, 7 (5), 2001035.*

2.1. Context

This work presents the efficacy of the BNNT interlayer as a heat mitigation tool to maintain the integrity of temperature-sensitive substrates during high energy-intensive fabrication of flexible electronics. As discussed in **Chapter 1**, bulk BNNTs have relatively high thermal conductivity properties and high resistance to oxidation, which can be applied as a protective coating to prevent generated heat from dissipating directly into the substrate. This first-time application of BNNTs as a nano-thin film in printed electronics motivated the exploration of different surface concentrations of the BNNT interlayer to maximize its' effectiveness at supressing heat accumulation at the substrate-trace interface. Varying energies of intense pulsed light were concurrently explored to maximize conductivity of the silver traces which determined the energy limitations that the BNNTs can withstand. Correlations were made between the effect of localized substrate deformation to the current carrying capacities for the traces with and without the BNNTs present. Lastly, the BNNT interlayer contributed to a faster rate of cooling of traces post-operation, indicating potential for usefulness from an operational standpoint.

2.2. Contributions

I led the compiling, visualizing and discussion of the results, as well as performed validation for the profilometric analyses and SEM-EDS imaging. Dr. Paquet and Dr. Kell performed preliminary experiments on the current carrying capacity and IR imaging. Dr. Sampson provided python coding assistance for the rate of cooling experiments. Boron nitride nanotubes were synthesized and dispersed by Dr. Martinez-Rubi, Dr. Guan, and Dr. Kim. All authors assisted with editing the manuscript.

2.3. Abstract

Printed electronics provide inexpensive and light weight electrical components to fuel emerging applications. One major challenge is the high temperature required to sinter conductive metal inks, which leads to thermal degradation of the substrate and subsequently poor performance. A boron nitride nanotube (BNNT) interfacial film is reported for thermal management in rapid processing of a printable silver molecular ink platform using intense pulsed light (IPL) sintering techniques. The inclusion of BNNT thin films of varying surface concentrations deposited between the substrate and the printed features reduces thermal damage to the substrate during sintering while simultaneously improving electrical performance, achieving a sheet resistance value as low as 140 mΩ sq^{-1}. A wide range of sintering energies ranging from 2.0 and 3.2 J cm^{-2} are investigated along with printed trace widths ranging from 5 mil (0.127 mm) to 20 mil (0.508 mm). Increases in the rate of cooling and in the current carrying capacity are confirmed with the inclusion of the BNNTs. Overall, the thin coating of BNNTs presents no drawbacks while significantly improving the electrical properties of IPL sintered conductive traces and thus represents a simple approach that will advance the adoption of IPL for fabricating printed electronic components.

2.4. Introduction

Large-scale production of flexible electronics hinges on developing economically viable printing technologies that can perform under rapid processing. Among the various types of printing techniques, such as inkjet,[1–3] lithographic,[4,5] and gravure[6] studied, screen printing is recognized as an inexpensive, high throughput technology to integrate functional inks on low-temperature flexible substrates and to mass-fabricate electronics. A wide range of ink formulations have already been successfully incorporated into electronics using screen-printing, including flake-based ink,[7] nanowire inks,[8] nanoparticle (NP) inks,[9–11] and molecular inks.[12,13] Molecular inks derived from metal carboxylate salts have become a viable option to address costly or performative limitations exhibited by flake-based and NP inks.[13] They achieve high electrical performance due to their near bulk conductivity, and mechanically robust traces can be printed with low surface roughness and superior adhesion onto flexible substrates. Through the decomposition of the metal complex by means of photonic or thermal sintering, several ink formulations containing salts such as silver i) and copper ii) ethylene glycol carboxylates, and silver neodecanoate have all demonstrated a

capacity to print highly conductive traces.[14–16] Silver neodecanoate (AgND) in particular can produce metallic traces that exhibit high current carrying capacity (CCC), low sheet resistivity, and low surface roughness upon printing.[13] Although AgND inks provide a performance-competitive alternative to particle-based inks, the high irradiative and thermal budget required to decompose and convert the ink to its metallic state necessitates a highly calibrated sintering sequence to avoid damaging the substrate. Optimizing this sequence is key in adapting molecular inks to large-scale electronics fabrication processes.

Photonic sintering in particular is a highly effective sintering method that allows for selective heating of the ink through irradiation of ultraviolet (UV) to infrared (IR) light.[17] Intense pulsed light (IPL) sintering is one such photonic sintering technique that provides an effective way of sintering metallic inks for a multitude of applications such as organic solar cells and thin film transistors.[13,18–20] The technique is well-suited for printable electronics, as it can sinter material on a timescale of milliseconds and therefore readily integrates into roll-to-roll processes.[21,22] IPL sinters printable inks by generating heat through the absorption of broadband, high-intensity pulsed light. Heat can be localized to the ink layer if the pulses of light are short enough that thermal equilibrium is not established between the ink and substrate layers. This unique feature of IPL sintering facilitates the use of inks that require high temperature processing, such as AgND ink[13] and graphene inks,[23,24] onto substrates that have low heat stabilities but are generally favored due to their low cost.[25] Currently, molecular inks can be processed using IPL on temperature-sensitive plastic substrates, such as polyethylene terephthalate (PET) and polycarbonate sheets. However, by using ink formulations that necessitate high sintering energies to maximize conductive performance, the direct underlying substrate can experience damage due to poor localized heat dissipation at the cured metallic ink and substrate interface.[13,26] As a result, careful control over the process is required, and a need for a wider processing window has been identified.

In order to combat the high temperatures that can cause such adverse effects, it is possible to introduce an interfacial film between the printed traces and the substrate in order to improve thermal heat diffusion. Rather than simply acting as a physical barrier to protect the substrate, certain materials have demonstrated efficient absorption and dissipation of heat, such as carbon nanotube (CNT) composites,[27] reduced graphene oxide/natural rubber films,[28] and ultra-nanocrystalline diamond microstructures.[29] Introducing a heat dissipating, electrically insulating layer would not only reduce the potential damage of the temperature sensitive substrate but

additionally perform as a thermal management layer for the metallic traces during operation at high voltages. An additional candidate for thermal management applications is boron nitride (BN). BN is inherently electrically insulating and exhibits a wide bandgap (5.0–6.0 eV) while demonstrating impressive chemical and thermal stability.[30,31] Additionally, BN networks can achieve thermal conductivity and mechanical durability that rivals the performance of their structurally similar CNT counterparts without exhibiting the characteristic electrical conductance that preclude CNTs in thermal management roles where electrical insulation is required.[32,33] Previous research has relied on inserting BN into polymer matrices rather than as a pure film due to the cost of synthesizing high purity BN dispersions. Chen et al. demonstrated that oriented BN nanosheets/ polyvinylidene fluoride nanocomposite films as heat sinks in field effect transistors can achieve a lower stable temperature and slower temperature increase upon operation than that of commercial silicone pads.[34] Shtein et al. used graphene nanoplatelets:nm-BN composites successfully in insulated electronic Schottky diodes, reducing the device's maximum operational temperature from 110 to 37 °C as a result of the BN improving the calculated effective thermal resistance.[35] In addition to BN:polymer composites, covalently and noncovalently functionalizing the outer surface of BN with polymers can simultaneously create a more uniform dispersion while further enhancing the thermal conductivity of the resulting composite film. To the derivative of BN, modified boron nitride nanotubes (BNNTs) have recently demonstrated their capability as a coating agent in a thin film format on different substrates,[36] especially on optical fibers with great coating stability and sensitivity to its environment,[37] and good thermal conductivity,[38] indicating their potential in variable applications. The versatility of BN and BNNTs as thermal conductors indicates that such favorable properties can be translated to the intensive temperatures that are experienced during IPL sintering as well as during device operation.

This work demonstrates the first-time use of modified BNNTs as a thin heat dissipating layer to reduce thermal damage toward PET substrates and molecular inks during IPL sintering. The beneficial properties of BNNTs come about during IPL sintering as well as postprinting as a thin layer between PET and the conductive silver traces. The BNNTs moderate thermal energy transfer during the IPL sintering process by assisting heat generated from sintering the silver traces to spread laterally, reducing localized overheating and warping of the PET and allowing a more uniform silver film to form with noticeably improved electrical properties. Additionally, the presence of BNNTs postsintering at the interface between the PET substrate and the silver trace

minimizes the heat transferred to PET generated through electrical conduction of the silver traces and thus allows the traces to reach higher currents before failing. This work showcases the simplicity of adding a BNNT thermal management interlayer to both improve performative properties of rapidly processable molecular inks while maintaining structural integrity of flexible, low temperature substrates.

2.5. Experimental Section

The nanotubes were synthesized by the hydrogen-assisted BNNT synthesis (HABS) process as previously reported.[39] Briefly, hexagonal BN powder (average 70 nm) was fed into a commercial induction plasma torch (Tekna PS-50, Tekna Systems, Inc.) operated with Ar, N_2, and H_2 gases. The as produced BNNT material was purified by use of molecular chlorine at elevated temperature to etch various impurities as reported recently.[40] Details on the preparation of the dispersions and noncovalent functionalization with regiorandom poly(3-hexylthiophene-2,5-diyl) (rra-P3HT) can be found in the work completed by Martinez-Rubi et al.[41] A 0.2 mg mL^{-1} suspension of rra-P3HT functionalized BNNTs in chloroform was spray-coated on Melinex using an Iwata Air Brush Studio Series Smart Jet air compressor to generate PET coated films containing BNNT surface concentrations of 36, 71, and 142 mg m^{-2}, respectively. An ink consisting of 15 g of AgND, 3.2 g of 2-ethyl-2-oxazoline, 0.8 g of 1-octanol, and additional polymer binders was printed using an American M&M S-912M small format screen printer fitted with a screen mesh of 360 counts per in. and 7 μm emulsion onto BNNT-coated Melinex and untreated Melinex (uncoated). Sets of silver traces with nominal widths varying from 5 to 20 mil (where 1 mil = 25.4 μm) were prepared through screen printing, then dried in a reflow oven for 15 min at 160 °C, as shown in **Figure 2.1**. The samples were photonically sintered using a Pulse Forge 1300 from NovaCentrix with the platen positioned to 1.0 cm. A light pulse of 1500 μs and voltages ranging from 290 to 320 V produced pulses with energies ranging from 2.0 to 3.2 J cm^{-2}. Resistances (R) across silver lines were measured using a multimeter and their sheet resistance (Rs) was calculated based on trace length (L) and nominal trace width (w), as shown in **Equation (1).**

$$R_S = R \times \frac{w}{L} \qquad [2.1]$$

Scanning electron microscopy (SEM) images were acquired using a Hitachi SU3500 SEM with an accelerating voltage of 5 kV. Energy-dispersive X-ray spectroscopy (EDS) was performed using an Oxford Instruments AZtecOne system, with x-act Silicon Drift Detector operated at 15 kV and 10 mm working distance. The chemical distribution of the sample was visualized with AZtecOne's X-ray mapping package. The CCCs were measured using a two-probe technique and multimeter. The resistance through lines of different widths was measured as the applied current was incrementally increased up to a current that caused electrical failure. At each current level, the current was maintained for 30 s before the resistance was recorded. The point of failure is defined as the current carrying capacity.

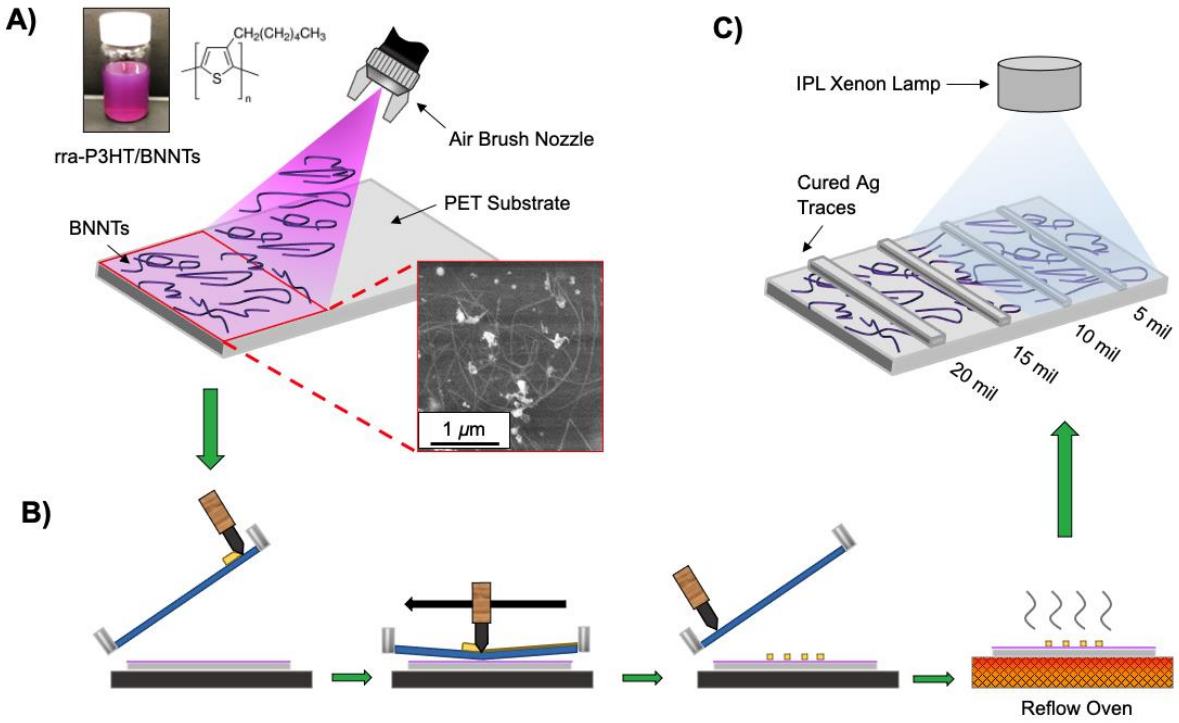

Figure 2.1. Schematic illustration of A) spray-coating of modified BNNT dispersion onto PET substrate with corresponding SEM imaging of resulting BNNT network B) screen-printing process and drying of silver molecular ink on BNNT-treated substrate, and C) photonic sintering of printed silver traces

Post-sintering assessment of the BNNT heat dissipation was carried out by applying various amounts of current using an Agilent E3631A power supply to the traces while monitoring the temperature using a Jenoptik IR-TCM HD IR camera equipped with a close-up lens, which resulted in an 81 μm spatial resolution. The traces and substrate were placed on thermal insulating foam to avoid conduction dissipation from the support structure. Experiments were repeated with

different current intensities and excitation time up to 60 s, while the temperature was recorded during both the heating and the cool off phases. The light transmission of the BNNT films on Melinex was measured using a Cary 5000 spectrometer, with an uncoated Melinex sample acting as a background for the measurement. **Figure 2.10** in the Supporting Information shows the transmission of 350–700 nm wavelength light through Melinex coated with films of 36, 71, and 142 mg m^{-2} of BNNTs. 2D scan profiles were obtained using cyberTECHNOLOGIES CT100 optical profilometer fitted with a white light sensor (cyberTECHNOLOGIES GmbH, Germany). A custom Python script was used to determine the average peak temperature of the thermal map by averaging the temperatures over all of the horizontal cross-sectional slices of an IR image and isolating the maximum temperature for a given time. The maximum temperature was then plotted as a function of time. Cooling curves for the different traces were generated by using the time at which the highest maximum temperature was recorded as the starting point, which is also the point at which the temperature starts decreasing due to the removal of the applied current. These curves were fit to an exponential decay law, as defined in **Equation (2)**, using nonlinear least-squares minimization and curve-fitting (LMFIT) *ConstantModel* and *ExponentialModel* in Python.

$$T(t) = T_{rt} + (T(0) - T_{rt})e^{-t/\tau} \quad [2.2]$$

where T(t) is the maximum temperature at time t, T_{rt} is room temperature or the final temperature to which the curves decay, T(0) is the maximum temperature at time t = 0s, and τ is the exponential time constant.[42] Resistance measurements completed using a multimeter measured 70, 64, 59, and 51 Ω for the 0, 36, 71, and 142 mg m^{-2} surface concentrations, respectively.

2.6. Results and Discussion

Previous work conducted by Kell et al. highlights several key benefits in using IPL sintering in flexible electronics printed on Kapton substrates.[13] The characteristic short and highly intense light pulse exposed to the silver traces during IPL sintering causes the silver to be formed under kinetically driven conditions. Such conditions have direct influence on both the morphology of the trace itself and the substrate underneath. The SEM image for the ink printed on PET substrate in **Figure 2.2A** shows damage sustained at the edges of the traces while the magnified SEM image of **Figure 2.2B** illustrates the high roughness and porous morphology of the silver trace. Previous studies show Kapton is unaffected by the sintering of the inks via IPL sintering,[13,21,43] but SEM

images show warping of the underlying substrate caused by excessive heat transferring from the silver trace to the PET substrate, while the porous and rough silver films are the result of converting the silver salt to metallic silver within millisecond timescales at high energies.

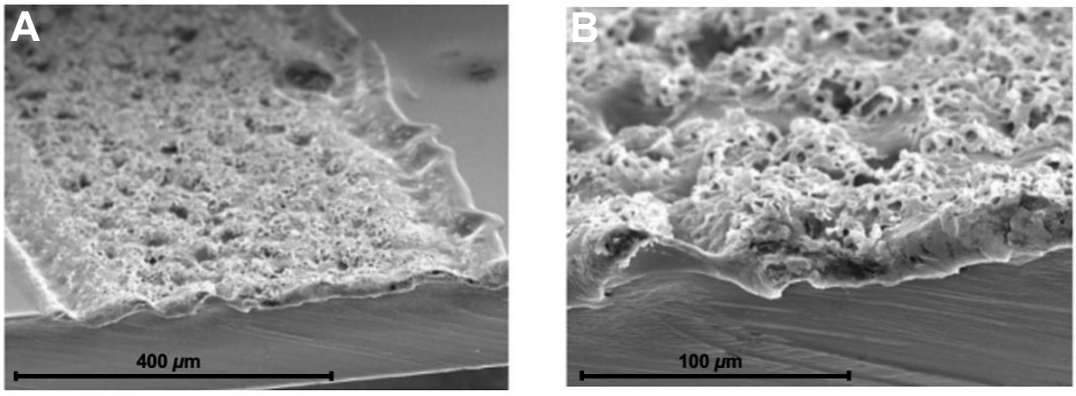

Figure 2.2. A) SEM image of the cross section of IPL sintered 20 mil silver trace printed on pristine PET and B) magnified cross section highlighting thermal damage to PET substrate

To address these shortcomings, BNNT films were introduced as a heat dissipating layer to redirect heat away from PET into the BNNT network during the sintering process, which in turn decreases the damage to the underlying substrate. PET substrates were pretreated with a thin coating of 36, 71, and 142 mg m^{-2} prior to screen printing molecular ink, as demonstrated in **Figure 2.1.** The relatively low concentrations of BNNTs on the surface of the substrate resulted in uniform and semitransparent films, achieving optical transmittance ranging between 99.0%, 96.0% and 93.0% at 589 nm for 36, 71, and 142 mg m^{-2}, respectively (**Figure 2.10**, the Supporting Information). SEM imaging of the BNNT film (**Figure 2.1A**) further shows the network and intersection of individual BNNTs once deposited onto the substrate surface. Although IPL sintering is an advantageous technique for rapidly sintering silver molecular inks, there is a limited range of applied energies that will successfully convert the silver salt into silver metal conductive traces. When lower intensities are used, the light pulse will not have sufficient energy to effectively convert the ink precursor and organic residue will be left behind, resulting in traces with poor or no conductivity. On the other hand, too high of an energy pulse may cause substantial thermal damage to the silver trace and the underlying substrate, resulting once again in nonconductive traces. Incorporation of BNNT onto PET as a thermal management tool can therefore best facilitate the rapid processing of high performance, high temperature molecular inks. To determine the IPL conditions that optimize the silver salt conversion to conductive metal traces, we photonically

sintered the silver traces that were printed on bare PET substrates and on BNNT-coated PET using irradiative energies ranging from 2.0 to 3.2 J cm^{-2}. To account for the effect that different optimal IPL energies have on traces of varying widths, a test pattern made up of traces with widths varying from 5 to 20 mil were evaluated. Narrow traces are more susceptible to damage by intense processing techniques and are therefore more likely to become nonconductive while wider traces buffer damage more effectively and therefore a broader range of sintering energies can be applied to convert them.[44] The following morphological and electrical characterization of the traces are thus presented with respect to the sintering energy used to generate the silver trace, the width of the trace, and the concentration of BNNT in the coating.

2.6.1. Morphological and Electrical Properties

As previously stated, the mechanism of IPL sintering consists of delivering high intensity light in short pulses to the printed silver ink on the PET substrate. The silver salt absorbs the light, initiating the conversion from silver precursor to silver metal with heat generated in the process. Based on the cross-sectional SEM images presented in **Figure 2.2**, it is known that sufficient heat can be generated to cause local melting of the PET substrate under and adjacent to the silver traces and cause the silver trace to form on a PET surface that has been deformed by heating above its glass transition temperature. **Figure 2.3** depicts the morphology of silver traces with a 20 mil width printed on a BNNT-coated PET substrate at varying BNNT surface concentrations, as well as traces printed on an untreated PET substrate. As one can see in **Figure 2.3A**, the sample with no BNNT coating displays an inhomogeneous film as illustrated by PET penetrating the edge and center of the silver trace (dark areas in the SEM), an indication that the reduction of the silver salt to metal using 2.62 J cm^{-2} within a condensed time scale generates heat in excess of the substrate's softening temperature. Compositional mapping using SEM–EDS in **Figure 2.4** highlights the presence of carbon in the dark regions, further indicating that the deformations in **Figure 2.3A** are a result of the softened or melted PET penetrating the silver film. In addition, the small amount of silver detected in **Figure 2.4D** within the carbon region can be attributed to silver being sintered onto the substrate as it was deformed during the IPL sintering process rather than a microcrack appearing post sintering. This indicates that without the coating of BNNTs present between the substrate and printed trace, the IPL conditions do not achieve the characteristic uniform film expected for highly conductive metallic traces.

In comparison, the coating of BNNTs on PET shown in **Figure 2.3B–D** improved the morphology of the converted silver, resulting in a more uniform film across the surface of the trace. In fact, as the BNNT surface concentration increases, the morphological defects become less apparent, with the traces printed on the 142 mg m^{-2} BNNT-coated PET substrate showing remarkably improved uniformity. High magnification SEM images shown in **Figure 2.11** in the Supporting Information and cross-sectional SEM images in **Figure 2.12** in the Supporting Information further emphasize that traces printed on BNNT-coated PET at high surface concentrations do not experience substrate warpage upon exposure to the high temperatures of IPL sintering to the same degree as traces printed on bare PET. Complementing 2D surface profiles demonstrating the improvement in trace morphology upon inclusion of the BNNTs can be found in **Figure 2.5**. Surface profiles of the 10 mil trace reveals valleys measured below the reflected substrate surface, indicating that the substrate melted, deformed and subsequently hardened within the short IPL sintering time span, leading to the described intermixing of the substrate and silver ink at the interface. Upon inclusion of the 142 mg m−2 BNNT film, the presence of such valleys found in the trace is diminished and the trace itself exhibits a lower root-mean-square roughness from 2.23 μm without BNNTs to 0.72 μm. It is clear that the PET inclusions in the silver trace progressively diminish with increasing BNNT concentrations particularly near the center of the trace, thus minimizing barriers to electrical conduction and presumably increasing the electrical conduction of the traces.

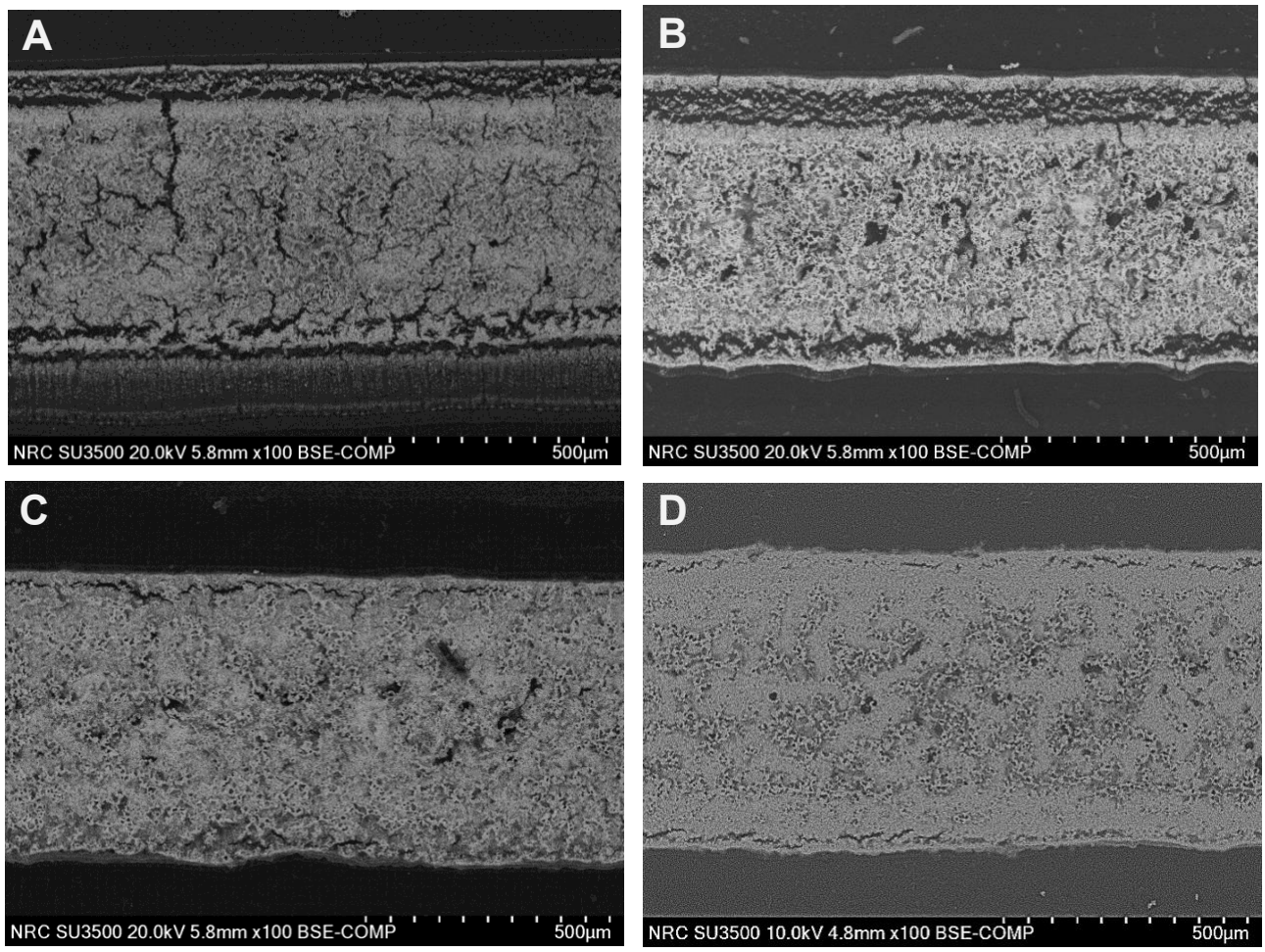

Figure 2.3 SEM images of 20 mil silver trace width printed on a PET substrate coated with BNNT surface concentrations of A) 0, B) 36, C) 71, and D) 142 mg/m^2 exposed to 2.62 J/cm^2 of sintering energy

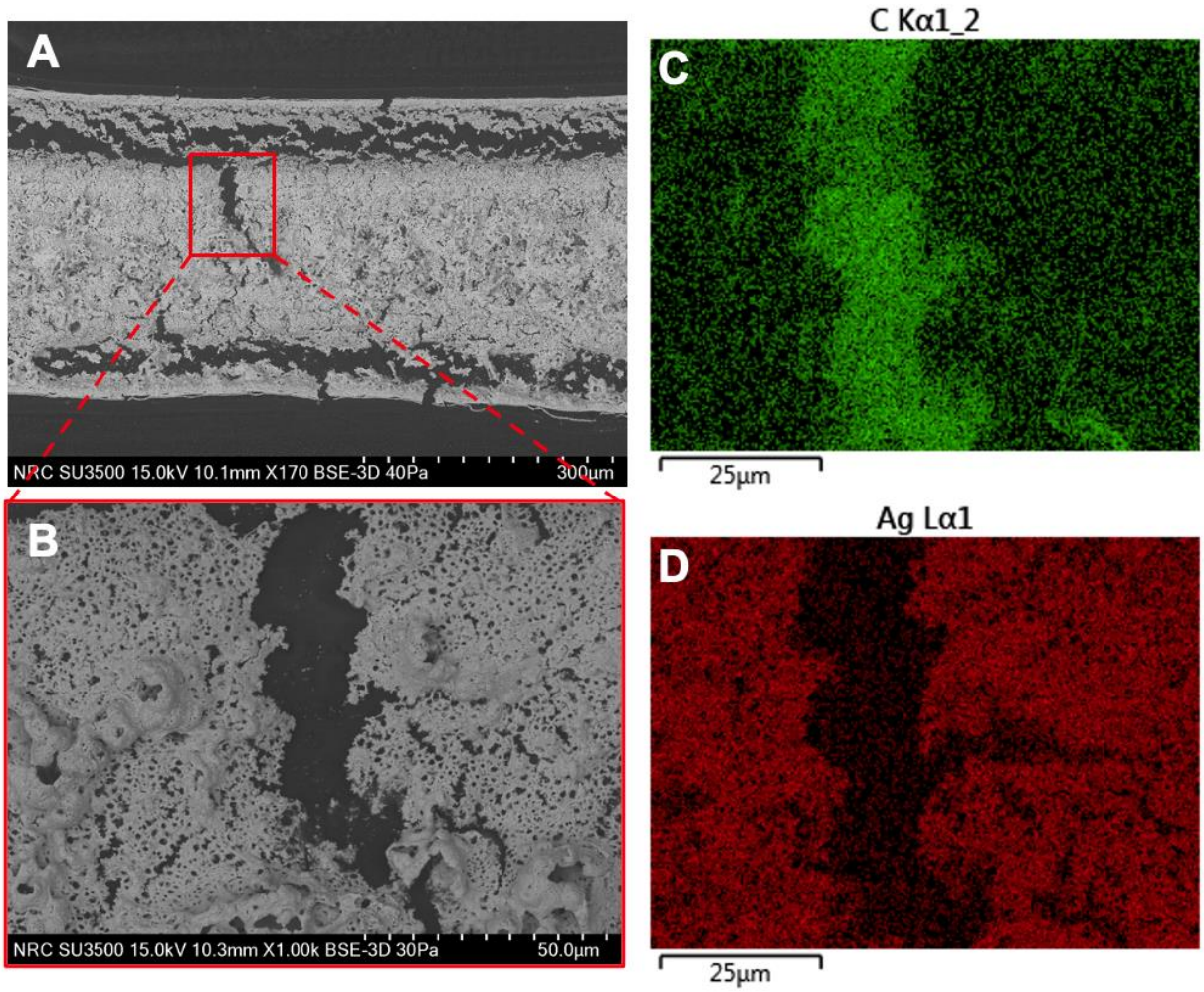

Figure 2.4 A) SEM-EDS image of 20 mil silver trace printed on a bare PET substrate and B) a magnified image of dark region indicative of PET penetrating the silver trace with corresponding compositional mapping of C) carbon (*C*) and D) silver (*Ag*)

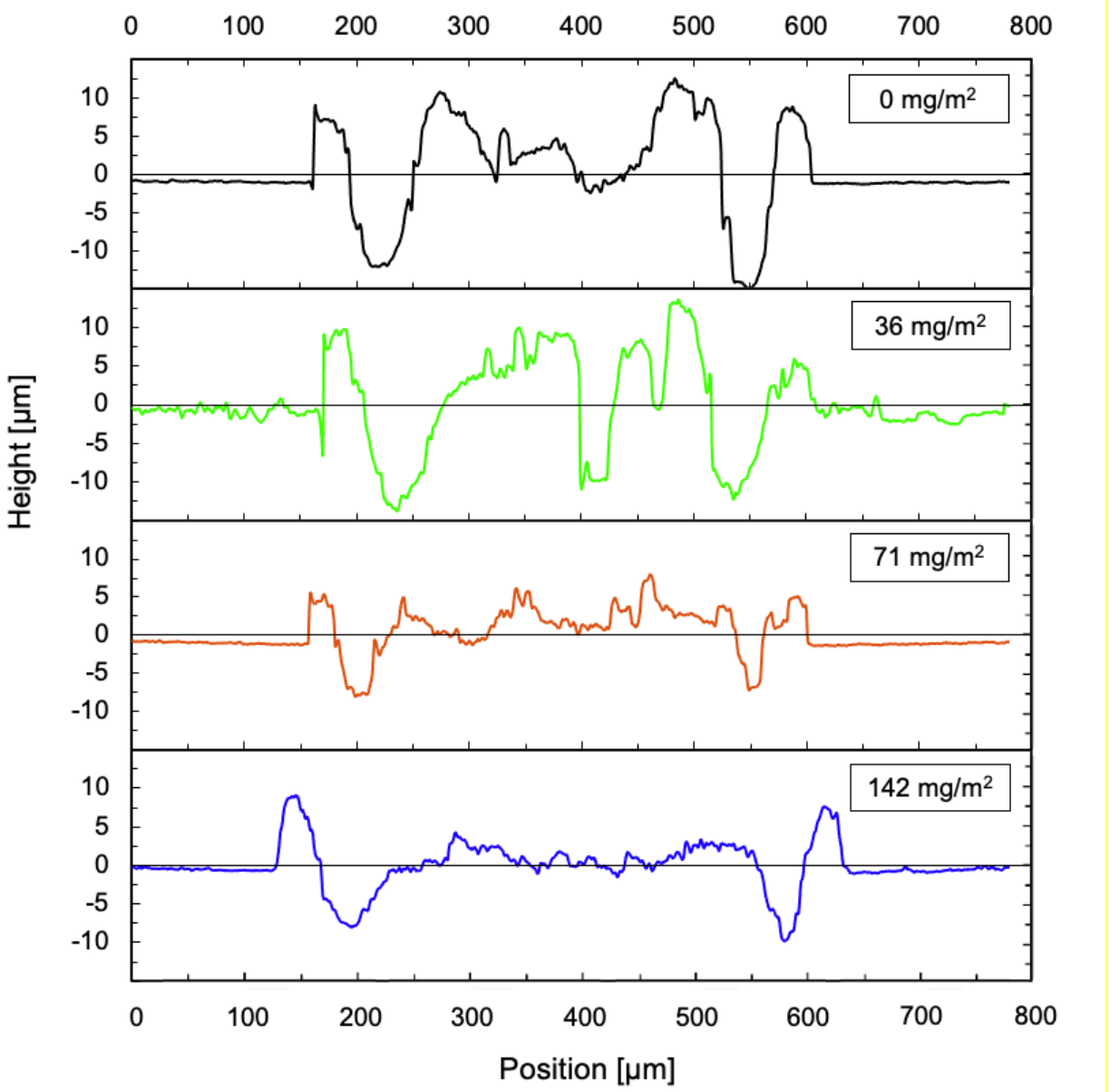

Figure 2.5. Two-dimensional scan profiles of the 10 mil silver trace printed on bare PET and BNNT-coated PET at surface concentrations of 36 mg/m^2, 71 mg/m^2, 142 mg/m^2

As demonstrated in **Figure 2.3**, the energy used to sinter the ink directly affects the characteristic silver salt conversion and ultimately the morphology and the conductivity of the silver traces. The energy required to convert the silver ink into conductive traces for different trace widths and concentrations of surface BNNTs was investigated and presented in **Figure 2.6**. **Figure 2.6A** presents the change in sheet resistance as a function of BNNT surface concentration in relation to applied sintering energy for the 20 mil line width. The BNNT coating decreased the

sheet resistance by ≈ 200% at nearly all sintering energies upon inclusion of the 142 mg m^{-2} BNNT interlayer, owing to the inherent properties of BNNTs capable of enhancing thermal mitigation. We propose that BNNTs act to insulate PET against the direct transfer of heat from the silver traces by diverting heat laterally, thereby minimizing damage done to the substrate immediately below the traces. As indicated by the lower and more consistent value of sheet resistances over the range of sintering energies for silver traces on BNNT, the BNNTs increase the robustness of the substrate during IPL-based silver reduction reaction. It is clear that a large BNNT concentration paired with high sintering energies produces uniform traces with improved electrical conductance.

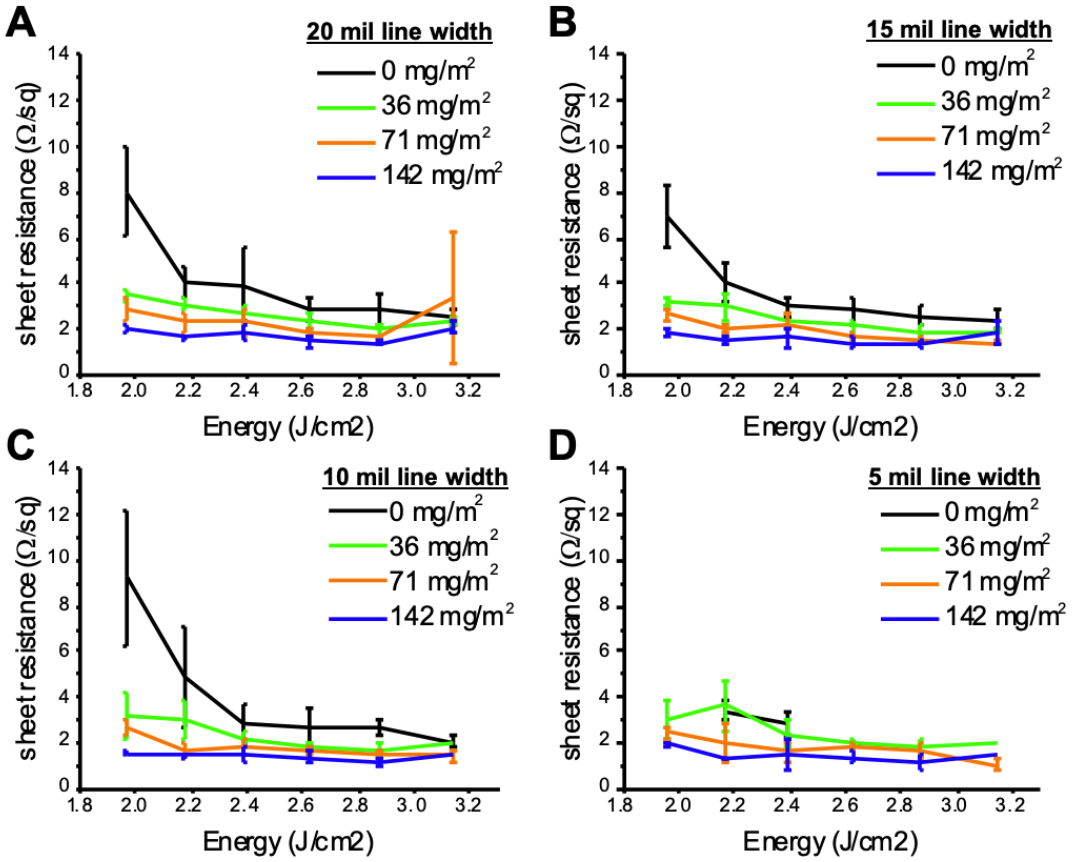

Figure 2.6. Effects of BNNT surface concentration on sheet resistance for A) 20 mil B) 15 mil C) 10 mil and D) 5 mil line width at varying IPL sintering energies

Similar trends are echoed in **Figure 2.6B,C**, where line widths of 15 and 10 mil, respectively are exposed to the identical BNNT concentrations and sintering energy range. Similar to **Figure 2.6A**, at higher BNNT concentrations and sintering energies, the overall sheet resistance decreased, indicative of a conduction pathway less impeded by defects. The effects of sintering

energy are especially apparent in **Figure 2.6D**, which represents sheet resistance values of the traces 5 mil in width. Smaller line widths have shown to be more susceptible to damage during energy-intensive processing measures simply due to the presence of less ink and lower mechanical durability.[45] As expected, exposing the 5 mil line width printed on untreated PET to sintering energies above 2.4 J cm^{-2} caused permanent thermal damage, resulting in nonconductive traces. However, 5 mil traces printed on the BNNT-coated substrates were able to withstand the same or higher thermal intensity of the IPL sintering process and produced functional traces at all investigated irradiation energies. Taken together, the data presented in **Figures 2.3–2.6** demonstrate that BNNTs can positively influence the manner at which silver molecular inks convert and form silver metal traces onto PET. From a practical point of view, the construction of radio frequency identification antennas,[46] low-pass filters,[13] and metal–insulator–metal devices,[13] to name only a few, all require conductors with traces ranging from 5 mil (or less) to at least 20 mil in width to function properly. Developing processes that can print uniform traces onto PET is critical for printed electronics manufacturing because it is the most inexpensive and most commonly used substrate. The ability for the BNNT interlayer to dissipate heat produced during rapid processing open ups the possibility to simultaneously IPL sinter traces with a wide range of line widths, enabling the potential high throughput production of such devices using roll-to-roll or sheet-to-sheet methods.

2.6.2 Thermal Properties

Printed circuits commonly fail as a result of joule heating at high currents that cause delamination. The improvements in electrical conductance presented above suggest that the BNNT interlayer is effective at dissipating heat away from the traces. By analogy, BNNTs should also transfer heat produced through joule heating as more current is passed through the traces. To determine if the BNNTs improve the heat dissipation of the traces and improve the CCC, IR thermal images monitored heat generated as a result of applying current to the traces. **Figure 2.7** shows the temperature maps of the heat generated from applying 100 mA for 60 s through the 10 mil trace width. Without BNNTs present, the peak temperature of the trace reaches temperatures higher than 380 K (>107 °C), seen in **Figure 2.7A**. Poor uniformity in the trace morphology as a result of the energy-intensive IPL conditions is responsible for such an uneven accumulation of heat at certain sections in the trace, highlighted by the red and pink coloration (representing high

temperatures). The apparent hotspots are typically a result of high local resistance attributed to areas in the trace where ink has melted into the substrate as previously shown in **Figures 2.3 and 2.4**. These local hotspots excessively accumulate heat and are likely the point of failure when high currents are applied. The 142 mg m^{-2} BNNT-coated sample shown in **Figure 2.7D** displays the largest improvement in peak temperature and qualitatively exhibits considerably lower heat accumulation, as there are little to no red and pink coloration present in the IR imaging.

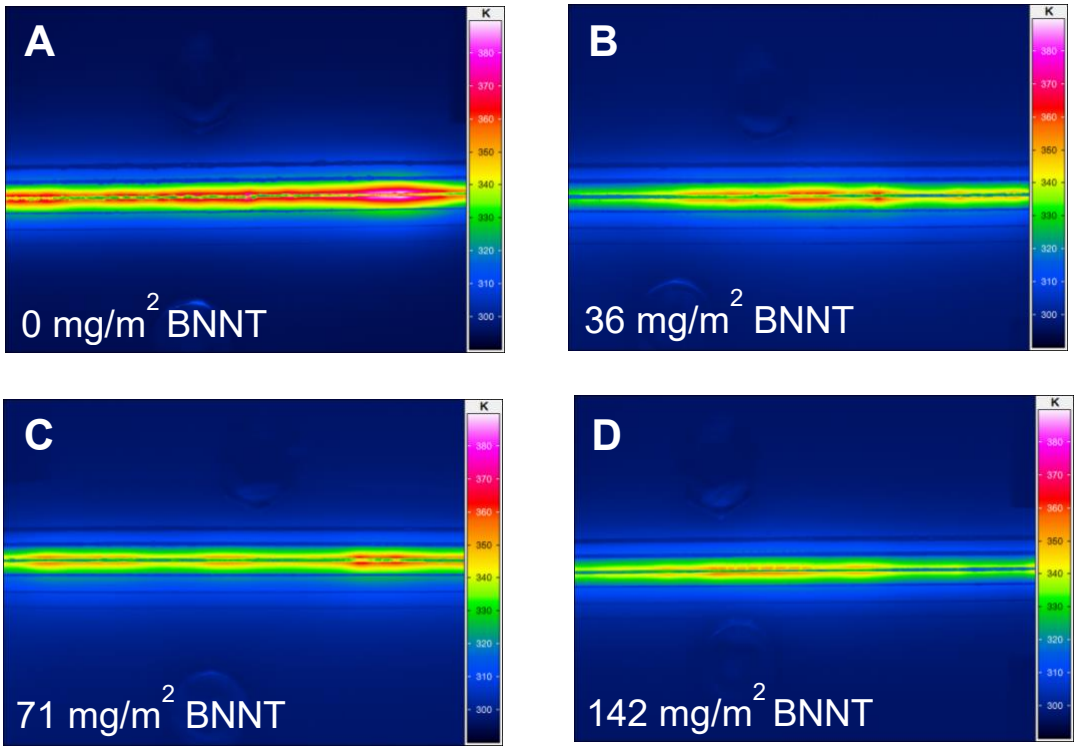

Figure 2.7. Infrared (IR) imaging of A) 0 mg/m^2 B) 36 mg/m^2 C) 71 mg/m^2 and D) 142 mg/m^2 BNNT surface concentration for 10 mil line width after 60s excitation at 100mA

To expand upon the results presented in **Figure 2.7**, heat dissipation was examined by monitoring the change in average maximum temperature across the 10 mil trace upon removal of the 100 mA applied current. **Figure 2.8** and **Figure 2.13** in the Supporting Information present the decrease in average maximum temperature over time for traces printed on the bare PET substrate and at each investigated BNNT surface concentration.

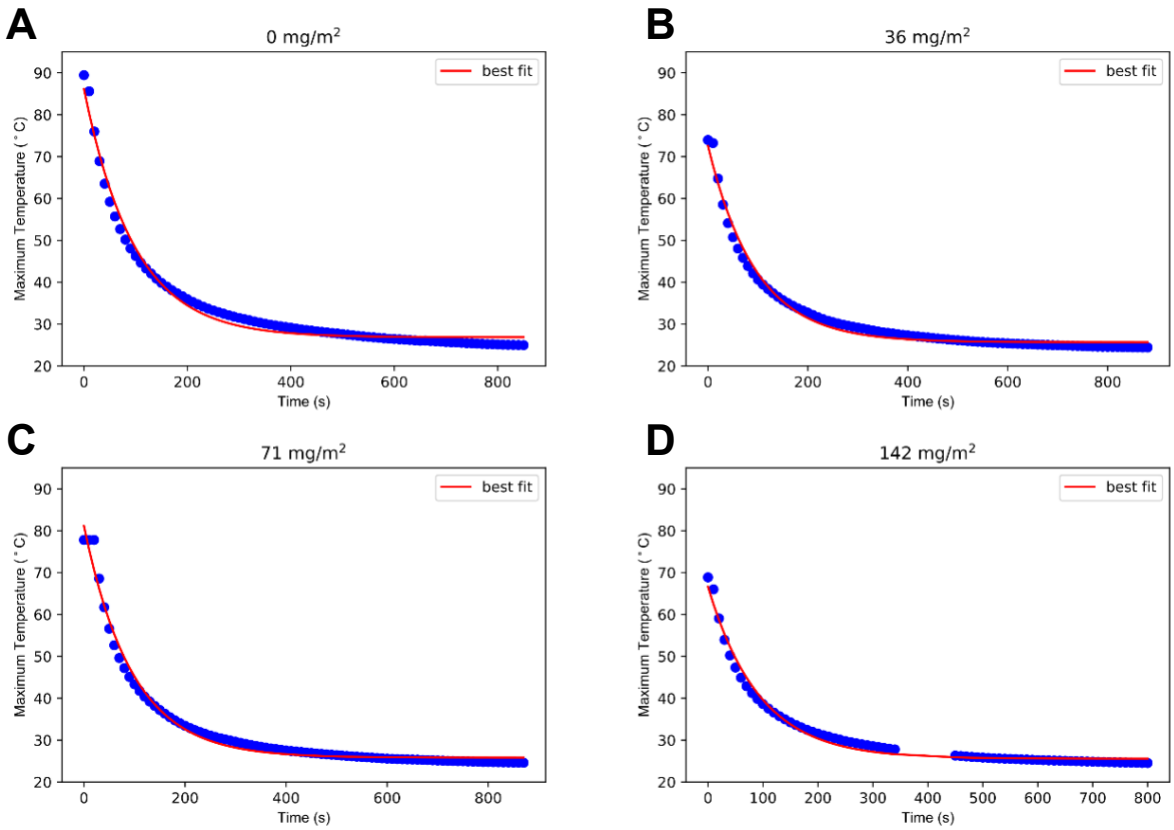

Figure 2.8. Measured change in average maximum temperature profiles over time for a 10 mil sample printed on A) bare PET and BNNT-coated PET at surface concentrations of B) 36, C) 71, and D) 142 mg/m^2 (blue data points) and the exponential decay fit (red line) calculated using LMFIT Python models after removal of 100 mA applied current

As a result of differences in the microstructures and varied print quality among samples, the traces investigated typically exhibited resistances within a range of ±10 Ω and thus experience varying degrees of resistive heating. In order to isolate the role of BNNT in heat dissipation from that of BNNTs improving trace microstructure and conductivity, the curves of **Figure 2.8** were fit to an exponential cooling decay equation (**Equation (2)**). The exponential factor τ, a relative measure of cooling time, is independent of the temperature of the traces and thus allows a comparison among traces despite their variations in peak temperatures. The exponential time constants, detailed in **Table 2.1** in the Supporting Information, are 97.35, 95.25, 95.24, and 93.26 for traces printed on substrates with 0, 36, 71, and 142 mg m^{-2}, respectively, indicating increasing rate of cooling (1/τ) with increasing BNNT concentrations. This increased cooling in BNNT-containing samples indicates that thermal heat is dissipating laterally along the x-direction away

from the traces and across the BNNT coating, diminishing heat transfer directly to the PET and thus lessening the damage to the underlying substrate.

The remarkable improvement in trace morphology that minimizes hotspots as well as the ability for the BNNT film to dissipate heat during applied current allows the traces to carry more current without failure. The CCC for printed silver traces has previously been determined on high temperature Kapton substrates.[13,47] Alhendi et al. demonstrated that morphological changes within the silver trace itself can limit the CCC when the experiments are carried out on Kapton. These studies show that the thermal stability of Kapton enable the visualization of thermal expansion of the silver trace at high current/high temperature prior to failure. Here we demonstrate that introducing a BNNT interlayer between the ink and PET enables the traces to produce CCC values similar to those presented in Kell et al. using an optimized thermal sintering process on a high temperature Kapton substrate.[13] **Figure 2.9** presents the improvement in CCC as a function of BNNT surface concentration for various trace widths. As the surface concentration increases, the CCC also increases, attributing to less defects (improved adhesion) in the silver film that can lead to failure as well as a denser network of nanotubes that aids in dissipating heat. High magnification SEM images of the BNNT networks at each investigated surface concentration are shown in **Figure 2.14** in the Supporting Information, further highlights the increase in tube density at increasing concentrations. This indicates that introducing a BNNT interlayer not only allows one to take advantage of the beneficial millisecond timescale of IPL sintering but can do so without impacting electrical performance.[48]

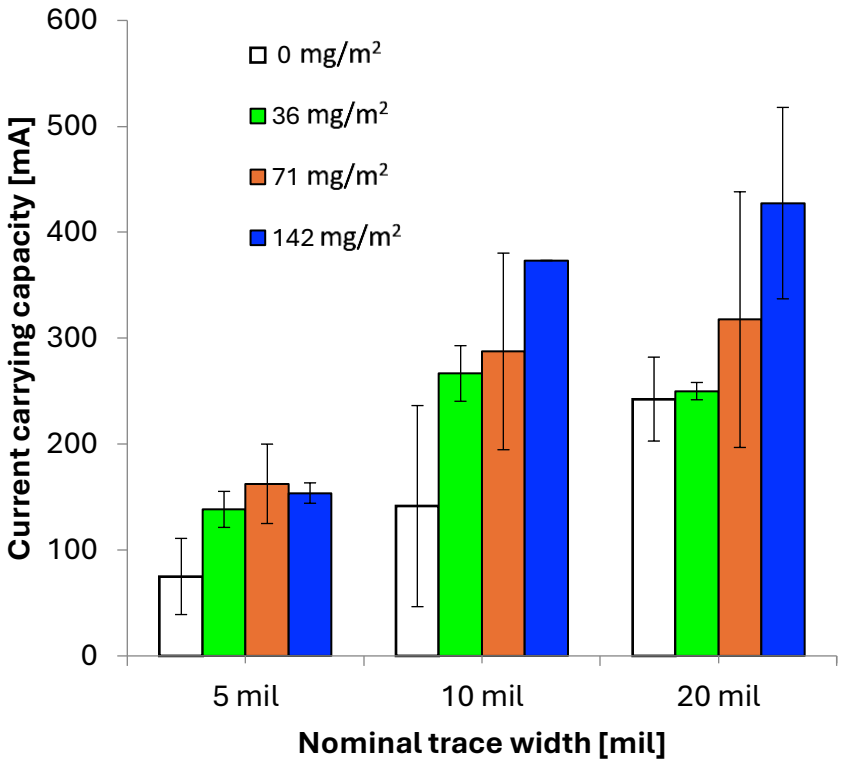

Figure 2.9. Change in current carrying capacity of investigated BNNT surface concentrations coated onto PET substrates and measured for 5 mil, 10 mil, and 20 mil silver trace line widths

Emerging interest in high power/high current applications such as large area lighting, as described by Keränen et al., can benefit from the increase in the CCC for inks printed on low thermal budget substrates such as PET, as the improvements in the CCC of the traces holds potential to increase light output.[49] Another high current application of interest is integrating the BNNT interlayer into printed heaters. We are currently investigating how the improvements in the uniformity of the traces processed by IPL sintering coupled with the ability for the underlying BNNT layer to dissipate and distribute the heat created during the application of the current influences printed heater performance.

2.7. Conclusion

In summary, conductive silver traces as narrow as 5 mil that are screen-printed onto BNNT-coated substrates and sintered using IPL display remarkable improvements in their electrical properties. The presence of BNNTs at the interface between the PET substrate and the silver ink disperses the heat generated during IPL sintering and thus minimizes the amount of heat transferred

to the PET that is in direct contact with the silver traces. As a result, the PET below and adjacent to the silver traces do not reach the high temperatures that would otherwise lead them to melt and mix with the silver to form a film with poor uniformity. As highlighted by the SEM images, the improved morphology not only leads to a consistent decrease in the sheet resistance upon increasing BNNT surface concentration, but the sheet resistance values also measured on BNNT-coated substrates stay relatively consistent over a wide range of both IPL energies and trace widths. Coating the substrate with an increasing surface concentration of BNNTs additionally reduced the average peak temperature across the trace while minimizing heat accumulation at local hotspots. Furthermore, the BNNT layer on PET also improves the CCC of all trace widths studied, enabling them to reach values similar to analogous inks printed on high temperature Kapton substrates. Utilizing screen-printing alongside IPL sintering on low cost, temperature sensitive PET demonstrates an established method of fabricating electronic structures derived from high temperature processable ink formulations.

2.8. Acknowledgements

This work was supported by the NSERC Green Electronics Network (GreEN) (grant number: NETGP 508526-17). We thank Benoit Simard for the BNNTs utilized in this study.

2.9. Supporting Information:

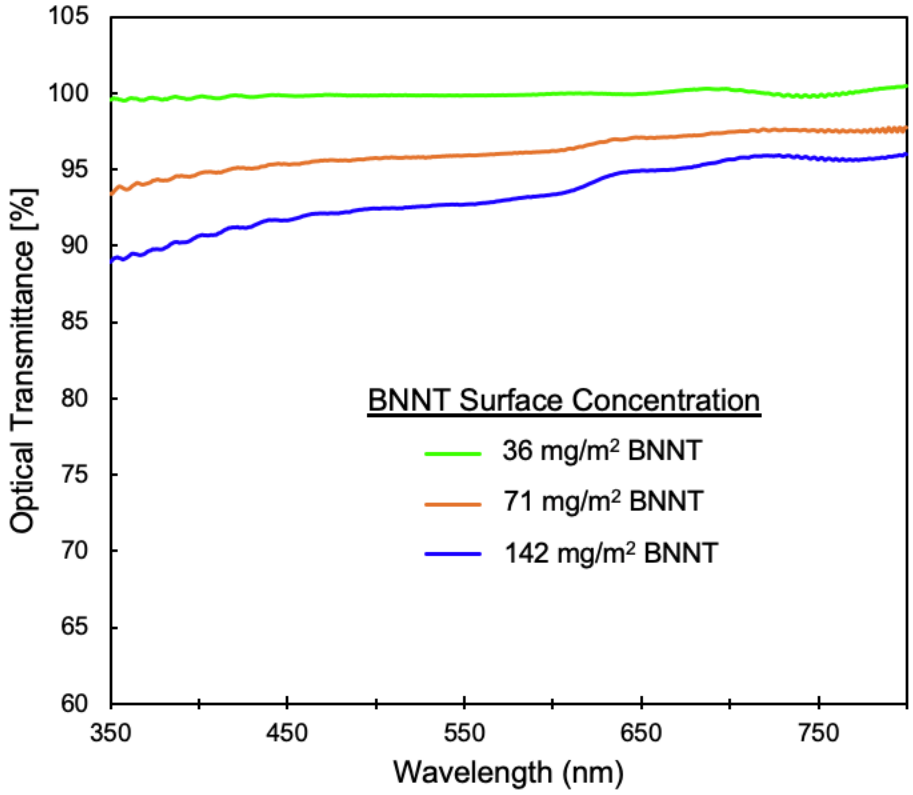

Figure 2.10. UV-Vis transmission spectrum for 36, 71, and 142 mg/m^2 BNNT-coated PET substrates, normalized against an untreated Melinex^{TM} substrate

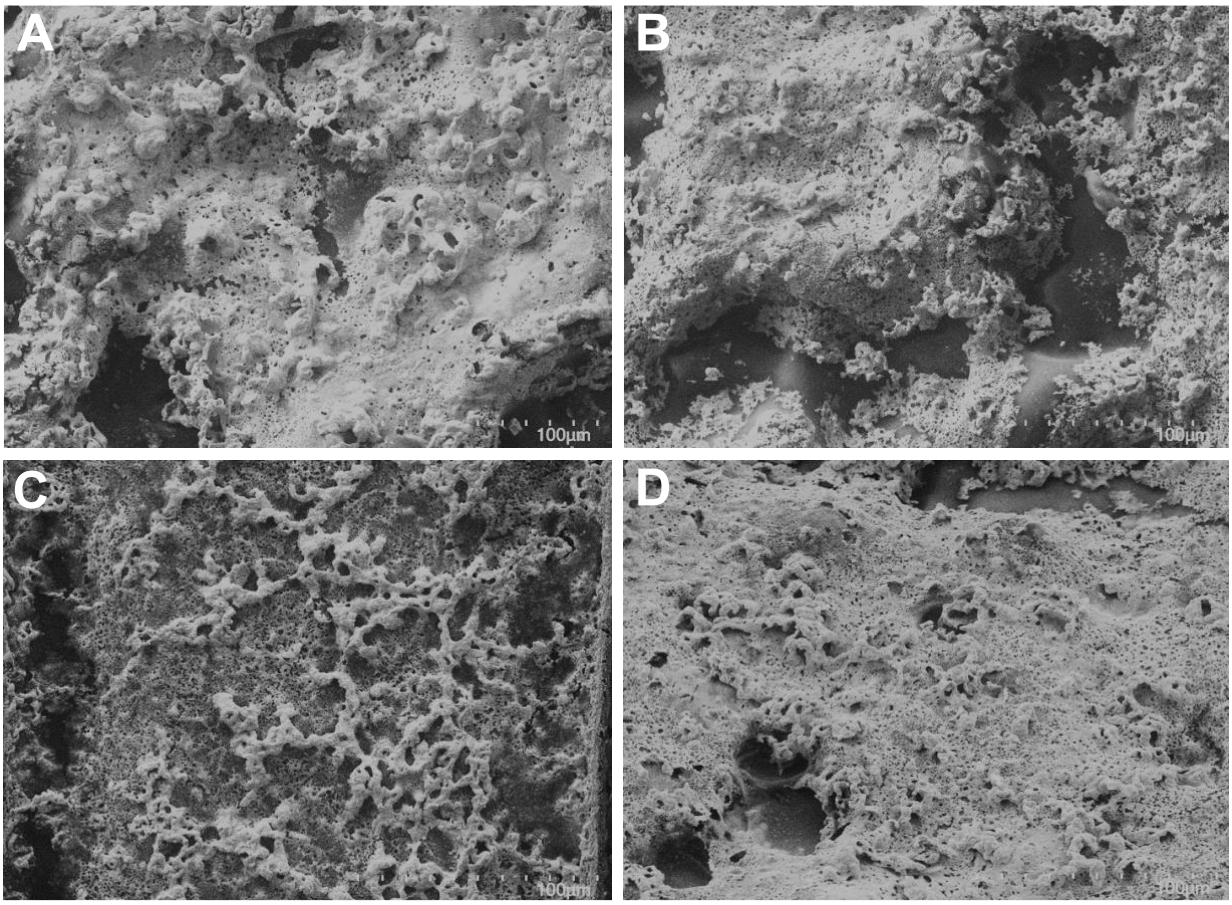

Figure 2.11. High magnification SEM images of silver traces printed on A) bare PET and BNNT-coated PET at surface concentrations of B) 36, C) 71, and D) 142 mg/m^2 highlighting warpage of the substrate upon IPL sintering

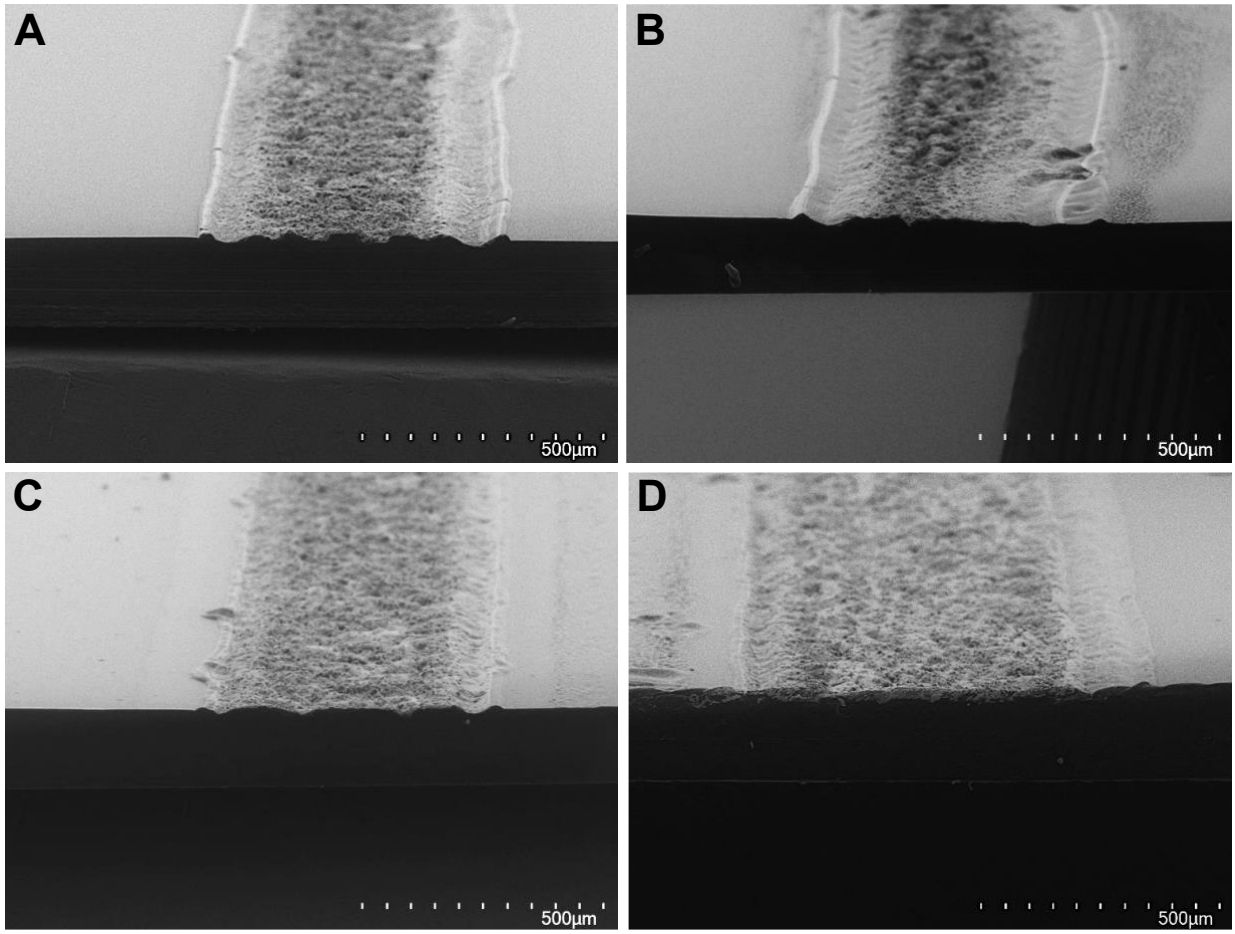

Figure 2.12. Cross-sectional SEM images of the 20 mil trace printed on A) bare PET and BNNT-coated PET at surface concentrations of B) 36, C) 71, and D) 142 mg/m^2

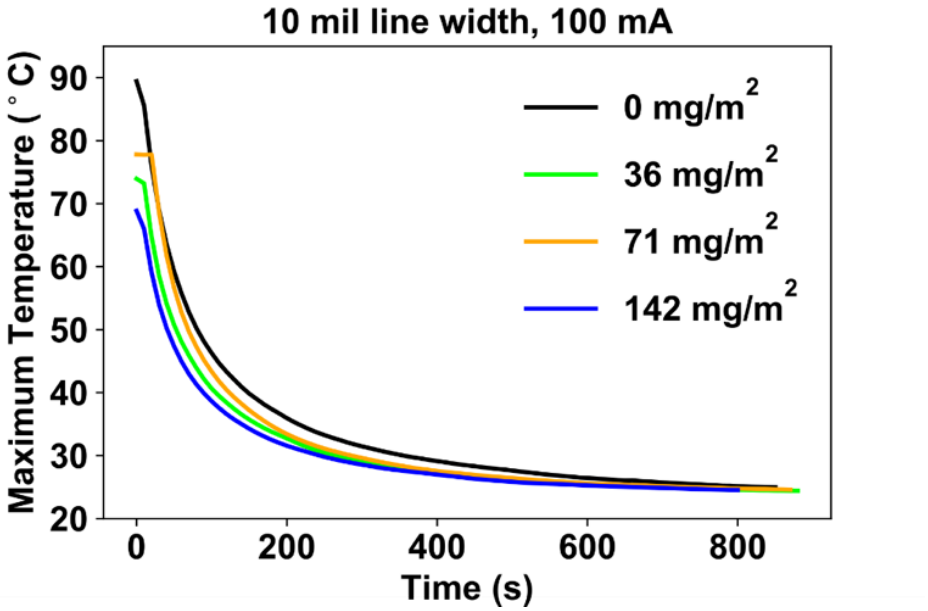

Figure 2.13. Averaged maximum temperature profiles as a function of time for a 10 mil sample printed on bare PET and BNNT-coated PET at surface concentrations of 36 mg/m^2, 71 mg/m^2, and 142 mg/m^2 after removal of 100mA of applied current until room temperature is reached

Table 2.1. Exponential time constants, amplitude, and room temperature values for the change in average peak temperature for investigated BNNT concentrations after removal of 100 mA current from 10 mil line width

Concentration [mg/m^2]	**Room Temperature [°C]**	**Amplitude [A]**	**Time Constant [τ]**
0	26.86	59.28	97.35
36	25.68	46.87	95.25
71	25.82	55.30	95.24
142	25.57	41.05	93.26

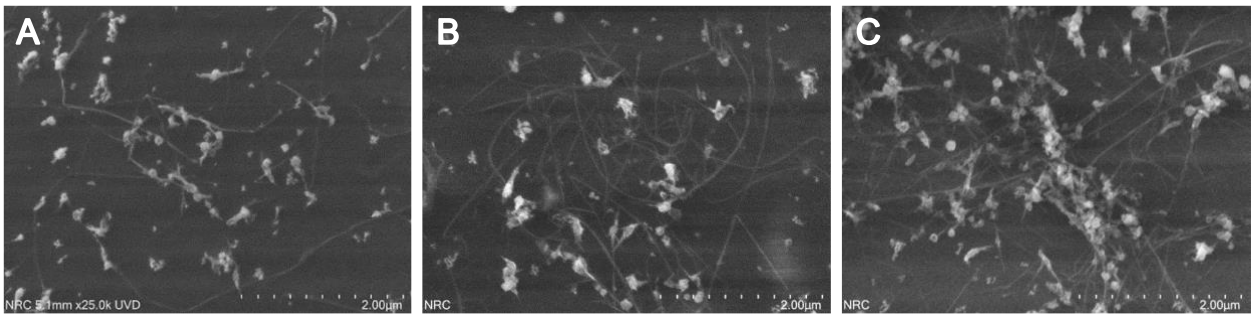

Figure 2.14. SEM images of spray-coated BNNT films at surface concentrations of A) 36, B) 71, and C) 142 mg/m^2 on PET substrates

2.10. References

(1) Capasso, A. Ink-Jet Printing of Graphene for Flexible Electronics_ An Environmentally Friendly Approach. *Solid State Commun.* **2015**, 11.

(2) Nayak, L. A Review on Inkjet Printing of Nanoparticle Inks for Flexible Electronics. *J. Mater. Chem. C* **2019**, 25.

(3) Raut, N. C.; Al-Shamery, K. Inkjet Printing Metals on Flexible Materials for Plastic and Paper Electronics. *J. Mater. Chem. C* **2018**, *6* (7), 1618–1641. https://doi.org/10.1039/C7TC04804A.

(4) Song, M.; Kim, H.-J.; Kim, C. S.; Jeong, J.-H.; Cho, C.; Lee, J.-Y.; Jin, S.-H.; Choi, D.-G.; Kim, D.-H. ITO-Free Highly Bendable and Efficient Organic Solar Cells with Ag Nanomesh/ZnO Hybrid Electrodes. *J. Mater. Chem. A* **2015**, *3* (1), 65–70. https://doi.org/10.1039/C4TA05294C.

(5) Guo, C. F.; Sun, T.; Liu, Q.; Suo, Z.; Ren, Z. Highly Stretchable and Transparent Nanomesh Electrodes Made by Grain Boundary Lithography. *Nat. Commun.* **2014**, *5* (1), 3121. https://doi.org/10.1038/ncomms4121.

(6) Homenick, C. M.; James, R.; Lopinski, G. P.; Dunford, J.; Sun, J.; Park, H.; Jung, Y.; Cho, G.; Malenfant, P. R. L. Fully Printed and Encapsulated SWCNT-Based Thin Film Transistors via a Combination of R2R Gravure and Inkjet Printing. *ACS Appl. Mater. Interfaces* **2016**, *8* (41), 27900–27910. https://doi.org/10.1021/acsami.6b06838.

(7) Cronin, H. M.; Stoeva, Z.; Brown, M.; Shkunov, M.; Silva, S. R. P. Photonic Curing of Low-Cost Aqueous Silver Flake Inks for Printed Conductors with Increased Yield. *ACS Appl. Mater. Interfaces* **2018**, *10* (25), 21398–21410. https://doi.org/10.1021/acsami.8b04157.

(8) Liang, J.; Tong, K.; Pei, Q. A Water-Based Silver-Nanowire Screen-Print Ink for the Fabrication of Stretchable Conductors and Wearable Thin-Film Transistors. *Adv Mater* **2016**, 11.

(9) Kim, Y.; Lee, B.; Yang, S.; Byun, I.; Jeong, I.; Cho, S. M. Use of Copper Ink for Fabricating Conductive Electrodes and RFID Antenna Tags by Screen Printing. *Curr. Appl. Phys.* **2012**, *12* (2), 473–478. https://doi.org/10.1016/j.cap.2011.08.003.
(10) Wu, W.; Liu, L.; Dai, Z.; Liu, J.; Yang, S.; Zhou, L.; Xiao, X.; Jiang, C.; Roy, V. A. L. Low-Cost, Disposable, Flexible and Highly Reproducible Screen Printed SERS Substrates for the Detection of Various Chemicals. *Sci. Rep.* **2015**, *5* (1), 10208. https://doi.org/10.1038/srep10208.
(11) Tam, S. K.; Ng, K. M. High-Concentration Copper Nanoparticles Synthesis Process for Screen-Printing Conductive Paste on Flexible Substrate. *J. Nanoparticle Res.* **2015**, *17* (12), 466. https://doi.org/10.1007/s11051-015-3277-x.
(12) Choi, Y.; Seong, K.; Piao, Y. Metal−Organic Decomposition Ink for Printed Electronics. *Adv. Mater. Interfaces* **2019**, *6* (20), 1901002. https://doi.org/10.1002/admi.201901002.
(13) Kell, A. J.; Paquet, C.; Mozenson, O.; Djavani-Tabrizi, I.; Deore, B.; Liu, X.; Lopinski, G. P.; James, R.; Hettak, K.; Shaker, J.; Momciu, A.; Ferrigno, J.; Ferrand, O.; Hu, J. X.; Lafrenière, S.; Malenfant, P. R. L. Versatile Molecular Silver Ink Platform for Printed Flexible Electronics. *ACS Appl. Mater. Interfaces* **2017**, *9* (20), 17226–17237. https://doi.org/10.1021/acsami.7b02573.
(14) Jahn, S. F.; Blaudeck, T.; Baumann, R. R.; Jakob, A.; Ecorchard, P.; Rüffer, T.; Lang, H.; Schmidt, P. Inkjet Printing of Conductive Silver Patterns by Using the First Aqueous Particle-Free MOD Ink without Additional Stabilizing Ligands †. *Chem. Mater.* **2010**, *22* (10), 3067–3071. https://doi.org/10.1021/cm9036428.
(15) Adner, D.; Wolf, F. M.; Möckel, S.; Perelaer, J.; Schubert, U. S.; Lang, H. Copper(II) Ethylene Glycol Carboxylates as Precursors for Inkjet Printing of Conductive Copper Patterns. *Thin Solid Films* **2014**, *565*, 143–148. https://doi.org/10.1016/j.tsf.2014.06.054.
(16) Shin, D.-Y.; Jung, M.; Chun, S. Resistivity Transition Mechanism of Silver Salts in the next Generation Conductive Ink for a Roll-to-Roll Printed Film with a Silver Network. *J. Mater. Chem.* **2012**, *22* (23), 11755. https://doi.org/10.1039/c2jm30198a.
(17) Wünscher, S.; Abbel, R.; Perelaer, J.; Schubert, U. S. Progress of Alternative Sintering Approaches of Inkjet-Printed Metal Inks and Their Application for Manufacturing of Flexible Electronic Devices. *J Mater Chem C* **2014**, *2* (48), 10232–10261. https://doi.org/10.1039/C4TC01820F.
(18) Polino, G.; Shanmugam, S.; Bex, G. J. P.; Abbel, R.; Brunetti, F.; Di Carlo, A.; Andriessen, R.; Galagan, Y. Photonic Flash Sintering of Ink-Jet-Printed Back Electrodes for Organic Photovoltaic Applications. *ACS Appl. Mater. Interfaces* **2016**, *8* (3), 2325–2335. https://doi.org/10.1021/acsami.5b11394.
(19) Galagan, Y.; Coenen, E. W. C.; Abbel, R.; van Lammeren, T. J.; Sabik, S.; Barink, M.; Meinders, E. R.; Andriessen, R.; Blom, P. W. M. Photonic Sintering of Inkjet Printed Current Collecting Grids for Organic Solar Cell Applications. *Org. Electron.* **2013**, *14* (1), 38–46. https://doi.org/10.1016/j.orgel.2012.10.012.
(20) Norita, S.; Kumaki, D.; Kobayashi, Y.; Sato, T.; Fukuda, K.; Tokito, S. Inkjet-Printed Copper Electrodes Using Photonic Sintering and Their Application to Organic Thin-Film Transistors. *Org. Electron.* **2015**, *25*, 131–134. https://doi.org/10.1016/j.orgel.2015.06.026.
(21) Kim, H.-S.; Dhage, S. R.; Shim, D.-E.; Hahn, H. T. Intense Pulsed Light Sintering of Copper Nanoink for Printed Electronics. *Appl. Phys. A* **2009**, *97* (4), 791–798. https://doi.org/10.1007/s00339-009-5360-6.

(22) Jang, Y.-R.; Joo, S.-J.; Chu, J.-H.; Uhm, H.-J.; Park, J.-W.; Ryu, C.-H.; Yu, M.-H.; Kim, H.-S. A Review on Intense Pulsed Light Sintering Technologies for Conductive Electrodes in Printed Electronics. *Int. J. Precis. Eng. Manuf.-Green Technol.* **2020**. https://doi.org/10.1007/s40684-020-00193-8.
(23) Secor, E. B.; Prabhumirashi, P. L.; Puntambekar, K.; Geier, M. L.; Hersam, M. C. Inkjet Printing of High Conductivity, Flexible Graphene Patterns. *J Phys Chem Lett* **2013**, 5.
(24) Secor, E. B.; Gao, T. Z.; Islam, A. E.; Rao, R.; Wallace, S. G.; Zhu, J.; Putz, K. W.; Maruyama, B.; Hersam, M. C. Enhanced Conductivity, Adhesion, and Environmental Stability of Printed Graphene Inks with Nitrocellulose. *Chem. Mater.* **2017**, *29* (5), 2332–2340. https://doi.org/10.1021/acs.chemmater.7b00029.
(25) Yang, W.; List-Kratochvil, E. J. W.; Wang, C. Metal Particle-Free Inks for Printed Flexible Electronics. *J. Mater. Chem. C* **2019**, *7* (48), 15098–15117. https://doi.org/10.1039/C9TC05463D.
(26) Ryu, C.-H.; Joo, S.-J.; Kim, H.-S. Intense Pulsed Light Sintering of Cu Nano Particles/Micro Particles-Ink Assisted with Heating and Vacuum Holding of Substrate for Warpage Free Printed Electronic Circuit. *Thin Solid Films* **2019**, *675*, 23–33. https://doi.org/10.1016/j.tsf.2019.02.020.
(27) Lee, T.-W.; Lee, S.-E.; Jeong, Y. G. Carbon Nanotube/Cellulose Papers with High Performance in Electric Heating and Electromagnetic Interference Shielding. *Compos. Sci. Technol.* **2016**, *131*, 77–87. https://doi.org/10.1016/j.compscitech.2016.06.003.
(28) Feng, C.-P.; Chen, L.-B.; Tian, G.-L.; Wan, S.-S.; Bai, L.; Bao, R.-Y.; Liu, Z.-Y.; Yang, M.-B.; Yang, W. Multifunctional Thermal Management Materials with Excellent Heat Dissipation and Generation Capability for Future Electronics. *ACS Appl. Mater. Interfaces* **2019**, *11* (20), 18739–18745. https://doi.org/10.1021/acsami.9b03885.
(29) Kim, T.-H.; Choi, W. M.; Kim, D.-H.; Meitl, M. A.; Menard, E.; Jiang, H.; Carlisle, J. A.; Rogers, J. A. Printable, Flexible, and Stretchable Forms of Ultrananocrystalline Diamond with Applications in Thermal Management. *Adv. Mater.* **2008**, *20* (11), 2171–2176. https://doi.org/10.1002/adma.200702434.
(30) Blase, X.; Rubio, A.; Louie, S. G.; Cohen, M. L. Stability and Band Gap Constancy of Boron Nitride Nanotubes. *Europhys. Lett. EPL* **1994**, *28* (5), 335–340. https://doi.org/10.1209/0295-5075/28/5/007.
(31) Chen, Y.; Zou, J.; Campbell, S. J.; Le Caer, G. Boron Nitride Nanotubes: Pronounced Resistance to Oxidation. *Appl. Phys. Lett.* **2004**, *84* (13), 2430–2432. https://doi.org/10.1063/1.1667278.
(32) Liang, Q.; Yao, X.; Wang, W.; Liu, Y.; Wong, C. P. A Three-Dimensional Vertically Aligned Functionalized Multilayer Graphene Architecture: An Approach for Graphene-Based Thermal Interfacial Materials. *ACS Nano* **2011**, *5* (3), 2392–2401. https://doi.org/10.1021/nn200181e.
(33) Yu, A.; Ramesh, P.; Sun, X.; Bekyarova, E.; Itkis, M. E.; Haddon, R. C. Enhanced Thermal Conductivity in a Hybrid Graphite Nanoplatelet – Carbon Nanotube Filler for Epoxy Composites. *Adv. Mater.* **2008**, *20* (24), 4740–4744. https://doi.org/10.1002/adma.200800401.
(34) Chen, J.; Huang, X.; Sun, B.; Jiang, P. Highly Thermally Conductive Yet Electrically Insulating Polymer/Boron Nitride Nanosheets Nanocomposite Films for Improved Thermal Management Capability. *ACS Nano* **2019**, *13* (1), 337–345. https://doi.org/10.1021/acsnano.8b06290.

(35) Shtein, M.; Nadiv, R.; Buzaglo, M.; Regev, O. Graphene-Based Hybrid Composites for Efficient Thermal Management of Electronic Devices. *ACS Appl. Mater. Interfaces* **2015**, *7* (42), 23725–23730. https://doi.org/10.1021/acsami.5b07866.
(36) Guan, J.; Simard, B. Modified Boron Nitride Nanotubes and Solution Thereof. US2020/0262703, 2020.
(37) Ding, H.; Guan, J.; Lu, P.; Mihailov, S. J.; Kingston, C. T.; Simard, B. Boron Nitride Nanotubes for Optical Fiber Chemical Sensing Applications. *IEEE Sens. Lett.* **2020**, *4* (10), 1–4. https://doi.org/10.1109/LSENS.2020.3023702.
(38) Jakubinek, M. B.; Niven, J. F.; Johnson, M. B.; Ashrafi, B.; Kim, K. S.; Simard, B.; White, M. A. Thermal Conductivity of Bulk Boron Nitride Nanotube Sheets and Their Epoxy-Impregnated Composites: Thermal Conductivity of Bulk Boron Nitride Nanotube Sheets. *Phys. Status Solidi A* **2016**, *213* (8), 2237–2242. https://doi.org/10.1002/pssa.201533010.
(39) Kim, K. S.; Kingston, C. T.; Hrdina, A.; Jakubinek, M. B.; Guan, J.; Plunkett, M.; Simard, B. Hydrogen-Catalyzed, Pilot-Scale Production of Small-Diameter Boron Nitride Nanotubes and Their Macroscopic Assemblies. *ACS Nano* **2014**, *8* (6), 6211–6220. https://doi.org/10.1021/nn501661p.
(40) Cho, H.; Walker, S.; Plunkett, M.; Ruth, D.; Iannitto, R.; Martinez Rubi, Y.; Kim, K. S.; Homenick, C. M.; Brinkmann, A.; Couillard, M.; Dénommée, S.; Guan, J.; Jakubinek, M. B.; Jakubek, Z. J.; Kingston, C. T.; Simard, B. Scalable Gas-Phase Purification of Boron Nitride Nanotubes by Selective Chlorine Etching. *Chem. Mater.* **2020**, *32* (9), 3911–3921. https://doi.org/10.1021/acs.chemmater.0c00144.
(41) Martinez-Rubi, Y.; Jakubek, Z. J.; Jakubinek, M. B.; Kim, K. S.; Cheng, F.; Couillard, M.; Kingston, C.; Simard, B. Self-Assembly and Visualization of Poly(3-Hexyl-Thiophene) Chain Alignment along Boron Nitride Nanotubes. *J. Phys. Chem. C* **2015**, *119* (47), 26605–26610. https://doi.org/10.1021/acs.jpcc.5b09049.
(42) Hobbie, R. K.; Roth, B. J. Exponential Growth and Decay. In *Intermediate Physics for Medicine and Biology*; Springer International Publishing: Cham, 2015; pp 33–51. https://doi.org/10.1007/978-3-319-12682-1_2.
(43) Niittynen, J.; Sowade, E.; Kang, H.; Baumann, R. R.; Mäntysalo, M. Comparison of Laser and Intense Pulsed Light Sintering (IPL) for Inkjet-Printed Copper Nanoparticle Layers. *Sci. Rep.* **2015**, *5* (1), 8832. https://doi.org/10.1038/srep08832.
(44) Paquet, C.; James, R.; Kell, A. J.; Mozenson, O.; Ferrigno, J.; Lafrenière, S.; Malenfant, P. R. L. Photosintering and Electrical Performance of CuO Nanoparticle Inks. *Org. Electron.* **2014**, *15* (8), 1836–1842. https://doi.org/10.1016/j.orgel.2014.05.014.
(45) Li, D.; Han, T.; Ruan, H. Solution-Assembled Ordered Grids Constructed with Silver Nanowires as Transparent Conductive Electrodes. *ACS Omega* **2018**, *3* (7), 7191–7195. https://doi.org/10.1021/acsomega.8b01320.
(46) Baumbauer, C. L.; Anderson, M. G.; Ting, J.; Sreekumar, A.; Rabaey, J. M.; Arias, A. C.; Thielens, A. Printed, Flexible, Compact UHF-RFID Sensor Tags Enabled by Hybrid Electronics. *Sci. Rep.* **2020**, *10* (1), 16543. https://doi.org/10.1038/s41598-020-73471-9.
(47) Alhendi, M.; Sivasubramony, R. S.; Weerawarne, D. L.; Iannotti, J.; Borgesen, P.; Poliks, M. D. Assessing Current-Carrying Capacity of Aerosol Jet Printed Conductors. *Adv. Eng. Mater.* **2020**, *22* (11), 2000520. https://doi.org/10.1002/adem.202000520.
(48) Mitra, D.; Mitra, K. Y.; Dzhagan, V.; Pillai, N.; Zahn, D. R. T.; Baumann, R. R. Work Function and Conductivity of Inkjet-Printed Silver Layers: Effect of Inks and Post-

Treatments. *J. Electron. Mater.* **2018**, *47* (3), 2135–2142. https://doi.org/10.1007/s11664-017-6024-5.

(49) Keränen, K.; Korhonen, P.; Rekilä, J.; Tapaninen, O.; Happonen, T.; Makkonen, P.; Rönkä, K. Roll-to-Roll Printed and Assembled Large Area LED Lighting Element. *Int. J. Adv. Manuf. Technol.* **2015**, *81* (1–4), 529–536. https://doi.org/10.1007/s00170-015-7244-6.

Chapter 3. Engineering silver microgrids with a boron nitride nanotube interlayer for highly conductive and flexible transparent heaters

This chapter is adapted from work published in "Advanced Materials Technologies": Wagner, K.; Kell, A. J.; Martinez-Rubi, Y.; Paquet, C.; Lessard, B. H. Engineering Silver Microgrids with a Boron Nitride Nanotube Interlayer for Highly Conductive and Flexible Transparent Heaters. Adv Materials Technologies 2022, 2200037.

3.1. Context

In this work**,** I translated the BNNT interlayer to be useful from an operational standpoint, taking advantage of the improved heat uniformity to increase transparent heater performance. Silver microgrid electrodes were designed and their geometry extensively explored, creating an in-depth relationship between maximizing optical transparency and conductivity through processing optimization. The optimal BNNT surface concentration determined in **Chapter 2** was deposited on polyethylene terephthalate substrates as an interlayer at the substrate-grid interface. As mentioned in **Chapter 1**, bulk BNNTs also exhibit high mechanical durability, and so the effectiveness of the BNNT interlayer to reduce mechanical stress on the grids upon ASTM bending tests was quantified and proven to increase the flexibility of the microgrids. Finally, applied voltage testing provided confirmation that microgrid heaters with the BNNT interlayer present achieved higher ohmic sintering, studying how this leads to a larger and more uniform temperature output without affecting the integrity of the temperature sensitive substrate.

3.2. Contributions

I prepared and deposited the BNNT dispersion with assistance from Dr. Martinez-Rubi and acquired surface energy measurements of the BNNT surface. I designed, printed and processed the transparent heater architectures with optimization assistance from Dr. Paquet and Dr. Kell. I measured solid-state UV-Vis and electrical resistance of all grid designs, as well as qualitative SEM images of the grids and corresponding profilometric analyses. I conducted both mechanical bending and crease testing and completed thermal testing and visualized corresponding IR imaging with input from Dr. Kell. I wrote the manuscript with input from Dr. Kell, Dr. Paquet, and Dr. Lessard.

3.3. Abstract

The use of flexible transparent conductive electrodes (TCEs) as printed heaters offers unique advantages where transparency is a necessary design feature. Many existing TCE materials however suffer from poor flexibility and require complex fabrication processes and thus are not commercially viable for such applications. The design and process optimization of screen-printable silver metal microgrids over a layer of boron nitride nanotubes (BNNT) to produce highly conductive and mechanically robust transparent heaters with high transparency and low power requirements is reported. Square and hexagonal geometries are investigated alongside varying line width and pitch combinations to produce 16 different grid designs with optical transparency ranging between 65% and 89% and resistance values as low as 2.90 Ω sq^{-1}. The BNNT thin film coating on polyethylene terephthalate substrates provides mechanical stability to the heater architecture by reducing the effects of deformation by up to 400%. The BNNT interlayer also contributes to an increase in thermal performance, achieving temperatures as high as 74.0 °C by initiating electrical sintering of the microgrids during heater operation which increases the Joule heating capacity of the features. Overall, this physical and material optimization provides a low-cost, printable microgrid architecture for high performing and stable applications as TCE-based heaters.

3.4. Introduction

The development and optimization of flexible transparent conductive electrodes (TCEs) has garnered interest for integration into next-generation organic electronics applications such as thin film transistors (TFTs),[1] organic photovoltaics (OPVs),[2–4] touch-sensitive interfaces,[5] and light emitting diodes (LEDs).[6] Conventional metal oxide-derived conductive materials such as indium tin oxide (ITO) are still predominantly employed as TCEs due to their excellent electrical properties (R_s = 10 Ω/sq) and notable optical transparency (T = 90%).[7,8] Despite such favourable properties, the feasibility of ITO electrodes for mass production has recently come into question. High-cost sputtering deposition techniques combined with finite indium resources are key limitations towards scale-up potential, while its' mechanical brittleness has made it a poor candidate for printable electronics.[9–11] Several viable flexible TCE alternative materials such as graphene,[12–14] carbon nanotubes,[12,14–16] metallic nanowires,[17,18] metallic grids,[6,19,20] and hybrid films[21–25] have emerged to circumvent the challenges of ITO electrodes in device architectures.

Silver metallic microgrids hold great potential as flexible TCEs due to their high degree of geometric tunability and versatility of available ink formulations compatible with high volume printing techniques such as screen-printing.[26,27] Ink formulations containing metal carboxylate salts, specifically silver neodecanoate (AgND), demonstrate a mechanically robust and highly conductive medium for fabricating silver features at low processing temperatures.[28–30] However, maximizing the electro-optical properties is key for TCE design to ensure that the payoff for high electrical performance does not negatively impact the resulting transparency of the electrode. Optimizing the electro-optical properties through careful selection of the TCE design, material selection and material processing conditions ensures that high conductive performance of the grids can be achieved with high optical transparency. One technique to improve the electro-optical properties of microgrid TCEs is to optimize the process that converts silver molecular ink into conductive and uniform metal traces. Photonic sintering in particular is an effective process to convert AgND into conductive Ag traces, with high line uniformity and density (increasing conductivity and reducing resistance). Photonic treatment is typically accomplished using techniques such as intense pulsed light (IPL) sintering, laser sintering, and ultra-violet (UV) assisted sintering.[31–33] UV treatments are valuable as they can produce conductive traces in 20% of the time required for thermal sintering, however, suitable UV-assisted sintering techniques typically require long processing times relative to IPL and laser sintering, reaching exposure times of up to 40 minutes.[30,34] Minimizing this time frame while still retaining optimal performance metrics is necessary for UV sintering to be considered a feasible technique for large-scale electrode fabrication. Therefore, microgrid design, trace morphology, surface chemistry, and UV light exposure will therefore all play a critical role in conductive performance and subsequently transparent heater thermal performance efficiency.

In addition to investigating microgrid TCE design and sintering process optimization, incorporating materials that work in synergy with the conductor can aid in enhancing mechanical and conductive performance. Improving the mechanical performance of flexible TCEs has been demonstrated through the incorporation of inert additives to the ink formulation, such as elastomers and polymer matrices,[35,36] however they often hinder the conductive performance of the trace. Alongside investigating additives to the ink formulation, it is also possible to integrate materials into the plastic substrate matrix in order to improve mechanical robustness rather than alter the ink formulation. Boron nitride nanotubes (BNNT) have high mechanical stability and

have been demonstrated in applications for improved mechanical endurance, however they are typically embedded into polymer matrices that act as the substrate in printed electronics.[37] To improve processability and accommodate rapid electronics printing, it's possible to use coating techniques to deposit BNNTs as a discrete film by utilizing solution-processable dispersions of BNNTs.[38,39] In addition to utilizing BNNT thin films as a buffer towards mechanical deformation, the inherent thermal conductivity and stability of the BNNT thin film interlayer can also provide beneficial thermal diffusion to areas within the microgrid shapes that are void of the Ag trace. It is clear that the optimized electro-optical properties of the high performance microgrid paired with the BNNT interlayer demonstrates specific interest in utilizing the microgrid in transparent heater applications.

Herein we demonstrate a trilateral approach of microgrid design optimization with the addition of a slot-die coated BNNT film for improved thermal conduction, flexibility, and electrical performance and illustrate its utility in TCE heater applications. The influence of grid geometry on optical transparency and resistance are investigated alongside optimized UVA assisted treatment to maximize electro-optical properties and achieve the development of microgrid heaters with fast Joule heating response. In addition, the presence of the BNNTs at the microgrid-substrate interface increases the dissipation of heat generated upon applying voltage towards the grid areas void of silver ink features and improves the microgrids resistance to mechanical deformation during repeated flexing cycles. This study highlights the mechanical and thermal improvements in TCE heaters when using BNNT thin films while providing critical structure property relationships between the electro-optical and morphological properties of silver traces made from AgND ink formulations.

3.5. Experimental Section

Synthesized BNNT material was non-covalently functionalized with regiorandom poly(3-hexylthiophene-2,5-diyl) (rra-P3HT) as detailed in the work completed by Martinez-Rubi et al., with a resulting concentration of 0.2 mg/mL in chloroform solvent.[40] The BNNT solution was subsequently slot-die coated onto polyethylene terephthalate (PET) substrates using an Automatic Research (GmBH) thin film coater fitted with the SC-150 slot-die applicator and a Harvard Apparatus standard infuse/withdraw PHD 22/2000 syringe pump. The coating speed (V) and solution flowrate (Q) were calculated as per the following equation:

$$t_{film} \equiv \frac{Q}{V \times W} \times S\% \; [cm] \qquad [3.1]$$

by setting the dry film thickness (t_{film}) to 30 nm, the coating width (W) to 17.5 cm, and the solid content (S%) to 1.32%, depositing a surface concentration of 142 mg/m^2.

The ink was prepared by mixing the polyester resin (Rokrapol) with 1-octanol and an oxazoline derivative at a 25:75 w/w ratio. Silver neodecanoate salt was then immediately dissolved within the solution. The mixture was placed in a centrifugal mixer (Thinky USA) for 30 minutes at 2000 RPM to ensure full dispersion of the silver salt within the mixture. The molecular ink was screen-printed onto bare polyethylene terephthalate (PET) and BNNT-coated PET substrates using an American M&M S-912M small format screen printer utilizing a SS360 stainless steel mesh (Dynamesh, IL) with an MM1 emulsion and an emulsion over mesh thickness of 7 μm. Printed samples were left exposed to air for 48 hours to evaporate the solvents under ambient conditions. Once dried, the samples were placed under a Dymax 5000-EC metal halide UV curing flood lamp at various durations initiating conversion of Ag^+ to Ag^0. The samples were then further dried at 40 ˚C for 20 min to remove any remaining solvent within the printed traces, and then subsequently thermally sintered at 160 ˚C for 1 hour to complete the conversion to a conductive Ag0 trace. Samples printed on bare PET substrates then underwent an inert Ar-plasma treatment under vacuum for 20 minutes.

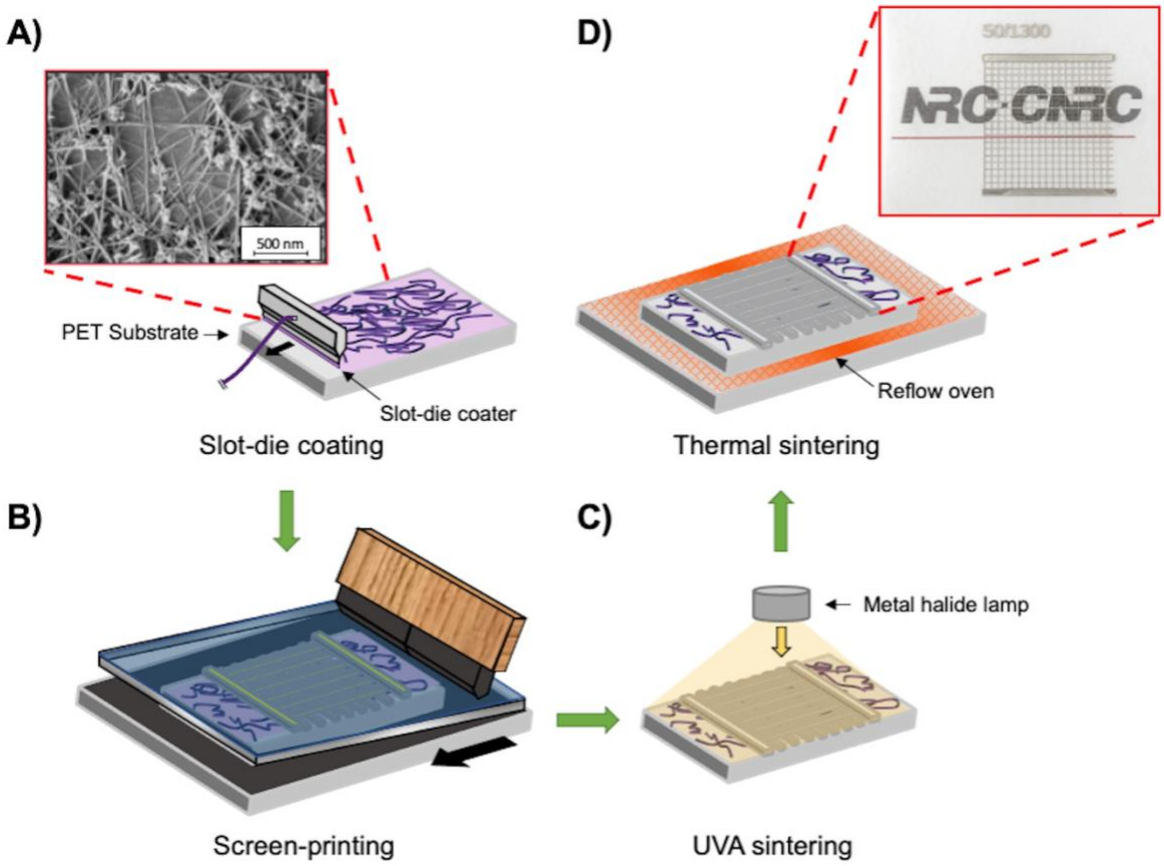

Figure 3.1. Schematic of A) slot-die coating process with SEM image of the dry BNNT film, B) screen-printing process, and C) UV treatment and D) thermal sintering processes with post-sintered 50/1300 square microgrid

3.5.1. Characterization

Resistance measurements of the printed traces were immediately taken post-processing as a function of ohms using a Fluke 115 Digital Multimeter. Probes were placed parallel on each electrical pad attached to the printed grid and moved across the pad to obtain an average of resistance measurements across the entire design. A Cary 5000 ultraviolet-visible (UV-Vis) spectrometer measured solid-state optical transmittance of the BNNT-coated PET film as well as the grid designs printed on bare PET and BNNT- coated PET, with a bare PET sample acting as the background measurement. Two-dimensional optical profilometry was completed using a cyberTECHNOLOGIES CT100 optical profilometer (cyberTECHNOLOGIES GmbH). Scanning electron microscopy (SEM) was completed using a Hitachi SU3500 and SU5000 microscope with back-scattering electron imaging and ultra-variable pressure detector with an accelerating voltage

of 15kV and 10 mm working distance. A ThermoFisher Scientific Apreo-2 SEM with an accelerating voltage of 500V and 3.1 mm working distance was used to obtain the high-resolution imaging of the slot-die coated BNNT film, as seen in **Figure 3.1**. Contact angle measurements were completed using a Biolin Scientific Attension Theta Optical Tensiometer with OneAttension software to measure the angles. The tensiometer was fitted with water as the solvent, and a Navitar camera captured images of the individual water droplets 10 seconds after deposition onto the substrate. The mechanical bend and crease tests were completed according to ASTM Standards (Designation: F 1683). For the tensile bend test, samples were rolled around a mandrel with a radius of 10 mm for a total of 500 cycles, where one cycle denotes a roll in one direction followed by a roll in the opposite direction, returning to its' original position. Resistance measurements were conducted every 25 cycles using a multimeter in the same manner as described above and placement of the probes on the electrical pad was kept consistent at the time of each measurement. The mechanical crease test was completed by loosely folding and securing the sample in half along the y-axis and then rolling a mandrel with a diameter of 68.6 mm weighing 1.0 kg across the folded sample perpendicular to the direction of the fold and back across to return to the original position. The sample was then unfolded, and the mandrel run across the sample in the same manner. Resistance measurements were completed before and after the test using a multimeter, with the measurement locations kept consistent.

Thermal imaging and temperature response was conducted using a U5857A TrueIR Thermal Imager by Keysight Technologies camera. A voltage bias was applied using a wiring system and conductive copper tape, and a connected multimeter provided measured conductance values. To generate the temperature versus time data, voltage was continuously applied to the grid design for five minutes with measurements taken every 10 seconds starting at time t = 0 s up until one minute after the voltage was removed. Corresponding images of the thermal response upon applied voltage were simultaneously taken every 10 seconds. The microgrids were placed such that no contact was made to support structures in order to avoid passive heat dissipation away from the printed feature. All thermal response testing was completed in the identical manner for both the microgrids printed on bare PET and those printed on BNNT-coated PET.

3.6. Results and Discussion

3.6.1 Electro-Optical Properties

Metal grid architectures hold several advantages as transparent heater systems due to their low cost, thermal and mechanical stability, as well as their technological readiness level in comparison to other material design platforms.[41] The ability to easily tune the geometric design and form factor of the traces yields a wide range of grid design combinations that can be used to optimize electrical and thermal properties. Furthermore, unlike metallic nanowire films that rely on randomized wire contact to form a conductive pathway, the characteristic uniform conductive pathways of metal grid architectures ensure high electrical performance. Research interest into the efficacy and optimization of metal grids as transparent heaters has grown in recent years, such as with work completed by Gupta et al. on investigating different geometries of Ag design patterns as flexible heaters and He et al. investigating the use of an Ag nanowire/PEDOT:PSS ink formulation in fabricating square and hexagonal grid TCEs for transparent heater applications.[19–21] Various tessellating grid patterns, including but not limited to squares, hexagons, triangles, and pentagons have been demonstrated as viable transparent and conductive grid patterns,[42–44] and as such it is important to further optimize electro-optical properties of the metal grids through tuning grid shape and line dimensions.

Typically, as grid line width increases, the electrical conductivity increases and optical transparency decreases, whereas when the pitch distance increases, the optical transparency increases, however the electrical conductivity decreases.[42,45] Herein, two different shapes, square and hexagonal, are investigated and a variety of pitch and width combinations are used to establish a relationship between transparency and conductivity. In this study, square and hexagonal shapes were chosen due to their geometric uniformity as a repeated pattern within the grid area, with hexagonal designs taking inspiration from biological aspects. To fully investigate the effect of geometry and form factor of the silver traces, grid patterns with pitch values ranging from 455 – 1300 μm for squares and 1150 – 2600 μm for hexagons were chosen. Nominal line widths ranging from 25 – 150 μm with identical line width combinations (25, 35, & 50 μm) for square and hexagonal geometries were chosen to further investigate how shape and pitch dictate the electro-optical performance of the grids. A schematic defining the geometry and line width and pitch measurements in the context of the grid patterns is displayed in **Figure 3.2A**. The average resistance (R_{avg}) as a function of optical transmittance (%T) is presented for all sixteen designs in

Figure 3.2B. Optical transmittance spectra of each grid pattern are shown in **Figure 3.10** and **Figure 3.11** for the hexagonal and square designs respectively.

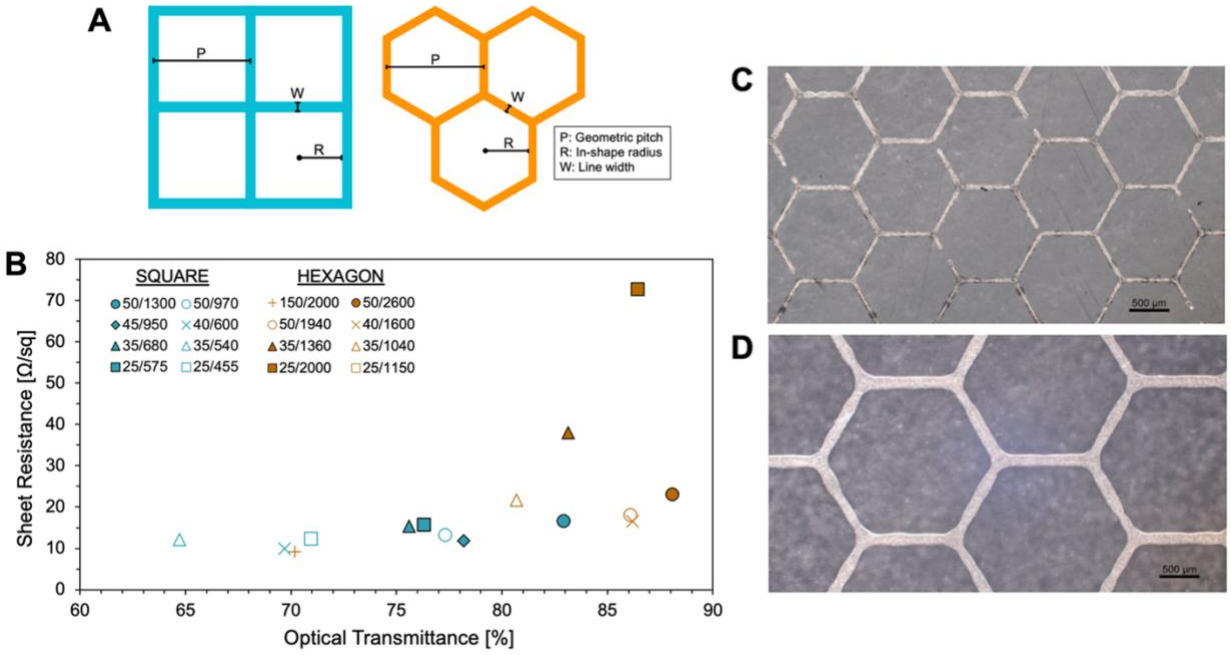

Figure 3.2. A) Schematic defining pitch, radius and line width measurements, B) Comparison of optical transmittance and sheet resistance for all hexagonal and square design combinations on bare PET and corresponding microscope images of the C) hexagonal 25/1150 and D) hexagonal 50/1940 grid patterns post-processing

As shown in **Figure 3.2B**, the hexagonal designs typically exhibited greater optical transparency due to their larger pitch and inherent internal angle sum, while the square designs generally measured at lower sheet resistances due to more available conductive pathways of the square design in the total grid area. Square grid designs exhibited relatively similar sheet resistance for each presented line and pitch combination, with only significant changes in varying transmittance (**Figure 3.2B**). For grid patterns with identical nominal line widths, particularly the square designs, it is evident that the sheet resistance does not decrease significantly upon reducing the pitch of the grid design and instead exclusively impacts the transparency. Therefore, there is no benefit in increasing the density of the lines, as it does not lead to improved conductance (lower sheet resistance) and ultimately reduces the optical transmittance. Additionally, when comparing grid designs of 25 µm line width against those with 50 µm line widths, the design with a combination of a large line width and a larger pitch has a significantly higher $\%T/R_{avg}$ ratio than a

grid design with a small line width and smaller pitch. This indicates that the conductive performance of the 50 µm line widths is superior to that of the 25 µm, regardless of whether the quantity of 25 µm lines were doubled to mimic the total silver percentage of the 50 µm line widths. We observed that nominal line widths ≤ 25 µm exhibited poor trace formation upon exposure to the processing methods, leading to inconsistent and nonconductive grids. **Figures 3.2C** and **3.2D** depict the difference in print quality of the hexagonal grid patterns with 25 µm and 50 µm line widths respectively. As the line width decreases, the printed traces have increasingly more defects that affects their conductivities, ultimately highlighting the resolution limits of screen-printing techniques for AgND ink formulations.

3.6.2. UV Treatment

A key component in the processing of molecular ink formulations is the use of ultraviolet (UV) light treatment, which consists of exposing the traces to irradiation within the 100 to 400 nm range.[30,33] Utilizing UV light as an irradiation source enables the selective heating of the molecular ink through efficient light absorption while avoiding any adverse effects to the surrounding substrate. The wavelength range of UV light exposure can be compartmentalized to four primary ranges: UVC (200-280 nm), UVB (280-320 nm), UVA (320-395 nm), and UVV (395-455 nm), which are obtained using different light sources.[46] UVA light in particular is considered one of the best wavelengths for curing molecular ink formulations, as the long-range wavelength is useful for the characteristic photoreduction of silver neodecanoate to silver metal nanoparticles. This has been previously demonstrated by Liu et al., showing that when silver oxalate is exposed to UVA light, there is a photoreduction of the silver salt to form silver nanoparticles.[30] The as-produced silver nanoparticles have a broad absorption band around 420 nm, so the output of the UVA lamp overlaps well with the absorption of these silver nanoparticles. As the silver nanoparticles absorb this light, heat is generated within the trace and allows it to dry. In the previous study, silver oxalate present in the ink (decomposing to silver at 80-120˚C) could be completely converted to metallic silver through the exposure to UVA light. Here we employ silver neodecanoate salt which decomposes to silver at approximately 150˚C, and as such the exposure to UVA light does not generate enough heat to fully convert to metallic silver. In this case, the UVA process removes the solvent and helps to control the line widths of the trace, and therefore the light exposure time influences grid conductivity and must be optimized. In this study, the printed traces are subjected

to varying UVA treatments, followed by a period of thermal sintering and an argon plasma surface treatment to achieve the highly conductive traces presented in **Figure 3.3**. **Figure 3.3A** and Figure **3.3B** depict the effects of investigating various UVA treatment time (0 to 20 min) as a function of measured sheet resistance for both square and hexagonal grids, respectively. The optimal UVA light exposure timeframe is determined to be 5 minutes, as it results in the lowest sheet resistance relative to each grid pattern. Grid coverage percentage also had a high impact on the resulting trends, where both the 150/2000 hexagonal design (11.9 %) and 35/540 square design (21.6 %) achieving the lowest resistance value of 2.90 Ω/sq. Following the trend observed in **Figure 3.2**, hexagonal traces measuring at a 25 μm nominal line width showed significantly lower conductive performance in comparison to the wider line widths, resulting in a much larger y-axis range in comparison to the data presented in **Figure 3.3A**. Even so, of the hexagonal grid patterns available at 25 μm width, the five-minute light exposure still resulted in the lowest sheet resistance against each investigated treatment time, shown inset on **Figure 3.3B**. **Figure 3.12** provides a magnification of **Figure 3.3B** at the same y-axis scale of 0 – 25 μm in order to provide a more in depth look into the trend of the hexagonal grids without the 25 μm line width microgrids present.

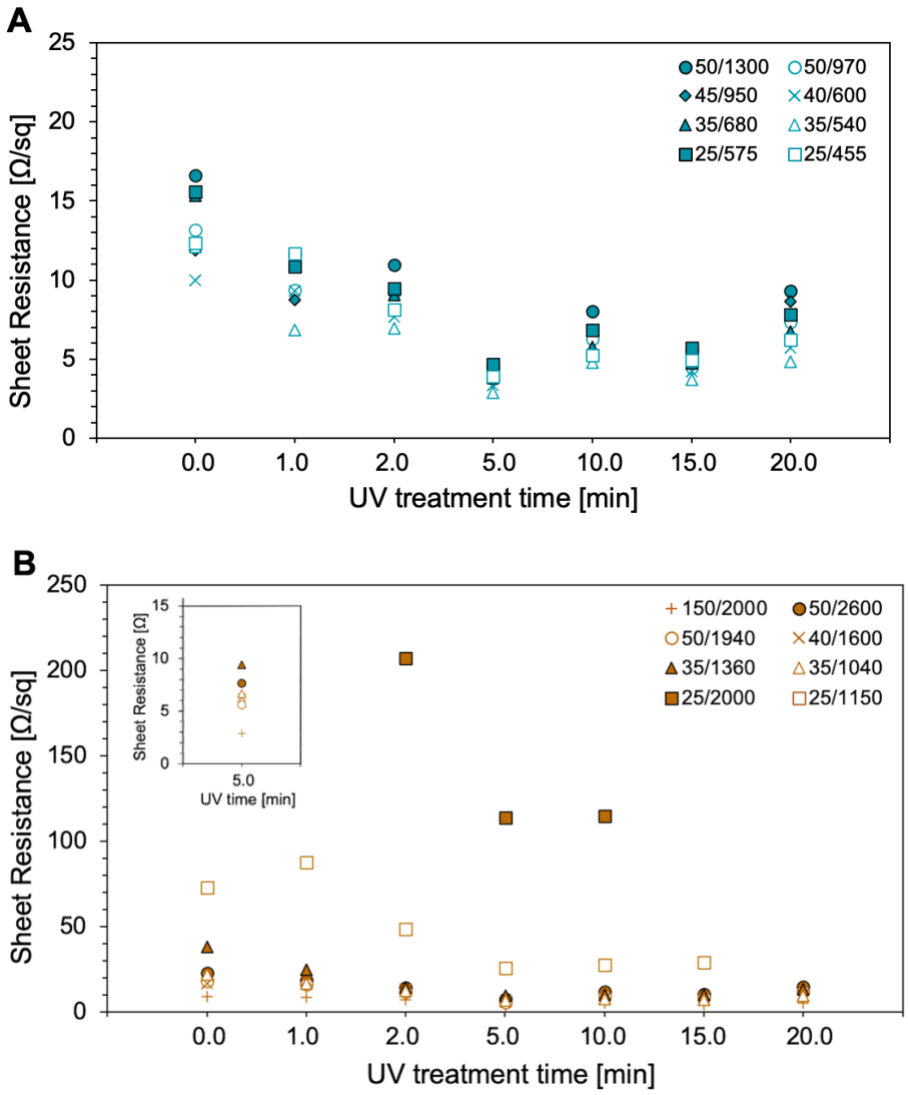

Figure 3.3. Influence of UVA treatment time on sheet resistance for A) square grid patterns and B) hexagonal grid patterns with 5-min treatment time inset

Scanning electron microscope (SEM) images shown in **Figure 3.4** highlight the dissimilarity of silver dispersion of the printed traces exposed to the 0-, 5- and 20-min UVA light exposure. Upon the formation of silver nanoparticles during the UV treatment process, the trace typically becomes pinned to the surface of the substrate, meaning that the edges of the ink do not spread significantly during the following thermal sintering process. When the traces are exposed to UVA light, the temperature increase resulting from the production of silver nanoparticles facilitates solvent removal and serves to pin the trace to the surface of the substrate such that the ink does not spread significantly during the following thermal sintering process.[30] This not only

produces narrower traces, but also improves the uniformity of the traces. The absence of UV treatment as shown in **Figure 3.4A** indicates that there were not enough silver nanoparticles formed during the thermal sintering process alone to pin the trace to the substrate, with **Figure 3.13** further demonstrating the presence of large µm particulates still present within the trace. The higher resistance for samples processed at low UVA sintering times can therefore be attributed to the fact that it has received less energy to convert Ag^{+} to Ag^{0}. Since the trace is not properly pinned to the substrate, this also causes the ink to spread further during the thermal sintering process, creating non-uniform traces and resulting in a line width of 133.5 µm measured post-processing, while the 5 min and 20 min UVA treatment led to line widths of 117 and 119 µm, respectively, further illustrating the benefit of UVA treatment. The 5 min treatment, shown in **Figure 3.4B** and **Figure 3.14**, demonstrates successful conversion of the silver neodecanoate to silver with uniform dispersion found throughout the trace intersection. The adequate amount of silver nanoparticles formed during the 5 min exposure time resulted in the lowest resistance and least amount of spreading due to the fact that the trace is adequately pinned to the substrate surface. In comparison, the 20 min UVA treatment in comparison resulted in an over-cured sample which can be observed in **Figure 3.4C** and **Figure 3.15**. Unlike the 0-min trace that still retained a large portion of the organic components in the trace, exposing the trace to an excessive amount of UVA light removes too many of the organic components that play an important role in assisting in the mobility of the remaining silver salt and silver nanoclusters to coalesce into the silver trace during the subsequent thermal sintering step.

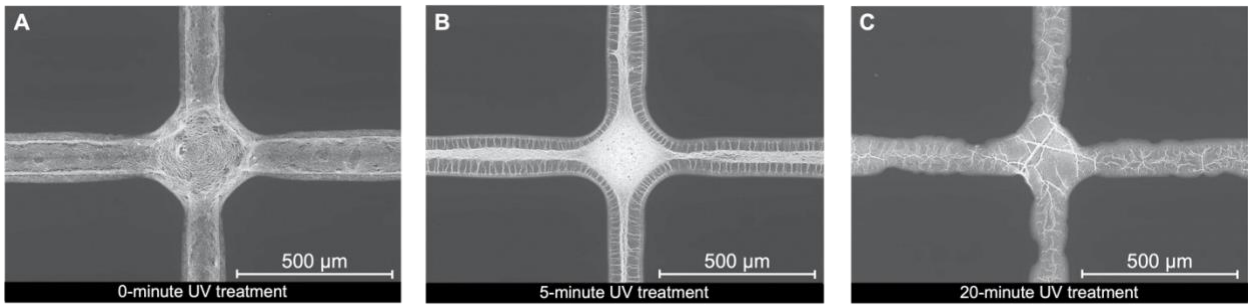

Figure 3.4. SEM images of a 50/1300 square trace intersection after exposure to a static halide UVA treatment for A) 0 minutes B) 5 minutes, and C) 20 minutes and thermal sintering on bare PET

Following the electro-optical optimization of the microgrid through grid design and sintering conditions, it is important to determine whether the designs comply with current industry standards. To achieve a good comparison, TCE grid designs that exhibit a transparency of ≥ 80% and $R_{avg} \leq 10$ Ω were of primary interest for further investigation.[47] Given the trends developed from the individual $\%T/R_{avg}$ of the grid designs in **Figure 3.2** and the optimized sintering conditions presented in **Figures 3.3** and **3.4**, there are four grid designs that exhibit the highest $\%T/R_{avg}$ at this criterion, specifically the square 50/1300 (82.9%, 4.5 Ω/sq), as well as the hexagonal 50/2600 (88.1%, 7.6 Ω/sq) 50/1940 (86.1%, 5.6 Ω/sq) and 40/1600 (86.2%, 6.3 Ω/sq) at optimized conditions. Therefore, these four primary microgrid designs will be further characterized for applications as transparent heaters.

3.6.3. Mechanical Properties

The ability for the printed microgrids to withstand deformation is imperative for producing functional printed electronics components, as significant mechanical damage can render the component non-conductive and therefore inoperable. BNNTs have demonstrated high mechanical stability at elevated temperatures and under mechanical stress when incorporated into a variety of different nanocomposite platforms, such as with polyvinyl alcohol, polyurethane, and other epoxy composites, however their use as a discrete film or as a coating is rarely studied.[48–50] The use of a thin BNNT interlayer at the substrate-trace interface has been initially demonstrated for use in rapid AgND ink processing to minimize the extent of deformation of low temperature substrates that sintering induces.[38] The thermal conductivity of the BNNT interlayer assisted in reducing warpage of the substrate and subsequently improved the morphology of printed silver lines, as well as reducing hot spot formation in the features when current was applied. However, no insight into the mechanical properties of the BNNT film were investigated in the previous work, and with the TCE microgrids having significantly thinner and more complex designs, the BNNT thin film may be sufficient in providing a degree of mechanical stability that will reduce the microgrids' susceptibility to damage during mechanical deformation. **Figure 3.1**6 demonstrates the change in contact angle of water on a clean and bare PET surface and a BNNT-coated PET substrate at a surface concentration of 142 mg/m2. Additionally, **Figure 3.17** highlights the change in optical transmittance upon coating the substrate of the four primary microgrid designs, which reduced the transparency by an average of 16.1% due to the visible translucence of the dried BNNT thin film.

In order to analyze the influence of the BNNT film on the flexibility and electrical performance of the grids, the microgrids printed on bare PET and BNNT-coated PET were subjected to 500 tensile bending cycles at a bending radius of 10 mm, with the change in resistance measured every 25 cycles, as shown in **Figure 3.5**. The microgrids printed on BNNT-coated PET exhibit a slower rate of change in resistance than those printed on bare PET, with the 50/2600 and 50/1940 hexagonal designs withstanding up to 425 bending cycles before a 10% increase in resistance was observed, changing from 7.25 Ω to 8.00 Ω (R/R_0 = 1.10) and 5.68 Ω to 6.35 Ω (R/R_0 = 1.12), respectively. In comparison, the microgrids printed on bare PET deteriorated quicker, reaching a 10% increase in resistance in as little as 100 bending cycles. Furthermore, the hexagonal designs exhibited a less pronounced change in resistance upon mechanical bending than the square design. This may be attributed to how mechanical stress is applied to the internal angles of each geometric shape, where the 90˚ of the square design is subjected to harsher deformation as pressure is being applied perpendicular by the mandrel, rather than the 120˚ of the hexagonal shape.

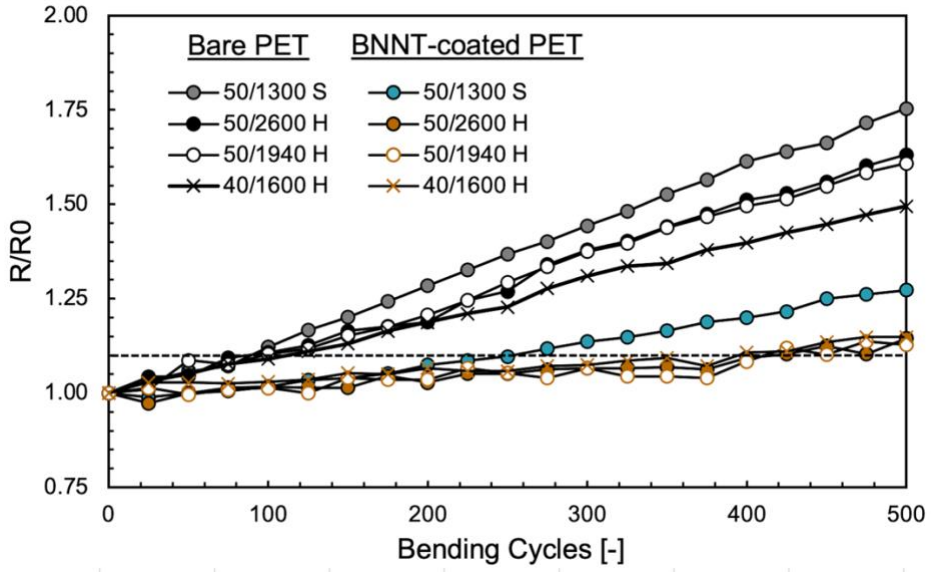

Figure 3.5. Change in sheet resistance of the square 50/1300, and hexagonal 50/2600, 50/1940, and 40/1600 printed on bare PET and BNNT-coated PET as a function of bending cycles

In order to investigate the effects of more severe mechanical deformation on the microgrids, tensile crease testing was completed on the microgrids printed on bare PET and on BNNT-coated PET. The results presented in **Figure 3.6A** demonstrate that the microgrids printed on BNNT-coated PET exhibit a lower change in resistance than the grids printed without the BNNT

interlayer for all four grid designs, exhibiting similar trends to **Figure 3.5**. Further insight into the effects of the crease testing on the trace integrity is shown in **Figure 3.6B** and **3.6C**, where 2D surface profiles and corresponding 3D optical microscope images show the different responses to mechanical damage. The trace printed on bare PET (**Figure 3.6B**) exhibits very distinct valleys throughout the trace profile below to the substrate surface, with peak to valley height roughness (Rt) measured at 1.18 μm and an increase in RMS roughness of 90 nm post crease testing. The harshness of the crease testing is further demonstrated in corresponding microscope images, showing large cracks in the surrounding substrate surface that penetrate into the trace, further highlighting how susceptible the traces on bare PET are to mechanical damage. In comparison, the trace profile printed on BNNT-coated PET (**Figure 3.6C**) demonstrates both a lower Rt value of 0.92 μm and a smaller change in RMS roughness of only 20 nm, and the valleys created as a result of the mechanical testing do not fall below the BNNT film surface. Additionally, the cracks in the substrate in **Figure 3.6B** are not translated to the BNNT surface in **Figure 3.6C**, and as such the severity of the mechanical damage to the trace printed on top of the BNNT film is reduced. This indicates that not only does the underlying BNNT layer have no adverse impact on the microgrid's adhesion to the substrate, but it can also prevent the silver traces from forming cracks as the BNNT network shifts to accommodate the bending process, without transferring stress to the silver traces and allowing the microgrid to maintain its' high conductivity. It is clear the BNNT interlayer serves to improve the mechanical durability and flexibility performance of the printed microgrid owing to the inherent physical properties of the BNNTs.

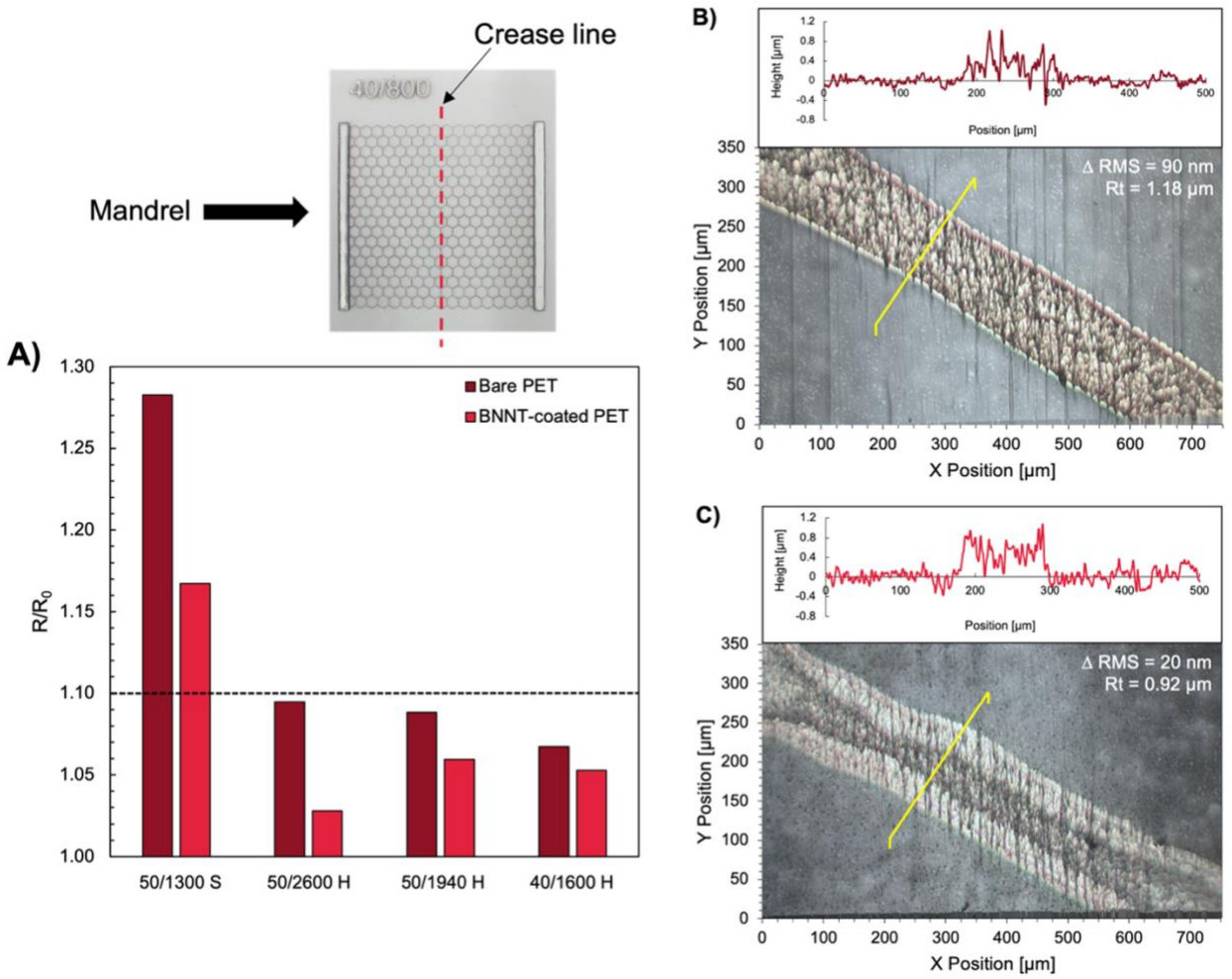

Figure 3.6. A) Change in resistance of the four primary grid designs after one crease testing cycle, with 2D surface profiles and corresponding 3D optical microscopic images of the 50/2600 H grid printed on B) bare PET and C) BNNT-coated PET post crease test

3.6.4. Thermal Properties

The microgrid transparent heaters operate through resistive heating, or the Joule heating effect, which occurs when current applied across a conductive material leads to heating.[51] Heating originates from random collisions between charge carriers and atomic ions within the conductor, converting kinetic energy from the electric field into thermal energy. As such, the conductor begins to exhibit a temperature increase until steady state is achieved, with the resulting power emitted defined as:

$$P = I^2 \times R \qquad [3.2]$$

Where P is the generated Joule power, I is the current travelling through the resistor, and R is the resistance of the conductor.[52] In this context, convective and radiative heat generation are considered negligible compared to conductive heat generation. Joule heating is considered efficient when the outputted power increases relative to the input voltage, indicating that electrical energy is being converted into Joule heating.[53]

Printed heater performance is primarily centered around its relationship between temperature and time, which stems from the correlation between conductivity and Joule heating efficiency and its impact on the achievable temperature of the heater. Furthermore, qualitative analysis of the uniformity of the heater area must also be considered, as any broken network connections within the microgrid can cause local heat accumulation upon applied current, resulting in an uneven thermal response. In order to analyze this relationship, the first parameter that is investigated is the steady-state temperature of the heater at an applied voltage. To determine whether the BNNT interlayer is beneficial to the printed heater architecture, the global average temperature-time response of the microgrids printed on bare PET and BNNT-coated PET were analyzed for the square 50/1300, and hexagonal 50/2600, 50/1940, and 40/1600 grids. An initial voltage of 1.0 V was applied to the microgrids for a continuous 300 seconds and then removed until the microgrid cooled back to room temperature. The voltage was then increased by a 0.5 V step size and the process repeated until measurements were completed up to an applied voltage of 2.5 V. The temperature-time response of the 50/1940 hexagonal microgrid fabricated on bare PET and on BNNT-coated PET is depicted in **Figure 3.7A** and **3.7B** respectively, as it showed the greatest temperature difference of the four primary microgrid designs. Temperature-time plots and corresponding thermal images for the 50/1300 square, 50/2600 hexagonal designs can be found in **Figures 3.18** and **3.19**, respectively. Average resistance measurements completed on the microgrid printed on bare PET was 4.70 Ω and the microgrid printed on BNNT-coated PET measured 4.60 Ω, so it can therefore be assumed that the difference in temperatures seen in **Figure 3.7B** are primarily due to the presence of the interlayer at the substrate-trace interface.

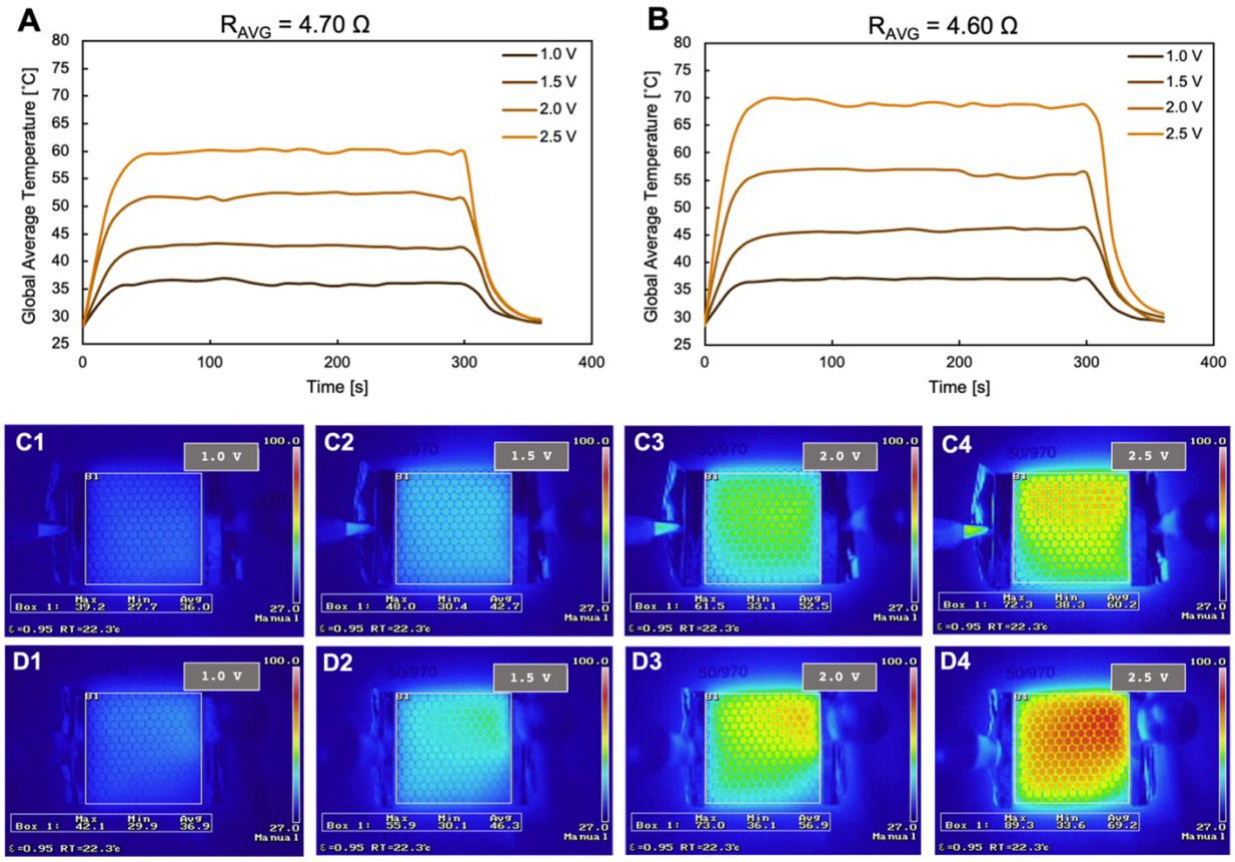

Figure 3.7. Measured global average temperature versus time for increasing applied voltages on the 50/1940 hexagonal grid design printed on A) bare PET and B) BNNT-coated PET, and corresponding thermal response imaging C1-4) printed on bare PET and D1-4) BNNT-coated for an applied voltages of 1.0, 1.5, 2.0, and 2.5 V at t = 150s

As shown in **Figure 3.7A** and **3.7B**, the BNNT interlayer directly assists in increasing the steady-state temperature of the microgrid across the entire investigated voltage range. The difference in achievable steady-state temperature becomes more pronounced at higher applied voltages, especially at 2.5 V, where the microgrid on BNNT-coated PET exhibits an average temperature increase of 13.1% compared to the microgrid printed on bare PET. Corresponding thermal images of the printed microgrid in operation as heater at 2.5 V is presented in **Figures 3.7C-D** and **3.20**, demonstrating the heightened temperature and subsequent heat distribution across the microgrid upon inclusion of the BNNT interlayer. Like the trends presented in **Figure 3.7**, the square 50/1300 and hexagonal 50/2600 microgrids printed on BNNT-coated PET exhibit a higher global average temperature at each of the investigated applied voltages than those printed on bare PET at identical and near identical measured resistances.

It is clear that the BNNT interlayer is assisting in efficiently diffusing heat across the area of the microgrid heater that is void of silver ink, increasing the internal heater area and subsequently the average temperature of the heater as shown in **Figure 3.7D4**. However, the inherent thermally conductive properties of BNNTs are not likely responsible for the sharp increase in temperature exhibited by the microgrid. At near-identical resistances (< 5% difference), all microgrids printed on BNNT-coated PET exhibited lower measured resistances over the duration of the heating experiments in comparison to the microgrids printed on bare PET at each investigated voltage, even though BNNTs exhibit characteristically electrically insulating properties. Upon further investigation, it was determined that the averaged resistance of the BNNT-coated PET microgrid had been reduced by up to 50% after exposure to the voltage testing range, as shown in **Table 3.1**.

Table 3.1. Change in resistance of grid patterns printed on bare PET and BNNT-coated PET and corresponding measured current at an applied voltage of 2.5 V

Substrate type	Grid specifications	Pre-testing resistance [ohm]	Post-testing resistance [ohm]	Measured current at 2.5 V [mA]
Bare PET	50/1300	7.5	7.7	647
	50/2600	10.7	10.8	456
	50/1940	9.9	8.7	499
	40/1600	10.8	10.8	393
BNNT-coated PET	50/1300	6.7	4.2	780
	50/2600	8.8	5.6	515
	50/1940	10.4	5.2	638
	40/1600	11.7	8.5	343

The larger improvement in conductivity of samples printed on BNNT-coated PET suggests that the interlayer is assisting in additional electrical sintering over the course of the testing time.[54] Electrical sintering has been previously demonstrated, where upon current being applied through a metallic feature, the resistive nature of ink can cause local Joule heating and sintering to occur simultaneously.[55] The heat generated within the traces causes the nanoparticles that were formed

during the conversion of the AgND to Ag film to become more coalesced, resulting in a more uniform, interconnected silver grid with less internal contact resistance. This improved distribution typically leads to higher conductivity and increases the Joule heating effect, subsequently increasing the thermal response as exhibited in **Figure 3.7B**. However, the improved thermal response is limited by the temperature sensitivity of the underlying substrate. Applying voltage to the microgrid directly printed on bare PET activates the electrical sintering process but causes the substrate to absorb heat from the microgrid at the substrate-feature interface, such that the semicrystalline nature of the substrate undergoes a phase change as it nears the glass transition temperature (T_g) of the substrate and results in the substrate softening. This softening can lead to warpage and subsequent hardening of the printed design, as previously demonstrated.[38] Surface profiles presented in **Figure 3.8A** and **Figure 3.8B**, show that after exposure to the 1.0-2.5 V testing range, the microgrid printed on bare PET has become significantly more deformed, with three clear areas in the post-tested trace (**Figure 3.8B**) below the substrate surface due to the substrate softening and hardening into the irregular morphology. The heat being absorbed by the substrate therefore contributes little to electrical sintering, as evident by the fact that there is little change in the measured resistance before and after testing. **Figure 3.8C** and **3.8D** show the change in trace morphology of the microgrid printed on BNNT-coated PET before and after exposure to the 1.0-2.5 V testing range, highlighting only slight softening of the substrate after testing, with significantly less deformation than the microgrid without the BNNT interlayer.

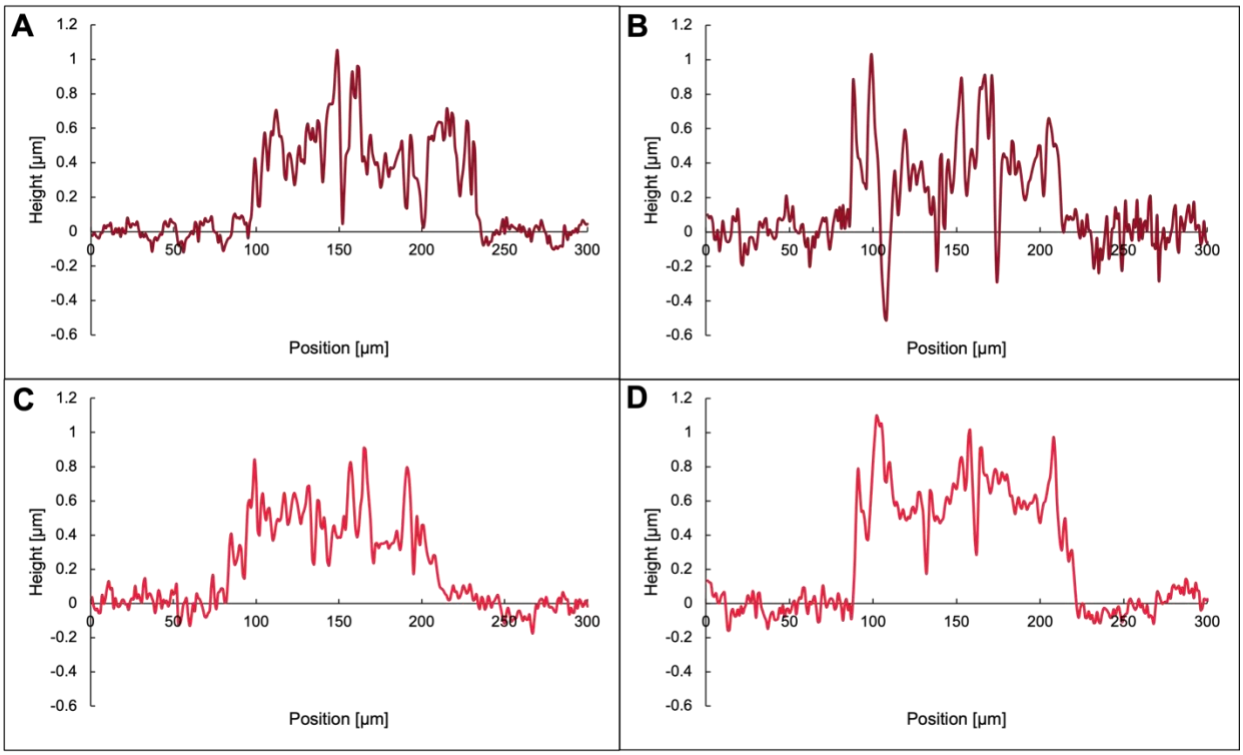

Figure 3.8. 2D Surface profiles of the 50/1300 microgrid printed on bare PET A) before and B) after being subjected to 1.0-2.5 V applied voltage range and 50/1300 microgrid printed on BNNT-coated PET C) before and D) after being subjected to 1.0-2.5 V applied voltage range

SEM images in Figure 9 further compare the difference in morphology of the silver microgrid traces printed on bare-PET (**Figure 3.9A-C**) and BNNT-coated PET (**Figure 3.9D-F**) before and after subjecting the microgrid to the 1.0-2.5 V thermal response test. The change in morphology of the microgrid trace on bare PET is shown in **Figure 3.9A** and **3.9B**, demonstrating that the substrate underwent significant softening and deformation upon exposure to the applied voltage to the point that the trace becomes no longer flush with the substrate surface, as was demonstrated in **Figure 3.8B**. In comparison, the trace morphology of the microgrid printed on BNNT-coated PET in **Figures 3.9D** and **3.9E** retains its' uniformity, with only slight deformation within the trace itself, indicating that the BNNT layer sufficiently deviated a large portion of heat accumulation at the substrate-feature interface to areas between the grid lines. Additional cross-section images of the microgrids clearly demonstrate a difference in morphology post-testing when the BNNT interlayer is placed between the microgrid architecture and the substrate, notably the higher silver density in the trace printed on BNNT-coated PET (**Figure 3.9F**). The BNNT layer therefore allows heat to flow through the network in a lateral direction, minimizing heating and

damaging of the substrate while also allowing resistive sintering to take place in the silver trace, ultimately improving the electrical conductivity and therefore Joule heating that causes the increase in temperature observed in **Figure 3.7B**.

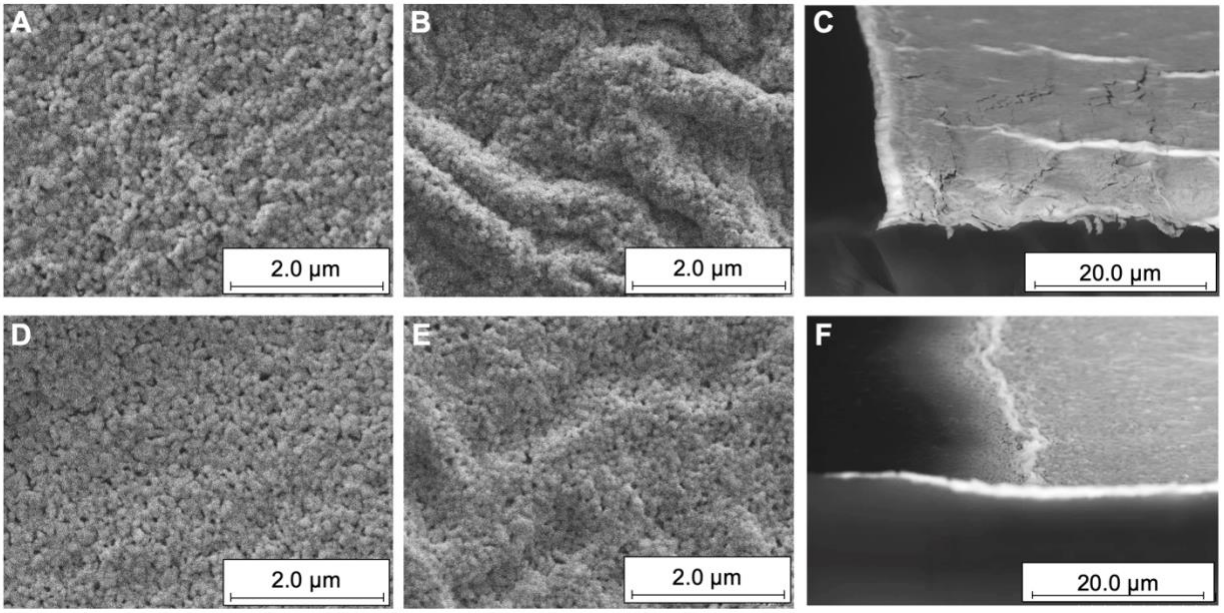

Figure 3.9. Cross-sectional SEM images of the 50/1300 square grid printed on bare PET A) before and B,C) after exposure to thermal response testing up to 2.5V and BNNT-coated PET D) before and E,F) after exposure to thermal response testing up to 2.5 V

3.7. Conclusion

We present the design and process optimization of square and hexagonal microgrid patterns for applications in transparent heaters, with the aid of a BNNT interlayer for improved heat distribution and flexible performance. The wide range of line width and pitch design criteria provide important insight into the electro-optical properties of the microgrids and determining four optimal designs compatible with industry standards and the screen-printing processing used to fabricate the microgrids. To improve upon the electro-optical properties of the microgrids, a tailored sintering process was investigated, and it was determined that exposure to a 5 min UVA light treatment prior to thermal sintering was sufficient for the molecular silver ink to achieve uniform and highly conductive printed features as low as 2.90 Ω/sq. Furthermore, the inclusion of the BNNT interlayer provided additional benefit to the microgrid architecture by increasing mechanical endurance to cyclic deformation by 400% of both square and hexagonal microgrids in

comparison to the microgrids printed on bare PET. The four primary microgrids successfully performed as transparent heater devices, exhibiting fast and highly stable temperature profiles upon applied voltage. The heating performance of the microgrids was increased upon inclusion of the BNNT interlayer, and it was determined that the film enables further electrical sintering of the traces during testing and reduced deformation of the microgrid traces, causing an increase in conductivity and subsequently Joule heating. This study provides a clear example of the benefit of using BNNT interlayers paired with optimized silver microgrids, leading to flexible, transparent heaters with improved mechanical stability and greater heater efficiency.

3.8. Acknowledgements

This work was supported by the NSERC Green Electronics Network (GreEN) (grant number: NETGP 508526-17). We thank Benoit Simard and Yadienka Martinez-Rubi (NRC) for the BNNTs utilized in this study. We also thank Olga Mozenson for assistance setting up the thermal camera.

3.9. Supporting Information

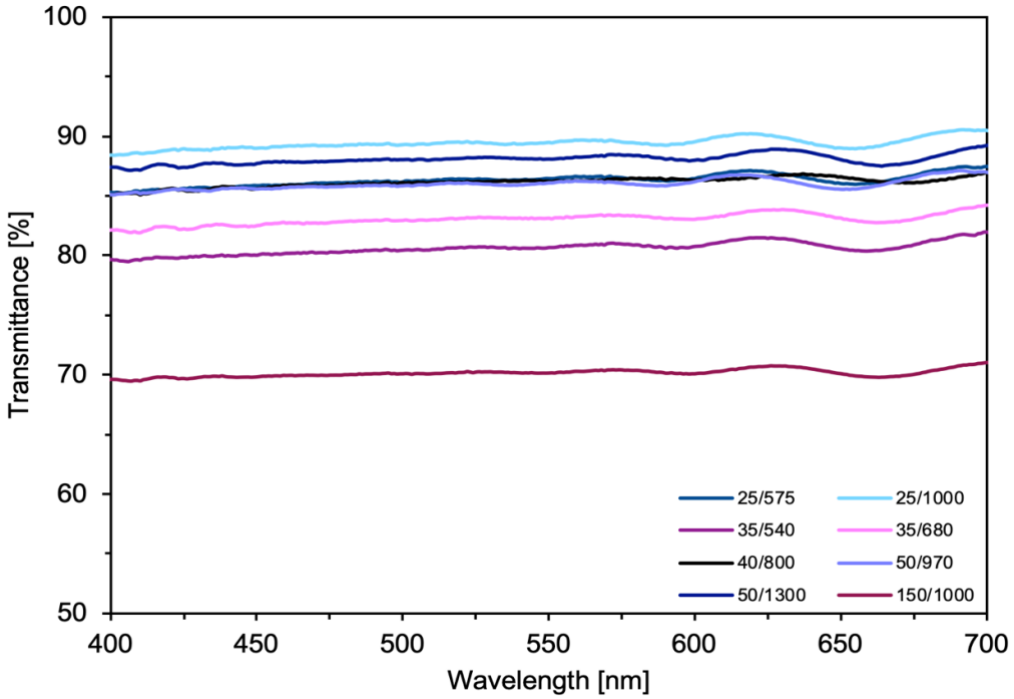

Figure 3.10. Optical transmittance spectrum for hexagonal grid patterns

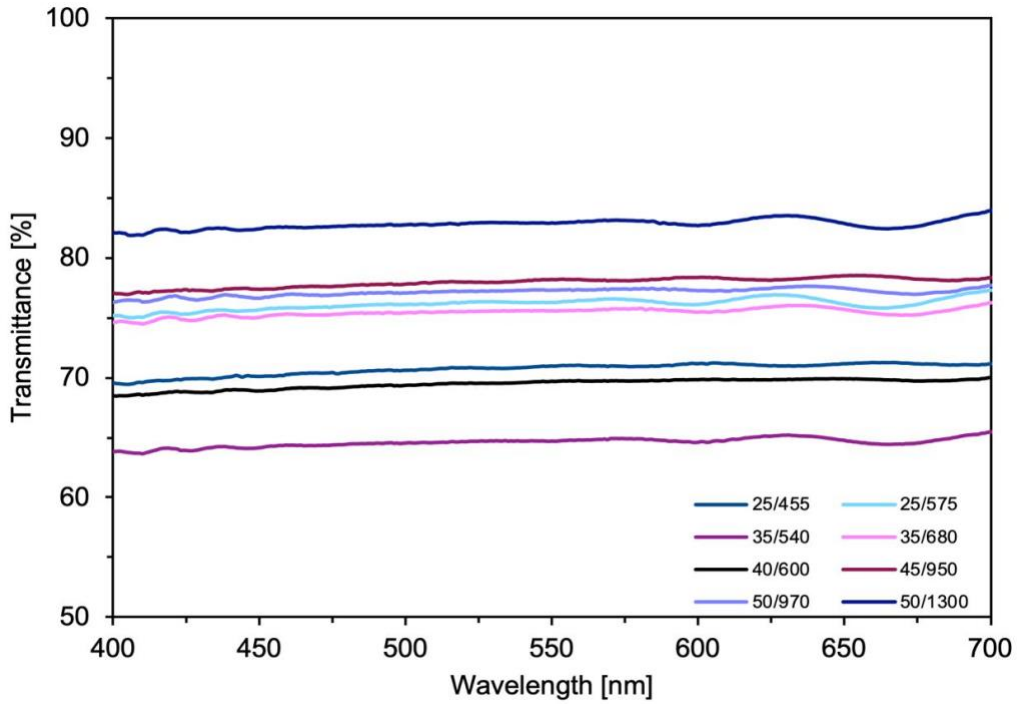

Figure 3.11. Optical transmittance spectrum for square grid patterns

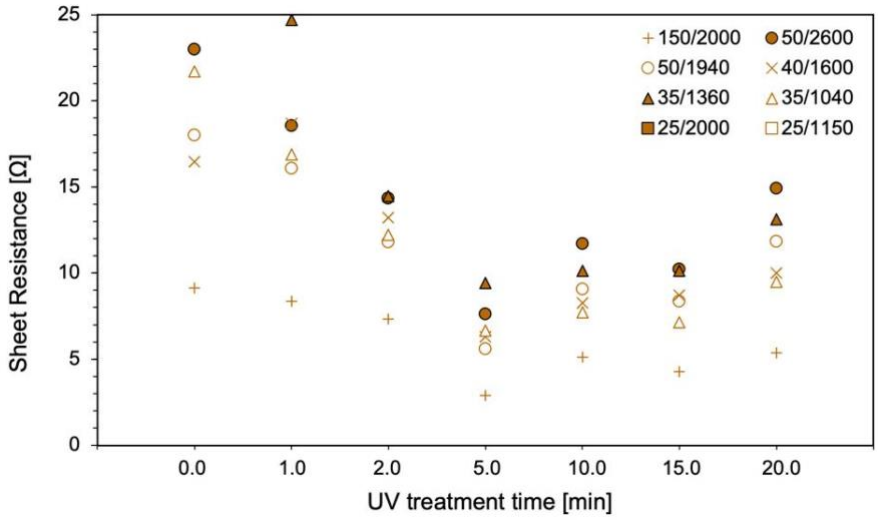

Figure 3.12. Influence of UVA treatment time on sheet resistance for hexagonal grid patterns at a y-axis scale of 0 – 25 µm

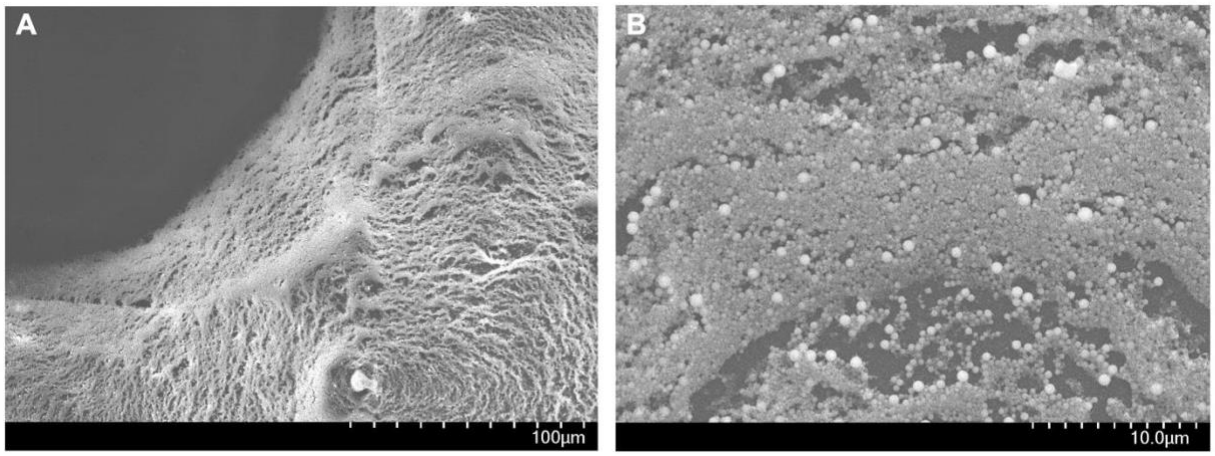

Figure 3.13. SEM images of a 50/1300 square trace intersection without exposure to a static halide UVA treatment at a A) 500X magnification and B) 3500X magnification

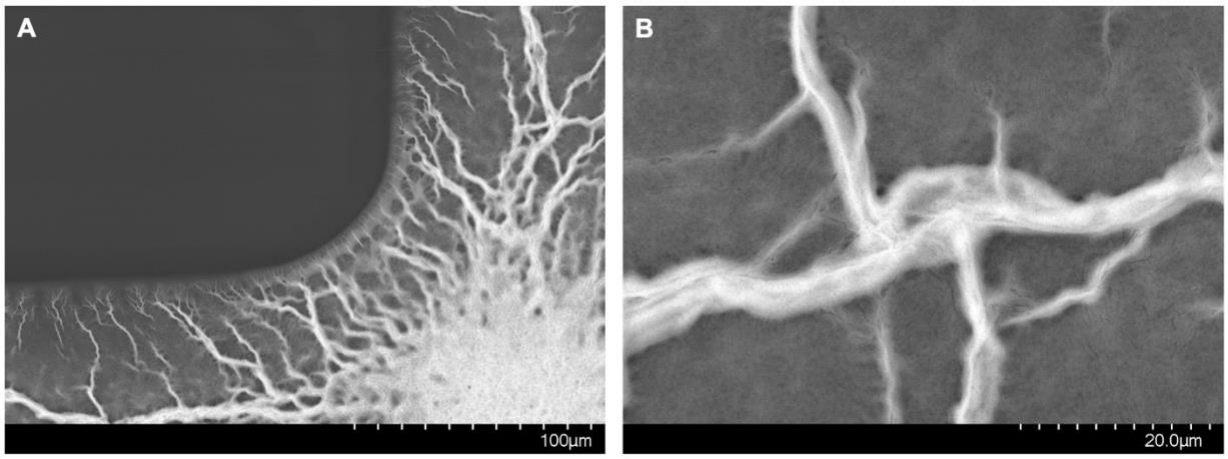

Figure 3.14. SEM images of a 50/1300 square trace intersection after 5-minute exposure to a static halide UVA treatment at a A) 500X magnification and B) 2000X magnification

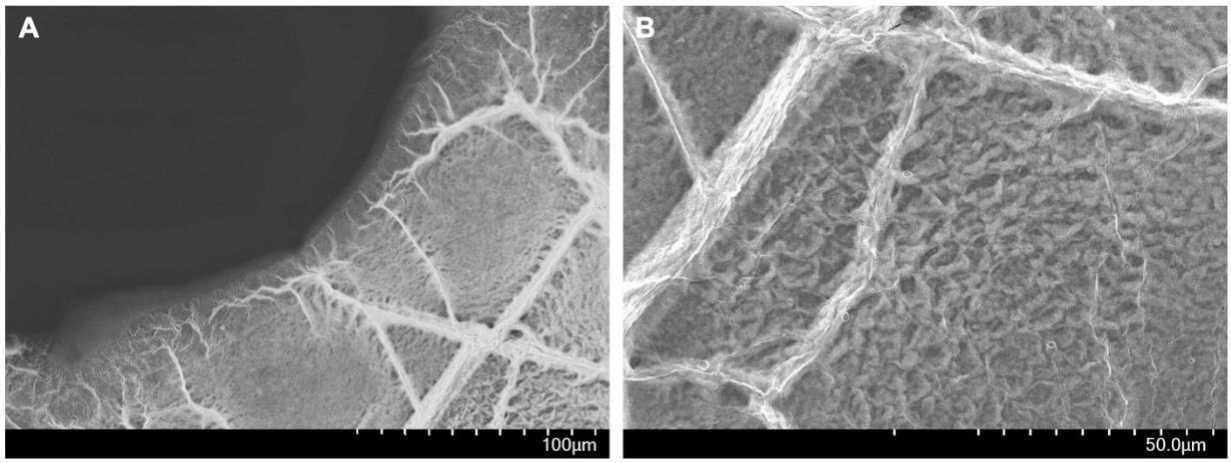

Figure 3.15. SEM images of a 50/1300 square trace intersection after 20-minute exposure to a static halide UVA treatment at a A) 500X magnification and B) 1100X magnification

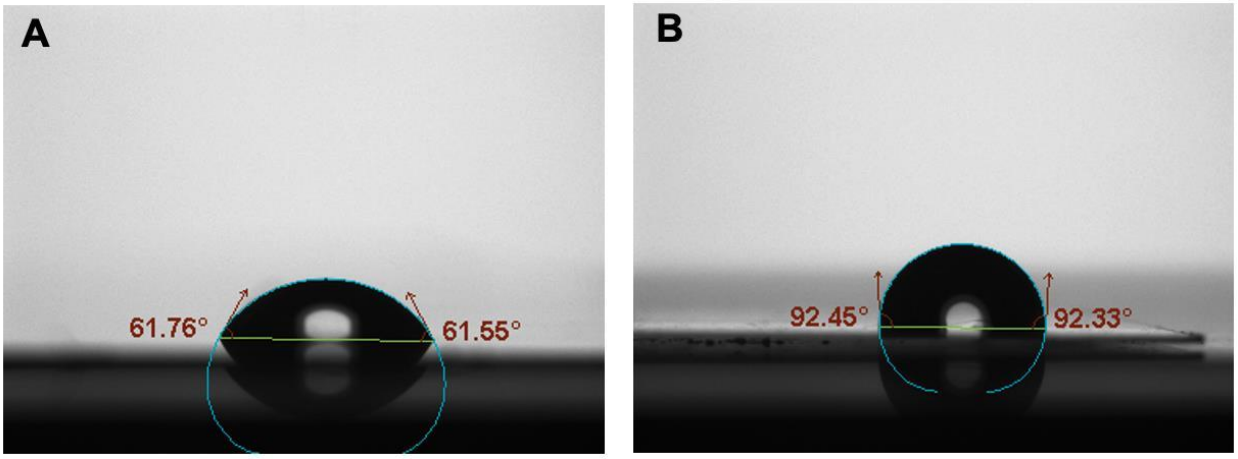

Figure 3.16. Contact angle measurement of water solvent onto A) bare PET substrate and B) BNNT-coated PET substrate at a surface concentration of 142 mg/m^2

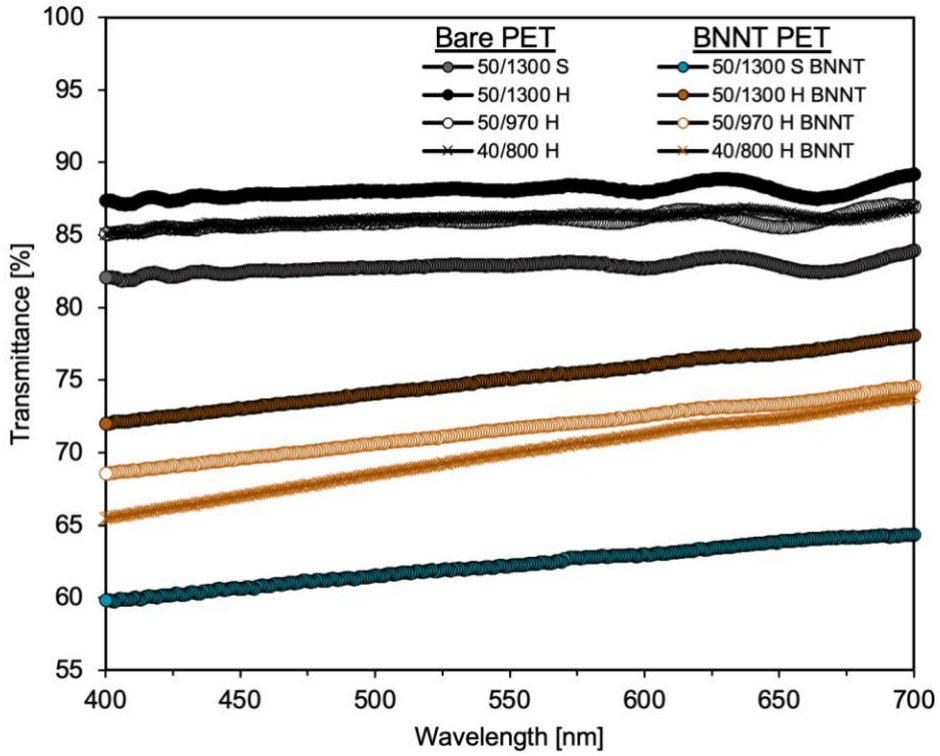

Figure 3.17. Comparison of optical transmission spectra for 50/1300S, 50/1300H, 50/970H, and 40/800H grid designs printed on bare PET and 142 mg/m^2 BNNT-coated PET substrates, normalized against an untreated Melinex^{TM} substrate

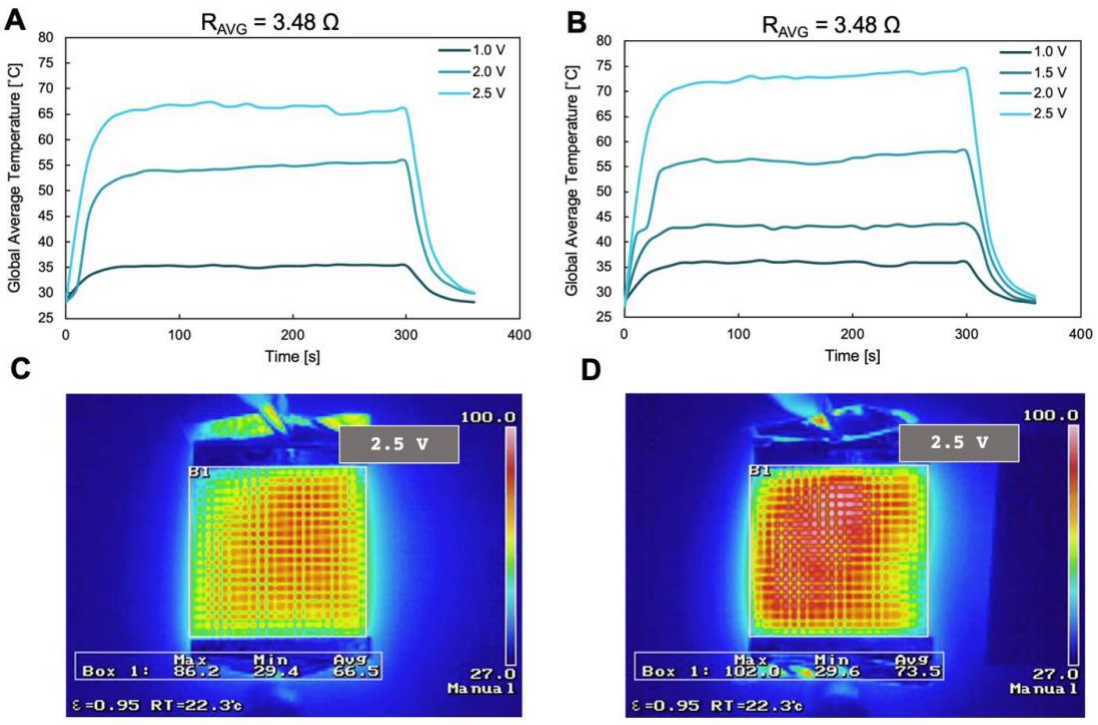

Figure 3.18. Measured global average temperature versus time for increasing applied voltages on the 50/1300 square grid design printed on A) bare PET and B) BNNT-coated PET, and corresponding thermal response imaging C) printed on bare PET and D) BNNT-coated for an applied voltage of 2.5 V

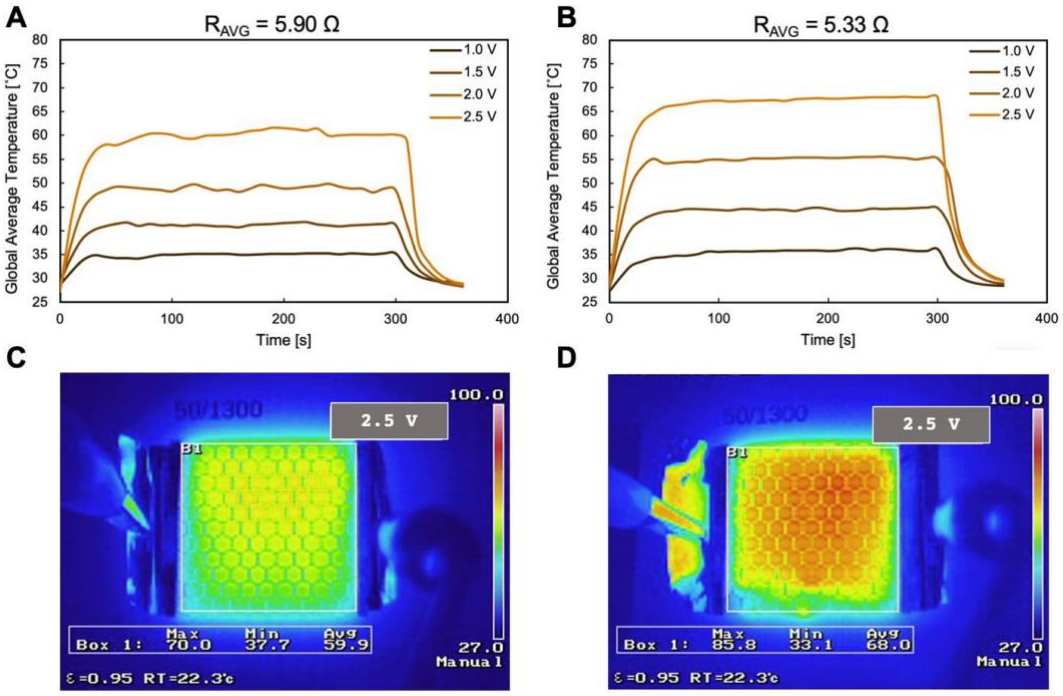

Figure 3.19. Measured global average temperature versus time for increasing applied voltages on the 50/1300 hexagonal grid design printed on A) bare PET and B) BNNT-coated PET, and corresponding thermal response imaging C) printed on bare PET and D) BNNT-coated for an applied voltage of 2.5 V

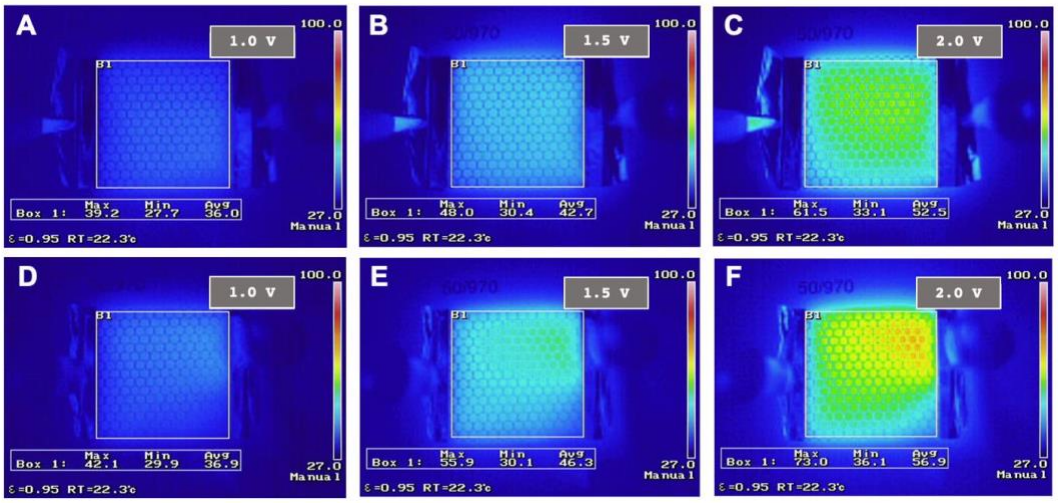

Figure 3.20. Comparison of thermal response imaging of the 50/970 hexagonal grid design printed on bare PET at A) 1.0 V, B) 2.0 V, C) 2.5 V and printed on BNNT-coated at applied voltages of D) 1.0 V, E) 1.5 V, and F) 2.0 V

3.10. References

(1) Sarkar, S. K.; Gupta, H.; Gupta, D. Flash Light Sintering of Silver Nanoink for Inkjet-Printed Thin-Film Transistor on Flexible Substrate. *IEEE Trans. Nanotechnol.* **2017**, *16* (3), 375–382. https://doi.org/10.1109/TNANO.2017.2658341.

(2) Krebs, F. C. All Solution Roll-to-Roll Processed Polymer Solar Cells Free from Indium-Tin-Oxide and Vacuum Coating Steps. *Org. Electron.* **2009**, *10* (5), 761–768. https://doi.org/10.1016/j.orgel.2009.03.009.

(3) Winther-Jensen, B.; Krebs, F. C. High-Conductivity Large-Area Semi-Transparent Electrodes for Polymer Photovoltaics by Silk Screen Printing and Vapour-Phase Deposition. *Sol. Energy Mater. Sol. Cells* **2006**, *90* (2), 123–132. https://doi.org/10.1016/j.solmat.2005.02.004.

(4) Galagan, Y.; Coenen, E. W. C.; Sabik, S.; Gorter, H. H.; Barink, M.; Veenstra, S. C.; Kroon, J. M.; Andriessen, R.; Blom, P. W. M. Evaluation of Ink-Jet Printed Current Collecting Grids and Busbars for ITO-Free Organic Solar Cells. *Sol. Energy Mater. Sol. Cells* **2012**, *104*, 32–38. https://doi.org/10.1016/j.solmat.2012.04.039.

(5) Hong, S.; Yeo, J.; Kim, G.; Kim, D.; Lee, H.; Kwon, J.; Lee, H.; Lee, P.; Ko, S. H. Nonvacuum, Maskless Fabrication of a Flexible Metal Grid Transparent Conductor by Low-Temperature Selective Laser Sintering of Nanoparticle Ink. *ACS Nano* **2013**, *7* (6), 5024–5031. https://doi.org/10.1021/nn400432z.

(6) Park, J. H.; Lee, D. Y.; Kim, Y.-H.; Kim, J. K.; Lee, J. H.; Park, J. H.; Lee, T.-W.; Cho, J. H. Flexible and Transparent Metallic Grid Electrodes Prepared by Evaporative Assembly. *ACS Appl. Mater. Interfaces* **2014**, *6* (15), 12380–12387. https://doi.org/10.1021/am502233y.

(7) Granqvist, C. G.; Hultåker, A. Transparent and Conducting ITO Films: New Developments and Applications. *Thin Solid Films* **2002**, *411* (1), 1–5. https://doi.org/10.1016/S0040-6090(02)00163-3.

(8) Chauhan, R. N.; Singh, C.; Anand, R. S.; Kumar, J. Effect of Sheet Resistance and Morphology of ITO Thin Films on Polymer Solar Cell Characteristics. *Int. J. Photoenergy* **2012**, *2012*, 1–6. https://doi.org/10.1155/2012/879261.

(9) Galagan, Y.; J.M. Rubingh, J.-E.; Andriessen, R.; Fan, C.-C.; W.M. Blom, P.; C. Veenstra, S.; M. Kroon, J. ITO-Free Flexible Organic Solar Cells with Printed Current Collecting Grids. *Sol. Energy Mater. Sol. Cells* **2011**, *95* (5), 1339–1343. https://doi.org/10.1016/j.solmat.2010.08.011.

(10) Li, Y.; Mao, L.; Gao, Y.; Zhang, P.; Li, C.; Ma, C.; Tu, Y.; Cui, Z.; Chen, L. ITO-Free Photovoltaic Cell Utilizing a High-Resolution Silver Grid Current Collecting Layer. *Sol. Energy Mater. Sol. Cells* **2013**, *113*, 85–89. https://doi.org/10.1016/j.solmat.2013.01.043.

(11) Tvingstedt, K.; Inganäs, O. Electrode Grids for ITO Free Organic Photovoltaic Devices. *Adv. Mater.* **2007**, *19* (19), 2893–2897. https://doi.org/10.1002/adma.200602561.

(12) Jeon, I.; Yoon, J.; Ahn, N.; Atwa, M.; Delacou, C.; Anisimov, A.; Kauppinen, E. I.; Choi, M.; Maruyama, S.; Matsuo, Y. Carbon Nanotubes versus Graphene as Flexible Transparent Electrodes in Inverted Perovskite Solar Cells. *J. Phys. Chem. Lett.* **2017**, *8* (21), 5395–5401. https://doi.org/10.1021/acs.jpclett.7b02229.

(13) Gao, Y.; Zhou, Y. S.; Xiong, W.; Jiang, L. J.; Mahjouri-samani, M.; Thirugnanam, P.; Huang, X.; Wang, M. M.; Jiang, L.; Lu, Y. F. Transparent, Flexible, and Solid-State Supercapacitors Based on Graphene Electrodes. *APL Mater.* **2013**, *1* (1), 012101. https://doi.org/10.1063/1.4808242.

(14) Hecht, D. S.; Hu, L.; Irvin, G. Emerging Transparent Electrodes Based on Thin Films of Carbon Nanotubes, Graphene, and Metallic Nanostructures. *Adv. Mater.* **2011**, *23* (13), 1482–1513. https://doi.org/10.1002/adma.201003188.
(15) Aloui, W.; Ltaief, A.; Bouazizi, A. Transparent and Conductive Multi Walled Carbon Nanotubes Flexible Electrodes for Optoelectronic Applications. *Superlattices Microstruct.* **2013**, *64*, 581–589. https://doi.org/10.1016/j.spmi.2013.10.027.
(16) Ferrer-Anglada, N.; Pérez-Puigdemont, J.; Figueras, J.; Iqbal, M. Z.; Roth, S. Flexible, Transparent Electrodes Using Carbon Nanotubes. *Nanoscale Res. Lett.* **2012**, *7* (1), 571. https://doi.org/10.1186/1556-276X-7-571.
(17) Liang, J.; Tong, K.; Pei, Q. A Water-Based Silver-Nanowire Screen-Print Ink for the Fabrication of Stretchable Conductors and Wearable Thin-Film Transistors. *Adv Mater* **2016**, 11.
(18) De, S.; Higgins, T. M.; Lyons, P. E.; Doherty, E. M.; Nirmalraj, P. N.; Blau, W. J.; Boland, J. J.; Coleman, J. N. Silver Nanowire Networks as Flexible, Transparent, Conducting Films: Extremely High DC to Optical Conductivity Ratios. *ACS Nano* **2009**, *3* (7), 1767–1774. https://doi.org/10.1021/nn900348c.
(19) Gupta, R.; Walia, S.; Hösel, M.; Jensen, J.; Angmo, D.; Krebs, F. C.; Kulkarni, G. U. Solution Processed Large Area Fabrication of Ag Patterns as Electrodes for Flexible Heaters, Electrochromics and Organic Solar Cells. *J. Mater. Chem. A* **2014**, *2* (28), 10930. https://doi.org/10.1039/c4ta00301b.
(20) Zhou, Z.; Walker, S. B.; LeMieux, M.; Leu, P. W. Polymer-Embedded Silver Microgrids by Particle-Free Reactive Inks for Flexible High-Performance Transparent Conducting Electrodes. *ACS Appl. Electron. Mater.* **2021**, *3* (5), 2079–2086. https://doi.org/10.1021/acsaelm.1c00107.
(21) He, X.; Shen, G.; Xu, R.; Yang, W.; Zhang, C.; Liu, Z.; Chen, B.; Liu, J.; Song, M. Hexagonal and Square Patterned Silver Nanowires/PEDOT:PSS Composite Grids by Screen Printing for Uniformly Transparent Heaters. *Polymers* **2019**, *11* (3), 468. https://doi.org/10.3390/polym11030468.
(22) Gao, T.; Li, Z.; Huang, P.; Shenoy, G. J.; Parobek, D.; Tan, S.; Lee, J.; Liu, H.; Leu, P. W. Hierarchical Graphene/Metal Grid Structures for Stable, Flexible Transparent Conductors. *ACS Nano* **2015**, *9* (5), 5440–5446. https://doi.org/10.1021/acsnano.5b01243.
(23) Ye, N.; Liang, T.; Zhan, L.; Kong, Y.; Xie, S.; Ma, X.; Chen, H.; Su, H.; Xu, M. High-Performance Bendable Organic Solar Cells With Silver Nanowire-Graphene Hybrid Electrode. *IEEE J. Photovolt.* **2019**, *9* (1), 214–219. https://doi.org/10.1109/JPHOTOV.2018.2876998.
(24) Zou, J.; Yip, H.-L.; Hau, S. K.; Jen, A. K.-Y. Metal Grid/Conducting Polymer Hybrid Transparent Electrode for Inverted Polymer Solar Cells. *Appl. Phys. Lett.* **2010**, *96* (20), 203301. https://doi.org/10.1063/1.3394679.
(25) Kang, J.; Jang, Y.; Kim, Y.; Cho, S.-H.; Suhr, J.; Hong, B. H.; Choi, J.-B.; Byun, D. An Ag-Grid/Graphene Hybrid Structure for Large-Scale, Transparent, Flexible Heaters. *Nanoscale* **2015**, *7* (15), 6567–6573. https://doi.org/10.1039/C4NR06984F.
(26) Lim, J. W.; Lee, Y. T.; Pandey, R.; Yoo, T.-H.; Sang, B.-I.; Ju, B.-K.; Hwang, D. K.; Choi, W. K. Effect of Geometric Lattice Design on Optical/Electrical Properties of Transparent Silver Grid for Organic Solar Cells. *Opt. Express* **2014**, *22* (22), 26891. https://doi.org/10.1364/OE.22.026891.

(27) Twomey, C.; Rong, D. X.; O'Hara, D. L.; Tonkin, D. C.; Keif, D. M. Printing Transparent Grid Patterns with Conductive Silver Ink with Flexography. 15.
(28) Valeton, J. J. P.; Hermans, K.; Bastiaansen, C. W. M.; Broer, D. J.; Perelaer, J.; Schubert, U. S.; Crawford, G. P.; Smith, P. J. Room Temperature Preparation of Conductive Silver Features Using Spin-Coating and Inkjet Printing. *J Mater Chem* **2010**, *20* (3), 543–546. https://doi.org/10.1039/B917266A.
(29) Kell, A. J.; Paquet, C.; Mozenson, O.; Djavani-Tabrizi, I.; Deore, B.; Liu, X.; Lopinski, G. P.; James, R.; Hettak, K.; Shaker, J.; Momciu, A.; Ferrigno, J.; Ferrand, O.; Hu, J. X.; Lafrenière, S.; Malenfant, P. R. L. Versatile Molecular Silver Ink Platform for Printed Flexible Electronics. *ACS Appl. Mater. Interfaces* **2017**, *9* (20), 17226–17237. https://doi.org/10.1021/acsami.7b02573.
(30) Liu, X.; Li, D.; Fukutani, H.; Trudeau, P.; Khoun, L.; Mozenson, O.; Sampson, K. L.; Gallerneault, M.; Paquet, C.; Lacelle, T.; Deore, B.; Ferrand, O.; Ferrigno, J.; Malenfant, P. R. L.; Kell, A. J. UV-Sinterable Silver Oxalate-Based Molecular Inks and Their Application for In-Mold Electronics. *Adv. Electron. Mater.* **2021**, *7* (9), 2100194. https://doi.org/10.1002/aelm.202100194.
(31) Altay, B. N.; Turkani, V. S.; Pekarovicova, A.; Fleming, P. D.; Atashbar, M. Z.; Bolduc, M.; Cloutier, S. G. One-Step Photonic Curing of Screen-Printed Conductive Ni Flake Electrodes for Use in Flexible Electronics. *Sci. Rep.* **2021**, *11* (1), 3393. https://doi.org/10.1038/s41598-021-82961-3.
(32) Jang, Y.-R.; Joo, S.-J.; Chu, J.-H.; Uhm, H.-J.; Park, J.-W.; Ryu, C.-H.; Yu, M.-H.; Kim, H.-S. A Review on Intense Pulsed Light Sintering Technologies for Conductive Electrodes in Printed Electronics. *Int. J. Precis. Eng. Manuf.-Green Technol.* **2020**. https://doi.org/10.1007/s40684-020-00193-8.
(33) Wünscher, S.; Abbel, R.; Perelaer, J.; Schubert, U. S. Progress of Alternative Sintering Approaches of Inkjet-Printed Metal Inks and Their Application for Manufacturing of Flexible Electronic Devices. *J Mater Chem C* **2014**, *2* (48), 10232–10261. https://doi.org/10.1039/C4TC01820F.
(34) Fritsch, J.; Wisser, F. M.; Eckhardt, K.; Bon, V.; Mondin, G.; Schumm, B.; Grothe, J.; Kaskel, S. A New Molecular Silver Precursor for the Preparation of Thin Conductive Silver Films. *J. Phys. Chem. Solids* **2013**, *74* (11), 1546–1552. https://doi.org/10.1016/j.jpcs.2013.05.022.
(35) Wang, J.; Jiu, J.; Nogi, M.; Sugahara, T.; Nagao, S.; Koga, H.; He, P.; Suganuma, K. A Highly Sensitive and Flexible Pressure Sensor with Electrodes and Elastomeric Interlayer Containing Silver Nanowires. *Nanoscale* **2015**, *7* (7), 2926–2932. https://doi.org/10.1039/C4NR06494A.
(36) Bettinger, C. J. Recent Advances in Materials and Flexible Electronics for Peripheral Nerve Interfaces. *Bioelectron. Med.* **2018**, *4* (1), 6. https://doi.org/10.1186/s42234-018-0007-6.
(37) Chen, X.; Zhang, L.; Park, C.; Fay, C. C.; Wang, X.; Ke, C. Mechanical Strength of Boron Nitride Nanotube-Polymer Interfaces. *Appl. Phys. Lett.* **2015**, *107* (25), 253105. https://doi.org/10.1063/1.4936755.
(38) Wagner, K.; Paquet, C.; Martinez-Rubi, Y.; Genest, M.; Guan, J.; Sampson, K. L.; Kim, K. S.; Kell, A. J.; Malenfant, P. R. L.; Lessard, B. H. Boron Nitride Nanotube Coatings for Thermal Management of Printed Silver Inks on Temperature Sensitive Substrates. *Adv. Electron. Mater.* **2021**, *7* (5), 2001035. https://doi.org/10.1002/aelm.202001035.

(39) Guan, J.; Kim, K. S.; Jakubinek, M. B.; Simard, B. pH-Switchable Water-Soluble Boron Nitride Nanotubes. *ChemistrySelect* **2018**, *3* (32), 9308–9312. https://doi.org/10.1002/slct.201801544.
(40) Martinez-Rubi, Y.; Jakubek, Z. J.; Jakubinek, M. B.; Kim, K. S.; Cheng, F.; Couillard, M.; Kingston, C.; Simard, B. Self-Assembly and Visualization of Poly(3-Hexyl-Thiophene) Chain Alignment along Boron Nitride Nanotubes. *J. Phys. Chem. C* **2015**, *119* (47), 26605–26610. https://doi.org/10.1021/acs.jpcc.5b09049.
(41) Papanastasiou, D. T.; Schultheiss, A.; Muñoz-Rojas, D.; Celle, C.; Carella, A.; Simonato, J.; Bellet, D. Transparent Heaters: A Review. *Adv. Funct. Mater.* **2020**, *30* (21), 1910225. https://doi.org/10.1002/adfm.201910225.
(42) Lee, H. B.; Jin, W.-Y.; Ovhal, M. M.; Kumar, N.; Kang, J.-W. Flexible Transparent Conducting Electrodes Based on Metal Meshes for Organic Optoelectronic Device Applications: A Review. *J. Mater. Chem. C* **2019**, *7* (5), 1087–1110. https://doi.org/10.1039/C8TC04423F.
(43) Zhou, H.; Song, Y. Fabrication of Silver Mesh/Grid and Its Applications in Electronics. *ACS Appl. Mater. Interfaces* **2021**, *13* (3), 3493–3511. https://doi.org/10.1021/acsami.0c18518.
(44) Lordan, D.; Burke, M.; Manning, M.; Martin, A.; Amann, A.; O'Connell, D.; Murphy, R.; Lyons, C.; Quinn, A. J. Asymmetric Pentagonal Metal Meshes for Flexible Transparent Electrodes and Heaters. *ACS Appl. Mater. Interfaces* **2017**, *9* (5), 4932–4940. https://doi.org/10.1021/acsami.6b12995.
(45) Kang, M.-G.; Kim, M.-S.; Kim, J.; Guo, L. J. Organic Solar Cells Using Nanoimprinted Transparent Metal Electrodes. *Adv. Mater.* **2008**, *20* (23), 4408–4413. https://doi.org/10.1002/adma.200800750.
(46) Lin, F.; Yin, D.; Li, T.; Lai, L.; Xia, M. Research on the Calibration of Ultraviolet Energy Meters; Han, S., Tan, J., Eds.; Beijing, China, 2016; p 101550P. https://doi.org/10.1117/12.2244603.
(47) Sepulveda-Mora, S. B.; Cloutier, S. G. Figures of Merit for High-Performance Transparent Electrodes Using Dip-Coated Silver Nanowire Networks. *J. Nanomater.* **2012**, *2012*, 1–7. https://doi.org/10.1155/2012/286104.
(48) Lu, X.; Nautiyal, P.; Bustillos, J.; Loganathan, A.; Zhang, C.; Chen, Y.; Boesl, B.; Agarwal, A. Hydroxylated Boron Nitride Nanotube-reinforced Polyvinyl Alcohol Nanocomposite Films with Simultaneous Improvement of Mechanical and Thermal Properties. *Polym. Compos.* **2020**, *41* (12), 5182–5194. https://doi.org/10.1002/pc.25785.
(49) Li, L.; Chen, Y.; Stachurski, Z. H. Boron Nitride Nanotube Reinforced Polyurethane Composites. *Prog. Nat. Sci. Mater. Int.* **2013**, *23* (2), 170–173. https://doi.org/10.1016/j.pnsc.2013.03.004.
(50) Rahmat, M.; Naftel, A.; Ashrafi, B.; Jakubinek, M. B.; Martinez-Rubi, Y.; Simard, B. Dynamic Mechanical Characterization of Boron Nitride Nanotube—Epoxy Nanocomposites. *Polym. Compos.* **2019**, *40* (6), 2119–2131. https://doi.org/10.1002/pc.24995.
(51) Gupta, R.; Rao, K. D. M.; Kiruthika, S.; Kulkarni, G. U. Visibly Transparent Heaters. *ACS Appl. Mater. Interfaces* **2016**, *8* (20), 12559–12575. https://doi.org/10.1021/acsami.5b11026.
(52) Sorel, S.; Bellet, D.; Coleman, J. N. Relationship between Material Properties and Transparent Heater Performance for Both Bulk-like and Percolative Nanostructured Networks. *ACS Nano* **2014**, *8* (5), 4805–4814. https://doi.org/10.1021/nn500692d.

(53) Kim, H.-J.; Kim, Y.; Jeong, J.-H.; Choi, J.-H.; Lee, J.; Choi, D.-G. A Cupronickel-Based Micromesh Film for Use as a High-Performance and Low-Voltage Transparent Heater. *J. Mater. Chem. A* **2015**, *3* (32), 16621–16626. https://doi.org/10.1039/C5TA03348A.
(54) Alhendi, M.; Sivasubramony, R. S.; Weerawarne, D. L.; Iannotti, J.; Borgesen, P.; Poliks, M. D. Assessing Current-Carrying Capacity of Aerosol Jet Printed Conductors. *Adv. Eng. Mater.* **2020**, *22* (11), 2000520. https://doi.org/10.1002/adem.202000520.
(55) Hummelgård, M.; Zhang, R.; Nilsson, H.-E.; Olin, H. Electrical Sintering of Silver Nanoparticle Ink Studied by In-Situ TEM Probing. *PLoS ONE* **2011**, *6* (2), e17209. https://doi.org/10.1371/journal.pone.0017209.

Chapter 4. Towards sustainable transparent flexible heaters: Integration of a BNNT interlayer using green solvent substitution

This chapter is adapted from work published in "Flexible and Printed Electronics": (1) Wagner, K.; Zou, S.; Martinez-Rubi, Y.; Kell, A. J.; Paquet, C.; Lessard, B. H. Towards Sustainable Transparent Flexible Heaters: Integration of a BNNT Interlayer Using Green Solvent Substitution. Flex. Print. Electron. 2023, 8 (2), 025005.

4.1. Context

In this work, I focused on improving the BNNT dispersion to increase the catalogue of chemically sensitive substrates that could be used high-operational printed electronics. Motivation was placed on removing harsh chlorinated base solvents in favour of an alcohol solvent. In addition to the solvent, the dispersive polymer was altered from poly(3-hexylthiophene) to polyvinyl butyral to improve tube-tube interactions in solution, and as such this study focuses on validating that the thermal and mechanical improvements the BNNT interlayer displayed in **Chapter 2** and **Chapter 3** are not compromised by film formation from the new solvent and polymer. One of the optimal transparent heater architectures in **Chapter 3** was employed as a device to explore and expand on the previous thermal and mechanical capabilities detailed in **Chapter 3**, providing an in-depth comparison with the previous interlayer's dispersive materials. This work successfully explores how the alcohol and polyvinyl butyral material combination results in nearly identical performance metrics with the chlorinated solvent on polyethylene terephthalate substrates, indicating sensitive substrates such as polylactic acid can be employed as substrate materials.

4.2. Contributions

I fabricated the BNNT alcohol-based dispersion with assistance from Dr. Martinez-Rubi. I deposited the BNNT film and printed and processed the transparent heater architectures. Dr. Zhou completed and visualized the atomic force microscopy data. I analyzed and visualized all profilometric analyses and corresponding microscope images. I completed the mechanical, average temperature thermal testing, and Dr. Kell completed the thermal cycling experiment. I visualized all mechanical and thermal data figures and was responsible for gathering qualitative IR imaging. I alongside Dr. Kell, Dr. Paquet, and Dr. Lessard contributed to the manuscript.

4.3. Abstract

Processing materials in electronics with non-toxic, green solvents can provide environmental benefits while reducing manufacturing health and safety challenges. Unfortunately, green solvents are often unable to provide comparable solubilizing characteristics and present challenges in printing and film formation compared to conventional organic solvents. Therefore, green materials are often developed in parallel to their processing method for successful implementation. In this study, we report on the use of a polyvinyl butyral (PVB) and ethanol solution as a replacement for poly (3-hexylthiophene-2,5-diyl) (P3HT) and chloroform and its' first demonstration in boron nitride nanotube (BNNT) thin film interlayers for improved thermal and mechanical performance in silver microgrid transparent heaters. Using PVB/ethanol led to comparable thin films of BNNT, achieving a clear tube network formation across the substrate surface and resulting in near identical optical transparency and surface energy measurements compared to the P3HT/chloroform system. Silver microgrids printed on BNNT-coated polyethylene terephthalate (PET) with PVB as dispersant exhibited a similar conductive performance to the microgrids printed on BNNT-coated PET with P3HT, providing the same level of mechanical endurance and maintaining thermal performance metrics upon applied voltage. The PVB and ethanol system presents an exemplary green material combination for the novel deposition of BNNT thin film interlayers for integration into transparent heaters.

4.4. Introduction

Printed electronics represents a growing field with enormous potential for providing low-cost sensors,[1–4] smart label packaging,[5] circuitry,[6,7] and more. Typically, the active coatings in these applications are printed using toxic or carcinogenic organic solvents.[8] As the large-scale deployment of printed electronics becomes a reality, environmental consequences over the use of these solvents increase in addition to growing concern towards the safety of printer operators. The choice of green solvents is limited, and often their chemical properties, such as vapor pressure, viscosity, and boiling point are different than existing organic solvents, making a simple change in solution rare.[9–14] The emphasis on sustainable electronics practices has transitioned to include device interlayers, which are useful in a variety of capacities including improving substrate roughness, printability, and ink adhesion for printed electronic devices.[15–17] Research on

incorporating ‘green’ solvents without compromising the integrity of the material or the device’s performance metrics is paramount for the integration of sustainable architectures.

Printed transparent heaters is an emerging electronic application that has found functions in automotive, aerospace and medical applications.[18–20] Recently, we reported the use of a boron nitride nanotube (BNNT) interlayer/film as an efficient heat dissipation layer which also improved mechanical and electrical performance of the resulting transparent heaters.[21] Martinez-Rubi et al have demonstrated successful dispersion of BNNTs using regio-random poly (3-hexylthiophene-2,5-diyl) (rra-P3HT) to produce highly uniform and individualized BNNT dispersions that can be printed effectively.[22] This rraP3HT and BNNT solution utilizes chloroform, a well-known harmful and carcinogenic solvent, however it provides the highest mole fraction solubility for P3HT.[23] Given the widespread use of rra-P3HT and BNNT solutions, it is of interest to investigate greener alternatives. Though chloroform solutions of rra-P3HT are effective, there are other polymers capable of interacting with and dispersing BNNT including polyvinyl alcohol, polyimide, polymethyl methacrylate, and polyvinyl butyral (PVB), all of which can be processed using green solvents such as ethanol and water.[24,25] PVB in particular has demonstrated efficient compatibility with BN material while providing good processability.[26–29]

In this study, we optimize the deposition of a PVB-modified BNNT using ethanol solvent to fabricate flexible microgrid heater architectures. We compare the solution properties and the printing processes to deposit the nanomaterial, as well as the resulting thin film properties to those obtained using P3HT and chloroform. We find that the use of PVB/ethanol provides a BNNT film with similar transmittance, resistance and mechanical properties compared to using P3HT/chloroform. When both polymer systems are utilized as dispersants to form BNNT interlayers between printed silver microgrid heaters and the substrate, they achieve similar heat-spreading properties, improve the temperature response, and reduce heat stress to the adjoining microgrid and underlying substrate in the same manner. We demonstrate a green solution for the deposition of active layers in emerging printed electronic applications that is easily adopted using standard coating methods.

4.5. Experimental Section

4.5.1. BNNT dispersion using $CHCl_3$ solvent

BNNT material was dispersed into two solutions using two different polymer and solvent combinations. Details regarding the synthesis and purification of the BNNT material can be found in works completed by Kim et al and Cho et al respectively.[30,31] BNNT material was added to chloroform ($CHCl_3$) solvent and non-covalently functionalized with rraP3HT (MW = 60–90 kDa) dissolved in $CHCl_3$ at an optimized 0.15 rra-P3HT:BNNT wt% ratio with the solution, and sonicated for 10 min between each addition of rra-P3HT.[22,32] Excess rra-P3HT polymer was removed through vacuum filtration and the remaining rra-P3HT:BNNT solid content was redispersed into chloroform with a resulting BN concentration of 0.2 mg ml^{-1}. The rra-P3HT:BNNT solution was deposited onto clean polyethylene terephthalate (PET) substrates using an SC-150 slot die applicator attached to an Automatic Research (GmBH) thin film coater and a Harvard Apparatus standard PHD 22/2000 syringe pump. Solvent was evaporated in ambient atmosphere for 30 s to achieve a calculated dry film thickness of 30 nm based on the coating speed, volumetric flowrate, coating width and solid content of the coating material.[21]

4.5.2. Dispersion using alcohol solvent

BNNT material was added to ethanol (EtOH) followed by the incremental addition of PVB (MW = 40–70 kDa) dissolved in EtOH and subsequent sonication for 10 min to give an optimized 1:1 PVB:BNNT wt% ratio and final BN concentration of 0.2 mg ml^{-1}. The PVB:BNNT dispersion was spray-coated using an Iwata Eclipse HP-CS Gravity Feed Dual Action Airbrush and IS850 Smart Jet Compressor onto clean PET substrates placed on a heated platform set to 40 ˚C to assist in solvent evaporation. The substrate was coated back and forth until the entire substrate was covered to create one layer of PVB:BNNT on the substrate surface. This process was repeated following rotating the substrate 90˚ and repeating the deposition process to achieve multiple layers of PVB:BNNTs, resulting in samples coated with 4, 8, 12, and 16 layers of the PVB:BNNT. In addition, PVB without BNNT material was dissolved in EtOH with a final PVB concentration of 0.2 mg ml^{-1} to mimic the solid content of the PVB:BNNT system and spray-coated onto clean PET substrates, totalling eight layers as described above.

4.5.3. Transparent heater fabrication

Silver molecular ink derived from silver neodecanoate was fabricated as described by Kell et al and screen-printed onto the dried BNNT-coated substrates as a grid pattern and processed through a combination of ultraviolet (UV) and thermal sintering techniques.[33] The grid pattern has a nominal line width of 50 μm, a pitch of 1300 μm and a total grid area of 1 × 1 inch. Further details regarding ink preparation as well as printing and processing details can be found in our previous work.[21]

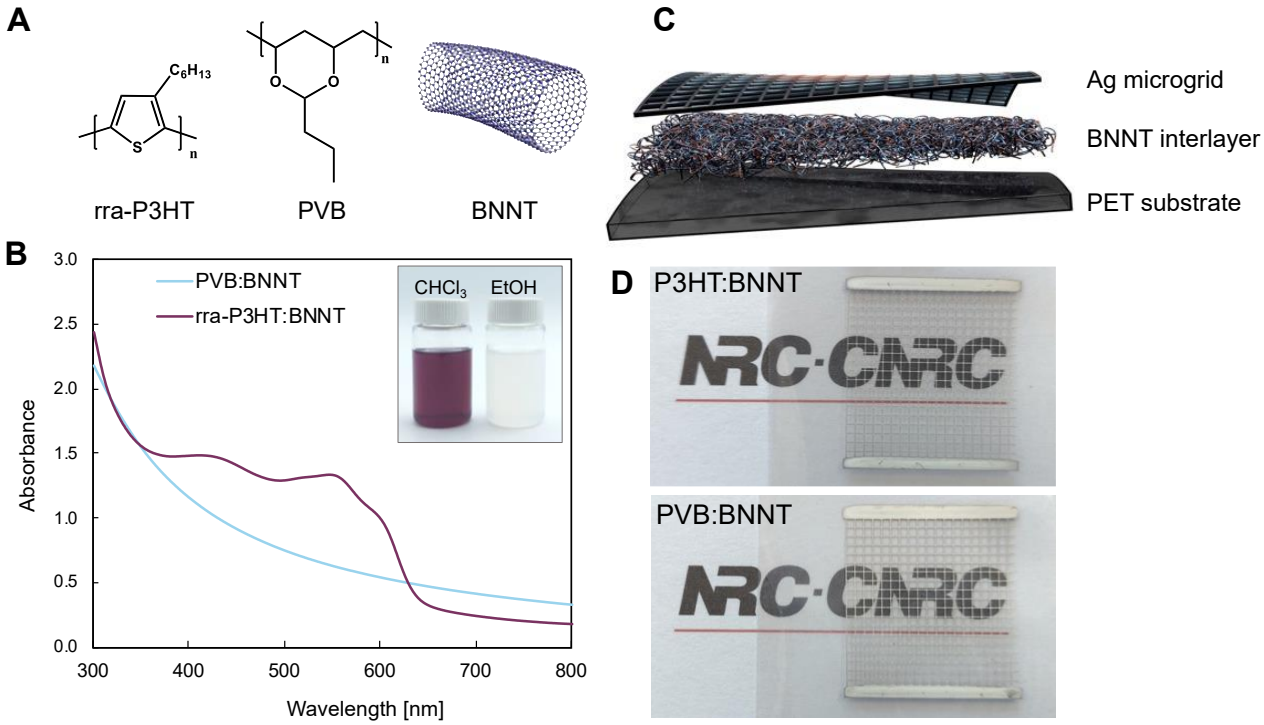

Figure 4.1. A) Image of rra-P3HT and PVB polymer with boron nitride nanotube structure with B) absorbance spectra and corresponding images of rra-P3HT:BNNT stable dispersion in chloroform and PVB:BNNT dispersed in ethanol and **C)** structure of transparent heater architecture containing PET substrate, BNNT interlayer, and printed silver (Ag) microgrid. Note: the BNNT-P3HT spectrum still contains excess P3HT ("bump" at ~ 450 nm). After filtration that excess polymer is removed and the "bump" at ~ 450 nm is no longer present. D) Images of square grids printed on rra-P3HT:BNNT-coated PET and PVB:BNNT coated PET demonstrating transparency over logo.

4.5.4. Characterization

After processing the ink, resistance measurements were taken using a handheld Fluke 115 Digital Multimeter by placing the probes onto the rectangular pads at either end of the printed grid to ensure proper connection and measuring across the pad for a total of four measurements across the entire grid structure. Absorption spectra (**Figure 4.1(B)**) and solid-state transmittance of the dried BNNT films on PET were taken using a Cary 5000 (UV–Vis) spectrometer, with optical transmittance (%T) measured to be 98.1% for the rra-P3HT:BNNT-coated PET and 97.2% for the PVB:BNNT-coated PET at a 500 nm wavelength (**Figure 4.5**). A Biolin Scientific Attension Theta Optical Tensiometer was used to analyze surface energy of the BNNT-coated PET and accompanying Navitar camera and OneAttension software completed contact angle measurements of the films using water as the solvent. AFM topography imaging was performed on a MultiMode AFM with a NanoScope V controller (Bruker Nano Surfaces Division, Santa Barbara, CA, USA), in the Peak Force QNM mode. The peak force with which the tip taps the sample surface was always kept at the lowest stable imaging level of 200–400 pN. Silicon nitride ScanAsyst-Air AFM probes (Bruker AFM Probes, Camarillo, CA, USA) were used in all peak force feedback measurements. Scanning electron microscopy (SEM) was completed using a Hitachi SU5000 microscope and ultra-variable pressure detector with an accelerating voltage of 0.9–1.2 kV and 3.2 mm working distance and a ThermoFisher Scientific Apreo-2 SEM with an accelerating voltage of 0.5 kV and 3.1 mm working distance. Two-dimensional optical profilometry traces were measured with a cyberTECHNOLOGIES CT100 optical profilometer (cyberTECHNOLOGIES GmbH) and corresponding microscope images were taken with a Zeiss Axioscope 517/Vario upright microscope. Mechanical data was gathered using a tensile bend test with a mandrel of 10 mm radius as described by ASTM Standards, Designation: F 1683. The microgrid was bent and spun around the mandrel and then returned to its initial position so that the entirety of the grid was passed over the mandrel twice, which is considered one cycle in the testing regime. After 25 bending cycles, the resistances were measured in the same consistent areas along the microgrid so as to ensure accurate measurements and this change in resistance was plotted against each 25 cycle increments. Change in resistance was measured every 25 cycles at four consistent locations using the handheld Fluke 115 Digital Multimeter to ensure accurate measurements in the same manner described previously. To complete thermal performance testing, 3M copper tape with conductive adhesive was secured to the printed silver areas on either end of the grid and a voltage bias applied

through a Global Specialties Model 1325 DC Power Supply. Continuous voltage was applied for 300 s and removed for 60 s, with corresponding thermal images and measured temperature response captured using a 5857 A TrueIR Thermal Imager by Keysight Technologies every 7 s during the testing time. For the thermal cycling test, a customized 3D printed clip was produced that allowed for a copper electrode to remain in contact with the printed electrodes on the microgrid. The power supply was connected to the copper electrodes using alligator clips. A picture of this clip is presented in the supporting information in **Figure 4.6**. Voltage was applied for 60 s and then removed for 60 s, representing one cycle, and then repeated for 18 cycles. The temperature response was captured with the same thermal camera used in the thermal performance testing.

4.6. Results and Discussion

Chlorinated solvents are being banned in several manufacturing processes, and as such a shift in favour of more environmentally friendly solvents, such as alcohols, is growing in the manufacturing of printed electronics.[34,35] BNNT inks are comprised of stable dispersions that use polymer-modified BNNTS dispersed in a solvent, and substitution of any of these components can lead to changes in their solution stabilities, processing qualities, as well as the resulting thin film properties. Therefore, when selecting a green solvent, the type of polymer and ratio of polymer to BNNT must be tuned to achieve optimal film properties. As detailed in the Experimental methods section, the PVB:BNNT system differs from the rra-P3HT:BNNT system in two key ways. First, the rra-P3HT can stabilize BNNTs at a 0.15:1 wt% ratio while the PVB requires a 1:1 wt% ratio to reach a similar level of dispersion stability, due to the different type of interactions involved between the polymer and the BNNTs. Second, the significant difference in boiling points of the two solvents impacted how the dispersion could be deposited to achieve high film uniformity. At 25 ˚C, the chloroform of the rra-P3HT:BNNT system has a vapour pressure roughly 2.5 times greater than ethanol present in the PVB:BNNT system (17.8 kPa vs. 7.9 kPa) with almost half the viscosity (0.54 mPa·s vs. 1.1 mPa·s).[36–38] In our previous study, we demonstrated that slot-die coating deposition methods achieved uniform films of the rra-P3HT:BNNT.[21] However, upon deposition of the PVB:BNNT system using the same slot-die coating procedure, the slow evaporation time of the ethanol solvent resulted in the solution pooling on the substrate surface and precipitation of the BNNTs, leading to poor dried film uniformity. Attempts to optimize the slot-die coating, including wet film thickness, blade height, blade speed, and depositing

temperature resulted in small areas of uniform film across a larger sample area, however large area film consistency was unattainable. Spray-coating was adopted to deposit the PVB:BNNT system by taking advantage of the atomized output from the spray gun on a substrate heated at 40 ˚C, leading to uniform thin films.

Varying layer depositions of 4, 8, 12, and 16 layers of the spray-coated PVB:BNNT dispersion were investigated to optimize conductive and thermal performance of the grids. A sufficient amount of layers is essential in determining a dense-enough network to take advantage of the heat spreading abilities of the BNNTs without disturbing the print quality or accumulating material waste. Upon printing of the microgrid onto the PVB:BNNT-coated substrates, those printed on 4 and 8 layers achieved very similar resistance values. However, those printed on 12 and 16 layers experienced a reduced print quality when the wet ink was deposited onto the substrate, and disconnects were visible within the grid mesh area. When measuring resistance post-processing, it was determined that the microgrid printed on 16 layers was non-conductive as a result of the poor printability and therefore could not be considered viable. Demonstration of the 4, 8 and 12 layer PVB:BNNT microgrids are shown in later experiments to confirm which architecture provides the most optimal conductive and thermal performance.

SEM imaging was conducted on the rraP3HT:BNNT and PVB:BNNT thin films. As shown in **Figures 4.2(A)** and **(B)**, the BNNTs with rra-P3HT were deposited across the film, and although evidence of tube bundling is apparent, there is a clear uniform and dense tube network across the entire substrate. The films also contain particulates of BN material however these components do not prevent the BNNTs from forming a uniform network. In **Figure 4.2(C)**, atomic force microscopy (AFM) height image of the rra-P3HT:BNNT film is presented and provides insight into the average roughness (R_a) of the film surface, measuring 20 nm. In **Figures 4.2(D)** and **(E)**, SEM images reveal that the eight-layer PVB:BNNT system deposited using spray coating also formed a sufficiently dense network of BNNTs on the substrate surface. The PVB:BNNT films appear denser than the rra-P3HT:BNNT, likely due to the greater polymer concentration in the solution or the multiple layers which were deposited. AFM height image of the eight-layer PVB:BNNT film is presented in **Figure 4.2(F)**, which measures the R_a of the film's surface to be 20 nm. To further characterize the thin films using AFM techniques, R_a and the root-mean-square roughness (R_q) were accumulated across a distribution of 20 different areas of the rraP3HT:BNNT and PVB:BNNT systems, respectively. The rra-P3HT:BNNT film exhibits a relatively even Ra

across the sample size (n = 20) between 18–28 nm and an R_q range of 26–38 nm. In comparison, the PVB:BNNT system reveals a greater variability for both the R_a and R_q values, ranging from 13–35 nm and 19–53 nm, respectively. Additional AFM images of both the rra-P3HT:BNNT and PVB:BNNT films can be found in **Figure 4.7** along with corresponding peak force error imaging to provide further insight into the variability of the films' surface morphology. **Figure 4.8** and **Table 4.1** provide further details regarding the plotted distribution of the R_a and R_q and the calculated mean, standard deviation, and median values of the rra-P3HT:BNNT and PVB:BNNT films.

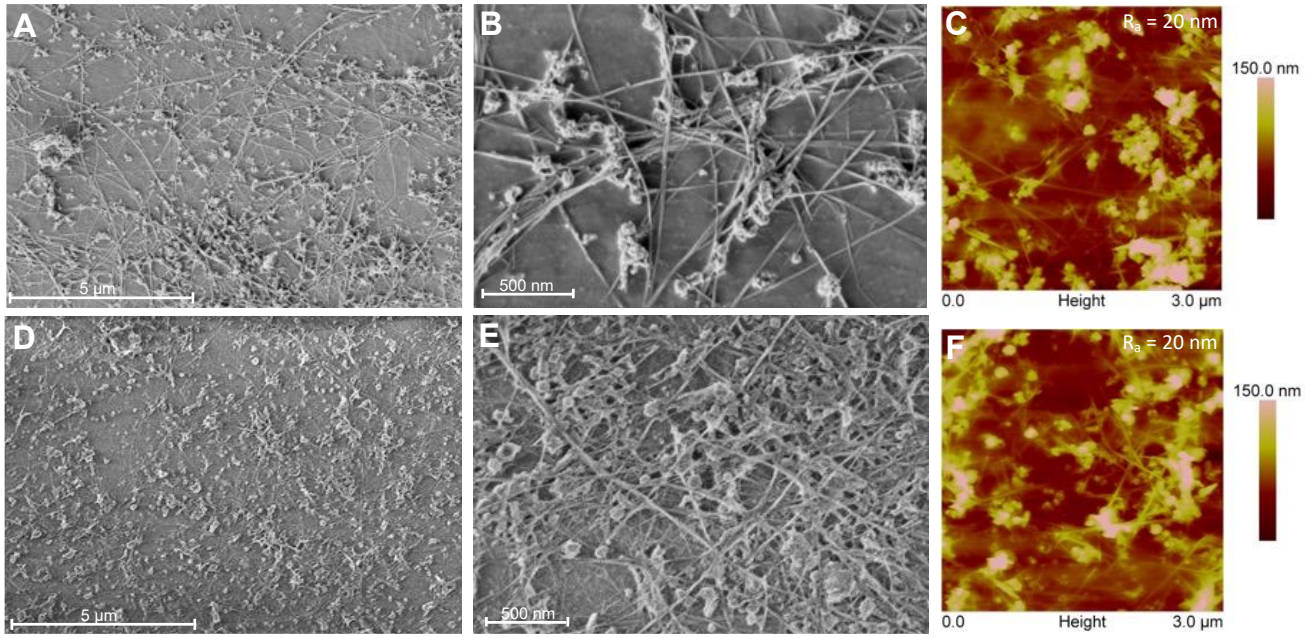

Figure 4.2. A) SEM images of rra-P3HT:BNNT deposited using slot-die coating methods and B) corresponding high magnification imaging and C) representative AFM height image of the rra-P3HT:BNNT system. D) SEM images of PVB:BNNT deposited using spray coating methods with E) corresponding high magnification of the PVB:BNNT system and F) representative AFM height image of the PVB:BNNT system.

The greater variability of the PVB:BNNT films is likely due to the increased polymer content that can accumulate on the surface of the samples or between layers of nanotubes and BN material resulting in a more uneven film. We expect greater variability in the surface roughness of the films deposited by atomized spray coating in comparison to slot die coating because it offers less control over the orientation of the BNNT resulting in some deposition of the nanomaterial perpendicular to the substrate surface. However, the surface roughness remains well below the

height of the silver microgrids printed onto the BNNT interlayer, and we do not believe the differences in surface roughness are causing any changes in performance as will be highlighted below.

Fabrication of transparent heaters is accomplished by depositing silver traces directly onto the BNNT-coated substrate.[21] A silver molecular ink was deposited as a square grid shape using screen printing methods on the BNNT-coated PET, where each square grid pattern measured a nominal line width of 50 μm, a nominal pitch of 1300 μm with a total grid area of 1 inch.^{2} The printed grid samples then underwent a consecutive UVA treatment and thermal sintering in order to initiate and complete the reduction from Ag^+ to Ag^0 to convert the ink into silver traces.[39] Resistance measurements conducted resulted in an averaged resistance of 1.89 ± 0.19 Ω across nine samples printed on rra-P3HT:BNNT-coated PET and an averaged resistance of 2.22 ± 0.20 Ω across ten samples printed on PVB:BNNT-coated PET. Optical 2D profilometry and microscope imaging of the traces are presented in figure 3 to investigate trace morphology. The surface profile of the rra-P3HT:BNNT system (**Figure 4.3(A)**), depicts varying peaks and valleys throughout the trace, with an average height of 0.62 μm, a maximum measured height of 1.29 μm and an R_q of 0.17 μm. Corresponding microscope images of the traces printed on rra-P3HT:BNNT-coated PET is presented in **Figure 4.3(B)**, and confirms the dense randomized networks of silver veins throughout the bulk of the trace that is directly responsible for the peaks and valleys measured in **Figure 4.3(A)**. Surface energy analysis was conducted on the BNNT film to provide insight into the interactions of the silver ink with the different surfaces during printing. As shown in **Figure 4.3(B)** inset, a 3 μL water drop deposited on the rra-P3HT:BNNT film results in a contact angle of 92.6˚ which is consistent with previous reports [21]. In comparison, the cross-sectional height profile of the trace printed on PVB:BNNT-coated PET in **Figure 4.3(C)** exhibits three distinct peaks on the trace surface at either end and in the middle of the trace, resulting in an average height measurement of 0.49 μm, a maximum height of 1.14 μm and an R_q of 0.10 μm. When analyzing the microscope image of the PVB:BNNT system in **Figure 4.3(D)**, the three peaks depicted in the surface height profiles are apparent by the more concentrated silver veins that formed during processing. Because the silver grids printed on PVB:BNNT are not as thick as those printed on the rra-P3HT:BNNT, that alongside the different surface morphology of the trace on PVB:BNNT likely leads to less silver metal present and subsequently the slight difference in electrical performance. The contact angle measurement for the PVB:BNNT system in **Figure 4.3(D)** inset

also presents a contact angle of 92.6˚, indicating that the increased surface roughness of the PVB:BNNT film as presented in **Figure 4.2** does not affect surface hydrophobicity, further evident by the similar measured trace widths (W) of 123 μm and 128 μm in **Figures 4.2(B)** and **4.2(D)** respectively.

The profilometry data also provides insight into the measured height of the polymer:BNNT coating from the surface of the PET substrate, with a maximum measured height of 105 nm for the rraP3HT:BNNT film and 191 nm for the PVB:BNNT film which is significantly higher relative to the rraP3HT:BNNT system. Slight difference in the manner that the silver salt converts to silver metal may be expected given that the thermal properties of the underlying BNNT films differ due to differences in the polymer and polymer:BNNT, as shown in the trace images in **Figure 4.3**.

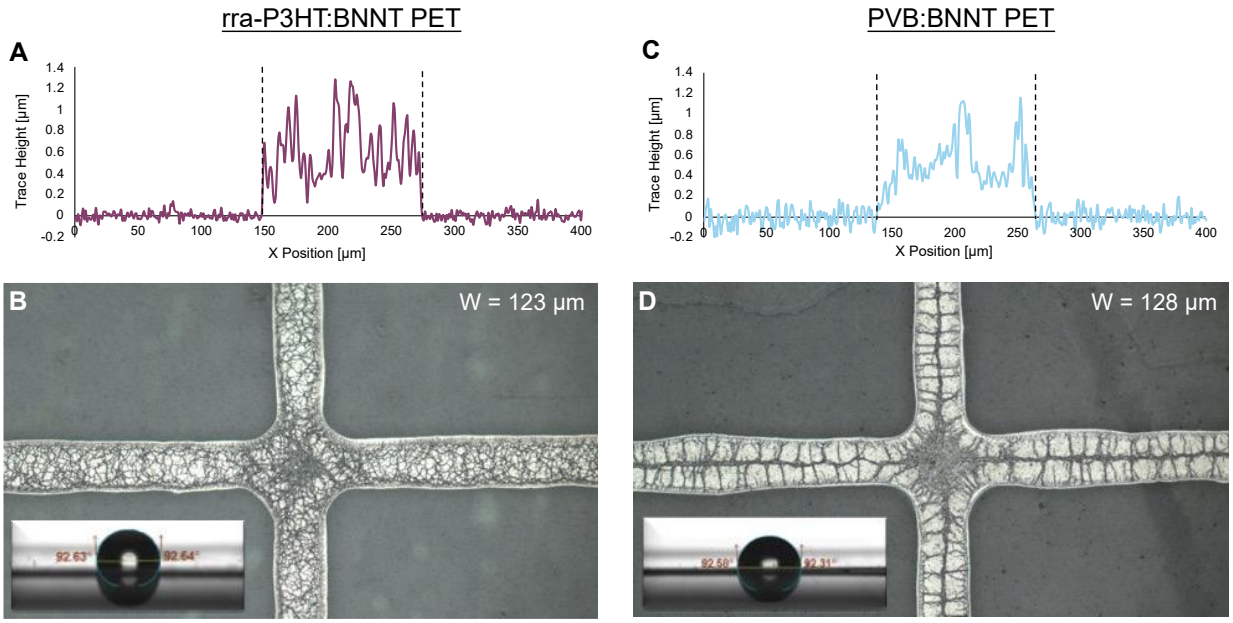

Figure 4.3. Optical 2D profilometry measurement of the 50/1300 grid sample printed on A) rra-P3HT:BNNT-coated PET with B) corresponding microscope images of the traces with contact angle image inset and optical 2D profilometry measurements of the 50/1300 grid sample printed on C) PVB:BNNT-coated PET substrates with D) corresponding microscope image of the trace with contact angle image inset.

The robustness of the printed microgrid traces on rra-P3HT:BNNT and PVB:BNNT were characterized by subjecting the microgrids to a series of tensile bending cycles, as shown in **Figure 4.4(A)**. Typically, a 10% increase in resistance is considered the maximum allowable increase before the samples are considered to have failed. Within the first 150 bending cycles, the microgrid

printed on PVB:BNNT-coated PET is able to maintain a smaller change in resistance when subjected to the tensile bending tests compared to the microgrid printed on rra-P3HT:BNNT. At roughly 150 cycles both the PVB:BNNT and rraP3HT:BNNT have a % change in resistance of over 10%, demonstrating both films exhibit near identical response to mechanical deformation. In addition to investigating mechanical robustness of the BNNT interlayers, the thermal response of the microgrid printed on each interlayer must also be tested. It has been shown that the inclusion of a BNNT interlayer between the plastic substrate and printed feature can improve the Joule heating effect through electrical sintering, leading to an increase in heat output from the microgrid.[21,40] However, substitution of the polymeric materials, differences in polymer solid content, and the morphology of the films may change the thermal response of the grids. The thermal performance of microgrids printed on 0, 4, 8 and 12 layers (R = 2.03, 2.50, 2.10, 2.05 Ω respectively) of PVB:BNNT was investigated to determine whether a sufficient network of BNNTs were deposited to take advantage of the thermal conductivity of the BNNT network and initiate their heat spreading abilities. Upon applied voltage of 2.5 V, the eight-layer sample provided a clear improvement in uniform Joule heating across the grid area, whereas the 4- and 12layer samples showed non-uniform thermal response with evident hot-spots throughout the grid area, as shown in **Figure 4.9**. As a result, the thermal performance of the silver microgrid printed on PVB-coated PET, rra-P3HT:BNNT-coated PET, and eight-layer PVB:BNNT-coated PET were further characterized. The measured resistances of the grids were 1.83 Ω, 2.00 Ω, and 2.05 Ω respectively. It is important to note that grids with similar base resistances were compared to ensure that observed differences were a result of the change in material selection. The grids were subjected to applied voltages of 1.0, 1.5, 2.0 and 2.5 V consecutively, with each voltage applied for 300 s with measurements taken every 7 s until 60 s after the voltage is removed. The averaged steady-state temperatures collected for 240 s at each applied voltage are presented in **Figure 4.4(B)**, excluding the measurements of the temperature ramp-up and cool down post testing.

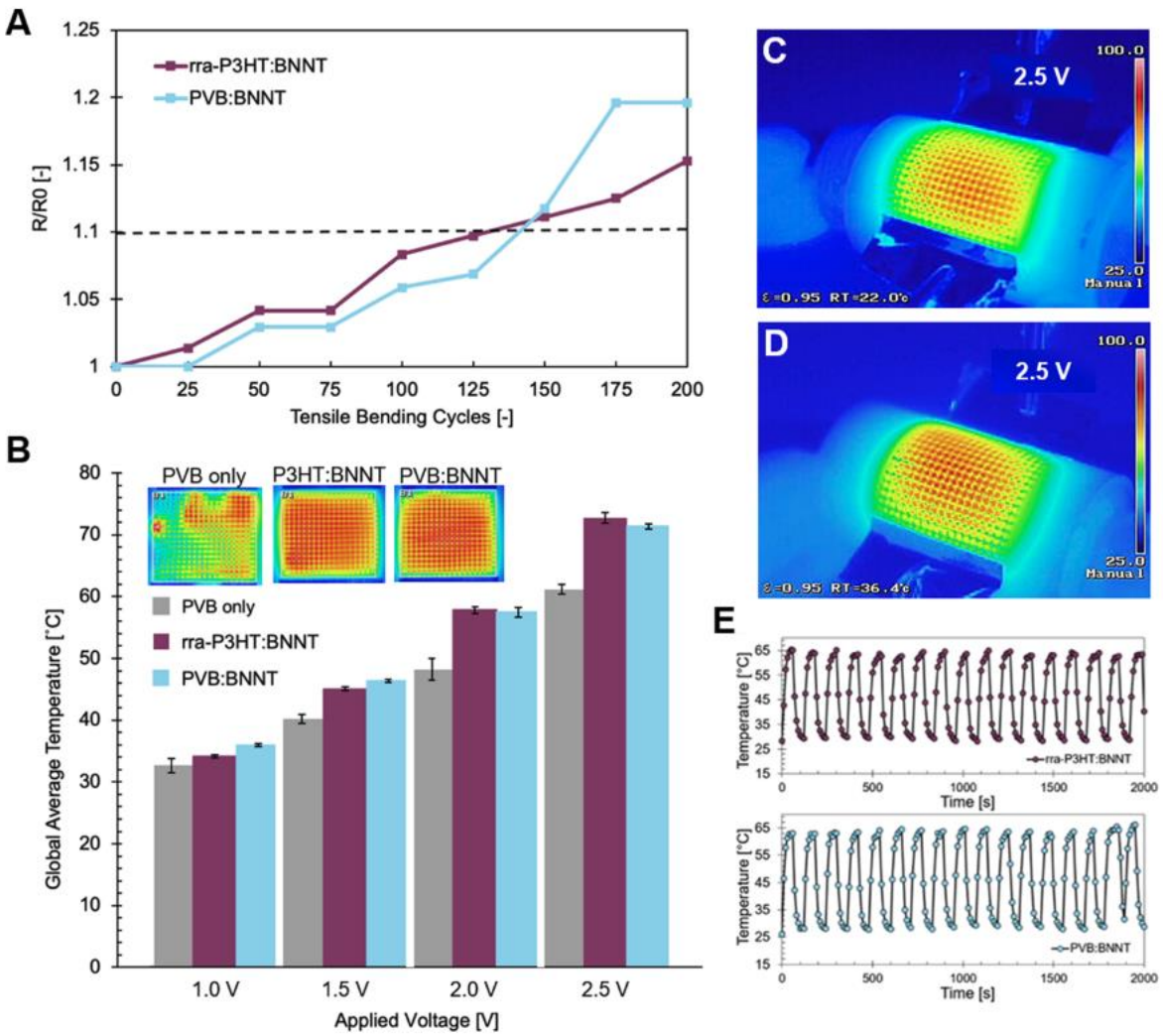

Figure 4.4. (A) Comparison of change in resistance of the Ag microgrids printed on rra-P3HT:BNNT-coated PET and PVB:BNNT-coated PET over 200 total tensile bending cycles. (B) Averaged global temperature response of the Ag microgrid printed on PVB film, rra-P3HT:BNNT and PVB:BNNT systems at applied voltages of 1.0, 1.5, 2.0 and 2.5 V with inset images at 2.5 V at t = 160 s (C) steady-state thermal response of the Ag microgrid printed on rra-P3HT:BNNT and (D) PVB:BNNT at t = 125 s upon applied 2.5 V flexed around a scintillation vial at t = 280 s and (E) thermal cycling response of Ag microgrids printed on rra-P3HT:BNNT and PVB:BNNT films respectively at an applied voltage of 2.3 V.

As shown in **Figure 4.4(B)**, the PVB:BNNT system has a near identical measured temperature response to that of the rra-P3HT:BNNT system at each applied voltage, indicating that the PVB polymer complex is able to support the BNNT material and allow it to dissipate heat

laterally across the grid area and improve the overall Joule heating response. In comparison, the microgrid printed onto the PVB-coated substrate shows an uneven temperature distribution and hot spot formation throughout the feature, indicating that the BNNTs are integral in spreading heat across the entire feature area. Characteristic thermal images of the steady state temperature response of the three microgrids at each applied voltage are provided in **Figures 4.10–4.12**. Both samples printed on BNNT-coated PET demonstrate an even and uniform distribution of heat across the entire grid area, with sufficient heat spreading on part from the BNNT interlayer as well as the high-quality trace morphology from both samples. Furthermore, the grids were also tested by wrapping and securing around a vial with a diameter of 2.8 cm, and the temperature response measured in the same manner as the flat thermal characterization. There is no hot spot formation or delamination as seen in the thermal imaging in **Figures 4.4(C)** and **(D)**, indicating that both the rraP3HT:BNNT and PVB:BNNT interlayers continue to assist in spreading heat laterally across the microgrid area to produce an even heat distribution even when flexed. Finally, to explore the operational stability of the polymer:BNNT interlayers, thermal cycling tests were completed on the 50/1300 microgrid printed on both rra-P3HT:BNNT and PVB:BNNT systems. As presented in **Figure 4.4(E)**, a voltage of 2.3 V was applied for 60 s and then removed for 60 s over a consistent 36 min testing period, with measurements of the global average temperature response across the entire grid area taken every 10 s. At near identical resistances of 1.50 and 1.56 Ω for the Ag microgrids printed on rra-P3HT:BNNT and PVB:BNNT interlayers respectively, both polymer:BNNT systems provide a sufficient and reliable platform to withstand the thermal cycling, achieving nearly identical temperature profiles with little degradation over time. This further demonstrates the ability for the PVB:BNNT to form a similar network to rra-P3HT:BNNT which can provide significant improvements in thermal performance in transparent thermal heaters.

4.7 Conclusion:

In this study we report the use of PVB and ethanol as a green alternative to using P3HT and chloroform for the printing of BNNT thin films. We determined that similar BNNT films, tube network formation, surface energy, and transparency can be obtained when optimizing the polymer to BNNT ratio and when using spray coating deposition techniques. A more variable surface roughness of the PVB:BNNT film did not affect the deposition of the molecular ink, and the microgrid transparent heater printed on PVB:BNNT-coated PET achieved similar resistance values

(2.22 ± 0.20 Ω) to that of the microgrid printed on rra-P3HT:BNNT-coated PET (1.89 ± 0.19 Ω) as well as a lower RMS roughness value of the trace surface post-processing. Furthermore, the PVB:BNNT-coated PET produced similar responses to tensile cyclic deformation, indicating that both BNNT interlayers can alleviate the mechanical stress imparted on the silver grid traces. Finally, the rra-P3HT:BNNT and PVB:BNNT systems exhibit near identical averaged temperature responses of 72.7 ± 0.80 ˚C and 71.4 ± 0.43 ˚C respectively upon applied voltage of 2.5 V. Therefore, this study demonstrates the ability for the PVB:BNNT system to form a sufficient tube network necessary to achieve similar mechanical and thermal performance metrics as the previous rra-P3HT:BNNT system while being processed using green solvents.

4.8. Acknowledgements

This work was supported by the NSERC Green Electronics Network (GreEN) (Grant No. NETGP 508526-17). We thank Mark Plunkett, Dean Ruth, Keun Su Kim, and Benoit Simard for the synthesis and purification of the BNNTs utilized in this study. We also thank Nic Milliken for the design and fabrication of the 3D-printed clips to test thermal cycling.

4.9. Supporting Information

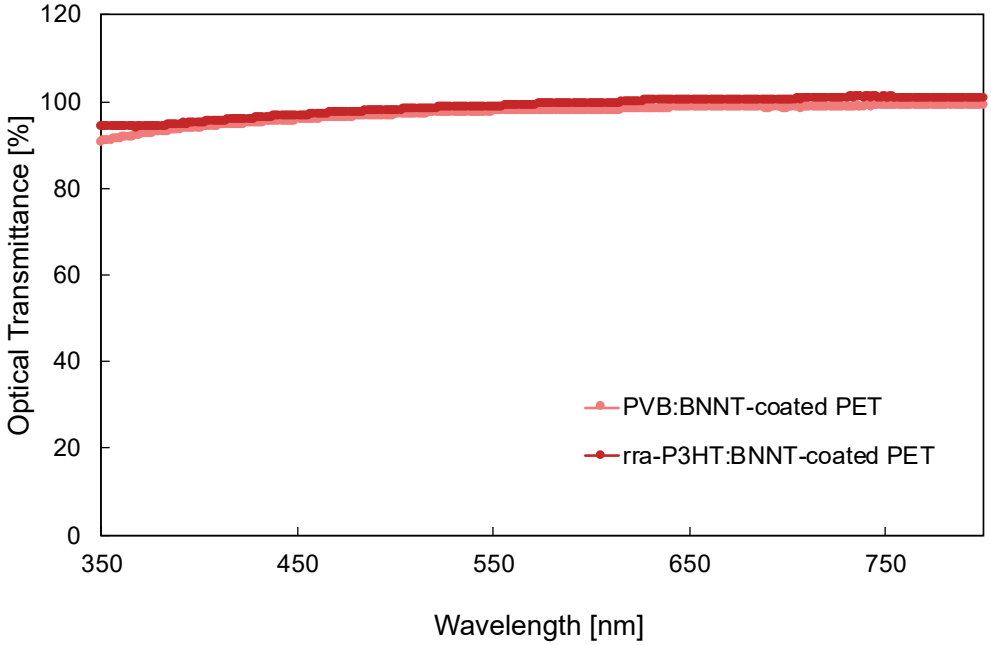

Figure 4.5. Optical transmittance spectrum of the rra-P3HT:BNNT-coated PET and PVB:BNNT-coated PET with bare PET acting as the background filter

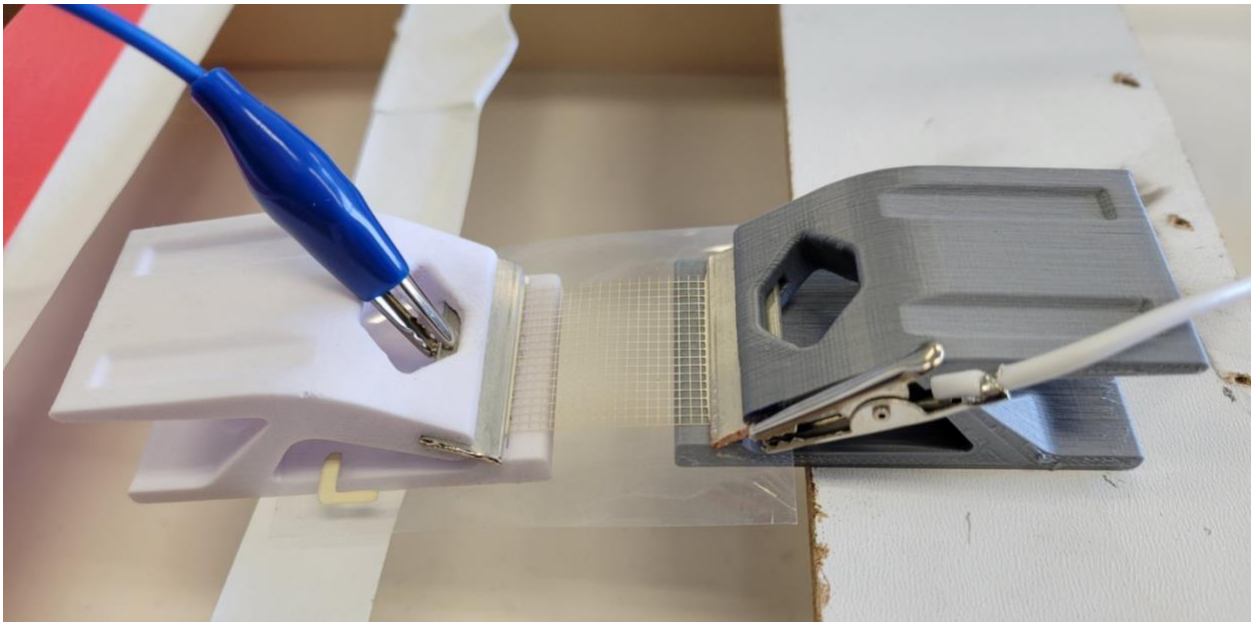

Figure 4.6. Thermal cycling test set-up with 3D-printed clips to secure copper tape onto electrical measuring pads of 50/1300 silver microgrid printed on PVB:BNNT-coated PET

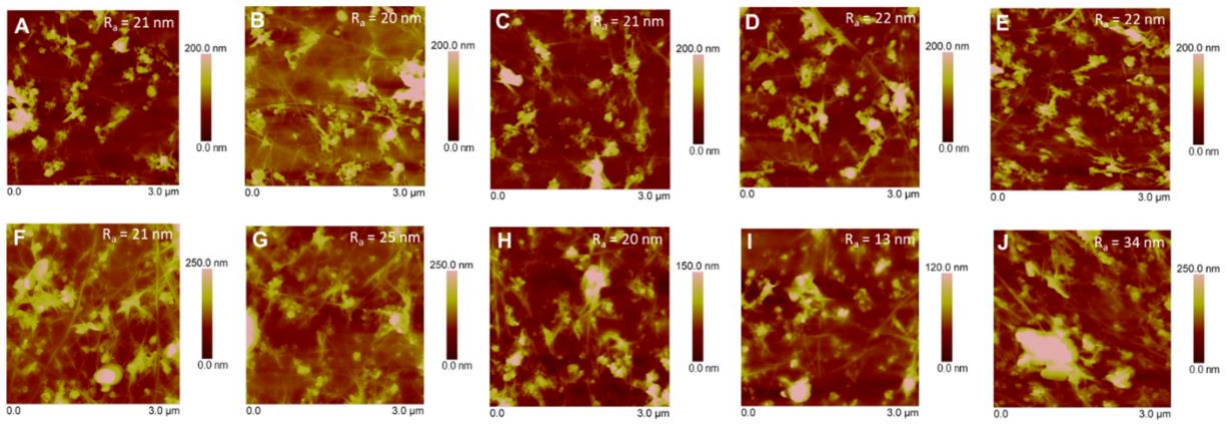

Figure 4.7. Atomic force microscopy height images of A-E) rra-P3HT:BNNT-coated PET and F-J) 8-layer PVB:BNNT-coated PET with a scanned area of 3.0 μm^2

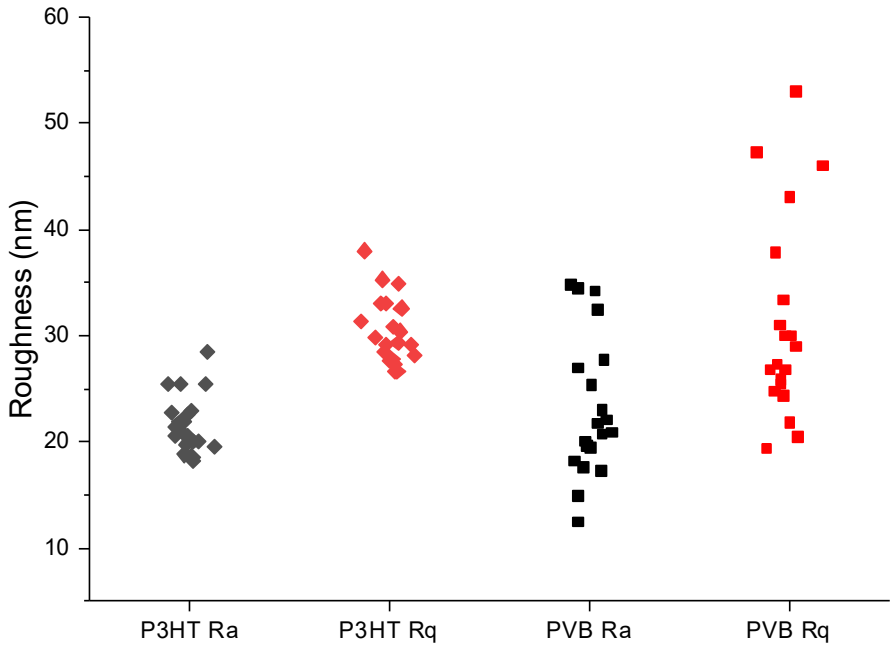

Figure 4.8. Graphical summary of measured average surface roughness (R_a) and RMS roughness (R_q) taken from atomic force microscopy (AFM) measurements of rra-P3HT:BNNT films (n = 20) and PVB:BNNT films (n = 20) with a measuring area of 3.0 μm^2

Table 4.1. Statistical data of atomic force microscopy measurements of average surface roughness (R_a) and RMS roughness (R_q) of rra-P3HT:BNNT-coated PET and PVB:BNNT-coated PET with a measuring area of 3.0 μm^2

	Sample Type	Sample Size	Mean [nm]	Standard Deviation [nm]	Median [nm]	SEM [nm]
Average Roughness (Ra)	P3HT	20	22	2.7	21	0.6
	PVB	20	23	6.6	21	1.5
RMS Roughness (Rq)	P3HT	20	30	3.1	30	0.7
	PVB	20	31	9.4	28	2.1

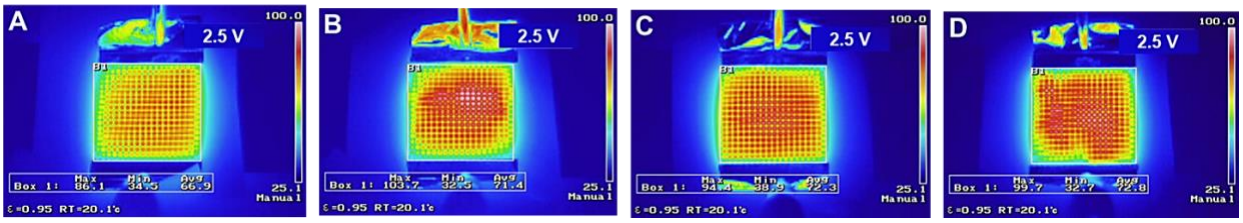

Figure 4.9. Infrared (IR) thermal imaging taken at t = 160 s of a 50/1300 Ag microgrid printed on A) bare PET, B) 4-layer, c) 8-layer and d) 12-layers of PVB:BNNT coatings on PET

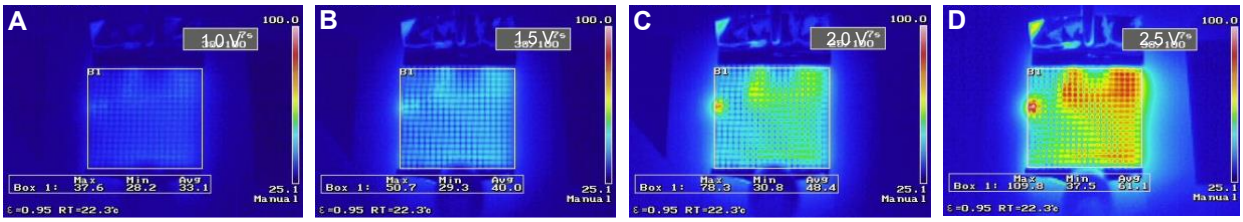

Figure 4.10. Infrared (IR) thermal imaging taken at t = 160 s of a 50/1300 Ag microgrid printed on PVB-coated PET subjected to applied A) 1.0 V, B) 1.5 V, C) 2.0 V, and D) 2.5 V

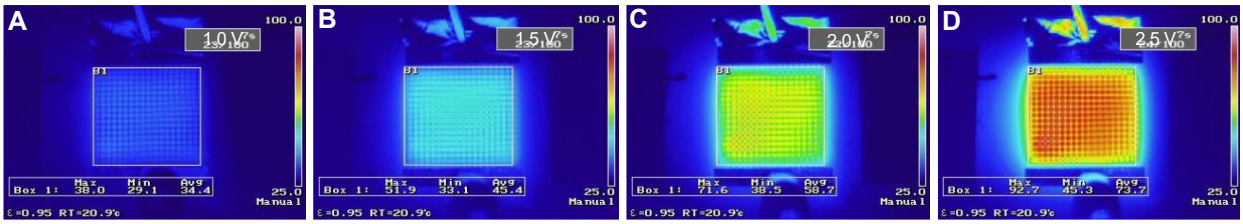

Figure 4.11. Infrared (IR) thermal imaging taken at t = 160 s of a 50/1300 Ag microgrid printed on rra-P3HT:BNNT-coated PET subjected to applied A) 1.0 V, B) 1.5 V, C) 2.0 V, and D) 2.5 V

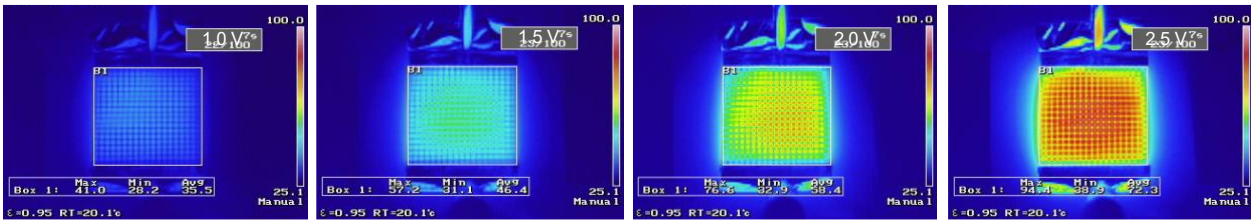

Figure 4.12. Infrared (IR) thermal imaging taken at t = 160 s of a 50/1300 Ag microgrid printed on PVB:BNNT-coated PET subjected to applied A) 1.0 V, B) 1.5 V, C) 2.0 V, and D) 2.5 V

4.10. References

(1) Baumbauer, C. L.; Anderson, M. G.; Ting, J.; Sreekumar, A.; Rabaey, J. M.; Arias, A. C.; Thielens, A. Printed, Flexible, Compact UHF-RFID Sensor Tags Enabled by Hybrid Electronics. *Sci. Rep.* **2020**, *10* (1), 16543. https://doi.org/10.1038/s41598-020-73471-9.

(2) Li, Z.; Khuje, S.; Chivate, A.; Huang, Y.; Hu, Y.; An, L.; Shao, Z.; Wang, J.; Chang, S.; Ren, S. Printable Copper Sensor Electronics for High Temperature. *ACS Appl. Electron. Mater.* **2020**, *2* (7), 1867–1873. https://doi.org/10.1021/acsaelm.0c00358.

(3) Lo, L.; Shi, H.; Wan, H.; Xu, Z.; Tan, X.; Wang, C. Inkjet-Printed Soft Resistive Pressure Sensor Patch for Wearable Electronics Applications. *Adv. Mater. Technol.* **2020**, *5* (1), 1900717. https://doi.org/10.1002/admt.201900717.

(4) Ma, L.-Y.; Soin, N. Recent Progress in Printed Physical Sensing Electronics for Wearable Health-Monitoring Devices: A Review. *IEEE Sens. J.* **2022**, *22* (5), 3844–3859. https://doi.org/10.1109/JSEN.2022.3142328.

(5) Machiels, J.; Appeltans, R.; Bauer, D. K.; Segers, E.; Henckens, Z.; Van Rompaey, W.; Adons, D.; Peeters, R.; Geiβler, M.; Kuehnoel, K.; Tempel, L.; Weissbach, T.; Hübler, A. C.; Verma, A.; Ferraris, E.; Deferme, W.; Buntinx, M. Screen Printed Antennas on Fiber-Based Substrates for Sustainable HF RFID Assisted E-Fulfilment Smart Packaging. *Materials* **2021**, *14* (19), 5500. https://doi.org/10.3390/ma14195500.

(6) Correia, V.; Mitra, K. Y.; Castro, H.; Rocha, J. G.; Sowade, E.; Baumann, R. R.; Lanceros-Mendez, S. Design and Fabrication of Multilayer Inkjet-Printed Passive Components for Printed Electronics Circuit Development. *J. Manuf. Process.* **2018**, *31*, 364–371. https://doi.org/10.1016/j.jmapro.2017.11.016.

(7) Chang, J. S.; Facchetti, A. F.; Reuss, R. A Circuits and Systems Perspective of Organic/Printed Electronics: Review, Challenges, and Contemporary and Emerging Design Approaches. *IEEE J. Emerg. Sel. Top. Circuits Syst.* **2017**, *7* (1), 7–26. https://doi.org/10.1109/JETCAS.2017.2673863.

(8) Savva, A.; Ohayon, D.; Surgailis, J.; Paterson, A. F.; Hidalgo, T. C.; Chen, X.; Maria, I. P.; Paulsen, B. D.; Petty, A. J.; Rivnay, J.; McCulloch, I.; Inal, S. Solvent Engineering for High-Performance n-Type Organic Electrochemical Transistors. *Adv. Electron. Mater.* **2019**, *5* (8), 1900249. https://doi.org/10.1002/aelm.201900249.

(9) Byrne, F. P.; Jin, S.; Paggiola, G.; Petchey, T. H. M.; Clark, J. H.; Farmer, T. J.; Hunt, A. J.; Robert McElroy, C.; Sherwood, J. Tools and Techniques for Solvent Selection: Green Solvent Selection Guides. *Sustain. Chem. Process.* **2016**, *4* (1), 7. https://doi.org/10.1186/s40508-016-0051-z.

(10) Campana, F.; Kim, C.; Marrocchi, A.; Vaccaro, L. Green Solvent-Processed Organic Electronic Devices. *J. Mater. Chem. C* **2020**, *8* (43), 15027–15047. https://doi.org/10.1039/D0TC03610B.

(11) Lee, J.; Park, S. A.; Ryu, S. U.; Chung, D.; Park, T.; Son, S. Y. Green-Solvent-Processable Organic Semiconductors and Future Directions for Advanced Organic Electronics. *J. Mater. Chem. A* **2020**, *8* (41), 21455–21473. https://doi.org/10.1039/D0TA07373C.

(12) Larsen, C.; Lundberg, P.; Tang, S.; Ràfols-Ribé, J.; Sandström, A.; Mattias Lindh, E.; Wang, J.; Edman, L. A Tool for Identifying Green Solvents for Printed Electronics. *Nat. Commun.* **2021**, *12* (1), 4510. https://doi.org/10.1038/s41467-021-24761-x.

(13) McDowell, C.; Bazan, G. C. Organic Solar Cells Processed from Green Solvents. *Curr. Opin. Green Sustain. Chem.* **2017**, *5*, 49–54. https://doi.org/10.1016/j.cogsc.2017.03.007.

(14) Kim, D.; Nunes, S. P. Green Solvents for Membrane Manufacture: Recent Trends and Perspectives. *Curr. Opin. Green Sustain. Chem.* **2021**, *28*, 100427. https://doi.org/10.1016/j.cogsc.2020.100427.
(15) Chen, Y.; Zhuang, X.; Goldfine, E. A.; Dravid, V. P.; Bedzyk, M. J.; Huang, W.; Facchetti, A.; Marks, T. J. Printable Organic-Inorganic Nanoscale Multilayer Gate Dielectrics for Thin-Film Transistors Enabled by a Polymeric Organic Interlayer. *Adv. Funct. Mater.* **2020**, *30* (40), 2005069. https://doi.org/10.1002/adfm.202005069.
(16) Sekine, T.; Ikeda, H.; Kosakai, A.; Fukuda, K.; Kumaki, D.; Tokito, S. Improvement of Mechanical Durability on Organic TFT with Printed Electrodes Prepared from Nanoparticle Ink. *Appl. Surf. Sci.* **2014**, *294*, 20–23. https://doi.org/10.1016/j.apsusc.2013.12.168.
(17) Domínguez, M. A.; Sosa-Sánchez, J. L. Copper Phthalocyanine Buffer Interlayer Film Incorporated in Paper Substrates for Printed Circuit Boards and Dielectric Applications in Flexible Electronics. *Solid-State Electron.* **2020**, *172*, 107898. https://doi.org/10.1016/j.sse.2020.107898.
(18) Yang, J.; Zi, D.; Zhu, X.; Li, H.; Li, Z.; Sun, L.; Zhang, G.; Wang, F.; Peng, Z.; Lan, H. Printed Flexible Transparent Electrodes for Harsh Environments. *Adv. Mater. Technol.* **2022**, *7* (5), 2101087. https://doi.org/10.1002/admt.202101087.
(19) Li, Z.; Chang, S.; Khuje, S.; Ren, S. Recent Advancement of Emerging Nano Copper-Based Printable Flexible Hybrid Electronics. *ACS Nano* **2021**, *15* (4), 6211–6232. https://doi.org/10.1021/acsnano.1c02209.
(20) Chen, X.; Yin, Y.; Yuan, W.; Nie, S.; Lin, Y.; Guo, W.; Su, W.; Li, Y.; Yang, K.; Cui, Z. Transparent Thermotherapeutic Skin Patch Based on Highly Conductive and Stretchable Copper Mesh Heater. *Adv. Electron. Mater.* **2021**, *7* (12), 2100611. https://doi.org/10.1002/aelm.202100611.
(21) Wagner, K.; Kell, A. J.; Martinez-Rubi, Y.; Paquet, C.; Lessard, B. H. Engineering Silver Microgrids with a Boron Nitride Nanotube Interlayer for Highly Conductive and Flexible Transparent Heaters. *Adv. Mater. Technol.* **2022**, 2200037. https://doi.org/10.1002/admt.202200037.
(22) Martinez-Rubi, Y.; Jakubek, Z. J.; Jakubinek, M. B.; Kim, K. S.; Cheng, F.; Couillard, M.; Kingston, C.; Simard, B. Self-Assembly and Visualization of Poly(3-Hexyl-Thiophene) Chain Alignment along Boron Nitride Nanotubes. *J. Phys. Chem. C* **2015**, *119* (47), 26605–26610. https://doi.org/10.1021/acs.jpcc.5b09049.
(23) Roesing, M.; Howell, J.; Boucher, D. Solubility Characteristics of Poly(3-Hexylthiophene). *J. Polym. Sci. Part B Polym. Phys.* **2017**, *55* (14), 1075–1087. https://doi.org/10.1002/polb.24364.
(24) Joy, J.; George, E.; Haritha, P.; Thomas, S.; Anas, S. An Overview of Boron Nitride Based Polymer Nanocomposites. *J. Polym. Sci.* **2020**, *58* (22), 3115–3141. https://doi.org/10.1002/pol.20200507.
(25) Sharma, S.; Setia, P.; Chandra, R.; Thakur, N. Experimental and Molecular Dynamics Study of Boron Nitride Nanotube-Reinforced Polymethyl Methacrylate Composites. *J. Compos. Mater.* **2020**, *54* (1), 3–11. https://doi.org/10.1177/0021998319851221.
(26) Zhi, C.; Bando, Y.; Terao, T.; Tang, C.; Kuwahara, H.; Golberg, D. Towards Thermoconductive, Electrically Insulating Polymeric Composites with Boron Nitride Nanotubes as Fillers. *Adv. Funct. Mater.* **2009**, *19* (12), 1857–1862. https://doi.org/10.1002/adfm.200801435.

(27) Wang, J.; Wang, N.; Liu, M.; Ge, C.; Hou, B.; Liu, G.; Sun, W.; Hu, Y.; Ning, Y. Hexagonal Boron Nitride/Poly(Vinyl Butyral) Composite Coatings for Corrosion Protection of Copper. *J. Mater. Sci. Technol.* **2022**, *96*, 103–112. https://doi.org/10.1016/j.jmst.2021.03.075.
(28) Ahn, H. J.; Eoh, Y. J.; Park, S. D.; Kim, E. S. Thermal Conductivity of Polymer Composites with Oriented Boron Nitride. *Thermochim. Acta* **2014**, *590*, 138–144. https://doi.org/10.1016/j.tca.2014.06.029.
(29) Wang, Z.; Liu, J.; Cheng, Y.; Chen, S.; Yang, M.; Huang, J.; Wang, H.; Wu, G.; Wu, H. Alignment of Boron Nitride Nanofibers in Epoxy Composite Films for Thermal Conductivity and Dielectric Breakdown Strength Improvement. *Nanomaterials* **2018**, *8* (4), 242. https://doi.org/10.3390/nano8040242.
(30) Kim, K. S.; Kingston, C. T.; Hrdina, A.; Jakubinek, M. B.; Guan, J.; Plunkett, M.; Simard, B. Hydrogen-Catalyzed, Pilot-Scale Production of Small-Diameter Boron Nitride Nanotubes and Their Macroscopic Assemblies. *ACS Nano* **2014**, *8* (6), 6211–6220. https://doi.org/10.1021/nn501661p.
(31) Cho, H.; Walker, S.; Plunkett, M.; Ruth, D.; Iannitto, R.; Martinez Rubi, Y.; Kim, K. S.; Homenick, C. M.; Brinkmann, A.; Couillard, M.; Dénommée, S.; Guan, J.; Jakubinek, M. B.; Jakubek, Z. J.; Kingston, C. T.; Simard, B. Scalable Gas-Phase Purification of Boron Nitride Nanotubes by Selective Chlorine Etching. *Chem. Mater.* **2020**, *32* (9), 3911–3921. https://doi.org/10.1021/acs.chemmater.0c00144.
(32) Martinez Rubi, Y.; Jakubek, Z. J.; Chen, M.; Zou, S.; Simard, B. Quality Assessment of Bulk Boron Nitride Nanotubes for Advancing Research, Commercial, and Industrial Applications. *ACS Appl. Nano Mater.* **2019**, *2* (4), 2054–2063. https://doi.org/10.1021/acsanm.9b00057.
(33) Kell, A. J.; Paquet, C.; Mozenson, O.; Djavani-Tabrizi, I.; Deore, B.; Liu, X.; Lopinski, G. P.; James, R.; Hettak, K.; Shaker, J.; Momciu, A.; Ferrigno, J.; Ferrand, O.; Hu, J. X.; Lafrenière, S.; Malenfant, P. R. L. Versatile Molecular Silver Ink Platform for Printed Flexible Electronics. *ACS Appl. Mater. Interfaces* **2017**, *9* (20), 17226–17237. https://doi.org/10.1021/acsami.7b02573.
(34) Medina-Gonzalez, Y.; Camy, S.; Condoret, J.-S. ScCO $_2$ /Green Solvents: Biphasic Promising Systems for Cleaner Chemicals Manufacturing. *ACS Sustain. Chem. Eng.* **2014**, *2* (12), 2623–2636. https://doi.org/10.1021/sc5004314.
(35) Heidari, S. M.; Anctil, A. Identifying Alternative Solvents for C60 Manufacturing Using Singular and Combined Toxicity Assessments. *J. Hazard. Mater.* **2020**, *393*, 122337. https://doi.org/10.1016/j.jhazmat.2020.122337.
(36) Oracz, P.; Kolasi, G. TOTAL VAPOUR PRESSURE MEASUREMENTS FOR BINARY MIXTURES OF METHANOL, ETHANOL, 1-PROPANOL AND 1-BUTANOL WITH BENZENE, TOLUENE AND p-XYLENE AT 313.15 K. *Fluid Phase Equilibria* **1987**, *35*, 253–278.
(37) Oswal, S.; Rathnam, M. V. Viscosity Data of Binary Mixtures: Ethyl Acetate + Cyclohexane, + Benzene, + Toluene, + Ethylbenzene + Carbon Tetrachloride, and + Chloroform at 303.15 K. *Can. J. Chem.* **1984**, *62* (12), 2851–2853. https://doi.org/10.1139/v84-482.
(38) Gonçalves, F. A. M. M.; Trindade, A. R.; Costa, C. S. M. F.; Bernardo, J. C. S.; Johnson, I.; Fonseca, I. M. A.; Ferreira, A. G. M. PVT, Viscosity, and Surface Tension of Ethanol: New Measurements and Literature Data Evaluation. *J. Chem. Thermodyn.* **2010**, *42* (8), 1039–1049. https://doi.org/10.1016/j.jct.2010.03.022.

(39) Liu, X.; Li, D.; Fukutani, H.; Trudeau, P.; Khoun, L.; Mozenson, O.; Sampson, K. L.; Gallerneault, M.; Paquet, C.; Lacelle, T.; Deore, B.; Ferrand, O.; Ferrigno, J.; Malenfant, P. R. L.; Kell, A. J. UV-Sinterable Silver Oxalate-Based Molecular Inks and Their Application for In-Mold Electronics. *Adv. Electron. Mater.* **2021**, *7* (9), 2100194. https://doi.org/10.1002/aelm.202100194.

(40) Wagner, K.; Paquet, C.; Martinez-Rubi, Y.; Genest, M.; Guan, J.; Sampson, K. L.; Kim, K. S.; Kell, A. J.; Malenfant, P. R. L.; Lessard, B. H. Boron Nitride Nanotube Coatings for Thermal Management of Printed Silver Inks on Temperature Sensitive Substrates. *Adv. Electron. Mater.* **2021**, *7* (5), 2001035. https://doi.org/10.1002/aelm.202001035.

Chapter 5. Improving printed and thermoformed conductors on polycarbonate with a BNNT thin film interlayer for next-generation in-mold electronics

This chapter is adapted from work submitted to "Advanced Electronic Materials": Wagner, K.; Kell, A. J.; Liu, X.; Gaburici, L.; Manion, J.; Paquet, C.; Lessard, B.H. Improving printed and thermoformed conductors on polycarbonate with BNNT a thin film interlayer for next-generation in-mold electronics. Advanced Electronic Materials, Submitted Manuscript.

5.1. Context

In this work, the mechanical durability and thermal conductance of the green-solvent BNNT interlayer studied in **Chapter 4** was applied to thermoforming applications to improve in-mold electronics performance. When transitioning from a 2D printed feature to a 3D structure, insight into how the ink and substrate simultaneously elongate was studied to maintain and maximize electrical performance as defects were introduced in the features. Incorporating the BNNT interlayer explores its usefulness as a buffer layer between the substrate and trace and develops a correlation between changes in electrical performance and substrate thinning during the thermoforming process. Furthermore, varying trace designs and thermoforming angles provided insight into how the change in percent elongation of the traces have on its' morphology and stability. In addition to electrical performance, the heat dissipation properties of BNNTs were once again studied similar to **Chapter 2**, focusing on how hot spot formation changes at defect points in the trace when the BNNT interlayer is included.

5.2. Contributions

I led the preparation and deposition of the BNNT interlayer, and Dr. Liu prepared the ink formulation used in this study. I printed, processed, and thermoformed the traces alongside optimization assistance from Dr. Kell, Dr. Liu, and Dr. Paquet. I completed electrical and thermal characterization and captured qualitative microscope images and SEM images alongside Mrs. Gaburici. I compiled and visualized data for the discussion section, and Dr. Manion completed all 3D renders of the thermoformed features. I wrote the manuscript with assistance from Dr. Kell, Dr. Paquet, Dr. Manion, and Dr. Lessard.

5.3. Abstract

The processes of thermoforming 2D printed electronics into 3D structures can introduce defects that compromise the electrical performance of in-mold electronics. Furthermore, printed and thermoformed electronic features are susceptible to thermal failure during high electrical power use due to temperature limitations of the thermoplastic substrates. We therefore report the use of a thin film boron nitride nanotube (BNNT) interlayer to directly reduce heat stress on linear and serpentine metallic traces on polycarbonate substrates thermoformed to spherocylindrical geometries at varying elongation percentages. We demonstrated that the BNNT interlayer helps to improve electrical conductivity of the traces along extreme elongation points, correlating substrate thinning to changes in resistance across the feature. Upon applying voltage, traces with the BNNT interlayer experience lower local temperatures at defects that create hot spots, delaying the traces from overheating and ultimately achieving a higher relative current carrying capacity. Thermoformed traces with the BNNT interlayer withstood a significantly higher output temperature, achieving almost 200˚C of generated heat, over 1.5 times higher than thermoformed traces on bare substrates. Overall, this study demonstrates the use of BNNT interlayers to facilitate more reliable and higher performing conductive metal traces for 3D electronics.

5.4. Introduction

Recent interest in 3D electronics has garnered motivation to move away from complex and costly printing techniques that deposit inks directly on 3D parts, such as aerosol jet and multi-axial direct ink writing, to low cost in-mold electronics fabrication.[1,2] When optimized using techniques with low-cost and low energy requirements, the resulting 3D architectures enable new unconventional applications which can expand how printed electronics are designed and integrated into everyday items for automotive,[3–5] aerospace,[6] packaging,[7–9] and medical device industries.[10,11]

In-mold electronics (IME) enable manufacturing of 3D electrical features without having to physically print in the third dimension. In one approach, IME uses thermoforming to convert heat-mouldable 2D substrates that have printed traces on their surfaces into 3D shapes. Once the printed ink has been processed into functional traces, the substrate is brought above its glass transition temperature (T_g), and is vacuum formed over a positive mould until it cools.[12] Traces printed onto the substrate are stretched alongside the substrate, as it accommodates the change in shape and volume transitioning from the 2D to the 3D, increasing susceptibility to failure due to

cracking of the conductive traces. Traces printed with traditional flake- and particle-based inks rely on contact of the metal particles to ensure a conductive feature, however as the substrate stretches during the thermoforming process, cracks form in the trace, breaking the metal-metal contact and rendering the trace non-conductive post-thermoforming.[13]

Molecular inks (MINK) are a class of conductive inks that are formulated with metal precursors. These inks are printed such that the metal precursor remains in its molecular state but can be processed into a metallic film during the thermoforming process. The advantage of using MINKs during thermoforming is that the ink trace will remain partially liquid as it undergoes the thermoforming process, allowing the ink to flow, remain crack-free and maintain its' conductivity following conversion to a 3D silver trace.[13] It must be noted that there are specific locations where substrate and traces elongate during the thermoforming process. Both the substrate and the traces in these elongated areas are thinner than the surrounding areas resulting in localized areas of higher resistance. This can cause localized temperature increases when large currents are applied to 3D circuits, and this bottleneck results in the trace material overheating and eventually melting/burning the underlying substrate, rendering the trace non-conductive.[14] Interlayers have been previously incorporated into printed device structures to improve performance,[15–17] thermal capacities,[18,19] and mechanical integrity,[20,21] however their benefits have not been extensively studied in the context of 3D electronics produced from thermoforming techniques. In recent studies, nano-thin interlayers of boron nitride nanotubes (BNNTs) were shown to improve current carrying capacity, overall thermal management capabilities, and mechanical durability of 2D printed electronics structures.[19,22] In the context of thermoforming, the BNNT properties should provide a level of thermal protection for generated conductive heat in the trace, contributing to reducing heat accumulation in areas where the conductive trace has thinned creating hot spots during use, therefore improving the trace operability over time. Thermoforming also causes strain on the traces because of the elongation required to produce 3D features from the original 2D structures. We have previously demonstrated incorporating BNNT interlayers between plastic substrates and conductive traces produced from MINK, enabling the traces to accommodate mechanical stresses related to repeated bending/flexing in comparison to the bare substrate. It is also of interest to understand if similar mechanical benefits are present for thermoformed MINK traces on BNNT interlayers and lead to improvements in the electrical properties of 3D traces.

This work reports the first use of a BNNT interlayer as a mechanical and thermal barrier to improve the electrical properties of thermoformed silver MINK traces printed on polycarbonate (PC) substrates. The high thermal conductivity and mechanical durability of the random network of BNNTs provides reinforcement to the printed traces upon intense deformation and elongation during the thermoforming process. The thermal dissipative properties of the nanotube network reduced hot spot formation at visible elongation points, leading to higher current carrying capacities of traces with the BNNTs present upon applying voltage.

5.5. Experimental Methods

5.5.1. BNNT dispersion and deposition

Boron nitride nanotube (BNNT) material and powdered polyvinyl butyral (PVB) was added to ethanol (EtOH) as a green-solvent stable BNNT dispersion. Details about the dispersion fabrication are available in work completed by Wagner *et al*.[23] This PVB:BNNT solution was spray-coated onto clean polycarbonate using an Iwata Eclipse HP-CS Gravity Feed Dual Action Airbrush and IS850 Smart Jet Compressor. During the spray-coating process, the substrate was placed on a heated platform set to 50˚C to assist in solvent evaporation. To ensure an even coating of nanotubes, the entire substrate was coated using a back-and-forth motion while moving down the substrate to avoid overlap. Once the solvent was dried, the substrate was rotated 90˚ and the process was repeated until 6 layers of nanotubes were deposited onto the substrate. Additional trials with 4-, 8-, and 10-layer samples were investigated, however 6 layers proved to be the optimal thickness.

5.5.2 Screen printing and thermoforming

Silver (Ag) molecular ink (MINK) was prepared using silver oxalate and an amino-based carrier. Further details about the ink synthesis and characterization can be found in work previously published by Liu *et al*.[13] The ink was stored at -15˚C and warmed to room temperature prior to printing. When the ink reached room temperature, it was screen-printed onto both bare and BNNT-coated polycarbonate (PC) substrates. After printing, the samples were immediately passed three consecutive times through a UV conveyor (America Ultraviolet^{TM}, 170 cm conveyor length) fitted with a gallium lamp and an iron lamp as described by Liu and coworkers.[13] Both lamps are set to mid-level intensity and the conveyor speed set to 30 feet per minute (FPM). Spectral data for one pass under both lamps at 30 FPM was measured using an EIT UV Power Puck II radiometer and

is tabulated in **Table 5.1**. Samples are thermoformed directly after the UV processing using a Formech 450DT thermoformer. Traces printed on PC substrates, both bare and BNNT-coated, are placed under the thermoformer heating element and exposed to 70% heat intensity for 50s. The heating element is removed, and the mould is immediately brought up until the mould platform is flush with the substrate. A vacuum is then applied to seal the substrate to the mould, and it is allowed to cool to room temperature before being removed from the mould. Temperature analysis of the substrate undergoing thermoforming was conducted using a Bokar XTC-Profiler fitted with 6 thermocouples, and corresponding XTC-Profiler software to correlate set power intensity and corresponding the maximum temperature the substrate reaches under these conditions. The change in temperature over 50s under 70% power is presented in the ESI under **Figure 5.6**.

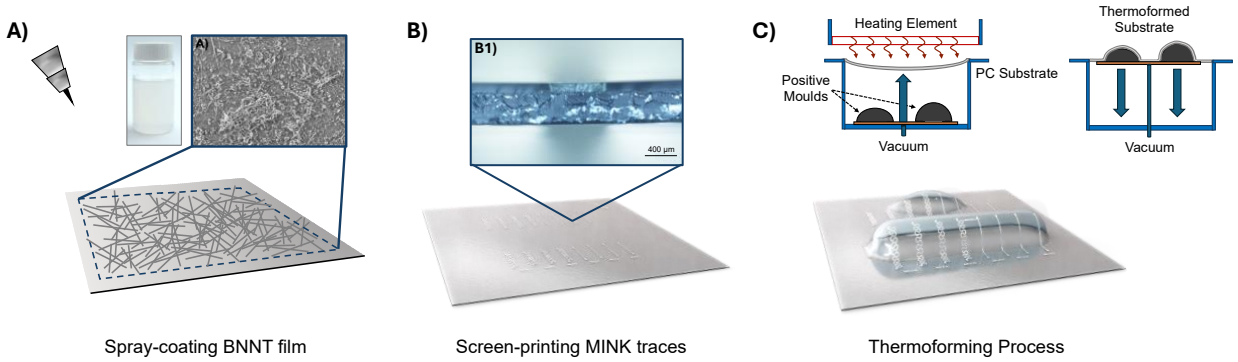

Figure 5.1. Schematic of A) spray-coating of the BNNT suspension onto bare PC substrates with inset SEM of the BNNT film (A1) B) 2D screen printing technique used to deposit the MINK onto the PC substrate, and C) thermoforming of the traces into 3D spherocylinder forms

5.5.3. Characterization

Resistance measurements were gathered using a Fluke 177 True RMS Multimeter. Measurements were taken from the printed electrical pad to ensure proper contact between the probes and the trace. The extent of elongation was manually measured across 25 data points using a ruler with a resolution of 0.5 mm to assess the change in length upon thermoforming. Current carrying capacity testing was completed using a Global Specialties 1325 voltmeter attached to the multimeter and alligator clips attached to the printed electrical pads to apply current. Starting at 1.0 V, a step increase of 1.0 V was applied to the traces every 60 s until the traces were no longer able to pass current and became non-conductive. Once stable, the measured current at each step

increase was also recorded. A thermal camera (Jenoptik Optical Systems) was used to capture the heat map images, taking photos every one second for the duration of the current carrying capacity (CCC) measurements, and then until the traces returned to room temperature. A Nikon SMZ800 DS Camera stereomicroscope fitted with a MKII fiber optic light was used to obtain surface images of the traces post-thermoforming, and an SU3500 scanning electron microscope gathered images of the nanotube interlayer and high magnification images of the traces post-thermoforming.

5.6. Results and Discussions

Thermoforming allows for the fabrication of 3D electrical interconnects from 2D thermoplastic substrates in a simple and accessible manner. A variety of 3D geometries can be conformed with thermoforming to yield desirable shapes for low-cost and scalable applications. However, upon translating the 2D substrate to 3D, the printed components and substrate must both stretch to accommodate the change in geometry.[24] It is therefore important to understand how the desired shape and angles of the moulds impact electrical properties of the elongated printed features on the 3D object, particularly their effect on current carrying capabilities of the stretched features. The highest point of elongation, visible where the substrate physically transitions from 2D to 3D, is a typical failure point in thermoformed traces using commercially available inks designed for these applications. The ability for traces made with MINK to maintain end-to-end conductivity upon thermoforming (even at elongations as high as 50%) highlights it as an ideal material for thermoforming applications. Combining MINK with the BNNT interlayers increases the mechanical and thermal stability of the conductive traces and subsequently improves electrical performance post-thermoforming.

As thermoforming angles and the height of the 3D feature increase, printed traces tend to become less conductive, due to subsequent thinning and/or cracking of the trace at the points of extreme elongation as the substrate is stretched more significantly. Therefore, it is important to correlate the thermoforming angle with substrate elongation upon thermoforming.[25] To better understand how the shape and height of the mould stretches the PC substrate, bare substrates were subjected to thermoforming angles of 17.5˚, 35.0˚, and 70.0˚ using spherocylindrical shapes. As shown in **Figure 5.2A**, a 5.0 cm x 20.0 cm rectangular grid was hand-drawn with 0.2 cm x 0.2 cm squares on a bare PC substrate directly on the area where the traces are printed. The marked substrate was then thermoformed and the change in square width was measured to collect percent

elongation data. Mould angles of 17.5˚ and 35.0˚ display changes in percent elongation of up to 13.3% and 23.3% elongation, whereas mould angles of 70.0˚ begin to show significant change in percent elongation, reaching up to 36.7%. This is further visualized in **Figure 5.2B** and **5.2C** which show a 3D render of the change in percent elongation at the 70.0˚, 35.0˚ and 17.5˚ respectively, as well as a quantified plot detailing the exact change in percent elongation in **Figure 5.2D**. This range provides insight into the level of deformation the traces undergo, particularly at the 2D to 3D transition point, where the percent elongation is highest and where conductivity is the most impacted. In addition to varying thermoforming angle, two different trace designs, linear traces with a nominal line width of 10 mil (254 μm) and serpentine traces with a nominal line width of 20 mil (508 μm), were subjected to each thermoforming angle deformation. Serpentine lines have been demonstrated to better accommodate natural deformation under stretching than linear traces because they can twist and buckle under strain. These different trace geometries will provide a good comparison of how different trace geometries impact thermoforming.[26]

5.6.1 Electrical Properties

During the thermoforming process, the substrate is stretched, and the point of highest elongation is created at the junction transitioning from the flat substrate to the curved substrate. It is also noteworthy that the extent of elongation increases as the angle and height of the mould increases. The electrical resistance is measured for both linear and serpentine traces after being subjected to thermoforming over moulds with 17.5, 35.0 and 70.0˚ mould angles and the data is presented in **Figure 5.2E** and **5.2F**, respectively. As shown with the linear traces, resistance values are similar both with and without the BNNTs present at lower mould angles, however with a 70.0˚ deformation, the traces on the BNNT interlayer have lower resistances than those without the BNNT interlayer. Corresponding standard deviations on the resistance measurements also show a smaller discrepancy when BNNT interlayers are present. In a similar result, the serpentine traces exhibit overall lower resistance values with BNNTs present, however with more similar consistent deviation than with the linear lines. Interestingly the benefit of using BNNTs is statistically significant with mould angles of 35.0˚ and 70.0˚ when using serpentine traces whereas it is only the case for 70.0˚ when using linear traces. In previous work, the inclusion of the BNNT interlayer has been demonstrated to alleviate mechanical stress imparted on 2D screen printed silver MINK, enabling the traces to better withstand repeated flexing/bending with little change in resistance.[19,23]

We suggest that the lower resistance values measured for the thermoformed traces on the BNNT layer in comparison to the bare substrate may also be due to this improved mechanical stability. Whereas physical separation between substrate and silver trace would be evident, the BNNT interlayer provides a buffering the strain exerted on the traces following elongation in a manner similar to that demonstrated for the 2D traces, again resulting in lower resistances and allows the trace to thin without compromising the electrical performance.

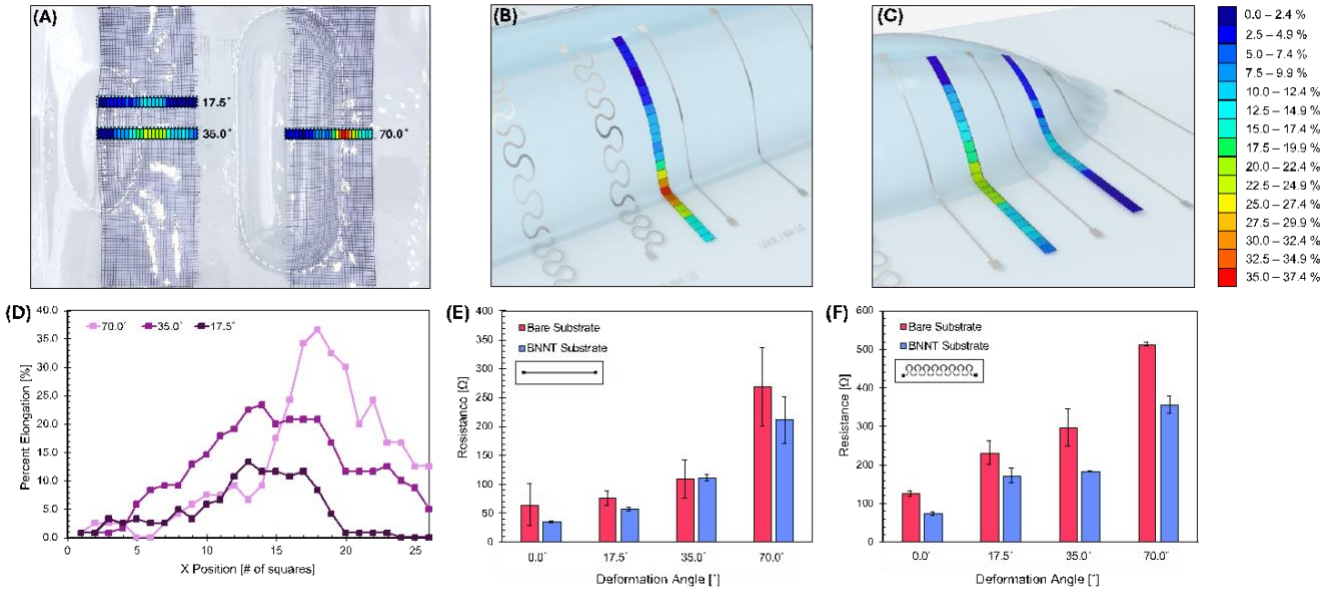

Figure 5.2. A) Photograph highlighting the points of elongation measured. Schematic visualizations of B) 70˚ and C) 35˚ and 17.5˚ samples. D) Percent elongation calculated using a running average, and E) resistance measurements of straight traces and F) serpentine traces subjected to each elongation angle with standard deviation error bars.

To better understand what morphological changes occur in the traces during the thermoforming process, the correlation between the electrical resistance and the thickness of the substrate is explored in **Figure 5.3**. The resistance of the trace was measured in 2.5 mm intervals totalling 15 sections across the length of each trace, and the change in the resistance between each section was calculated and recorded. A digital caliper with an accuracy of 0.01 mm was used to measure the change in substrate thickness, where 100% was the substrate's nominal width of 0.5 mm, and subsequent percentage decreases represent the remaining substrate thickness post-thermoforming. **Figure 5.3A and 5.3B** provide a comparison for linear traces on bare and BNNT-

coated traces respectively, thermoformed over the mould with 70˚ angles to best highlight the effects of thermoforming on the traces. A clear correlation between the change in resistance and substrate thickness exists and illustrates that the traces are most affected in the areas that undergo the greatest elongation. This is particularly evident in the areas where the substrate thickness falls below 85% of its original thickness and the resistance reaches a maximum. While the change in electrical resistance is similar between the linear traces, there is an improvement in the delta change in resistance for serpentine traces printed on BNNT-coated PC against bare PC substrate, as shown in **Figure 5.3C and 5.3D**.

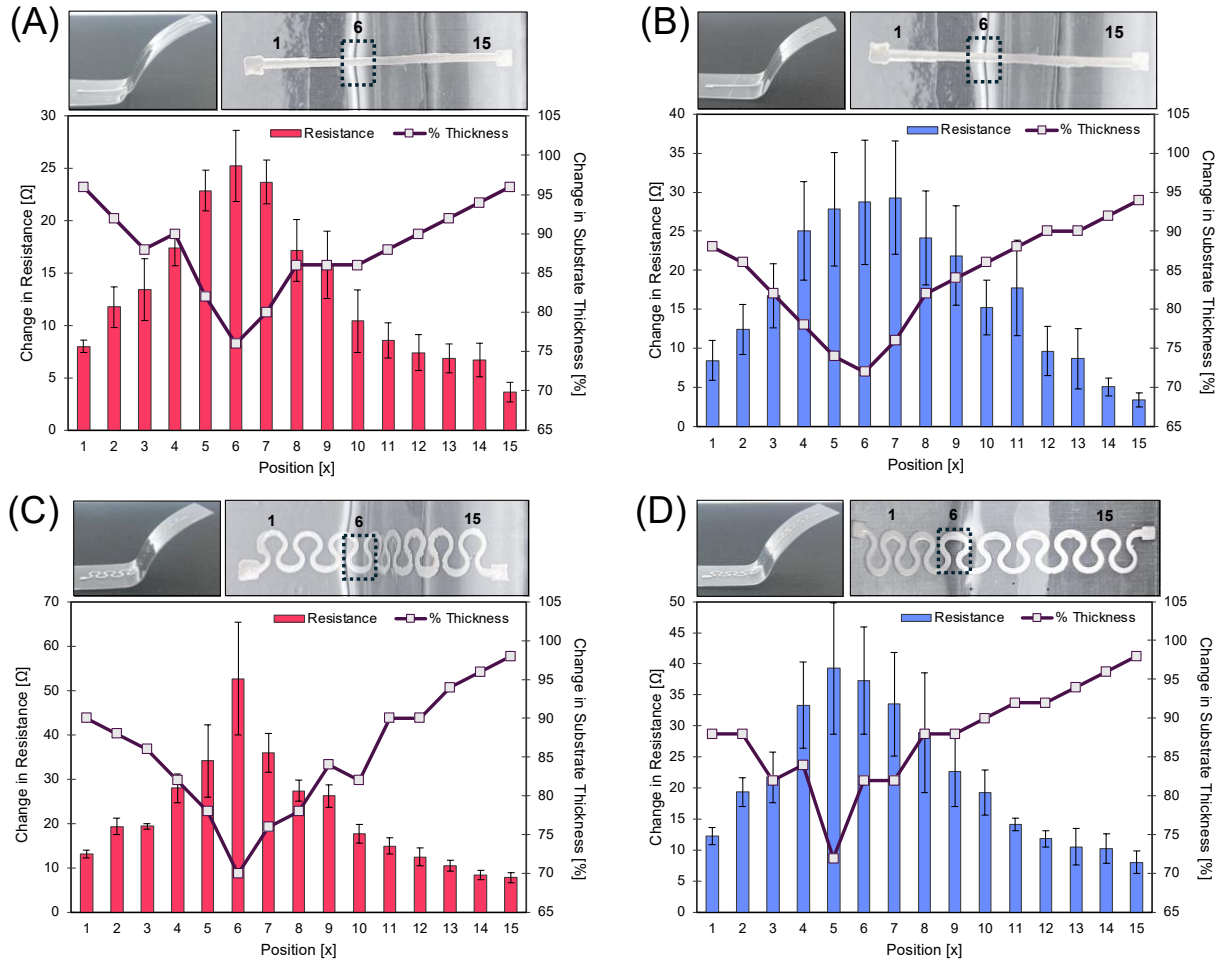

Figure 5.3. Comparison of change in resistance across the trace length against thinning of the substrate upon thermoforming for linear traces on A) bare and B) BNNT-coated substrates and serpentine traces on C) bare and D) BNNT-coated substrates. Sample population for standard deviation calculation is n = 5 for each figure.

SEM images in **Figure 5.7** highlight the elongation point of the linear trace on the BNNT network after thermoforming compared to the bare substrate, where the BNNTs can be observed through the silver ink pores that are present in the traces. These images demonstrate how the BNNTs are well distributed below the traces, which can help provide bridges when the ink is thinned at the inflection point. Furthermore, **Figures 5.8 and 5.9** show microscope images of the thermoformed linear and serpentine traces measured in **Figure 5.3** on either side of the elongation point, particularly the flat section and curved edges. These images confirm no definitive damage across the areas of the trace, indicating that the deformation is localized to the junction point as shown in the SEM.

5.6.2 CCC Testing and Thermal Properties

There are several examples in the literature where functional 3D devices have been produced through thermoforming. These applications typically require quite low currents (powering LEDs), so the localized increases in resistance caused by thermoforming do not negatively impact the device performance. However, it is of interest to understand how thermoforming affects the electrical properties of the traces as increasingly higher currents are applied to them. This is relevant for developing more advanced IME applications that require demanding electrical performance such as heaters and printed power lines to replace wires for driving devices requiring more power than simple LEDS. To understand how thermoforming impacts the electrical performance of the traces, CCC measurements were conducted on the 3D traces on both bare PC and on traces deposited on the BNNT-coated PC. CCC measurements characterize how much current a conductor can withstand before it becomes non-conductive. In the context of printed electronics, the loss of conductivity is typically caused by the underlying plastic substrate warping or more drastically melting, causing a deformation that severs the conductor.[27] CCC measurements are typically recorded for traces printed on plastic substrates, and while printing MINKs in the 2D produces traces with uniform trace thickness and surface roughness, the thinning of the trace upon thermoforming can affect the maximum current that can be carried.

During CCC testing, voltage is applied to a trace, leading to the current increasing and subsequently the temperature of the trace increasing due to Joule heating, which is monitored using an IR thermal camera. The resulting temperature uniformity can be measured and recorded, with regions where the trace is thinner creating hot spots that can be visualized as a likely point of failure and indication that the CCC has been reached. **Figure 5.4** presents the CCC measurements

on a straight and flat trace acting as a control and compares them to a straight and serpentine trace elongated over a spherocylinder mould with a 70.0˚ angle, as well as the corresponding maximum temperature at each applied voltage. It should be noted that traces with very similar resistances were chosen to isolate the effects of the BNNT interlayer. Traces were subjected first to 1.0 V, which was then increased at increments of 1.0 V held for 60 s each, until the measured current fell to 0 mA, indicating the traces were no longer conductive. In this context, the CCC is defined as the ability for the trace to maintain its current for the entirety of its 60s interval. Furthermore, the point of failure (POF) is defined as the highest recorded current one second before the trace fails. The voltage value presented for the POF is higher than the reported CCC, as it represents a voltage at which the trace failed prior to completion of the 60s interval. **Figure 5.4** shows thermal images corresponding to the images taken during the CCC tests, providing insight into the quality of the trace printed on bare and BNNT coated substrates during stable operation, as well as the measured maximum temperature of the hotspots that led to failures in the trace at the POF voltage. As expected, when 2D traces of the MINK are characterized on both bare PC and over the BNNT interlayer in **Figure 5.4A**, the CCC and resulting temperature of the traces are uniform and can reach temperatures close to the T_g of the PC substrate ($T_g \approx 140$˚C) at which time the traces burn out because the underlying substrate deforms and the traces become non-functional. Consistent with our previous reports, the maximum temperature that the traces can reach before melting is higher for the traces printed on the BNNT interlayer in comparison to the bare substrate. Additionally, the CCC of the control trace is almost identical to the BNNT samples until 5 V, where the CCC and maximum temperature for the trace printed on BNNT coated substrates began to increase above that printed on bare coated substrates. This phenomenon can be attributed to the BNNTs assisting in ohmic sintering of the traces, where a decrease in the resistance of the traces upon increasing applied voltage was measured, which ultimately led to a higher temperature output. [23] We have reported this previously for a similar molecular ink printed with the BNNT interlayer on PET substrates. As shown in Figure 3, thermoforming produces localized areas of higher resistances at the site of elongation for 3D traces. It has been previously reported that electron flow (i.e. current) in less efficient through areas of higher resistance, and the restricted electron flow causes localized temperature increases. The hotspot created in the area of elongation s likely to be a failure point in theses CCC experiments. However, we expect the BNNT interlayer

to provide a level of protection between the substrate and the trace to act as a heat dissipator and reduce thermal stress at the harsh elongation points compared to bare substrates.

Figure 5.4B shows the CCC measurements for the straight trace printed on PC with the BNNT interlayer and thermoformed using a mould with 70˚ angles, resulting in an improvement in both the CCC and the ability for the substrate to withstand temperature increases that occur when high currents are applied. Comparing traces of similar measured resistance, the trace printed on BNNT coated substrates outperforms the trace without, leading to operation up to 13 V whereas the traces on bare substrate reach their CCC at 9 V. Furthermore, the thermal conductivity of the BNNTs assists in reducing the temperature accumulation at the most significant elongation point, as evident by the lower maximum temperature at each applied voltage until failure. This can be attributed to the BNNTs' acting as a buffering layer to dissipate generated heat across the nanotube intersections and away from the trace, so the PC substrate no longer softens and deforms the silver trace, instead allowing the trace to operate for longer before failing. A similar comparison is done on serpentine trace that have also been thermoformed with a spherocylinder shaped mould with a 70.0˚angle in **Figure 5.4C**. While not as pronounced, a similar trend is observed with the serpentine traces, where those printed on BNNT coated substrates exhibit lower maximum temperature at the inflection point and ultimately can withstand more current, failing at 15 V whereas the bare substrate counterparts fail at 13 V. The improvement in CCC values and operating temperature/voltage is improved using BNNT interlayers both in 2D and 3D printed silver traces.

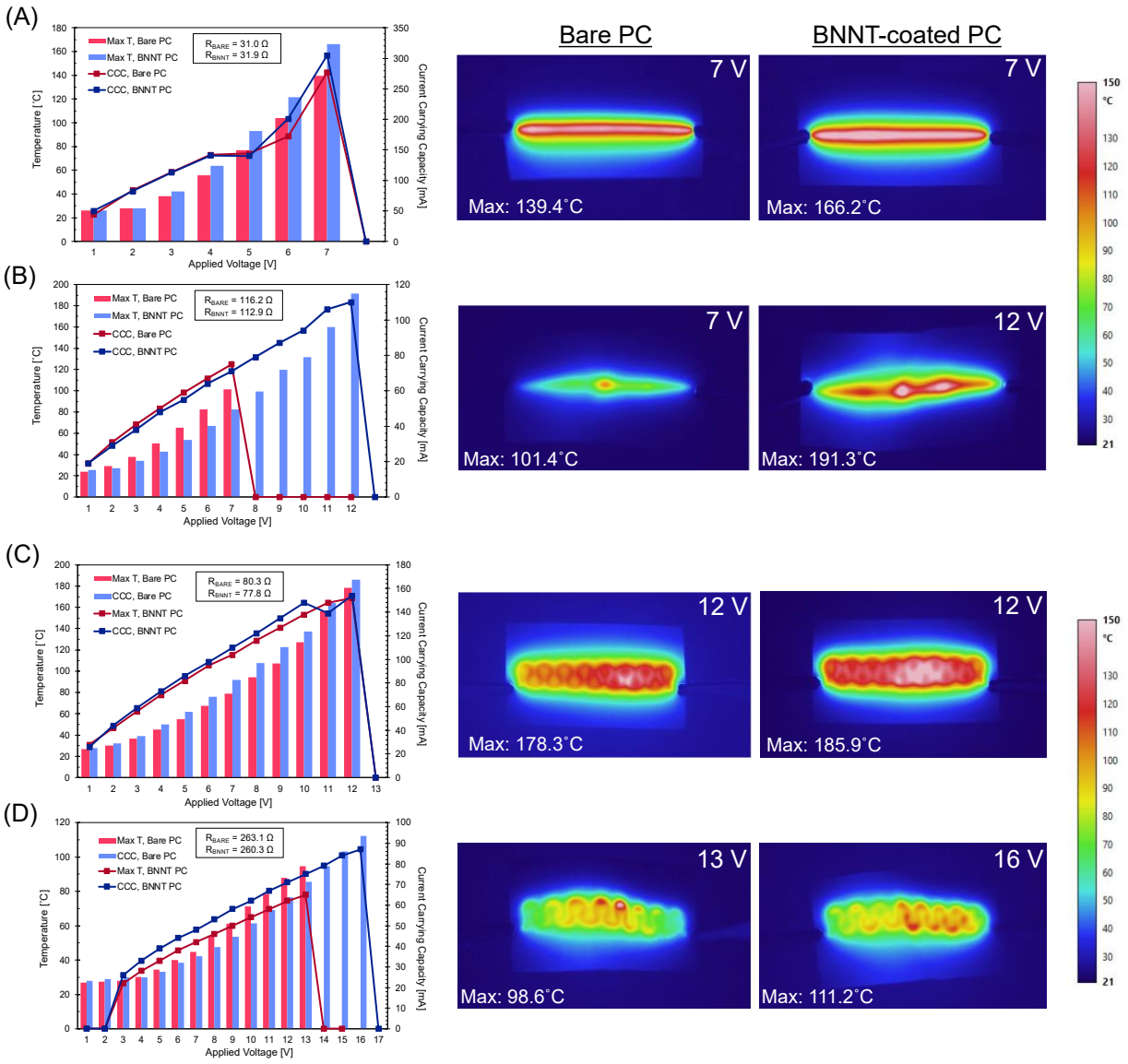

Figure 5.4. Current carrying capacity and corresponding temperature response at increasing applied voltage for straight line traces on A) a flat substrate, B) thermoformed with a spherocylinder shaped mould with a 70.0˚angle, and a serpentine trace on C) a flat substrate D) thermoformed with a spherocylinder shaped mould with a 70.0˚angle comparing traces printed on bare PC and BNNT-coated PC substrates. Applied voltage was maintained for 60s before increasing to the next voltage, at a step size of 1.0 V.

Further insight in the point of failure, found in **Figure 5.5**, is shown through the corresponding trace tested in **Figure 5.4B**. As the highest point of elongation causes a localized

increase in the electrical resistance, the areas of high resistance will cause a higher temperature output due to nonuniform current distribution. There is significant temperature increase present in the region of highest elongation in the trace, and as previously mentioned, exceeding the T_g of the underlying substrate will result in deformation and loss of current because the traces fracture. **Figure 5.5A** is a photograph of the linear trace thermoformed on bare PC shows clear deformation/melting of the substrate leading to cracks that run across the width of the trace. Notably, the damage is localized to this area only no adverse changes to the trace morphology on either side of the hot spot are visible. This once again demonstrates that it is only the point of elongation (and localized high resistance) that causes the temperature increase and trace failure during the CCC experiment for these 3D traces. Similar images in **Figure 5.5B** are produced for the linear trace thermoformed on the BNNT-coated substrate, showing significant warpage/deformation locations overlapping the thermal camera images mapping the highest temperatures with the areas of high as expected. While both sets of traces fail, the traces thermoformed with the BNNT interlayer ultimately fail at higher currents and corresponding higher temperatures because the BNNT network is able to dissipate the generated heat away from the hotspot throughout the nanotubes before affecting the substrate. Therefore, the trace can withstand higher temperatures before failure, even when the traces exhibit near-identical resistance values.

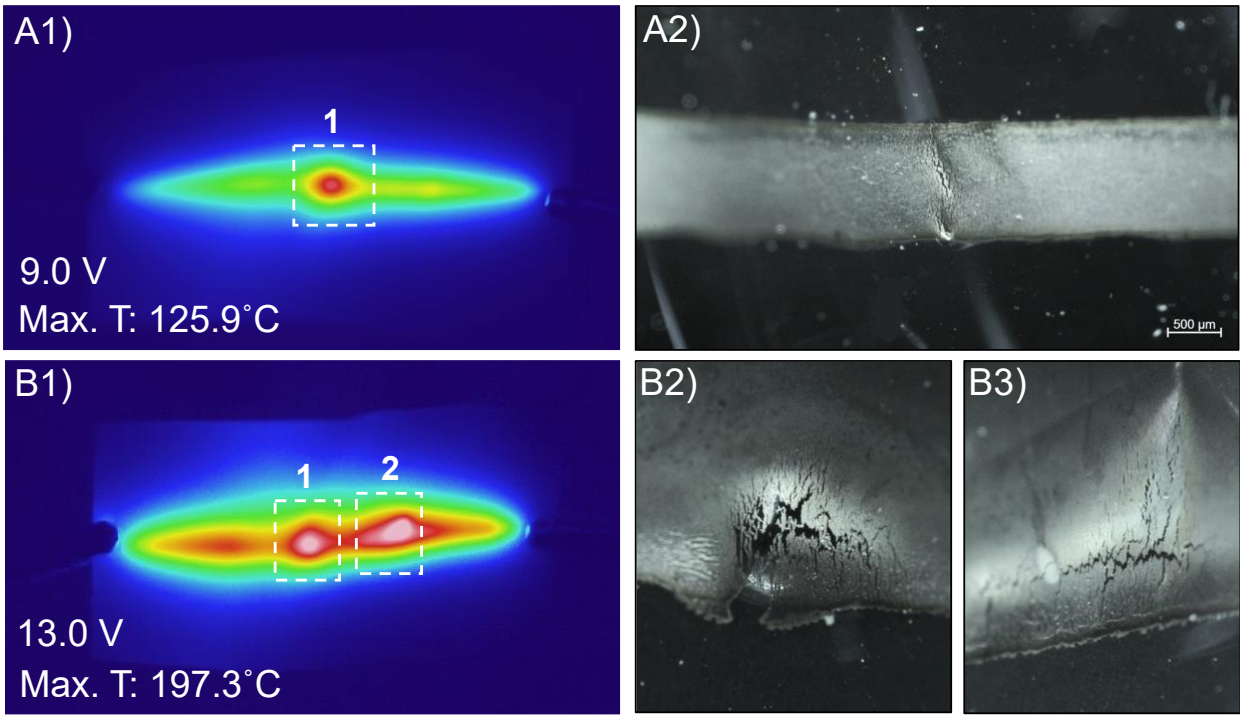

Figure 5.5. Point of failure images of a linear trace thermoformed with a spherocylinder shaped mould with a 70.0˚angle on bare PC substrate with A1) thermal image, A2) corresponding microscope image of failure point, and point of failure images on the BNNT-coated substrate of B1) thermal image and B2,3) corresponding failure point microscope images

5.7. Conclusions

We successfully demonstrated the utility of BNNT interlayers for improving electrical performance of thermoformed traces. We show that regions of high elongation across thermoformed traces cause adverse effects to the CCC of the trace due substrate/trace thinning, resulting in localized high electrical resistance areas, and leading to drastic temperature increases when high currents are applied to the traces. BNNT interlayers assisted in reducing the initial electrical resistance of both linear and serpentine thermoformed traces at nearly all explored thermoforming angles, likely acting as a buffer layer as the traces are stretched. Additionally, thermal dissipation properties of the BNNT network delayed deformation of the underlying substrate caused by heat generated in the trace when subjected to high operational voltages/currents, leading to an increase in CCC of the thermoformed traces when the BNNT interlayer was present. Overall, this study demonstrates the use of BNNT interlayers to improve

the electrical performance of silver MINK traces for IME through thermoforming processes and provide thermal protection when the substrate exceeds its glass transition temperature

5.8. Acknowledgements

This work was supported by the NSERC Green Electronics Network (GreEN) (grant number: NETGP 508526-17). We thank Yadienka Martinez-Rubi and Kim Keun-Su for the BNNTs utilized in this study.

5.9. Supporting Information

Table 5.1. Spectral data for one pass under both the iron and gallium lamps set to medium intensity at 30 FPM was measured using an EIT UV Power Puck II radiometer

Light Wavelength [-]	[mJ/cm^2]	[mW/cm^2]
UVA	767.170	1327.328
UVB	529.607	659.086
UVC	137.968	169.414
UVV	1833.184	2969.880

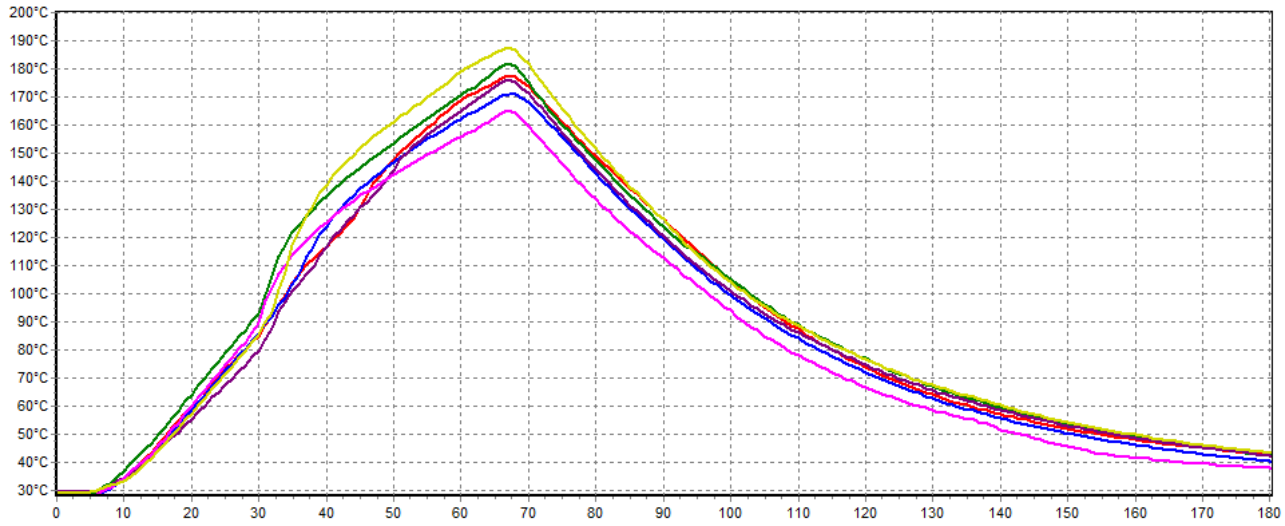

Figure 5.6. Change in temperature at six areas of a 450DT thermoformer, each set to 70% power and exposed for 60s. Measured and plotted using Bokar XTC-Profiler and compatible XTC-Profiler software.

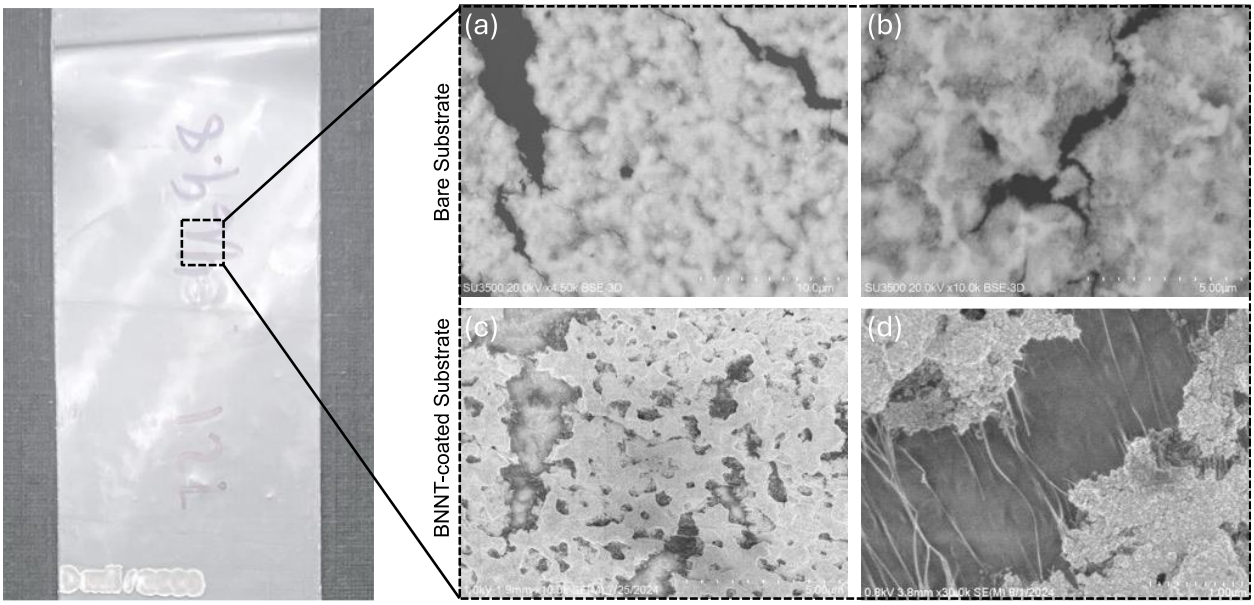

Figure 5.7. SEM images of linear 70˚ thermoformed trace taken at the highest point of elongation, on a bare substrate at (a) 4.50k, and (b) 10.0k magnification, and the trace printed on 6-layer thick spray-coated boron nitride nanotubes on PC substrates, BNNT-coated substrates, highlighting the nanotube network underneath at (c) 10.0k, and (d) 30.0k magnification

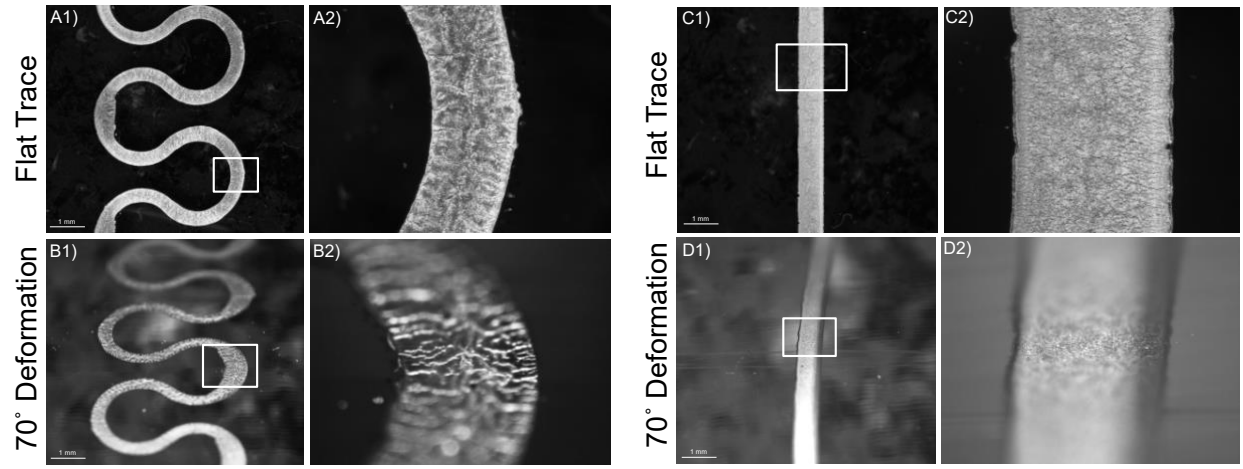

Figure 5.8. Microscope images of Ag MINK printed on bare PC substrates, comparing trace quality after thermoforming on a flat surface or subjected to 40% elongation, or 70˚ deformation. Serpentine traces are shown A) on the flat surface of the substrate and B) along the curved edge of the 3D feature. Straight traces are shown C) on the flat surface of the substrate and D) along the curved edge of the 3D feature. Images denoted with a '1' represent a magnification of 1.0X, and '2' represents a magnification of 6.3X for all presented images.

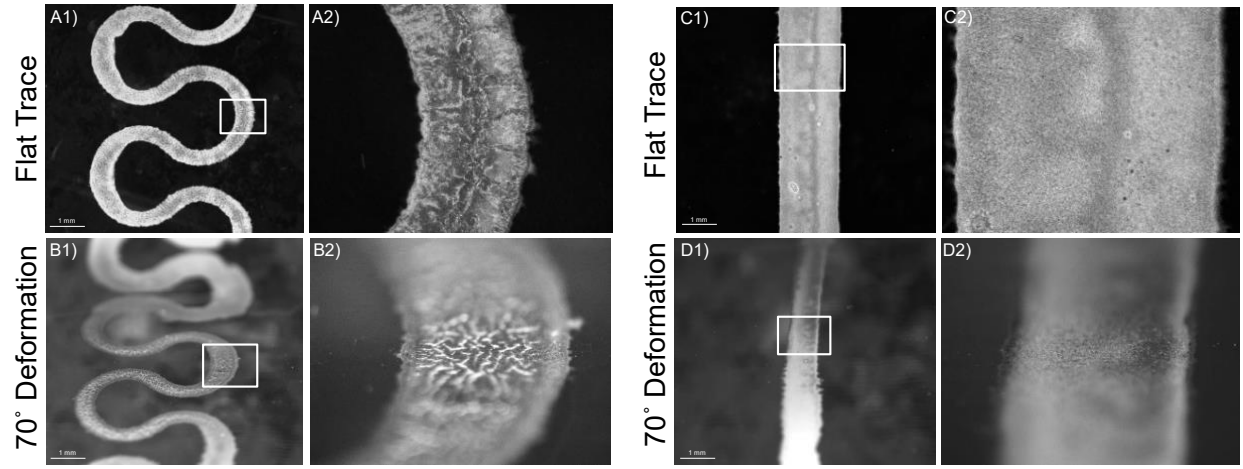

Figure 5.9. Microscope images of Ag MINK printed on BNNT-coated PC substrates, comparing trace quality after thermoforming on a flat surface or subjected to 40% elongation, or 70˚ deformation. Serpentine traces are shown A) on the flat surface of the substrate and B) along the curved edge of the 3D feature. Straight traces are shown C) on the flat surface of the substrate and D) along the curved edge of the 3D feature. Images denoted with a '1' represent a magnification of 1.0X, and '2' represents a magnification of 6.3X for all presented images.

5.10. References

(1) Anas, S.; Khan, M. Y.; Rafey, M.; Faheem, K. Concept of 5D Printing Technology and Its Applicability in the Healthcare Industry. *Mater. Today Proc.* **2022**, *56*, 1726–1732. https://doi.org/10.1016/j.matpr.2021.10.391.

(2) Lai, J.; Wang, M. Developments of Additive Manufacturing and 5D Printing in Tissue Engineering. *J. Mater. Res.* **2023**, *38* (21), 4692–4725. https://doi.org/10.1557/s43578-023-01193-5.

(3) Srinivasan, K.; Muthuramalingam, T. In-Depth Scrutinization of In- Mold Electronics for Automotive Applications. *J. Phys. Conf. Ser.* **2021**, *1969* (1), 012064. https://doi.org/10.1088/1742-6596/1969/1/012064.

(4) Lall, P.; Harsha, A.; Kulkarni, S.; Miller, S. Oscillator Performance on Thermoformed Additive In-Mold Electronics for Automotive Applications. In *ASME 2024 International Technical Conference and Exhibition on Packaging and Integration of Electronic and Photonic Microsystems*; American Society of Mechanical Engineers: San Jose, California, USA, 2024; p V001T06A008. https://doi.org/10.1115/IPACK2024-141877.

(5) Gong, Y.; Cha, K. J.; Park, J. M. Deformation Characteristics and Resistance Distribution in Thermoforming of Printed Electrical Circuits for In-Mold Electronics Application. *Int. J. Adv. Manuf. Technol.* **2020**, *108* (3), 749–758. https://doi.org/10.1007/s00170-020-05377-9.

(6) Barragán, J.; Kell, A.; Liu, X.; Shin, S.; Mandache, C.; Djokic, D.; Bennett, D.; Houlahan, K.; Genest, M.; Lessard, B. H.; Paquet, C. Next-Generation Embedded Printed Sensors for Near-Field Monitoring of High-Performance Composites. *Adv. Eng. Mater.* **2025**, *27* (4), 2401332. https://doi.org/10.1002/adem.202401332.

(7) Valavan, A.; Komolafe, A.; Harris, N. R.; Beeby, S. Vacuum Thermoforming for Packaging Flexible Electronics and Sensors in E-Textiles. *IEEE Trans. Compon. Packag. Manuf. Technol.* **2023**, *13* (5), 715–723. https://doi.org/10.1109/TCPMT.2023.3283015.

(8) Hoffmann, G.-A.; Wienke, A.; Reitberger, T.; Franke, J.; Kaierle, S.; Overmeyer, L. Thermoforming of Planar Polymer Optical Waveguides for Integrated Optics in Smart Packaging Materials. *J. Mater. Process. Technol.* **2020**, *285*, 116763. https://doi.org/10.1016/j.jmatprotec.2020.116763.

(9) Zulfiqar, S.; Saad, A. A.; Sharif, M. F. M.; Samsudin, Z.; Ali, M. Y. T.; Ani, F. C.; Ahmad, Z.; Abdullah, M. K. Alternative Manufacturing Process of 3-Dimensional Interconnect Device Using Thermoforming Process. *Microelectron. Reliab.* **2021**, *127*, 114373. https://doi.org/10.1016/j.microrel.2021.114373.

(10) Zhou, W.; Cheng, F.; Cai, C.; Fu, Y. Bioinspired Dry-State Polylactic Acid Adhesives-Based Wearable Sensor with Reversible Adhesive Performance in Harsh Environments via Building Hierarchical Liquid Metal Bead Structure. *Compos. Sci. Technol.* **2023**, *242*, 110207. https://doi.org/10.1016/j.compscitech.2023.110207.

(11) Gul, J. Z.; Khan, M.; Rehman, M. M.; Mohy Ud Din, Z.; Kim, W. Y. Preparation and Performance Analysis of 3D Thermoformed Fluidic Polymer Temperature Sensors for Aquatic and Terrestrial Applications. *Sensors* **2023**, *23* (20), 8506. https://doi.org/10.3390/s23208506.

(12) Beltrão, M.; Duarte, F. M.; Viana, J. C.; Paulo, V. A Review on In-mold Electronics Technology. *Polym. Eng. Sci.* **2022**, *62* (4), 967–990. https://doi.org/10.1002/pen.25918.

(13) Liu, X.; Li, D.; Fukutani, H.; Trudeau, P.; Khoun, L.; Mozenson, O.; Sampson, K. L.; Gallerneault, M.; Paquet, C.; Lacelle, T.; Deore, B.; Ferrand, O.; Ferrigno, J.; Malenfant, P. R. L.; Kell, A. J. UV-Sinterable Silver Oxalate-Based Molecular Inks and Their Application

for In-Mold Electronics. *Adv. Electron. Mater.* **2021**, *7* (9), 2100194. https://doi.org/10.1002/aelm.202100194.

(14) Yao, L.-W.; Lin, Y.-R.; Lai, C.-C.; Wei, H.-F.; Wang, C.-W. In-Mold Heat Radiating Simulation and Verification of In-Mold Electronics. In *2024 IEEE Intelligent Vehicles Symposium (IV)*; IEEE: Jeju Island, Korea, Republic of, 2024; pp 3030–3034. https://doi.org/10.1109/IV55156.2024.10588735.

(15) Cesarini, M.; Brigante, B.; Caironi, M.; Natali, D. Reproducible, High Performance Fully Printed Photodiodes on Flexible Substrates through the Use of a Polyethylenimine Interlayer. *ACS Appl. Mater. Interfaces* **2018**, *10* (38), 32380–32386. https://doi.org/10.1021/acsami.8b07542.

(16) García-Peña, N. G.; Nabil, M.; Pourjafari, D.; Peralta-Domínguez, D.; Padrón-Hernández, W. Y.; Franco-Bacca, A. P.; Ríos-Flores, A.; Heredia-Cervera, B. E.; Escalante, R.; Rodríguez Gattorno, G.; Acosta, M.; Pistor, P.; Anta, J. A.; Oskam, G. Improving the Performance of Carbon-Based Perovskite Solar Cells by the Incorporation of a Screen-Printed $NiCo_2O_4$ Interlayer. *ACS Appl. Energy Mater.* **2025**, *8* (3), 1446–1457. https://doi.org/10.1021/acsaem.4c01720.

(17) Park, M. J.; Wang, C.; Seo, D. H.; Gonzales, R. R.; Matsuyama, H.; Shon, H. K. Inkjet Printed Single Walled Carbon Nanotube as an Interlayer for High Performance Thin Film Composite Nanofiltration Membrane. *J. Membr. Sci.* **2021**, *620*, 118901. https://doi.org/10.1016/j.memsci.2020.118901.

(18) Tsuruta, A.; Masuda, Y.; Murayama, N. Synthesis of an Effective Interlayer between a Functional Oxide Film and Si_3N_4 Substrate. *J. Ceram. Soc. Jpn.* **2023**, *131* (8), 437–444. https://doi.org/10.2109/jcersj2.23028.

(19) Wagner, K.; Kell, A. J.; Martinez-Rubi, Y.; Paquet, C.; Lessard, B. H. Engineering Silver Microgrids with a Boron Nitride Nanotube Interlayer for Highly Conductive and Flexible Transparent Heaters. *Adv. Mater. Technol.* **2022**, 2200037. https://doi.org/10.1002/admt.202200037.

(20) Domínguez, M. A.; Sosa-Sánchez, J. L. Copper Phthalocyanine Buffer Interlayer Film Incorporated in Paper Substrates for Printed Circuit Boards and Dielectric Applications in Flexible Electronics. *Solid-State Electron.* **2020**, *172*, 107898. https://doi.org/10.1016/j.sse.2020.107898.

(21) Chen, Y.; Zhuang, X.; Goldfine, E. A.; Dravid, V. P.; Bedzyk, M. J.; Huang, W.; Facchetti, A.; Marks, T. J. Printable Organic-Inorganic Nanoscale Multilayer Gate Dielectrics for Thin-Film Transistors Enabled by a Polymeric Organic Interlayer. *Adv. Funct. Mater.* **2020**, *30* (40), 2005069. https://doi.org/10.1002/adfm.202005069.

(22) Wagner, K.; Paquet, C.; Martinez-Rubi, Y.; Genest, M.; Guan, J.; Sampson, K. L.; Kim, K. S.; Kell, A. J.; Malenfant, P. R. L.; Lessard, B. H. Boron Nitride Nanotube Coatings for Thermal Management of Printed Silver Inks on Temperature Sensitive Substrates. *Adv. Electron. Mater.* **2021**, *7* (5), 2001035. https://doi.org/10.1002/aelm.202001035.

(23) Wagner, K.; Zou, S.; Martinez-Rubi, Y.; Kell, A. J.; Paquet, C.; Lessard, B. H. Towards Sustainable Transparent Flexible Heaters: Integration of a BNNT Interlayer Using Green Solvent Substitution. *Flex. Print. Electron.* **2023**, *8* (2), 025005. https://doi.org/10.1088/2058-8585/acc9d2.

(24) Chtioui, I.; Bossuyt, F.; de Kok, M.; Vanfleteren, J.; Bedoui, M. H. Arbitrarily Shaped Rigid and Smart Objects Using Stretchable Interconnections. *IEEE Trans. Compon. Packag. Manuf. Technol.* **2016**, *6* (4), 533–544. https://doi.org/10.1109/TCPMT.2015.2511077.

(25) Arias-García, F. I.; Lozano-Hernandez, N.; Ruldua, M. L. M.; Baig, E. F. Effect of Epoxy Conductive Adhesive on Film Deformation During the Thermoforming Process for In-Mold Electronic Devices. *Adv. Mater. Technol.* **2024**, 2401026. https://doi.org/10.1002/admt.202401026.
(26) Park, S.; Ban, S.; Zavanelli, N.; Bunn, A. E.; Kwon, S.; Lim, H.; Yeo, W.-H.; Kim, J.-H. Fully Screen-Printed PI/PEG Blends Enabled Patternable Electrodes for Scalable Manufacturing of Skin-Conformal, Stretchable, Wearable Electronics. *ACS Appl. Mater. Interfaces* **2023**, *15* (1), 2092–2103. https://doi.org/10.1021/acsami.2c17653.
(27) Alhendi, M.; Sivasubramony, R. S.; Weerawarne, D. L.; Iannotti, J.; Borgesen, P.; Poliks, M. D. Assessing Current-Carrying Capacity of Aerosol Jet Printed Conductors. *Adv. Eng. Mater.* **2020**, *22* (11), 2000520. https://doi.org/10.1002/adem.202000520.

Chapter 6. Conclusions and Future Work

6.1 Overall Conclusions

The application of BNNTs as an interfacial layer for the thermal management of molecular ink-based printed electronics is an effective strategy for improving both fabrication and operational capabilities of 2D and 3D printed traces. The inherent thermal conductivity and mechanical properties of a randomized nanotube network supported heat dissipation on temperature-sensitive thermoplastic substrates, as well as improved flexibility and increased electrical performance of visible stress points within trace electrodes and transparent heater architectures.

In **Chapter 2** of this thesis, we explored the efficacy of the BNNT interfacial layer to mitigate thermal damage upon thermoplastic substrates as a consequence of high energy processing to sinter 2D printed MINK traces into conductive features. This work observed the effects of varying surface concentrations of the BNNT interfacial layer across a range of applied intense pulsed light energies to optimize the effect of the BNNTs thermal dissipation techniques, confirming that a high surface concentration of 142 mg mL^{-1} provided optimal protection to prevent the heat generated in the trace from dissipating into the underlying substrate. Qualitative images demonstrated that the BNNT interlayer successfully retained the desired morphological traits of the printed trace, subsequently maximizing its' inherent conductive performance as well as its' current carrying capacity. Furthermore, exploring a range of trace widths demonstrated that the higher surface concentrations of the BNNT interlayer successfully converted the thinner traces that otherwise would have remained non-conductive post-sintering due to the morphological changes of the small material platform. Finally, temperature decay analysis confirmed that traces printed on higher BNNT surface concentrations achieved a higher rate of cooling. This work served as a first demonstration of the BNNT interlayer as a protective coating for thermoplastic substrates during the fabrication of traces using high energy processing techniques favourable in high-throughput electronics fabrication.

In **Chapter 3** of this thesis, we applied the thermal dissipative properties studied in **Chapter 2** towards an operational application to improve the heating quality of transparent heaters. This work pushes the boundaries of more complex printed designs, and as such microgrid electrodes were utilized in this study as the transparent heater architecture. Initial design

parameters of square and hexagonal geometry as well as optimization of ultraviolet curing techniques were explored to simultaneously maximize transparency and conductive performance. Once optimized, the highly concentrated BNNT interlayer film was integrated between the grid electrode and the thermoplastic substrate. Upon applied voltage, thermal imagery and analysis observed a higher and more uniform temperature output across the grid electrode with the BNNT interlayer present. As the BNNTs are particularly useful in dissipating heat away from the trace-substrate interface as shown in **Chapter 2**, an increase in the temperature output was unexpected. Additional exploration of the electrical properties revealed that the heat accumulated in the BNNTs was providing tertiary sintering to the grid electrodes, and as such the conductivity of the trace increased after applied voltage. This higher conductivity led to the higher power output and ultimately the higher temperature observed, in addition to the heat spreading capabilities of the BNNT network providing a more even heat distribution across the heater architecture. Similar analysis on the morphology of the traces pre- and post-operation confirmed that the BNNTs once again reduce warpage of the substrate and trace, likely maintaining performance metrics and contributing to the improved temperature output. This work also expanded on how the mechanical durability of the BNNTs could assist in removing stress imparted on the traces when flexed. Tensile bending cycles and crease testing confirmed a slower change in the resistance with electrodes where the BNNTs were incorporated.

In **Chapter 4** of this thesis, we investigated the substitution of chlorinated solvents for alcohol solvents as a dispersive medium in the BNNT solution, to provide thermal management solutions towards chemically sensitive printed device materials. The traditional chloroform solvent was exchanged for ethanol, and the dispersive polymer was changed from P3HT to PVB to ensure compatibility with the new solvent system. Fundamental changes in the solvent interactions were extensively analyzed on the previously explored electrical, thermal and mechanical properties discussed in **Chapter 3**. Initial exploration of the BNNT film itself produced similar surface roughness values through AFM measurements, however higher standard deviation on the BNNT-PVB film was calculated. Near identical surface energies were observed using contact angle measurements, and morphological analysis of the printed trace indicate very similar conductive and profilometric analyses post-processing, owing to the secure underlying nanotube network. Tensile bend testing revealed an identical failure point between the two systems, and voltage application achieved a uniform temperature distribution when 2D and while flexed. Finally, on/off

response testing revealed a stable temperature response for 60s intervals over a 30-minute timeframe, highlighting the longevity of the heater architecture on flexible substrates and confirming that the EtOH-PVB system is a suitable replacement for the chlorinated solvent.

Finally, in **Chapter 5** of this thesis, we explored the use of the BNNT interfacial film to reduce stress imparted on individual linear and serpentine traces exposed to thermoforming as a method of transitioning 2D printed electronics into conductive 3D features. This work demonstrated that at high thermoforming angles, the inclusion of the BNNT interlayer improved the metal-to-metal contact at harsh elongation points, demonstrating improved morphology and mechanical durability of the traces as the underlying substrate is stretched. This was corroborated by electrical characterization, showing a lower change in resistance as the substrate is thinned when the BNNT interlayer is present, as well as less variation across samples. This improved electrical performance translated well into thermal analysis, demonstrating that thermoformed traces experienced lower hot spot formation at the inflection point, which led to higher current carrying capacity.

Overall, this thesis demonstrates novel applications of BNNT thin interfacial layers for use in printed electronics. We fabricate, optimize and conclude that when using molecular inks, the BNNT layers improves the fabrication and operation of printed electronic features by increasing the thermal management and the mechanical properties of the final traces in both screen printed and thermoformed parts. These discoveries will aid future researchers in developing more robust printed electronics for a plethora of emerging applications.

6.2 Recommendations for Future Work

As this thesis presents the novel introduction of a BNNT interfacial layer in flexible electronics, there is still significant work to be done expanding into various material combinations not only for the BNNT dispersion itself, but also certain device layers. Furthermore, as printed electronics becomes more prevalent in everyday technological applications and attempts for more compact device structures are targeted, thermal management solutions will continue to be on the forefront of improving device operability and longevity. There are two areas of future work that I think will be of interest in utilizing the BNNT interlayer; one that focuses on the use of an unconventional substrate material for printed electronics, and one that explores other intrinsic properties of the BNNTs for printed electronics not yet acknowledged in this thesis.

6.2.1 BNNTs for mitigating thermal stress on poly(lactic) acid substrates

Poly-lactic acid (PLA) substrates have become a viable option for printed electronics, providing a biodegradable and biocompatible platform for single-use and disposable devices.[1–3] PLA substrates however have high sensitivity to chlorinated solvents, as well as a low glass transition temperature (T_g) of approximately 63˚C.[4,5] This chemical and temperature sensitivity can severely limit not only the available molecular ink formulations whose conductivity is dependent on its' functional chemistry, but also the curing and thermal processing conditions necessary to successfully convert the ink into conductive traces. Commercialized PLA substrates are typically thin, ranging from 20-40 μm, as fabrication processes for thicker substrates lead to defects that reduce the integrity of the substrate. There are many researched examples of the usefulness of PLA substrates in printed electronics devices, however, only recently has PLA been explored as a substrate in thermoforming.[6–8] The low T_g of the PLA substrate directly influences the thermoforming conditions, as temperature optimization to allow the substrate to properly shift between the amorphous and crystalline states without melting the substrate is key to creating formed PLA substrates.[9] Furthermore, the ink is processed during thermoforming, and so the amount of time that the PLA can withstand underneath the heating element of the thermoformer will also affect the trace morphology and conductive performance. Finding conditions that can facilitate both features is key to fabricated and functional thermoformed traces on PLA substrates.

As previously demonstrated in **Chapter 2** and **Chapter 3**, the BNNT interlayer successfully mitigated damage to the underlying substrate because of heat generated in the trace and dissipated into the substrate during both fabrication and operation respectively. Furthermore, the transition to alcohol-based solvents in **Chapter 4** created a chemically compatible BNNT interlayer for chemically sensitive substrates like PLA. Finally, as demonstrated in **Chapter 5**, the use of the BNNTs will improve the trace morphology upon elongation of the substrate and thinning of the trace transitioning from a 2D trace into a 3D feature. The points of interest in a study of this direction would therefore optimize the usefulness of the BNNTs on simultaneously reducing heat transfer to the PLA substrate when using high energy and high throughput processing techniques and providing a level of mechanical and thermal robustness when thermoforming, with the goal of reinforced PLA-based disposable packaging or sensor applications.

I have already completed initial optimization of thermoforming PLA with the BNNT interlayer, exploring the boundaries of UV curing as a processing tool to maximize conductivity while minimizing thermal damage to the substrate. Because of the PLA's low T_g, the temperature within the UV curing chamber must stay below that of the substrate while simultaneously curing the ink, and so factors such as light intensity percentage, distance from the light source, and time under exposure all affect the integrity of the surrounding substrate and influence the quality of the trace. Furthermore, various thermoforming conditions have also been explored, optimizing for the heat intensity, time under exposure, and effect of ramp up temperature on the success of transitioning the PLA into a crystalline state without causing it to melt and successfully creating thermoformed conductive traces on PLA. Through this optimization, traces with and without BNNT were studied, to determine whether the thin film of nanotubes was enough to prevent significant thermal damage to the substrate and the printed traces.

We determined that incorporation of the BNNT interlayer led to excessive spreading of the desired molecular ink formulation as shown in the cross-sectional images in **Figure 6.1** and **6.2**, likely due to the chosen carrier in the ink formulation and its interactions with the non-covalently functionalized BNNT surface. After UV curing, traces with varying width (1–20 mil nominal width) were subjected to a trapezoidal mould with a 35˚ thermoforming degree and it was determined that those formed with the BNNT interlayer present produced higher conductive traces across one of the harsh elongation points, as shown in **Figure 6.2**, indicating that the BNNTs were sufficient in improving conductive performance of thermoformed traces on commercial PLA substrates. It is also shown that while the printed traces have a larger width, the BNNTs assisted in improving the morphology of the ink on PLA substrates, also visualized in **Figure 6.2**, where less cracking is visible at higher line widths of 15 mil and 20 mil.

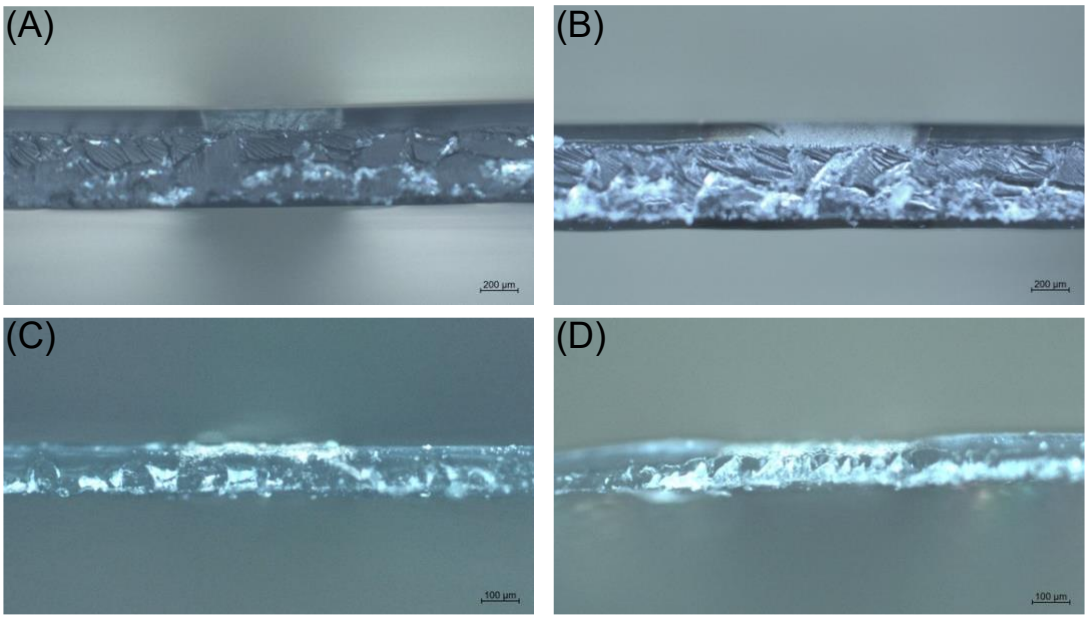

Figure 6.1. Cross-sectional microscope images of silver MINK traces printed on polycarbonate substrates A) without, and B) with the BNNT interlayer. Similar images are taken of traces printed on 90 micron-thick PLA substrates C) without, and D) with the BNNT interlayer present.

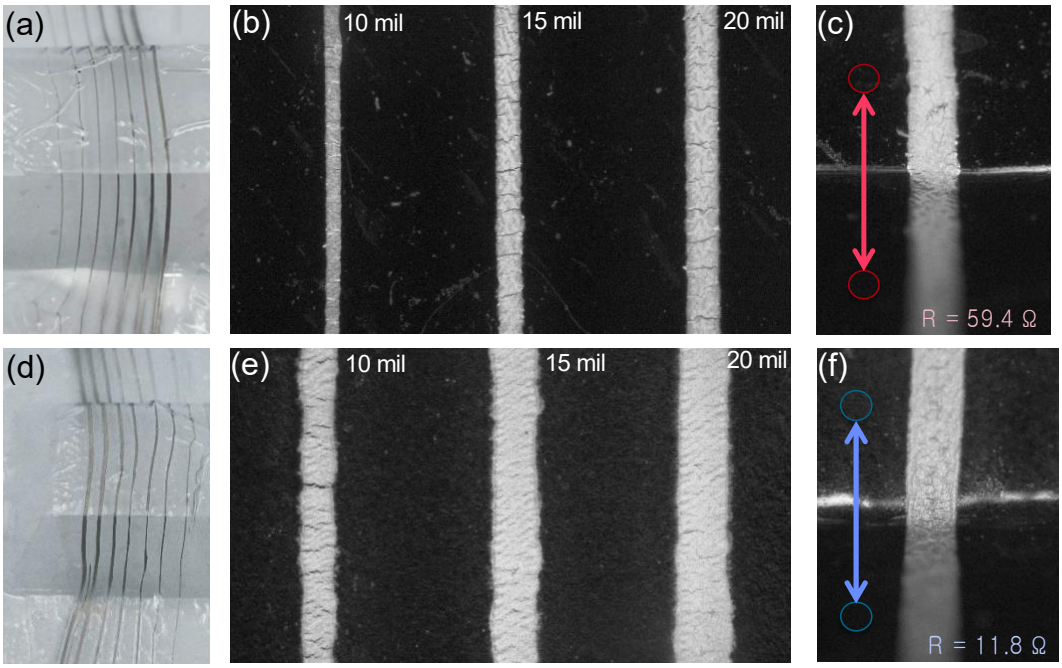

Figure 6.2. Images of thermoformed silver MINK traces subjected to a 35˚ trapezoidal mould on bare substrate with corresponding microscope images of traces along the top of the mould and at one of the harsh elongation points on A-C) bare PLA and D-F) BNNT-coated PLA respectively

While these initial tests of silver MINK on thermoformed PLA produced respectable electrical performances, the thinness of the PLA substrate led to challenges in reproducibility. The commercial substrates acquired for this study were only 40 μm thick, and while they could be successfully thermoformed on their own with no ink, they were too thin to withstand the curing process necessary to reduce the ink into its metallic state. Hot pressing was employed to bond two sheets of PLA to create a new substrate with a measured thickness of 90 μm, which was used to create the thermoformed features presented in **Figure 6.2**. However, variability of the hot-pressing process created an inconsistent seal between the two sheets, and as such there was too much variability in the electrical performance of multiple traces post-thermoforming to constitute a successful demonstration of MINK traces on PLA. Furthermore, due to this performance inconsistency, thermal testing like those done throughout the thesis Chapters 2 – 5 could not be conducted. To continue this study, it is recommended to employ thicker commercial PLA substrates, as it is the current limiting factor in isolating for the effects of the BNNTs. If the BNNTs demonstrate to improve the effects of processing and thermoforming conditions with the substrate as they are hypothesized to, a relationship between thickness of the substrate and BNNT surface concentration should be explored to determine if there is an optimal balance in maintaining the substrate's integrity and optical transparency of the substrate if thicker BNNT interlayers are required.

6.2.2 Radiation shielding of printed electronics for space applications

There has an influx of materials research to miniaturize and reduce the weight of spacecrafts and satellites going into orbit, some leading to commercialization of 3D-printed space craft components.[10,11] At its base, printed electronics could provide an easy and reliable platform to replace rigid and heavy wiring components used in traditional crafts and reduce the overall weight of the spacecraft. Electronic devices, such as solar cell arrays and sensors, could benefit from transitioning to fully printable devices on flexible substrates, as they can also be moulded to unconventional architectures, as has been shown through thermoforming techniques in **Chapter 5** of this thesis, further reducing the volume requirements of the spacecraft.[12] However, electronic devices, primarily on the exterior of the craft, require research to withstand harsh pre- and post-launch environments, such as extreme fluctuations of temperature, pressure, humidity, and the

effects of space radiation once in orbit.[13,14] For space radiation complications in particular, BN materials have become a fast-growing option to act as a well-performing solution.[15]

As demonstrated across multiple chapters in this thesis, BNNTs exhibit several key properties that can be taken advantage of to improve both electrical and thermal performance parameters in printed electronic devices. One property left unexplored in this thesis is BNNTs' intrinsic radiation shielding properties, with recent research highlighting its usefulness in medical applications and as mentioned, orbiting aerospace applications. Spacecrafts and satellites are affected by significant radiation damage, as they are constantly bombarded by electrons and protons, solar energetic particles (SEP), and galactic cosmic radiation (GCR) when no longer protected by the earth's atmosphere and magnetosphere.[16,17] When humans and spacecraft are exposed to GCR, the interactions with the spacecraft can generate neutrons and gamma rays from nuclear collisions of high-charge particles, and as such pose an issue for spacecraft longevity as well as human health in space environments.[18–20] Since one of the limiting factors of commercial spaceflight is the cost of the components and the fuel required to send such heavy machinery into orbit, it is important for researchers to explore low-density and low-weight materials, like BNNTs, that still hold the desired radiation shielding properties.

The elemental materials of BNNTs and other BN material includes boron, which has the largest neutron capture cross section, as well as nitrogen, which as well as has a higher neutron capture cross section than carbon.[15] Furthermore, enriching the BNNTs with the isotope ^{10}B or hydrogen has been shown to improve the neutron capture radius and make it more effective at radiation shielding.[21,22] In research surrounding radiation shielding using BN and BNNT materials, it has centered around composite materials that are significantly thicker ($\geq$ 1 mm) to maintain a level of mechanical stability, however BN material's low density does not significantly limit the weight of the craft or payload.[23–26] Since BNNT interlayers have been demonstrated as a stable free-standing film in **Chapters 2 – 4** of this thesis, it is hypothesized that it could be integrated as an encapsulation layer in exterior sensing devices to reduce radiation damage to the physical and chemical components of the device, without compromising any required transparency of the device.

I recommend developing a structure property relationship between the extent of protection from radiation damage printed traces and underlying substrate, against the required surface density of nanotube network to be useful in efforts to retain translucency of the substrate. Furthermore,

new functionalization of the nanotubes could be explored to improve the radiation capture potential of atomic oxygen, which is known to cause ion damage to spacecrafts and satellites in low-earth orbit, requiring various chemical compatibility experiments to tailor useful materials with the harsh environment limitations of space flight.

6.3 References

(1) Ma, M.; Wang, X.; Liu, K.; Chen, S.; Shi, Y.; He, H.; Wang, X. Achieving Simultaneously Toughening and Flame-Retardant Modification of Poly(Lactic Acid) by in-Situ Formed Cross-Linked Polyurethane and Reactive Blending with Ammonium Polyphosphate. *J. Mater. Sci.* **2022**, *57* (9), 5645–5657. https://doi.org/10.1007/s10853-022-06887-5.

(2) Tasangtong, B.; Sirichan, K.; Hasoon, C.; Na Nongkhai, P.; Rodthongkum, N.; Sameenoi, Y. Fabrication of Biocompatible and Biodegradable Cloth-Based Sweat Sensors Using Polylactic Acid (PLA) via Stencil Transparent Film-Printing. *Sens. Actuators B Chem.* **2024**, *408*, 135513. https://doi.org/10.1016/j.snb.2024.135513.

(3) Rai, P.; Mehrotra, S.; Gautam, K.; Kar, A. K.; Saxena, A.; Patnaik, S.; Anbumani, S.; Pandey, A.; Priya, S.; Sharma, S. K. Polylactic Acid/Tapioca Starch/Banana Peel-Based Material for Colorimetric and Electrochemical Biosensing Applications. *Carbohydr. Polym.* **2023**, *302*, 120368. https://doi.org/10.1016/j.carbpol.2022.120368.

(4) Hsiao, M.; Nagai, K. Degradation Phenomenon of Compostable Poly(Lactic Acid) Films Induced by Pure Halogenated Liquid Chemicals and Mixtures with Water. *Polym. Degrad. Stab.* **2024**, *229*, 110997. https://doi.org/10.1016/j.polymdegradstab.2024.110997.

(5) Ayutthaya, W. D. N.; Poompradub, S. Thermal and Mechanical Properties of Poly(Lactic Acid)/Natural Rubber Blend Using Epoxidized Natural Rubber and Poly(Methyl Methacrylate) as Co-Compatibilizers. *Macromol. Res.* **2014**, *22* (7), 686–692. https://doi.org/10.1007/s13233-014-2102-1.

(6) Goument, C.; Gerges, T.; Lombard, P.; Lakhdar, H.; Arli, M.; Gilmus, V. M.; Lambert, S. A.; Allard, B.; Charmeau, J.-Y.; Cabrera, M. In-Mold Electronics on Poly(Lactic Acid): Towards a More Sustainable Mass Production of Plastronic Devices. *Int. J. Adv. Manuf. Technol.* **2023**, *125* (5–6), 2643–2660. https://doi.org/10.1007/s00170-023-10878-4.

(7) Popescu, D.; Baciu, F.; Vlăsceanu, D.; Marinescu, R.; Lăptoiu, D. Investigations on the Fatigue Behavior of 3D-Printed and Thermoformed Polylactic Acid Wrist–Hand Orthoses. *Polymers* **2023**, *15* (12), 2737. https://doi.org/10.3390/polym15122737.

(8) Gonon, H.; Srisa, A.; Promhuad, K.; Chonhenchob, V.; Bumbudsanpharoke, N.; Jarupan, L.; Harnkarnsujarit, N. PLA Thermoformed Trays Incorporated with Cinnamaldehyde and Carvacrol as Active Biodegradable Bakery Packaging. *Food Packag. Shelf Life* **2023**, *38*, 101123. https://doi.org/10.1016/j.fpsl.2023.101123.

(9) Lee, R. E.; Guo, Y.; Tamber, H.; Planeta, M.; Leung, S. N. S. Thermoforming of Polylactic Acid Foam Sheets: Crystallization Behaviors and Thermal Stability. *Ind. Eng. Chem. Res.* **2016**, *55* (3), 560–567. https://doi.org/10.1021/acs.iecr.5b03473.

(10) Ishfaq, K.; Asad, M.; Mahmood, M. A.; Abdullah, M.; Pruncu, C. Opportunities and Challenges in Additive Manufacturing Used in Space Sector: A Comprehensive Review. *Rapid Prototyp. J.* **2022**, *28* (10), 2027–2042. https://doi.org/10.1108/RPJ-05-2022-0166.

(11) Levchenko, I.; Bazaka, K.; Belmonte, T.; Keidar, M.; Xu, S. Advanced Materials for Next-Generation Spacecraft. *Adv. Mater.* **2018**, *30* (50), 1802201. https://doi.org/10.1002/adma.201802201.
(12) Plis, E. A.; Badura, G. The Spectral Characterization of Novel Spacecraft Materials in the Low Earth Orbit Environment. *J. Astronaut. Sci.* **2024**, *71* (2), 15. https://doi.org/10.1007/s40295-024-00436-9.
(13) Altino, K.; Burns, K. L.; Barbré, R. E.; Leahy, F. Analyzing the Impacts of Natural Environments on Launch and Landing Availability for NASA's Exploration Systems Development Programs. In *SpaceOps 2014 Conference*; American Institute of Aeronautics and Astronautics: Pasadena, CA, 2014. https://doi.org/10.2514/6.2014-1647.
(14) Paternò, G. M.; Robbiano, V.; Fraser, K. J.; Frost, C.; García Sakai, V.; Cacialli, F. Neutron Radiation Tolerance of Two Benchmark Thiophene-Based Conjugated Polymers: The Importance of Crystallinity for Organic Avionics. *Sci. Rep.* **2017**, *7* (1), 41013. https://doi.org/10.1038/srep41013.
(15) Cheraghi, E.; Chen, S.; Yeow, J. T. W. Boron Nitride-Based Nanomaterials for Radiation Shielding: A Review. *IEEE Nanotechnol. Mag.* **2021**, *15* (3), 8–17. https://doi.org/10.1109/MNANO.2021.3066390.
(16) Rahman, M.; Shankar, D.; Santra, S. Analysis of Radiation Environment and Its Effect on Spacecraft in Different Orbits. **2017**.
(17) Ghazizadeh, M.; Estevez, J. E.; Kelkar, A. D.; Joint School of Nanoscience and Nanoengineering, North Carolina A&T State University and University of North Carolina at Greensboro, USA. Boron Nitride Nanotubes for Space Radiation Shielding. *Int. J. Nano Stud. Technol.* **2015**, 1–2. https://doi.org/10.19070/2167-8685-150007e.
(18) McCarthy, E. F. Perspective: Skeletal Complications of Space Flight. *Skeletal Radiol.* **2011**, *40* (6), 661–663. https://doi.org/10.1007/s00256-011-1100-z.
(19) Sihver, L.; Kodaira, S.; Ambrozova, I.; Uchihori, Y.; Shurshakov, V. Radiation Environment Onboard Spacecraft at LEO and in Deep Space. In *2016 IEEE Aerospace Conference*; IEEE: Big Sky, MT, USA, 2016; pp 1–9. https://doi.org/10.1109/AERO.2016.7500765.
(20) Wang, J.-A. J.; Jr, R. C. S.; Ellis, R. J.; Hunter, H. T. Radiation Effects on Spacecraft Structural Materials; 2002.
(21) Thibeault, S. A.; Kang, J. H.; Sauti, G.; Park, C.; Fay, C. C.; King, G. C. Nanomaterials for Radiation Shielding. *MRS Bull.* **2015**, *40* (10), 836–841. https://doi.org/10.1557/mrs.2015.225.
(22) Estevez, J. E.; Ghazizadeh, M.; Ryan, J. G.; Kelkar, A. D. Simulation of Hydrogenated Boron Nitride Nanotube's Mechanical Properties for Radiation Shielding Applications. **2014**, *8* (1).
(23) Özdemir, T.; Güngör, A.; Reyhancan, İ. A. Flexible Neutron Shielding Composite Material of EPDM Rubber with Boron Trioxide: Mechanical, Thermal Investigations and Neutron Shielding Tests. *Radiat. Phys. Chem.* **2017**, *131*, 7–12. https://doi.org/10.1016/j.radphyschem.2016.10.012.
(24) Saadu Itas, Y.; Baballe, A.; Alodhayb, A.; Haldhar, R.; Hossain, M. K. Radiation Shielding Properties of 35-XBaO-15CaO-5Al2O3-10B2O3-35SiO2-XBNNT (X=5, 10, 15, 20) Glass Reinforced with Boron Nitride Nanotubes. *Opt. Mater.* **2024**, *148*, 114957. https://doi.org/10.1016/j.optmat.2024.114957.
(25) Knott, J. C.; Khakbaz, H.; Allen, J.; Wu, L.; Mole, R. A.; Baldwin, C.; Nelson, A.; Sokolova, A.; Beirne, S.; Innis, P. C.; Frost, D. G.; Cortie, D.; Rule, K. C. Few-Layer

Hexagonal Boron Nitride / 3D Printable Polyurethane Composite for Neutron Radiation Shielding Applications. *Compos. Sci. Technol.* **2023**, *233*, 109876. https://doi.org/10.1016/j.compscitech.2022.109876.

(26) Bacca, N.; Zhang, C.; Paul, T.; Sukumaran, A. K.; John, D.; Rengifo, S.; Park, C.; Chu, S.-H.; Mazurkivich, M.; Scott, W.; Agarwal, A. Tribological and Neutron Radiation Properties of Boron Nitride Nanotubes Reinforced Titanium Composites under Lunar Environment. *J. Mater. Res.* **2022**, *37* (24), 4582–4593. https://doi.org/10.1557/s43578-022-00708-w.

Chapter 7: Additional Contributions

7.1. Aerosol jet printed temperature sensors using an environmentally friendly bilayer dielectric

Tousignant, M. N.; Tischler, V.; Wagner, K.; Lin, Z. S.; Brusso, J.; Izquierdo, R.; Lessard, B. H. Aerosol Jet Printed Temperature Sensors Using an Environmentally Friendly Bilayer Dielectric. *Flex. Print. Electron.* **2024**, *9* (1), 015012.

Publication Date: March 15th, 2024

DOI: doi.org/10.1088/2058-8585/ad2ece.

Abstract:

With the rise of the internet of things and applications such as smart packaging, the need for low cost, disposable temperature sensors with minimum environmental impact are critical. In this study, we report fully printed capacitive temperature sensors made from bio-degradable dielectric materials. All layers were aerosol jet printed, and the areal capacitance was characterized at several temperatures between room temperature (22 ˚C) and 80 ˚C. Using a bilayer dielectric structure, a layer of poly (vinyl alcohol) (PVA) was encapsulated with polycaprolactone (PCL) through interfacial crosslinking to protect it against humidity. Various concentrations and layer amounts of PVA were investigated, with the most effective capacitors consisting of a single layer of PVA deposited from a 5.0 mg ml^{-1} solution followed by a layer of the UV-crosslink-able PCL deposited from 2.0 mg ml^{-1} solution, achieving a 43 ± 6% increase in areal capacitance at 80 ˚C when compared to room temperature, measured at a frequency of 501 Hz.

Contributions:

I visualized the 3D profilometry images for this study and edited and reviewed the manuscript.